UNIVERSITY OF SOUTHAMPTON

FACULTY OF NATURAL AND ENVIRONMENTAL SCIENCES

School of Ocean and Earth Science

Palaeoceanographic change during the Palaeocene/Eocene thermal maximum in Arctic Spitsbergen

by

Adam J. Charles

Thesis for the degree of Doctor of Philosophy

July 2011

ABSTRACT

The interaction of the ocean, atmosphere and ice in the Arctic region plays a critical role in modulating global climate. However, recent observations have illustrated the region is changing rapidly in response to anthropogenically-induced warming. Given the uncertainty in climate model predictions, one way to analyse the response of the Arctic to warming is to generate records through transient warm intervals from the geological past. However, the most pronounced warming event of the Cenozoic, known as the Palaeocene/Eocene thermal maximum (PETM), is poorly documented in the Arctic region.

Therefore, in order to place further constraints on environmental conditions in the high Arctic during the PETM, this thesis documents results from two new PETM localities in the Spitsbergen Central Basin, the BH9/05 core and the Bergmanfjellet outcrop section. Results from sedimentological, palynofacies and dinoflagellate cyst (dinocyst) analyses have been compared to previous results from the Longyearbyen section (Spitsbergen) and Intergrated Ocean Drilling Project Site 302-4A in order to analyse spatial and temporal changes across the event in this high Arctic setting. Analysis of Fe and Mn XRF time-series from core BH9/05 has been used to construct a cyclostratigraphic age model to constrain temporal changes. Together with radio-isotopic dating of a bentonite layer within the PETM, the cyclostratigraphic age model implies that the onset of the event occurred on a falling limb of the 405 kyr eccentricity cycle (between 55.728 and 55.964 Ma). Given that other early Palaeogene transient warming events (hyperthermals) have consistently been documented at the peak of both 100 and 405 kyr eccentricity cycles, or on the rising limb of such cycles, this suggests the PETM may have been initiated by a different mechanism compared to other hyperthermals.

Furthermore, comparison of dinocyst assemblages across the Spitsbergen Central Basin illustrates a pronounced influx of the low salinity tolerant taxon *Senegalinium* during the PETM, consistent with a regime of enhanced precipitation and runoff. Such conditions led to salinity stratification, which together with elevated productivity and the warming of Arctic waters led to sedimentary anoxia and enhanced burial of marine organic matter. As the mechanisms driving anoxia and elevated productivity seen in the Central Basin would be expected to occur across the Arctic region, it is probable that the enhanced burial of contemporary marine organic matter was a pan-Arctic phenomenon in marginal settings. Given the burial of this type of organic matter sequesters carbon directly from the exogenic system, this suggests that the Arctic would have been a significant carbon sink during the PETM.

Contents

Appendix 2: Constraints on the numerical age of the Palaeocene/Eocene boundary

Includes:

File A2.1: Readme detailing the contribution of Adam J. Charles to the Charles *et al*. (2011) publication

File A2.2: Copy of Charles *et al*. (2011), *Geochem. Geophys. Geosyst*., *12*, doi:10.1029/2010GC003426

File A2.3: Data utilised in Charles *et al*. (2011)

Appendix 3: Data generated for Chapter 3; A low salinity Arctic during the Palaeocene/Eocene thermal maximum: new evidence from dinoflagellate cysts

Includes:

File A3.1: Dinocyst data from core BH9/05 and Bergmanfjellet, and carbon isotope data from the latter locality. All data generated by Adam J. Charles. Note the slides utilized to generate the dinocyst data are deposited within the University of Southampton collection.

Appendix 4: Data generated for Chapter 4; Reconstructing basin-scale carbon burial during the Palaeocene/Eocene thermal maximum in Arctic Spitsbergen

Includes:

File A4.1: TOC data from Bergmanfjellet, and palynofacies data from core BH9/05. All data generated by Adam J. Charles.

Appendix 5: Slow release of fossil carbon during the Palaeocene–Eocene Thermal Maximum (Cui *et al*. 2011)

Includes:

File A5.1: Readme detailing the contribution of Adam J. Charles to the Cui *et al*. (2011) publication

File A5.2: Copy of Cui *et al*. (2011), *Nat. Geosci.*, *4*, 481-485

File A5.3: Copy of Cui *et al*. (2011) supplementary material

Appendix 6: representative images of key dinocyst taxa

Includes:

File A6.1: Plate containing images of key dinocyst taxa utlised in Chapter 3 to infer palaeoceanographic changes

List of figures

Chapter 1: Introduction

Chapter 2: Constraints on the numerical age of the Palaeocene/Eocene boundary

Chapter 3: A low salinity Arctic during the Palaeocene/Eocene thermal maximum: new evidence from dinoflagellate cysts

Chapter 4: Reconstructing basin-scale carbon burial during the Palaeocene/Eocene thermal maximum in Arctic Spitsbergen

Chapter 5: Discussion, conclusions and future work

List of tables

DECLARATION OF AUTHORSHIP

I, Adam Charles

declare that the thesis entitled

Palaeoceanographic change during the Palaeocene/Eocene thermal maximum in Arctic Spitsbergen

and the work presented in the thesis are both my own, and have been generated by me as the result of my own original research. I confirm that:

- this work was done wholly or mainly while in candidature for a research degree at this University;
- where any part of this thesis has previously been submitted for a degree or any other qualification at this University or any other institution, this has been clearly stated;
- where I have consulted the published work of others, this is always clearly attributed;
- where I have quoted from the work of others, the source is always given. With the exception of such quotations, this thesis is entirely my own work;
- I have acknowledged all main sources of help;
- where the thesis is based on work done by myself jointly with others, I have made clear exactly what was done by others and what I have contributed myself;
- part of this work has been published as: Charles *et al*. (2011), *Geochemistry*, *Geophysics*, *Geosystems*, 12, doi:10.1029/2010GC003426.

Signed: ……..

Date:……

Acknowledgements

The work presented within this thesis could not have been carried out without the advice and support I received from friends and colleagues, as well as the logistical and financial backing of several organisations. I would like to extend my gratitude to everyone listed below, as they all contributed to the work presented here.

The project was funded by the Natural Environment Research Council (NERC), with additional support from Shell UK. James Eldrett and Willem Schuurman of Shell UK require a special mention for implementing the CASE partnership with Shell, as well as co-ordinating my trips to Aberdeen. The work undertaken in Spitsbergen would not have been possible without the aid from Store Norske Spitsbergen Grubekompani, who provided logistical help on multiple occasions, as well as permitting access to drill core material for sampling. I am especially grateful to Nils Tokheim and Malte Jochmann, as both gave up their time on numerous occasions to provide me with help and advice.

I consider myself to be very fortunate to have worked with two PhD supervisors who were always available for a quick chat and some helpful advice to boost my spirits, Ian Harding and John Marshall. The time I spent discussing my science with Ian and John dramatically improved my writing, critical thinking and ability to discuss my science with others, for which I am extremely grateful.

At the onset of my PhD, I was lucky enough to attend the first meeting of the Worldwide University Networks paleo-Arctic Climates and Environments (WUN pACE) meeting in Spitsbergen. The results of the subsequent collaborations are evident in the following chapters, and so I would like to extend my thanks to WUN pACE organiser-in-chief Tim White, who put in countless hours to get the project online and keep it going. In 2008, WUN pACE sampled core BH9/05, with Henning Dypvik, Jeno Nagy, Lars Riber, David Jargvoll, and Jonna Poikolainen requiring a special mention for their exertions in the core store. During this time, John Hurley's logistical advice regarding the use of the Niton UK XRF scanner was invaluable. The WUN research mobility programme also kindly funded a month's placement at Utrecht University, where helpful discussions with Henk Brinkhuis, Appy Sluijs, Sander Houben and Peter Bijl took place.

Whilst processing my palynology and TOC samples in the lab, Shir Akbari provided a tremendous amount of logistical help, as well as interesting stories to keep me going. I would also like to thank Mike Bolshaw and Dave Spanner for the help they provided when I was generating my carbon isotope data, as well as Paul Cornick at Petrostrat for

discussions regarding dinocyst taxonomy. Steve Bohaty also deserves special thanks for the excellent advice he gave me whilst dealing with the reviewers' comments for the first Spitsbergen paper published in EPSL. Along the same lines I would also like to thank Dan Condon, Heiko Pälike, Ying Cui, Lee Kump and Ian Croudace for their contributions to the recently published *Geochemistry Geophysics Geosystems* paper (Chapter 2), which dramatically helped to improve the manuscript. The efforts of Rebecca Hodgkinson, Marcus Badger and Richard Pancost have also made the conclusions to Chapter 4 much more robust, and their contributions are therefore much appreciated.

Others requiring a special mention include Paul Wilson, who provided me with some part-time lab work enabling me to write up in Southampton, which permitted me to discuss my science with other scientists on a daily basis as I wrote the thesis. Working in the lab during the arduous task of completing the thesis also proved to be a good distraction, with Megan Spencer and Cristina Sghibartz providing amusing anecdotes and banter to keep my spirits up. For the same reason, I would also like to thank all my friends who have kept me going of the last four years, especially Anna Kaczmarska, Aldo Aquino-Cruz and Pornsri Mingkwan, who were there from the start. Last, but by no means least, I would like to thank my family for their unconditional support, saying the right things at the right time, and for the number of times they have had to put up with me complaining to them about my data, without understanding what I was talking about! To all of you, I would like to say a giant thank you, I hope this thesis justifies all the help and advice you have given me through the years!

Chapter 1: Introduction

1.1 The importance of the Arctic climate system

The interaction of the ocean, atmosphere and ice in the Arctic plays a critical role in modulating global climate, and modern temperature records illustrate that the region is warming at a faster rate than lower latitudes in response to anthropogenically induced global warming (IPCC AR4 2007). The volume of both Arctic sea ice and continental ice sheets affects planetary albedo, which in turn regulates the net amount of solar radiation absorbed at the Earth's surface and thus surface temperatures (IPCC AR4 2007). A consequence of the current temperature increases in high northern latitudes is the rapid decline in both the volume and geographic extent of the Arctic sea ice (Comiso *et al*. 2008; Stroeve *et al*. 2008). This has led to predictions that summer (September) sea ice will be lost before the year 2100, and potentially as soon as 2037 (Boé *et al*. 2009; Wang and Overland 2009). The increased temperatures have also resulted in an increase in mass wasting from continental ice caps (IPCC AR4 2007) which, coupled with increases in precipitation, have resulted in an increase in freshwater runoff into the Arctic Ocean and North Atlantic via the Fram and Denmark straits (Peterson *et al*. 2002, 2006). Such increased runoff will decrease water density and therefore hinder the formation of North Atlantic deep water (Rahmstorf 2002). In this way perturbations in Arctic climate have, and will continue to exert, a major influence on global thermohaline circulation and thus global climate (Rahmstorf 2002).

However, there is a considerable degree of uncertainty associated with climate models which suggest the response of the region to global climate change (Figure 1.1). Although the models agree that Arctic surface air temperatures will rise further, estimates of mean temperature rise by the year 2100 range from +2.8ºC to +7.8ºC (mean ensemble value +5 ºC, A1B scenario; IPCC AR4 2007). These estimates are further complicated by the uncertainty associated with the quantity of fossil fuels that will be released by future generations, which alters the mean ensemble temperature increase depending on the quantity of fossil fuels incorporated in the model runs (mean 5.2ºC increase in A2 scenario; 3.4ºC B2 scenario; IPCC AR4 2007). Similar uncertainties exist in predictions of precipitation changes (Figure 1.1). Again, models agree that precipitation will increase in the Arctic region by 2100 (mean ensemble value +18%, A1B scenario), with the greatest increases in winter (December, January, February). However, the range of the predicted precipitation change is significant, with minimum predicted increases of 10 %, and maxima of 28 % (IPCC AR4 2007).

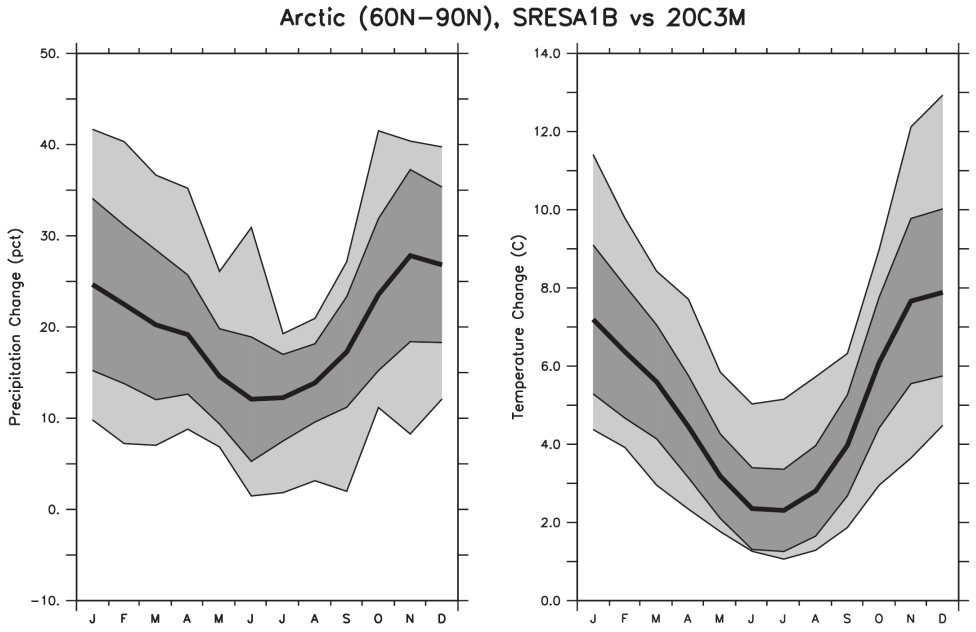

Figure 1.1: Projected annual precipitation and temperature changes in the Arctic region (above 60˚N) for the A1B scenario. Changes were calculated by subtracting the average temperature and precipitation changes from 1980-1999 from those from 2080-2099 for the IPCC model ensemble (21 models). Thick black line represents the average, with the dark grey line represent the 25 and 75% quartiles respectively. Light grey shaded region represents the total range of the models. From IPCC AR4 (2007).

1.2 Informing Arctic climate predictions using an ancient fossil analogue: the Palaeocene-Eocene thermal maximum

Given the uncertainty inherent in future climate predictions, one way to provide empirical data demonstrating the response of Arctic climate to transient warming events is to generate climatic records of such events from the geological past. One such event, the Palaeocene-Eocene thermal maximum (PETM, ~56 Ma; Kennett and Stott 1991; Sluijs *et al*. 2007a), has been taken as an ancient analogue for anthropogenic global warming. The different boundary conditions in the Palaeogene (such as plate tectonic configuration [Figure 1.2], ocean circulation and the lack of continental ice sheets) prevent direct quantitative comparisons between modern warming and that inferred at the PETM. Despite this, analysis of the forcing mechanisms and their associated feedbacks, leads and lags may illustrate how the Earth system responds to transient climatic perturbations. A summary of the key aspects of the PETM is given below.

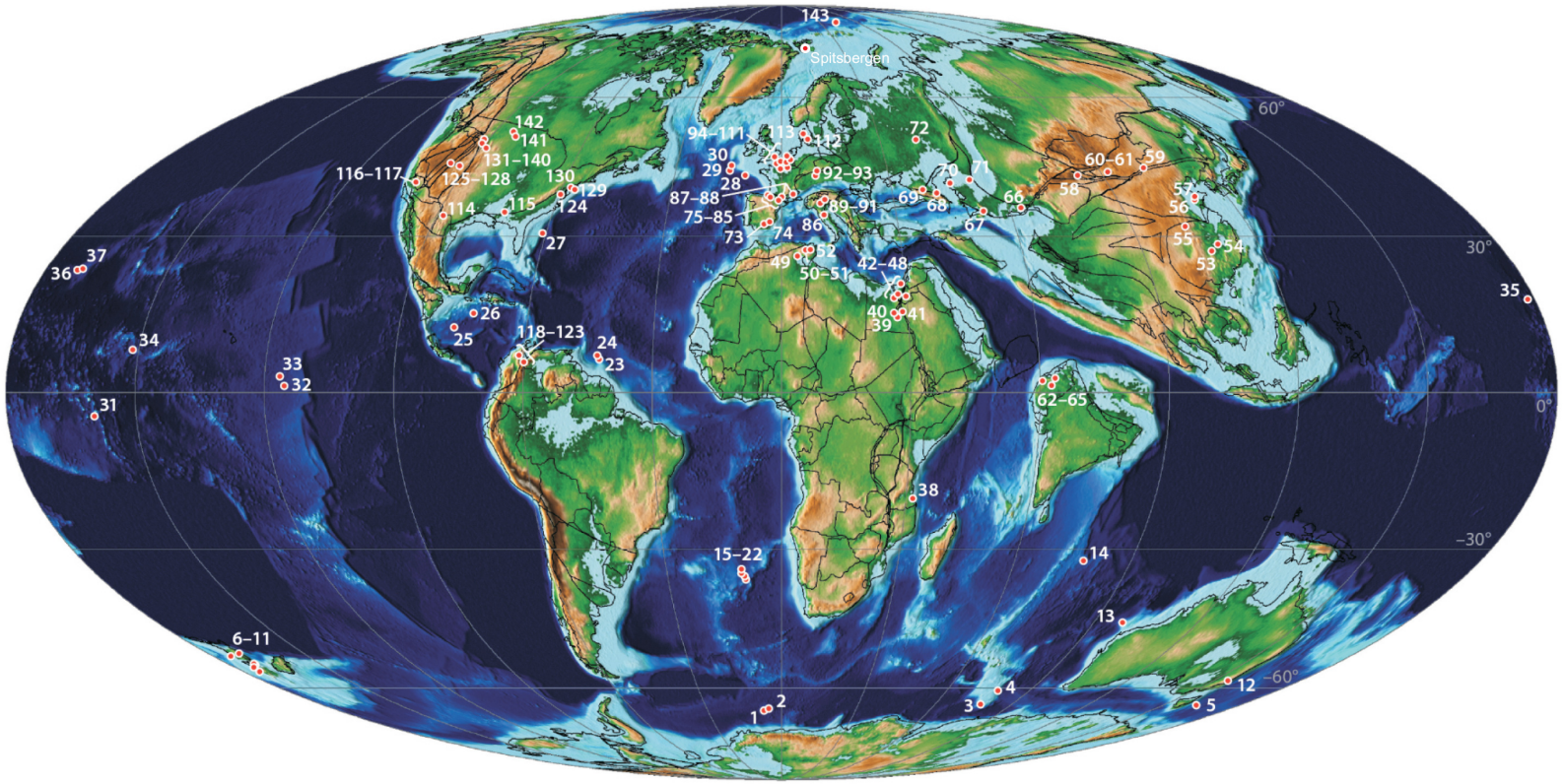

Figure 1.2: Global palaeogeographic reconstruction at ~56 Ma (equatorial projection), illustrating the position of Palaeocene/Eocene boundary sections (modified after McInerney and Wing 2011). See supplemental Table 1 of McInerney and Wing (2011) for full list of site localities. Note the dearth of localities documented in the high northern latitudes.

1.2.1 Transient temperature changes in the exogenic system

Numerous multi-proxy datasets illustrate that atmospheric, sea surface and deep water temperatures increased on a global scale at the PETM (Figures 1.3-1.5; Kennett and Stott 1991; Bains *et al*. 1999; Thomas *et al*. 2002; Zachos *et al*. 2003, 2006, 2008; Tripati and Elderfield 2005; Wing *et al*. 2005; Sluijs *et al*. 2006; 2007b; 2011; Weijers *et al*. 2007; Secord *et al*. 2010). The transient temperature change is recorded by inorganic proxies including bulk carbonate (Bains *et al*. 1999), Mg/Ca and $\delta^{18}O$ from planktonic and benthic foraminiferal calcite (Figure 1.3; Kennett and Stott 1991; Thomas *et al*. 2002; Zachos *et al*. 2003, 2006, 2007, 2008; Tripati and Elderfield 2005), both phosphate and carbonate in mammal tooth enamel (Secord *et al*. 2010), and soil carbonates (Koch *et al*. 1995; Wing *et al*. 2000). Such changes are also recorded from fossil plant leaves (Wing *et al*. 2005), as well as the tetraether lipids of both marine and terrestrial archea (TEX_{86} and the MBT index proxies respectively, Figures 1.4-1.5; Sluijs *et al*. 2006; 2007b; 2011; Zachos *et al*. 2006; Weijers *et al*. 2007). The rises in sea surface temperatures these proxies record range from 5ºC in the tropics (Zachos *et al*. 2003) up to 8-9ºC at the mid-latitudes and poles (Figure 1.3; Kennett and Stott 1991; Sluijs *et al*. 2006; Zachos *et al*. 2006). Such changes are corroborated by proxies for annual mean air temperature, with an ~5˚C rise derived from the mid-latitude Bighorn Basin (Wing *et al*. 2000, 2005; Secord *et al*. 2010), and an ~8˚C rise in the high Arctic (Site 302-4A; Figure 1.5; Weijers *et al*. 2007). Similarly, Mg/Ca and $\delta^{18}O$ proxies indicate deep water temperature increases of ~5˚C (Kennett and Stott 1991; Tripati and Elderfield 2005; Zachos *et al*. 2008). Given the number of different proxies recording this transient temperature increase and the global scale of the records, the temperature rise during the PETM is a robust signal. Furthermore, recent high-resolution studies have suggested that the onset of warming preceded the marked perturbation of the carbon cycle during the PETM (Thomas *et al*. 2002; Sluijs *et al*. 2007b; Secord *et al*. 2010), which has implications for the trigger mechanism of the event (see Section 1.2.8).

1.2.2 The carbon isotope excursion

Stable carbon isotope records ($\delta^{13}C$) demonstrate a marked perturbation of the global carbon cycle during the PETM, with a sharp (2.5-6 ‰) negative carbon isotope excursion (CIE) recorded in both organic and inorganic carbon in marine and terrestrial settings (Figures 1.3-1.7; e.g. Kennett and Stott 1991; Koch *et al*. 1992; Bains *et al*. 1999; Thomas *et al*. 2002; Zachos *et al*. 2003, 2005, 2006, 2007, 2008; Magioncalda *et al*. 2004; Sluijs *et al*. 2006; 2007b; 2011; Handley *et al*. 2008, 2011; Robinson 2011). Together with the shoaling of the calcite compensation depth at the PETM (Section 1.2.5), the negative CIE implies the injection of isotopically light carbon into the exogenic system, either in the form of methane or carbon dioxide (Dickens *et al*.

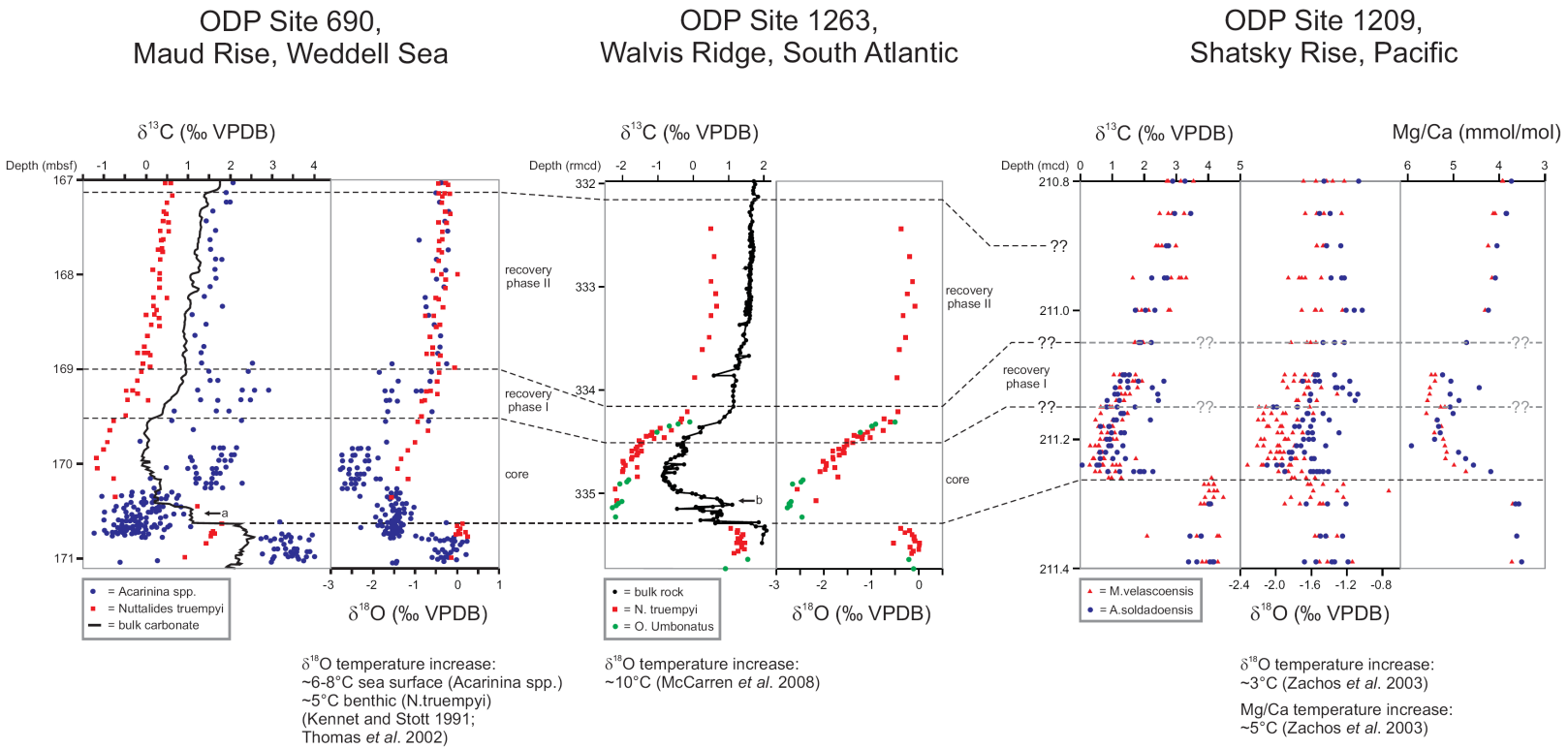

Figure 1.3: Selected deep marine records of the Palaeocene/Eocene boundary. ODP Site 690 bulk carbonate record from Bains *et al*. (1999), with foraminferal isotopic records from Kennett and Stott (1991), Thomas *et al*. (2002) and Kelly *et al*. (2005). ODP Site 1263 bulk carbonate record of Zachos *et al*. (2005), with foraminferal isotopic records from McCarren *et al*. (2008). ODP Site 1209 data from Zachos *et al*. (2003). Note that Site 690 and 1263 foraminiferal isotopic records contain both multi-and single specimen analyses, whilst records from Site 1209 are from single specimens only. CIE phases defined by changes in bulk carbonate (following Röhl *et al*. [2007]) are shown for ODP Sites 690 and 1263. Identification of CIE phases at Site 1209 is complicated by the absence of a bulk record and the scatter associated with $\delta^{13}C$ records of single specimen foraminifera. Arrows 'a' and 'b' indicate intervals where bulk records may be biased by changes in microfossil assemblage/reworking (see text for details).

1995; Kurtz *et al*. 2003; Svensen *et al*. 2004; Higgins and Schrag 2006). Theoretically, the magnitude of the PETM CIE can be used to determine the amount of carbon injected into the exogenic system to cause the inferred warming (Dickens *et al*. 1995, 1997; Panchuk *et al*. 2008; Zeebe *et al*. 2009; Cui *et al*. 2011). Furthermore, the CIE shape can be used together with age models for the PETM to derive the rate of carbon injection at the onset of the event (e.g. Cui *et al*. 2011). Several studies have indeed focused on constraining the magnitude and shape of the PETM CIE (e.g. Bains *et al*. 1999; Bowen *et al*. 2004; Smith *et al*. 2007; Handley *et al*. 2008; Diefendorf *et al*. 2010).

The shape of the PETM CIE has thus been used to split the event into two parts, the 'core' and 'recovery' intervals respectively, with the latter commonly divided into two phases (Figures 1.3-1.4 and 1.6-1.7). A third phase with enhanced burial of carbonate has also been proposed by Murphy *et al*. (2010), but the global correlation of this interval is highly problematic as it can only be defined in oceanic settings. The onset of the PETM is defined as an abrupt negative shift in $\delta^{13}C$ values, which marks the beginning of the 'core' interval of the CIE (Figures 1.3-1.7; Sluijs *et al*. 2007a). Within the core of the CIE, $\delta^{13}C$ values remain relatively depleted compared to pre-CIE values, often resulting in a 'plateau' of $\delta^{13}C$ values (e.g. Bains *et al*. 1999; Magioncalda *et al*. 2004; Zachos *et al*. 2005; Sluijs *et al*. 2007a; 2007b). Subsequently the exponential return of $\delta^{13}C$ to heavier isotopic values defines the 'recovery' interval (Röhl *et al*. 2007; Bowen and Zachos 2010), with an initial more rapid increase to heavier values (phase I) followed by a gradual return to stable (flat trajectory) values in recovery phase II (Figures 1.3-1.7; Röhl *et al*. 2007).

However, whilst the broad trends in the CIE shape described above are consistent between different depositional settings, records are complicated by differences in both the magnitude of the CIE, and changes in $\delta^{13}C$ superimposed on the overall CIE shape (e.g. Sluijs *et al*. 2007a). Such changes can be caused by site specific artefacts, as well as the individual isotopic fractionation factors associated with the different parameters recording carbon cycle perturbation. For example, Bains *et al*. (1999) analysed bulk carbonate $\delta^{13}C$ records from ODP sites 1051 (Blake Nose) and 690 (Weddell Sea), and argued that these records were representative of the CIE shape, as similar inflection points were observed at both localities. Bains *et al*. (1999) argued that short-lived plateau regions between the onset and peak of the CIE (e.g. arrow 'a' in Figure 1.3) were indicative of multiple phases of carbon injection during the onset of the PETM. However, analysis of single specimen foraminifera illustrated no intermediate $\delta^{13}C$ values were present in Site 690 (Figure 1.3; Thomas *et al*. 2002), and nannofossil records illustrate that the plateau regions in the 690 bulk carbonate record correspond

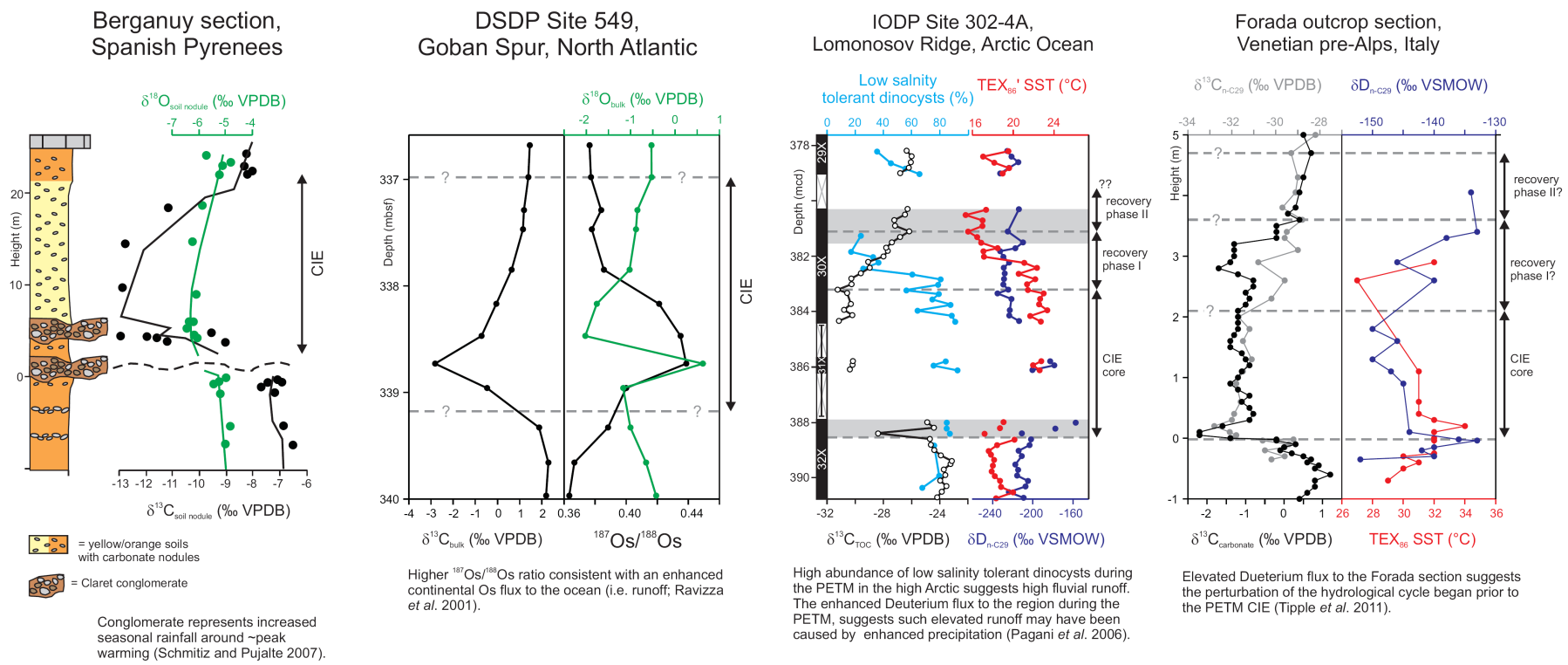

Figure 1.4: Evidence for coupled temperature and hydrological change during the PETM, from selected localities. Berganuy section lithostratigraphy, soil nodule $\delta^{13}C$ and $\delta^{18}O$ data from Schmitz and Pujalte (2007). Black and Green solid lines represent 3pt running average of $\delta^{13}C$ and $\delta^{18}O$ of soil nodules, respectively. DSDP Site 549 data from Ravizza *et al.* (2001). Note the CIE phases are not defined at Berganuy and Site 549 owing to the low resolution $\delta^{13}C$ data. IODP Site 302-4A data from Sluijs *et al.* (2006), other than deuterium data (from Pagani *et al.* 2006). Grey shaded areas represent areas of drilling disturbance. Forada outcrop section data from Tipple *et al.* (2011). CIE phases at Site 302-4A and Forada are plotted according to the definitions of Röhl *et al.* (2007). Note the most enriched deuterium values and the occurrence of a fluvial megafan occur at (or preceeding) the onset of the PETM CIE in Forada, Site 302-4A and Berganuy. This suggests the onset of hydrological cycle perturbation began at/preceding the CIE onset.

to marked assemblage changes. Thus the plateaux may therefore be artefacts of such changes (Bralower 2002). Similar artefacts have been observed in the bulk carbonate record of Site 1263 (Leg 208, Walvis Ridge; arrow 'b' in Figure 1.3), where nannofossil reworking after the PETM onset resulted in a transient positive excursion of bulk $\delta^{13}C$ values within the CIE (Raffi and De Bernardi 2008). This suggests that the plateau regions observed by Bains *et al*. (1999) are artefacts of analysing bulk records composed of several sources of carbonate. The shape of $\delta^{13}C$ records from oceanic records is further complicated by carbonate dissolution at the onset of the PETM (see Section 1.2.5), which led to corrosion and therefore an hiatus at the onset of the event (Zachos *et al*. 2005; McCarren *et al*. 2008). Typically, this results in a jump in $\delta^{13}C$ values, leading to an apparent steepening of the onset region of the PETM CIE (e.g. Figure 1.3; McCarren *et al*. 2008).

1.2.3 The duration of the PETM

To date, bathyal sections have typically been utilised to construct age models which constrain the duration of the PETM CIE (e.g. Norris and Röhl 1999; Röhl *et al* 2000; 2007; Farley and Eltgroth 2003; Murphy *et al*. 2010). Ages for magnetostratigraphic reversals were initially used to derive average sedimentation rates via linear interpolation, enabling the calculation of the CIE duration (e.g. Kennet and Stott 1991). These time scales have subsequently been refined using cyclostratigraphy, with the sedimentation rates derived from palaeomagnetic reversals used to test for the presence of orbital cycles within time series datasets (e.g. Norris and Röhl 1999; Röhl *et al* 2000; 2007; Abdul Aziz *et al* 2008). The identification of precession cycles (~21 kyr), and the number of these cycles within the PETM CIE at ODP Site 1051 led to the first cyclostratigraphic estimate for the duration of the CIE (~150 ±20 kyr, 7 precession cycles; Norris and Röhl 1999). Subsequently, comparison of Site 1051 with Site 690 led to the identification of an hiatus at the base of a chalk clast layer in the former, and a revised estimate of 210-220 kyr for the duration of the CIE (11 precession cycles) based on the stratigraphically more complete Site 690 (Röhl *et al*. 2000). However, time series datasets from multiple sites on the Walvis Ridge illustrated that the number of precession cycles at Site 690 was overestimated by Röhl *et al*. (2000), owing to the low signal-to-noise ratio in Ca records at this site (Röhl *et al*. 2007). Analysis of the Walvis Ridge sites and additional barium data from Site 690 led Röhl *et al*. (2007) to calculate a CIE duration of 170 kyr (8.5 precession cycles; Figure 1.7), with similar estimates derived from terrestrial sections in the Bighorn Basin (157 kyr, 7.5 precession cycles, Polecat Bench and Red Butte sections: Abdul-Aziz *et al*. 2008).

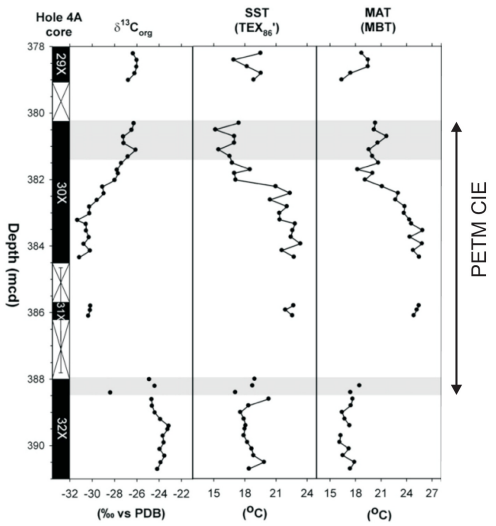

Figure 1.5: Sea surface (SST) and annual mean air temperature (MAT) changes across the PETM from the Arctic (Site 302-4A, Lomonosov Ridge, Arctic Ocean). MAT records derived using the Methylation index of Branched Tetraethers (MBT) proxy (see Weijers *et al*. [2007] for details). Grey bars indicate intervals of drilling disturbance. Bulk organic carbon and TEX_{86}' records from Sluijs *et al*. (2006), with MAT record from Weijers *et al*. (2007).

However, as noted in Section 1.2.5, the deep sea records utilised in the studies just described are affected by carbonate dissolution, leading to the truncation of cycles in time series records, and therefore the underestimation of the duration of the CIE onset (Röhl *et al*. 2007). This problem is compounded by the changes in sedimentation rate associated with the change from carbonate to clay deposition, preventing filtering of time-series records in the depth domain and making cycle identification subjective (Murphy *et al*. 2010). Finally, the use of bulk carbonate records to define the duration of particular phases of the CIE is also problematic, as the admixed nature of these records may have altered the shape of the CIE (e.g. Figure 1.3; Bralower 2002; Raffi and De Bernardi 2008), thus hindering correlation between different depositional settings.

One way to avoid some of the problems associated with cyclostratigraphic PETM records in bathyal settings is to construct extraterrestrial ^{3}He age models (Farley and Eltgroth 2003; Murphy *et al*. 2010). On the timescale of the PETM the ^{3}He flux to the sediment has been inferred to have been constant, and therefore the concentration of extraterrestrial ^{3}He in the sediment can be used to infer sedimentation rates (Farley and Eltgroth 2003; Murphy *et al*. 2010). Farley and Eltgroth (2003) argued that the duration of the entire PETM was <120 kyr based on ^{3}He records from Site 690.

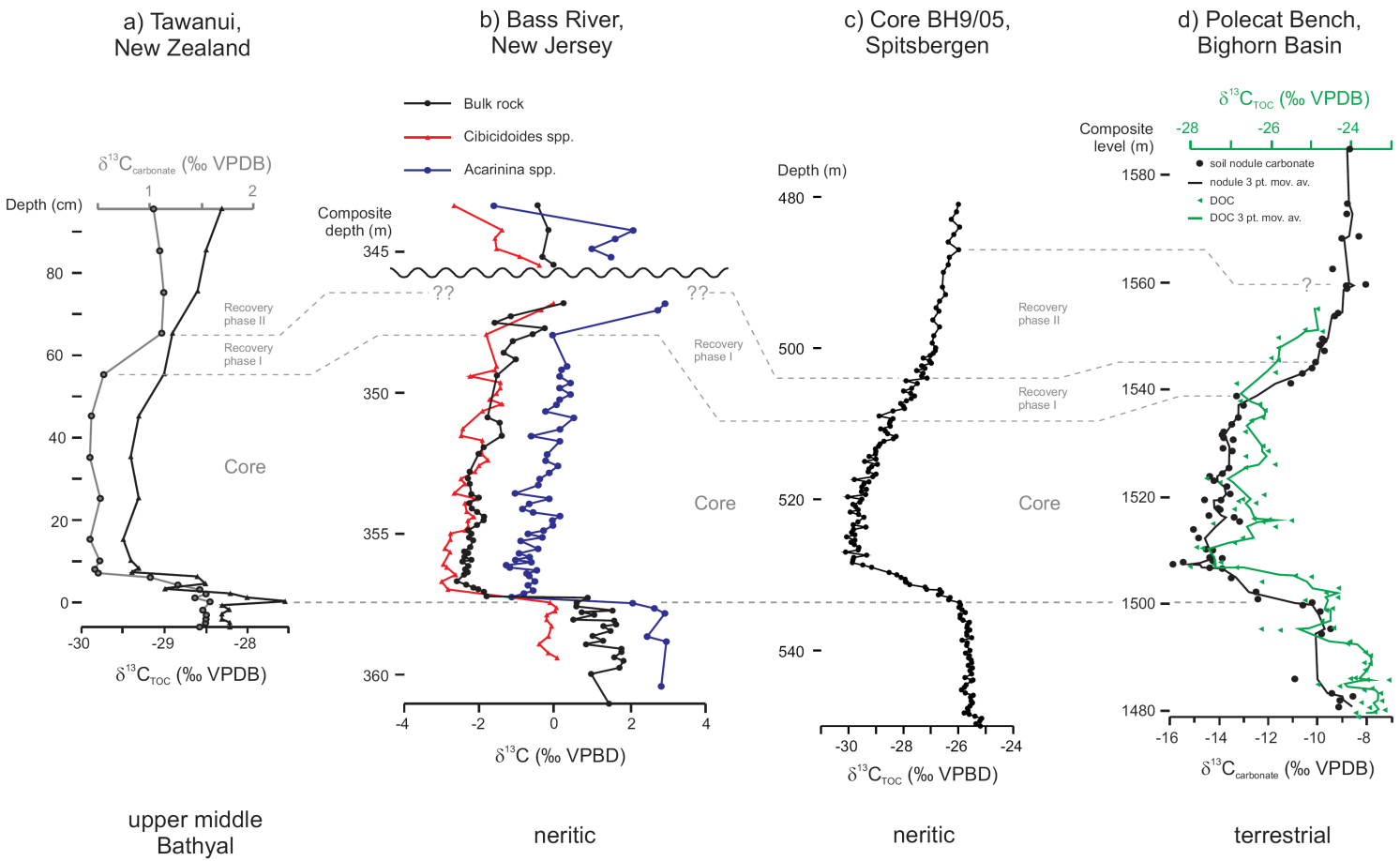

Figure 1.6: expressions of the PETM CIE from different parameters and settings (note that deep marine CIEs are illustrated in Figure 1.3). **a)** Tawanui, New Zealand, from Crouch *et al*. (2003). **b)** Bass River, New Jersey, from John *et al*. (2008). **c)** Core BH9/05, Spitsbergen, from Cui *et al*. (2011). **d)** Polecat Bench, Bighorn Basin. Dispersed organic carbon (DOC) and soil carbonate nodule records from Magioncalda *et al*. (2004) and Bowen *et al*. (2001) respectively. Phases of the CIE (as defined by Röhl *et al*. 2007) are plotted for comparison.

However, after accounting for core expansion, and the revised estimates for the duration of magnetochrons in this interval (Westerhold *et al*. 2007), the duration of the PETM was revised to 90 ±10 to 140 ±30 kyr (Sluijs *et al*. 2007a). Subsequently, Murphy *et al*. (2010) derived a duration of 217 +44/-31 kyr based on a ^{3}He age model from ODP Site 1266. Therefore the durations of the PETM calculated from ODP sites 690 and 1266 do not overlap within their quoted uncertainties, even after estimates were revised for Site 690. Such an offset may (at least in part) be related to the age models used to calculate the flux of extraterrestrial ^{3}He to the sites of deposition within the 'calibration intervals' required for this method (see Murphy *et al*. 2010 for discussion).

1.2.4 Eustatic variations across the PETM

Given the global distribution of marginal marine PETM sections, eustatic variations can be assessed through the analysis of sea level proxies at different localities. Data from the Atlantic, Pacific and Arctic Oceans, and the Tethys and Turgay Strait regions all illustrate evidence for sea level rise during the PETM (Table 1.1). The global distribution and number of sites illustrating such evidence mitigates against localised effects (e.g. tectonics, isostacy), indicating the sea level rise associated with the PETM was eustatic in nature. Evidence of highly expanded continental margin sections in New Jersey (Sluijs *et al*. 2008b) and Spitsbergen (Harding *et al*. 2011, file A1.2, Appendix 1) has suggested that the onset of sea level rise preceded the PETM CIE, providing further evidence to support the contention that environmental change began prior to the CIE onset.

1.2.5 Ocean acidification

The CIE marking the PETM is synchronous with a pronounced drop in the percentage of carbonate at many locations on a global scale (Crouch *et al*. 2003a; Dupuis *et al*. 2003; Zachos *et al*. 2005; Guisberti *et al*. 2007; McCarren *et al*. 2008; Egger *et al*. 2009; Leon-Rodriguez and Dickens 2010). In Atlantic oceanic sites, the decline in carbonate is interpreted as a >2 km shoaling of the calcite compensation depth (CCD; Zachos *et al*. 2005), resulting in increased carbonate dissolution with depth (McCarren *et al*. 2008), and reduced sedimentation rates in bathyal-abyssal settings (Farley and Eltgroth 2003; Röhl *et al*. 2007; Murphy *et al*. 2010). Pacific and Southern Ocean sites were less affected by carbonate dissolution (e.g. Zachos *et al*. 2003), with a reversed carbonate ion gradient (relative to the present day) from the Atlantic to the Pacific (Zeebe and Zachos 2007). Carbonate dissolution would have been driven by the injection of methane and/or carbon dioxide into the exogenic system (Dickens *et al*. 1995). This resulted in an increased dissolved inorganic carbon (DIC) content (with a constant alkalinity), which acts to decrease carbonate ion concentration, lowering the

ocean saturation state and leading to CCD shoaling (e.g. Kump *et al*. 2009; Ridgwell and Schmidt 2010). Conversely, during the recovery interval of the PETM bathyal settings demonstrate elevated carbonate percentages (Kelly *et al*. 2005; 2010; Leon-Rodriguez and Dickens 2010). Such high carbonate content may have been driven by enhanced weathering during the recovery interval of the CIE (Dickens *et al*. 1997; Kelly *et al*. 2005; Kump *et al*. 2009). Specifically, increased weathering would enhance bicarbonate ion concentration in the oceans, in turn leading to elevated carbonate formation and an 'overshoot' of the CCD to depths exceeding those before the PETM, enhancing carbonate burial in oceanic settings (Dickens *et al*. 1997; Kump *et al*. 2009).

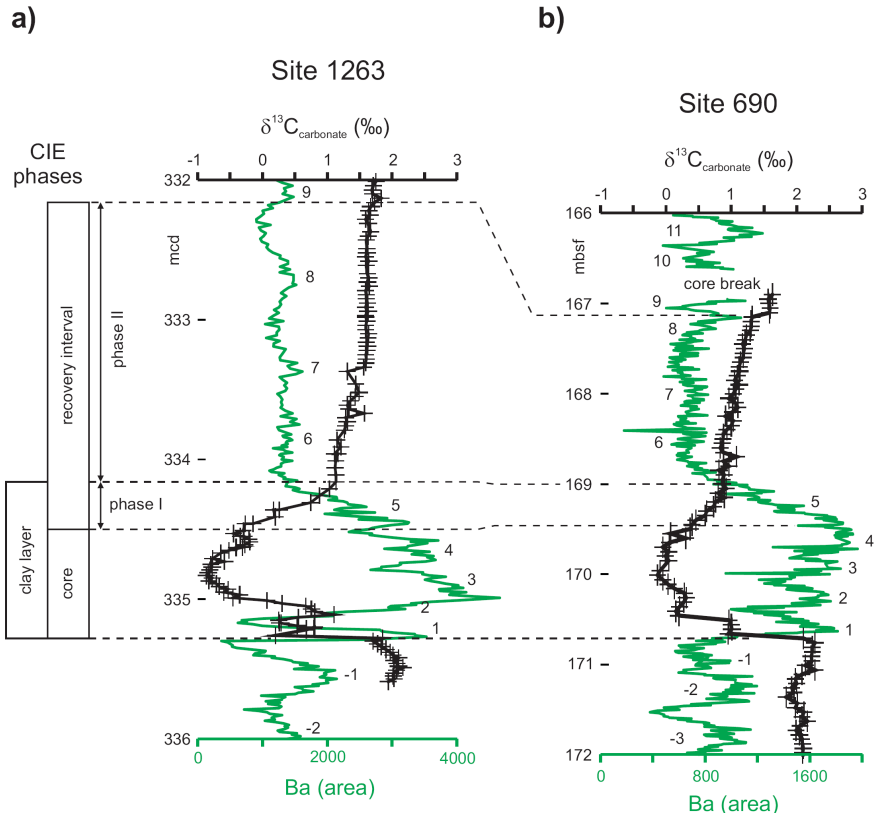

Figure 1.7: Cyclostratigraphic records of the PETM from **a)** ODP Site 1263 (Leg 208; Walvis Ridge) and **b)** ODP Site 690 (Leg 113, Weddell Sea) reproduced from Röhl *et al*. (2007). $\delta^{13}C_{carbonate}$ records from Zachos *et al*. (2005) for Site 1263, and from Bains *et al*. (1999) for Site 690. Ba records and precession cycle numbers from Röhl *et al*. (2007).

Nannofossil records have been utilised to interpret potential changes in surface water acidity, with the suggestion that lower surface water pH resulted in the presence of malformed morphotypes of certain nannofossil species at multiple sites (Jiang and Wise 2006; Raffi and De Bernardi 2008). However, this hypothesis has been challenged by Bown and Pearson (2009), who argue that the relatively low number of extinctions (up to 10 %) and malformed species (<3 % of known taxa) suggest that marked surface water acidification did not occur. This is corroborated by the continuous deposition of shallow water carbonate during the CIE at ODP Site 871 (Limalok Guyot; Robinson 2011), as well as the lack of a calcification bias in nannofossils during the interval of pronounced taxanomic turnover at the PETM (both heavily calcified and fragile taxa appear and disappear within the event: Gibbs *et al*. 2006a). Furthermore, the Sr/Ca productivity indicator also suggests carbonate production in nannofossils remained constant across the PETM interval (Gibbs *et al*. 2010). A recent modelling study also found that surface waters were not undersaturated with respect to carbonate during the PETM, for carbon release scenarios of 2180 gigatonnes of carbon over 1 kyr, and 6840 gigatonnes of carbon over 10 kyr (Ridgwell and Schmidt 2010).

1.2.6 The hydrological cycle and redox changes

Typically, continental margin sections show an increase in sedimentation rates during the PETM, believed to be caused by enhanced terrestrial runoff which resulted in increased mass accumulation rates of siliciclastics and organic carbon (John *et al*. 2008; Sluijs *et al*. 2008a). This, coupled with increases in weathering intensity (Ravizza *et al*. 2001; Dallanave *et al*. 2010), precipitation (Schmitz and Pujalte 2007) and an enhanced deuterium flux to the high Arctic (Pagani *et al*. 2006), has been used as evidence for an intensification of the hydrological cycle initiated at PETM onset (Figure 1.4). Changes in the hydrological cycle may also be linked to changes in redox conditions in neritic localities, through changes in runoff and stratification (Figure 1.8). Evidence for decreased oxygenation in neritic localities has been documented on a global scale (Gavrilov *et al*. 1997; 2003; Bolle *et al*. 2000; Sluijs *et al*. 2006; Lippert and Zachos 2007; Weller and Stein 2008; Handley *et al*. 2011; Harding *et al*. 2011), dramatically illustrated by the deposition of a sapropel unit in sections across Asia (Gavrilov *et al*. 1997; 2003; Bolle *et al*. 2000). It has been proposed that the enhanced runoff caused by the intensified hydrological cycle led to elevated nutrient concentrations in neritic localities, enhancing planktonic productivity and biological oxygen demand (BOD). Elevated runoff is also believed to have resulted in enhanced stratification (e.g. Sluijs *et al*. 2008a; Sluijs and Brinkhuis 2009), which together with elevated BOD reduced oxygen levels in neritic localities (Figure 1.8).

Table 1.1: Evidence for eustatic sea level rise during the Palaeocene-Eocene boundary (Modified after Harding *et al.* 2011)

Region	Location	Site	Evidence	References
Atlantic	New Jersey margin	Wilson Lake & Bass River	Geochemical: lower branched index of tetraethers (BIT) index ratios within PETM Biological: most offshore dinocyst assemblages within PETM Sedimentological: decreasing percentage of >63 μm grain size fraction going into PETM	Cramer *et al.* (1999); John *et al.* (2008); Sluijs *et al.* (2008b)
		Clayton	Sedimentological: change from ~40% glauconite rich sand preceeding PETM to ~1% within PETM Biological: change from inner neritic to middle neritic benthic foraminiferal assemblages (with highest tau values) within PETM, with highest percentage of planktonic foraminifera	Gibson *et al.* (1993); Gibson & Bybell (1994)
	North Sea	Doel - Belgium	Sedimentological: regional unconformities above and below PETM suggesting sea level lowstands. Resumption of marine deposition within PETM suggests sea level transgression Biological (Doel, Belgium only): decreasing percentage of terrestrial palynomorphs, increasing percentage of aquatic palynomorphs toward minimum $\delta^{13}C$ values	Steurbaut *et al.* (2003); Sluijs *et al.* (2008b)
		Woensdrecht - The Netherlands		Sluijs *et al.* (2008b)
		Southeast England		Powell *et al.* (1996)
		Mungo Field	Maximum flooding surface inferred during *Apectodium augustum* acme in Beyond Petroleum (BP) stratigraphic framework	Payne *et al.* (2005)
	Spain	4 sections: (Campo to Bacamorta)	Sedimentological: unconformity representing subaerial exposure replaced by aggradational alluvial plain deposits laterally interfingered with marine deposits within PETM	Pujalte & Schmitz (2006); Pujalte *et al.* (2009)
Pacific	Californian margin	Lodo Gulch & Tumey Gulch	Sedimentological: decreasing percentage of >63 μm grain size fraction going into PETM	John *et al.* (2008)
	New Zealand	Tawanui	Biological: most offshore dinocyst assemblages within the PETM	Crouch & Brinkhuis (2005); Sluijs *et al.* (2008b)
		Kumara	Sedimentological: terrestrial sedimentation precedes and postdates marine PETM sediments Biological: Transition from no marine palynomorphs before the CIE to >30 % marine palynomorphs with marine dinocysts during the CIE Geochemical: decline in n-alkane terrigenous to aquatic ratio, carbon preference index and odd-over-even predominance during the PETM	Sluijs *et al.* (2008b); Handley *et al.* (2011)
Arctic	Lomonosov Ridge	Site 302-4A	Geochemical: lower BIT index & increase in Rock Eval hydrogen index within PETM Biological: decreased percentage of terrestrial palynomorphs within PETM	Sluijs *et al.* (2006; 2008a)
	Spitsbergen	Longyearbyen	Geochemical: decreasing quartz percentages toward minimum $\delta^{13}C$ values within the PETM, elevated H/C ratios indicating more marine influence during CIE Biological: most offshore dinocyst assemblages & decreased percentage of terrestrial palynomorphs within PETM	Harding *et al.* (2011)
Tethys	Egypt to Israel depth transect	6 sections: Gebel Duwi (Eygpt) to Ben Gurion (Israel)	Biological (Gebel Duwi only): Increased abundances of outer neritic & upper bathyal Ostracods at PETM Sedimentological: lowstand deposition immediately preceding PETM replaced by black shale deposition with fish debris indicative of transgressive systems tract during the CIE	Speijer & Morsi (2002); Speijer & Wagner (2002)
	Georgia – Tadjikistan epicontinental sea	6 sections: Kheu River (Georgia) to Kurpai (Tadjikistan)	Sedimentological: Erosive unconformity representing subaerial exposure below the PETM replaced by marine deposition (fish scales and marine dinocysts preserved) at the onset of the event Geochemical: Elevated hydrogen index values within the PETM indicate a more marine influence	Crouch *et al.* (2003b) Gavrilov *et al.* (1997; 2003)
Turgay Strait	Kazakhstan	Sokolovsky quarry	Biological: most offshore dinocyst assemblages within PETM	Iakovleva *et al.* (2001)

Decreases in the amount of bioturbation at Site 690 (Weddell Sea; Kennett and Stott 1991) and in New Zealand (Nicolo *et al*. 2010), together with the development of sedimentary laminations through the PETM at Site 999 (Caribbean Sea; Bralower *et al*. 1997), and geochemical evidence for lower oxygen conditions from ODP Leg 208 sites (Walvis Ridge; Chun *et al*. 2010), all suggest that decreases in oxygen content also occurred globally in bathyal settings. However, the low percentage of organic carbon and surface water oligotrophic microfossil assemblages (Section 1.2.7) indicates that decreased oxygenation at these localities was not caused by enhanced productivity and BOD (Bralower 2002; Tremolada and Bralower 2004). However, the redox changes can be explained if the PETM CIE was caused by the injection of methane hydrates into the ocean, as the oxidation of the released methane in the water column would lower oxygen levels within intermediate water masses (Figure 1.8; Tremolada and Bralower 2004; Nicolo *et al*. 2010; Dickens 2011).

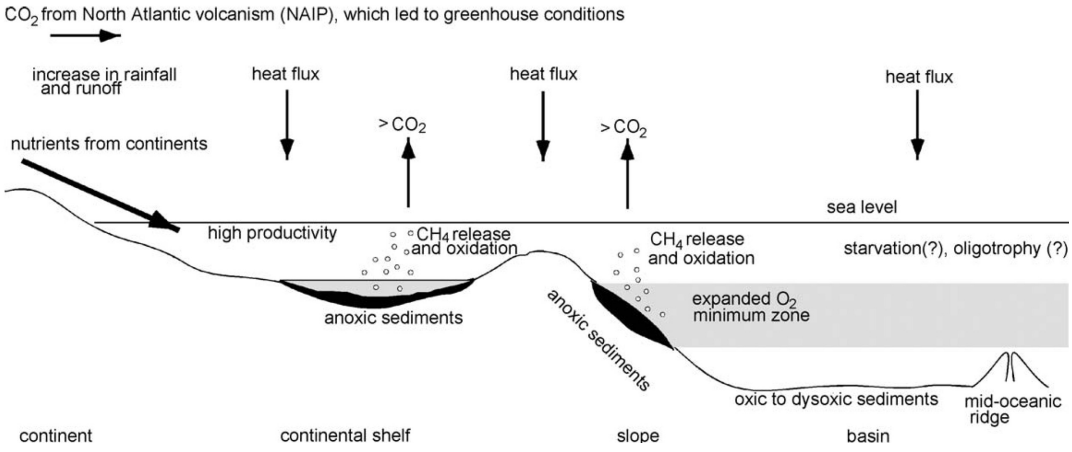

Figure 1.8: Schematic diagram of probable palaeoceanographic conditions in continental margin and oceanic settings during the PETM (from Tremolada and Bralower 2004).

1.2.7 Floral and faunal change

Pronounced floral and faunal changes occurred during the PETM, with migrations and increased taxonomic turnover documented in both marine and terrestrial settings (Koch *et al*. 1992; Kelly *et al*. 1996, 1998; Clyde and Gingerich 1998; Bralower 2002; Wing *et al*. 2005; Gibbs *et al*. 2006a; Harrington and Jaramillo 2007; Bown and Pearson 2009; Jaramillo *et al*. 2010). Calcareous and agglutinated benthic foraminifera suffered marked extinctions at the onset of the event, with ~30-50 % of calcareous species becoming extinct (Kennet and Stott 1991; Thomas 1998; Takeda and Kaiho 2007). Conversely, originations and migrations of warm-water planktonic foraminiferal taxa have also been documented (Kelly *et al*. 1996, 1998), indicating the response of

benthic and planktonic foraminiferal communities was decoupled during the PETM (Thomas 1998). Such a response was probably caused by differential changes to surface water and benthic environments (e.g. Sections 1.2.5 and 1.2.6).

Increased rates of extinction (up to 10 % of species) and origination are observed in nannofossils during the PETM, with the most pronounced taxanomic turnover observed within the core of the CIE interval (Bralower 2002; Tremolada and Bralower 2004; Gibbs *et al*. 2006a; Bown and Pearson 2009). Marked differences in nannofossil assemblages are also observed between neritic and oceanic settings, with an increased abundance of mesotrophic taxa in neritic localities indicating enhanced productivity (Gibbs *et al*. 2006b). Conversely, elevated abundances of oligotrophic taxa are observed in open ocean settings (Monechi *et al*. 2000; Bralower 2002; Tremolada and Bralower 2004; Bown and Pearson 2009). This implies an enhanced productivity gradient between neritic and oceanic settings during the PETM, which was probably the result of enhanced continental runoff in neritic settings, together with increased stratification in the open ocean (Gibbs *et al*. 2006b).

In addition, a global PETM acme in the dinocyst genus *Apectodinium* is inferred to be (at least partially) caused by a combination of both surface water warming and increased nutrient availability in neritic localities (Figure 1.9; Brinkhuis *et al*. 1994; Bujak and Brinkhuis 1998; Crouch *et al*. 2001, 2003a, 2003b; Egger *et al*. 2003; Sluijs and Brinkhuis 2009; Harding *et al*. 2011; Sluijs *et al*. 2011). However, whilst high-nutrient warm surface waters occurred in shelf settings during other intervals of geological time, the global acme of one genus is a unique event in the dinocyst record. Therefore, the involvement of another as yet unknown factor(s) has been invoked as being responsible for the global acme of *Apectodinium* at the PETM (Sluijs and Brinkhuis 2009).

In terrestrial settings, high taxanomic turnover is recorded in both plant and mammalian communities, with the latter also experiencing transient dwarfism during the PETM (e.g. Clyde and Gingerich 1998; Wing *et al*. 2005; Jaramilo *et al*. 2010). A significant reduction in the size of terrestrial ichnofossils in the Bighorn Basin, Wyoming, during the CIE suggests dwarfism was not restricted to mammals (Smith *et al*. 2009). Analysis of plant macro- and micro-fossils has demonstrated the poleward migration of tropical taxa to the mid-latitudes during the PETM in North America (Wing *et al*. 2005), with the extinction of ~20 % of palynoflora in the Gulf Coast region (Harrington and Jaramillo 2007). Conversely, plant diversity and origination rates increased in the South American tropics (Jaramilo *et al*. 2010), which may indicate the response of tropical plant communities was highly variable on a spatial scale. Evidence

for such spatial heterogeneity may also be recorded in the Arctic, given the dominance of angiosperm pollen at Site 302-4A (Sluijs *et al*. 2006), and its near-absence in the Longyearbyen section, Spitsbergen (Harding *et al*. 2011).

1.2.8 The trigger mechanism

The initial trigger mechanism of the carbon injection and subsequent warming at the Palaeocene Eocene boundary remains controversial, with several different hypotheses having been proposed. It has been suggested that the PETM could have been caused by the oxidation of $\geq 5 \times 10^3$ gigatonnes of organic carbon in the form of CO_2, evolved from either from a global conflagration (Kurtz *et al*. 2003), or the desiccation of an epicontinental seaway (Higgins and Schrag 2006). However, to date little proxy evidence exists to support these mechanisms. Furthermore, Dickens (2011) has argued that the desiccation of epicontinental seaways also occurred at other times during the Palaeogene which are not linked to transient warming events, and such a mechanism was therefore unlikely to have caused the PETM.

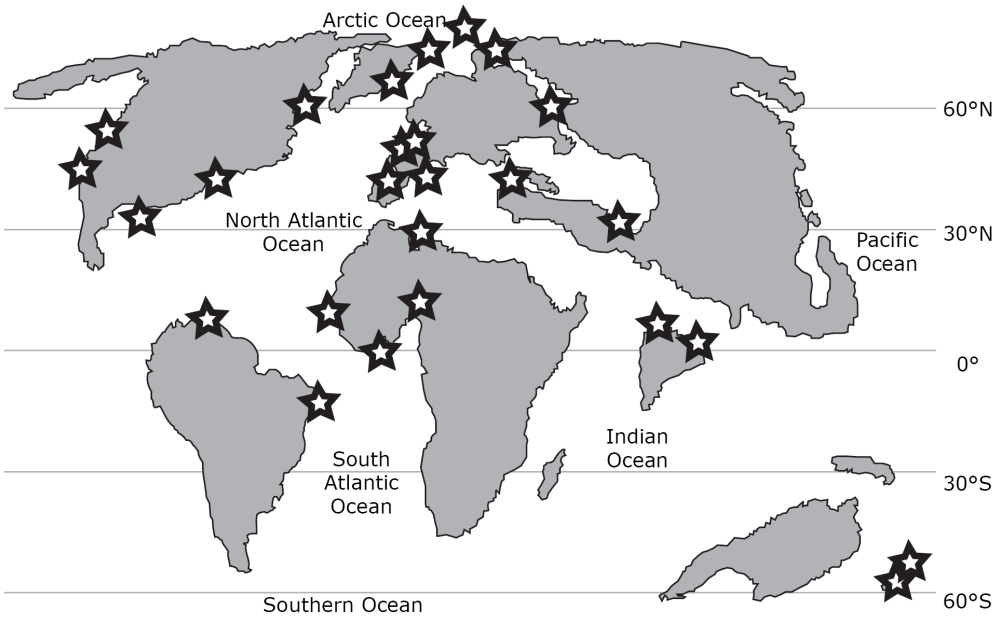

Figure 1.9: Geographic distribution of the dinocyst *Apectodinium* during the PETM, from Sluijs *et al*. (2007a; see their Figure 4, for the references associated with individual localities).

The most widely accepted hypothesis for the cause of the PETM is the dissociation of 1-2x10^3 gigatonnes of methane hydrate, which would account for the observed magnitude of the CIE (Dickens *et al*. 1995, 1997; Zeebe *et al*. 2009; Cui *et al*. 2011). Various mechanisms which may have been responsible for the dissociation of such a volume of methane hydrate include large-scale sediment failure on continental slopes (Katz *et al*. 1999), mantle plume-induced uplift (Maclennan and Jones 2007), or changes in ocean circulation (Bice and Marotzke 2002; Lunt *et al*. 2010). The rise in temperature and/or changes in pressure invoked by the aforementioned mechanisms would have resulted in changes to the hydrate stability field, resulting in the release of methane and the 2.5 – 6 ‰ CIE in the exogenic system. To release methane hydrates *via* changes in temperature, an initial warming must have preceded the CIE, and evidence for this phenomenon has been put forward from terrestrial (Secord *et al*. 2010) and marine continental margin sections (New Jersey, North Sea; Sluijs *et al*. 2007b), as well as Southern Ocean localities (Thomas *et al*. 2002). One plausible mechanism which may have resulted in pre-CIE warming is the synchronous emplacement of the North Atlantic Igneous province, an event which would have released large quantities of carbon dioxide (Storey *et al*. 2007). Hydrothermal vent systems in the Vøring and Møre basins have been documented in seismic profiles and dated to the Palaeocene-Eocene boundary (Svensen *et al*. 2004, 2010). Methane released from these vent systems may thus have triggered the pre-CIE warming required to initiate the PETM, or may have even released enough methane to cause the event itself (Svensen *et al*. 2004, 2010). However, the precise cause of any purported pre-CIE warming remains contentious. A full discussion of the possible causes of the PETM is provided by Sluijs *et al*. (2007a), who also explore the recovery of the global climate system after the carbon injection.

1.3 The PETM in high northern latitudes

Given that the polar regions represent an end-member scenario for meridional temperature and hydrological gradients, information constraining the climatic conditions in such settings is essential to understand Earth system processes in the Palaeogene, and to constrain global climate models (e.g. Sluijs *et al*. 2008a). However, until recently (prior to 2004) no high northern latitude PETM sites had been documented, owing to the lack of continental land masses in the Arctic region, the poor age control on those successions that were known, and also the logistical constraints on ocean drilling through Arctic sea ice to retrieve seafloor sediment records. Whilst data on Arctic Palaeogene climates has been provided from terrestrial deposits (e.g. Jahren and Sternberg 2002; 2003; Uhl *et al*. 2007; Greenwood *et al*.

2010), obtaining robust age constraints in such settings has proved problematic (e.g. Jahren and Sternberg 2002).

The Integrated Ocean Drilling Program (IODP) Leg 302 (usually referred to as the Arctic Coring Expedition [ACEX]) was the first to core Palaeocene-Eocene boundary sediments from the Arctic Ocean (Figure 1.10; Backman *et al*. 2006; Moran *et al*. 2006). The PETM interval was identified through the presence of sub-tropical dinocyst taxon *Apectodinium*, together with CIEs in bulk organic matter and n-alkanes (Figure 1.11; Sluijs *et al*. 2006; Pagani *et al*. 2006). Despite the core gaps within the PETM CIE, records from Site 302-4A have indicated that summer-biased Arctic sea surface temperatures may have reached ~23 ºC during the PETM (Figure 1.11; Sluijs *et al*. 2006), with coeval surface air temperatures of ~25 ºC (Figure 1.5; Weijers *et al*. 2007). Given the global temperature increase, an enhanced deuterium flux to the high Arctic during the CIE has been interpreted as evidence for increased moisture transport to the region (Figure 1.4; Pagani *et al*. 2006). This together with increased sedimentation rates, terrestrial palynomorph and n-alkane concentrations during the PETM (Sluijs *et al*. 2008a; Weller and Stein 2008), is consistent with an environment where high precipitation resulted in high runoff (Sluijs *et al*. 2008a). Given that analysis of dinocyst assemblages and fish bones indicate low salinity conditions (Sluijs *et al*. 2006; 2008a; Waddell and Moore 2008; Gleason *et al*. 2009), it is probable that elevated precipitation and runoff resulted in water column stratification (Sluijs *et al*. 2008a). In addition, there is evidence for photic zone euxinia during the CIE (Figure 1.11; Sluijs *et al*. 2006; Stein *et al*. 2006; Weller and Stein 2008), with the combined effects of stratification, high productivity and warming probably causing a decline in oxygen levels in the water column (Sluijs *et al*. 2006; 2008a).

More recently, work on the Palaeogene succession in the Spitsbergen Central Basin (Figure 1.10) has revealed that the PETM is recorded in the marine mudstones of the Frysjaodden Formation (Cui *et al*. 2011; Harding *et al*. 2011; see files in Appendix 1 and 5). An *Apectodinium* acme together with a -4 ‰ CIE in bulk organic carbon ($\delta^{13}C_{TOC}$) have been used to identify the PETM near Longyearbyen (Figure 1.12; Harding *et al*. 2011; data archived in file A1.3, Appendix 1), with a CIE of the same magnitude in core BH9/05 drilled near Sveagruva (Cui *et al*. 2011, Appendix 5). Given the 30 m and 50 m stratigraphic thickness of the CIE in Longyearbyen and core BH9/05 respectively (Cui *et al*. 2011; Harding *et al*. 2011), the Spitsbergen succession permits a high resolution analysis of the PETM in a high northern latitude setting. Data from the Longyearbyen section have demonstrated that sea level rise preceded the onset of the PETM CIE (Figure 1.12), illustrating that the CIE lagged the onset of environmental change in the Arctic (Harding *et al*. 2011). In addition, dinocyst assemblages from Longyearbyen

also suggest salinity-driven stratification, with low salinity tolerant dinocysts inhabiting a freshwater cap above more saline waters below (Harding *et al*. 2011).

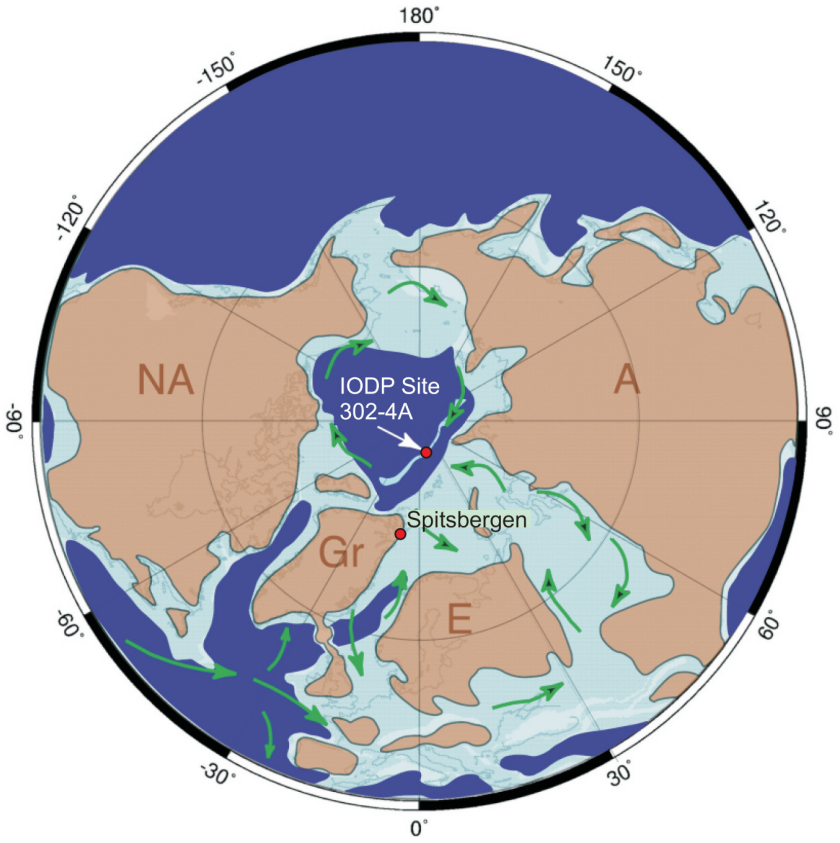

Figure 1.10: Palaeogeographic reconstruction of the Arctic region at ~50 Ma (polar projection). Red dots illustrate the high Arctic PETM sections documented to date, IODP Site 302-4A (Lomonosov Ridge), and the Central Basin (Spitsbergen). Green arrows indicate the direction of possible oceanographic currents. A = Asia, E = Europe, Gr = Greenland, NA = North America. Modified after Backman *et al*. (2006).

Similar to Site 302-4A, the increased abundance of pyrite and amorphous organic matter (AOM) in the Longyearbyen section has been used as evidence for a decline in oxygen levels during the PETM (Harding *et al*. 2011). However, the organic linings of benthic foraminifera are also observed within the CIE interval at this site (Harding *et al*. 2011). Although it might be argued that the very low abundances of these organic linings may be reworked (Harding *et al*. 2011), an alternative explanation is that transient more oxygenated pulses briefly permitted small numbers of forams to colonise the site (akin to the benthic fauna of the Kimmeridge Clay; Jenkins 2000).

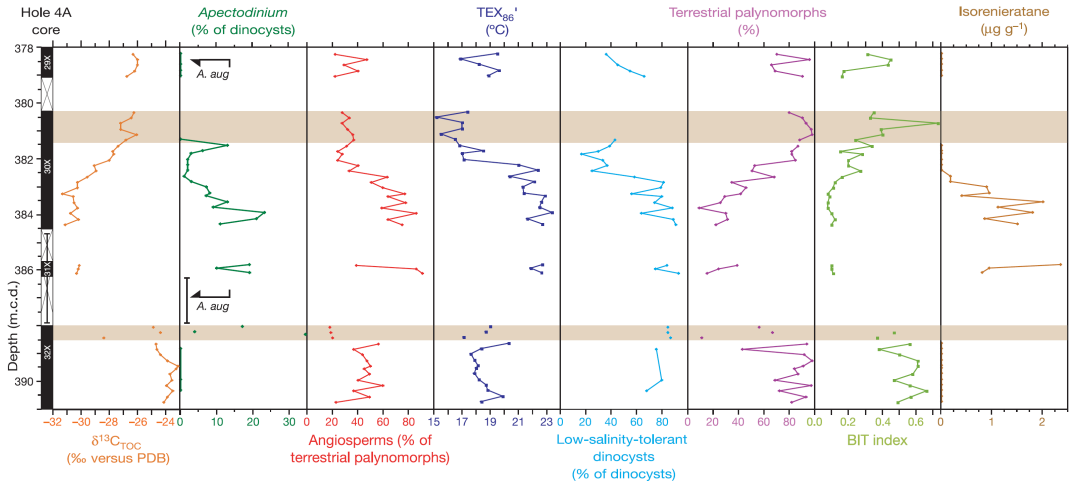

Figure 1.11: Geochemical and palynological records from Site 302-4A (Leg 302: Lomonosov Ridge), from Sluijs *et al.* (2006). Vertical black bars on left indicate intervals of core recovery, with horizontal shaded bars representing regions of drilling disturbance. Note the presence of green sulphur bacterial biomarker isorenieratene, indicative of photic zone euxinia during the CIE.

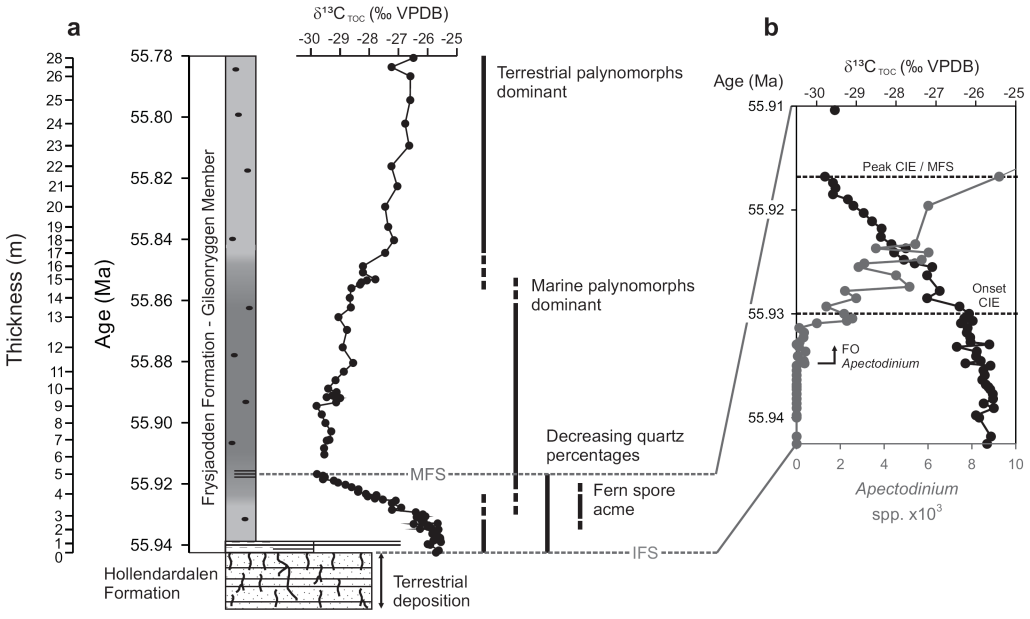

Figure 1.12: a) Summary of lithological, geochemical and palynological changes during the PETM in the Longyearbyen section, Spitsbergen (from Harding *et al.* 2011; data and manuscript archived in files A1.2 and A1.3, Appendix 1). **b)** Expanded view of the onset interval of the carbon isotope excursion.

Thus, whilst evidence exists for a decline in oxygen levels during the PETM in Spitsbergen (Harding *et al*. 2011), such a decline may not have been as pronounced as that observed at Site 302-4A (Sluijs *et al*. 2006; Stein *et al*. 2006; Weller and Stein 2008). Other differences between the Longyearbyen Section and Site 302-4A include the abundance of angiosperm pollen, which is abundant at the latter locality (Figure 1.11; Sluijs *et al*. 2006) but exceedingly rare in the Longyearbyen section (Harding *et al*. 2011). Given the more pronounced fractionation of angiosperm *versus* gymnosperm biomarkers in the Arctic during the PETM (Schouten *et al*. 2007), the difference in floral composition may (at least in part) explain the different magnitude of the $\delta^{13}C_{TOC}$ isotopic excursions in Spitsbergen and Site 302-4A (~4 ‰ and ~6 ‰ respectively: Sluijs *et al*. 2006; Cui *et al*. 2011; Harding *et al*. 2011). Given the proximal palaeoenvironmental settings of both the Longyearbyen Section and Site 302-4A, the differences CIE magnitude, angiosperm pollen abundance (and potentially oxygenation), may be caused by localised conditions superimposed on regional Arctic trends. Such differences between the sections therefore make it difficult to assess which (if either) was representative of the Arctic region during the PETM. Furthermore, the coring gaps in Site 302-4A prevent comparison between this site and the Longyearbyen section during the onset and peak of the PETM CIE. Harding *et al*. (2011) argued for maximum flooding during the peak CIE (Figure 1.12), with subsequent maximum stratification ~33 kyr after the CIE onset: but the coring gaps at Site 302-4A prevent these key hypotheses from being tested on a regional Arctic basis. This together with the differences between Site 302-4 and the Longyearbyen section, poses the following questions:

1. How widespread and strongly developed was anoxia/euxinia in high northern latitudes during the PETM?
2. How pronounced was the spatial oceanographic variability in high northern latitudes during the PETM?
3. How pronounced was spatial and temporal biotic variability across the PETM in the Arctic, and what factors were driving such changes in biotic assemblage?

1.4 Aims of this report

Given the stratigraphically expanded nature of the Palaeogene succession (e.g Cui *et al*. 2011; Harding *et al*. 2011; file A1.3, Appendix 1), the Spitsbergen Central Basin provides the temporal resolution required to further constrain conditions in the high Arctic during the PETM. To this end two additional PETM localities in the Central Basin are analysed in this study, in order to assess palaeoceanographic conditions across the

basin during this hyperthermal event. In light of the questions posed above (Section 1.3), analyses of the successions developed in core BH9/05 and a new PETM outcrop section at Bergmanfjellet are documented in Chapters 3 to 5, with the following aims:

1. To constrain any possible changes in bottom water oxygen levels across the PETM in Spitsbergen (Chapter 3), and assess how such changes affect carbon burial (Chapter 4).
2. To constrain temporal and spatial biotic changes in the Central Basin through the PETM (Chapter 3).
3. To construct an age model in order to provide a time frame in which to assess the rate of potential biological and oceanographic changes observed across the PETM interval (Chapter 2).

1.5 Objectives

In order to realise the aims proposed above, a series of objectives were defined. The numerical designation of each objective below matches the corresponding aim in Section 1.4:

1. To perform analyses of sedimentological, biomarker, micopalaeontological (dinoflagellate cysts) and palynofacies data across the PETM interval to provide qualitative constraints on bottom water oxygen levels and potential changes in the composition of carbon buried.
2. To analyse dinoflagellate cyst assemblages across the PETM in core BH9/05 and the Bergmanfjellet outcrop section in order to constrain temporal biotic changes across the PETM. To compare the new data with previous results from the Longyearbyen section to identify biotic events occurring on both a local and basinal scale, thus further constraining spatial variability in biotic assemblages.
3. To collect and analyse Fe and Mn concentration data in order to construct a cyclostratigraphic age model *via* time series analysis, for core BH9/05.

1.6 Geological setting

Spitsbergen is the largest island in the Svalbard Archipelago, situated on the NW corner of the Barents Shelf (Figures 1.10 and 1.13). Several Palaeogene sedimentary basin successions are now exposed on Spitsbergen, the largest being the Central Basin, with preserved deposits spanning an area of around 60 x 200 km (Steel *et al*. 1981, 1985; Harland 1997; Dallman *et al*. 1999). All three localities discussed within this thesis lie within the Central Basin (Figure 1.13), with the PETM being located in the Gilsonryggen

Member of the Frysjaodden Formation (Figures 1.14-1.15; Harding *et al*. 2011). Harland (1997; and references therein) provides a comprehensive overview of the stratigraphy of the Central Basin and the other Palaeogene depocentres on Spitsbergen. The stratigraphic nomenclature used in this report adheres to that proposed by Dallman *et al*. (1999).

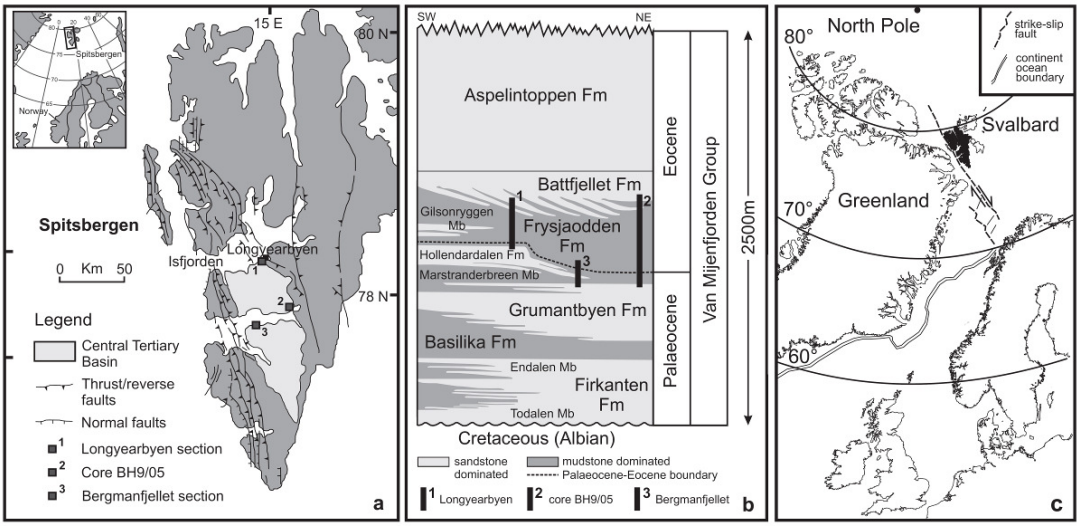

Figure 1.13: Modern and Palaeoceanographic context of the Spitsbergen Central Basin. **a)** Map of Spitsbergen, illustrating the position of two PETM localities, the Longyearbyen section and core BH9/05 (after Uroza and Steel 2008; Blythe and Kleinspehn 1998). **b)** The Palaeogene stratigraphy of the Central Basin, Spitsbergen (after Steel *et al*. 1985). **c)** Palaeoceanographic reconstruction of Spitsbergen (black) in the Eocene (after Mosar *et al*. 2002).

1.6.1 Palaeogeography and tectonic setting

During the Palaeogene Spitsbergen was situated at ~75˚N (Harland 1997), and attached to the NE corner of Greenland, but with the progressive opening of the northern North Atlantic a predominantly transpressional dextral strike-slip motion between the two continental masses was initiated by the early Eocene (Figure 1.13; Kellogg 1975; Müller and Spielhagen 1990; Harland 1997). Henceforth the Central Basin developed as a foreland basin (Kellogg 1975; Helland-Hansen 1990), with sediment shed from the rising West Spitsbergen Orogenic Belt coupled with subsidence resulting in a thick sedimentary succession (up to 2.5 km; Helland-Hansen 1990).

The basin margins in the Eocene were constrained by the orogenic belt to the west (Helland-Hansen 1990; Müller and Spielhagen 1990) and by the distribution of Permian strata to the northeast (chert clasts from these strata were eroded and rafted into the basin during deposition of the Frysjaodden Formation: Birkenmajer and Narebski 1963;

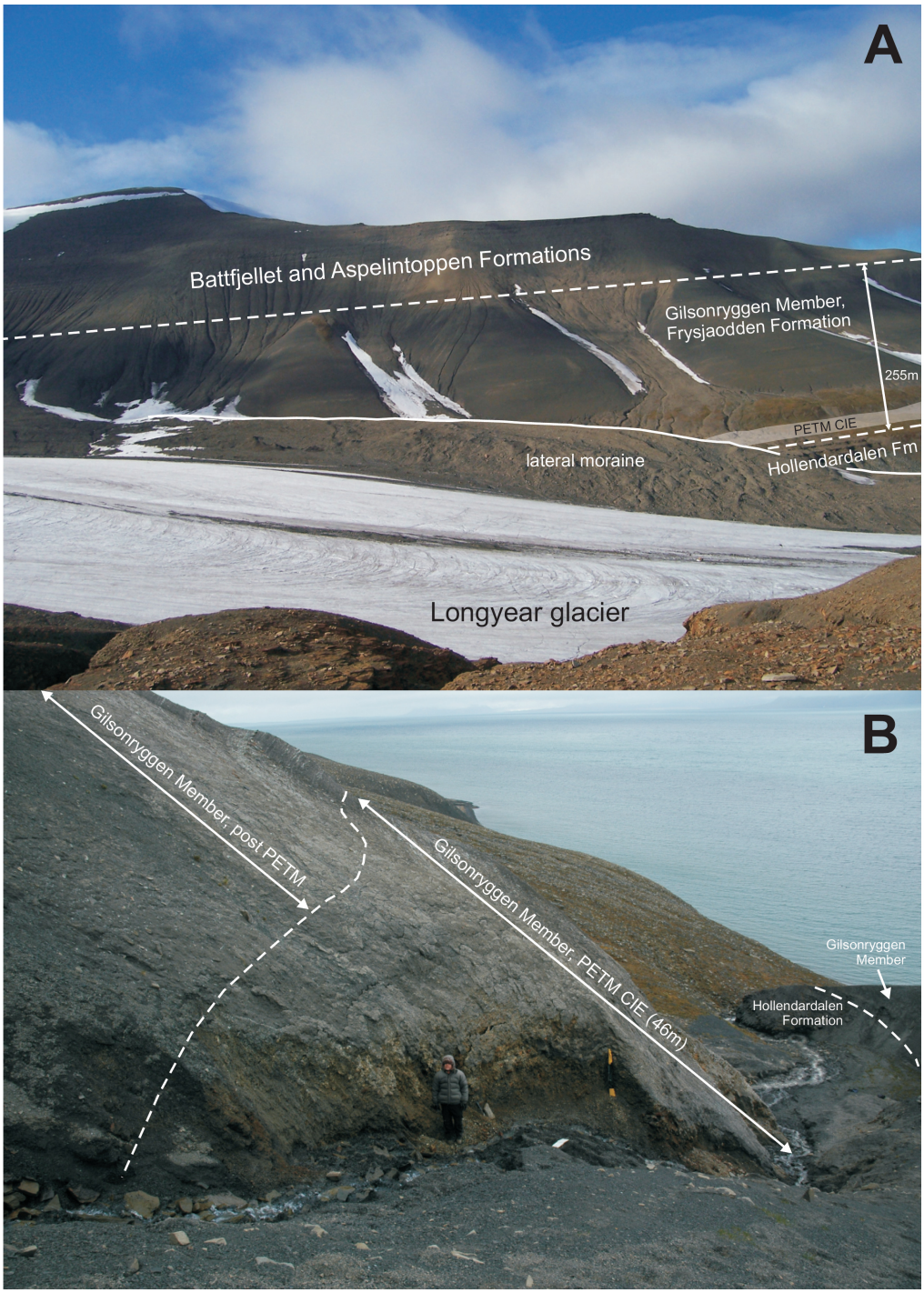

Figure 1.14: Outcrop expression of the Gilsonryggen Member, Frysjaodden Formation, Spitsbergen. **A)** View of Nordenskiöldfjellet taken from Sarkofagen mountain, near Longyearbyen (See file A1.2, Appendix 1 for lithostratigraphic log). Photograph taken looking northeast. Note the position of the PETM immediately above the Hollendardalen Formation. **B)** View of the northern slope of Bergmanfjellet, South coast of Van Mijenfjorden (see Figure 3.2 for lithostratigraphic log). Photo taken looking northwest. Author for scale. Note the yellow-brown expression of the mudstones deposited within the PETM CIE, compared to the dark grey mudstones, above and below this interval.

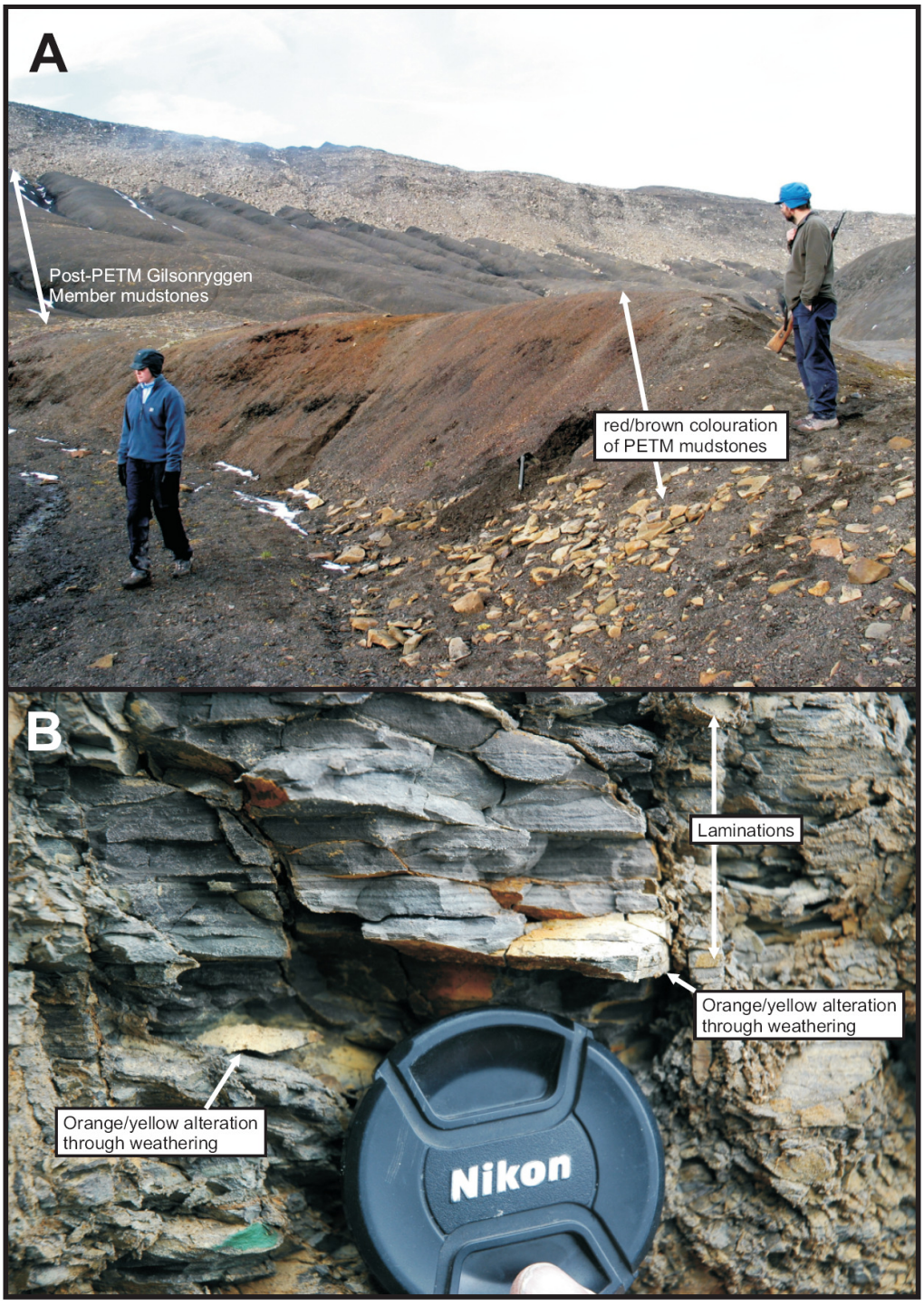

Figure 1.15: Expression of the PETM at outcrop level. **A)** Sediments deposited within the CIE on Nordenskiöldfjellet (Longyearbyen section; see file A1.2, Appendix 1 for lithostratigraphic log). Note the red/brown alteration of the PETM sediments at this locality. **B)** Close up of sediments deposited within the PETM at Bergmanfjellet, illustrating pronounced laminations within the CIE and orange/yellow alteration of sediments at this locality. Photo taken ~92m height on log in Figure 3.2.

Bikenmajer *et al*. 1972; Kellogg 1975; Dalland 1977). There is consensus that the southern margin of the basin was open, with a marine connection to the opening North Atlantic at this time (Livšic 1974; Kellogg 1975; Müller and Spielhagen 1990; Harland 1997). However, the position of the eastern margin of the basin is poorly constrained. Livšic (1974) suggested a restricted basin predominantly closed to the east based on bivalve assemblages, which are comprised entirely of euryhaline taxa, but conversely, Helland-Hansen (1990) argued that the predominance of wave- and storm-generated sedimentary structures coupled with the sedimentary architecture suggested a basin open to both the south and east.

The Palaeogene stratigraphy of the Spitsbergen Central Basin consists of a lower predominately transgressive succession with an eastern sediment provenance (the Firkanten to Grumantbyen formations, including two transgressive-regressive cycles: Kellogg 1975; Bruhn and Steel 2003; Nagy 2005), and an upper regressive megasequence (the Frysjaodden to Aspelintoppen formations; Figure 1.13) sourced from the West Spitsbergen Orogenic Belt (Steel *et al*. 1981; Helland-Hansen 1990).

The Palaeogene succession of the Central Basin rests unconformably on Cretaceous or older strata (Figure 1.13). Cretaceous sedimentation took place in a continental shelf setting (the Carolinefjellet Formation) but was terminated by uplift initiated in the north which resulted in an unconformity truncating Albian to Palaeocene sediments (Kellogg 1975; Harland 1997). The onset of Palaeogene deposition in the Central Basin is marked by the deltaic coal-bearing strata of the Firkanten Formation, the lowermost transgressive-regressive sequence in the basin (Bruhn and Steel 2003; Nagy 2005). Delta fans built out from both the north and the east, resulting in deposition of proximal-distal facies along a northeast-southwest transect (Kellogg 1975). The basal coal-bearing delta plain deposits (Todalen Member) are overlain by transgressive delta front sandstones (the Endalen Member), which interfinger with prodeltaic deposits (the Kolthoffberget Member) to the southwest (Steel *et al*. 1981; Nagy 2005). At the top of the Endalen Member a regionally developed alluvial conglomerate marks the top of the transgressive-regressive cycle (Kellogg 1975; Bruhn and Steel 2003).

The marginal marine nature of the basin is corroborated by both lagoonal and marine agglutinated foraminiferal assemblages in the Firkanten Formation (Nagy 2005), together with marine bivalves (Livšic 1974). The overlying transgressional mudstones and siltstones of the Basilika Formation were also deposited in marginal marine conditions, with both brackish-water agglutinated forams (Vonderbank 1970) and sparse marine dinocysts present (Manum and Throndsen 1986). The Basilika Formation grades into the regressive sandstones of the Grumantbyen Formation,

which, although thoroughly bioturbated for the most part, preserve rare hummocky-cross stratification implying deposition above storm wave base (Dalland 1977; Bruhn and Steel 2003). A regionally developed conglomerate on top of the Grumantbyen Formation marks the top of the second transgressive-regressive cycle (Kellogg 1975; Dalland 1979; Bruhn and Steel 2003).

The base of the Frysjaodden Formation marks the onset of the predominantly regressive succession recorded in the upper stratigraphic units (Helland-Hansen 1990). The formation predominantly comprises structureless mudstones and siltstones containing chert dropstones, which increase in abundance toward the northeast (Birkenmajer and Narebski 1963; Birkenmajer *et al*. 1972; Dalland 1977; Dallman *et al*. 1999). In northwestern regions of the basin, the regressive tidal deltaic sandstones of the Hollendardalen Formation are intercalated with the Frysjaodden Formation (Dallman *et al*. 1999). The Hollendardalen Formation consists of siltstones at the base which grade upwards into sandstones with bivalves and rare plant fossils, with intermittent rootlet beds and coal seams up to 1m thick at the top of the unit (Figure 1.16; Livšic 1974; Dallman *et al*. 1999; Harding *et al*. 2011).

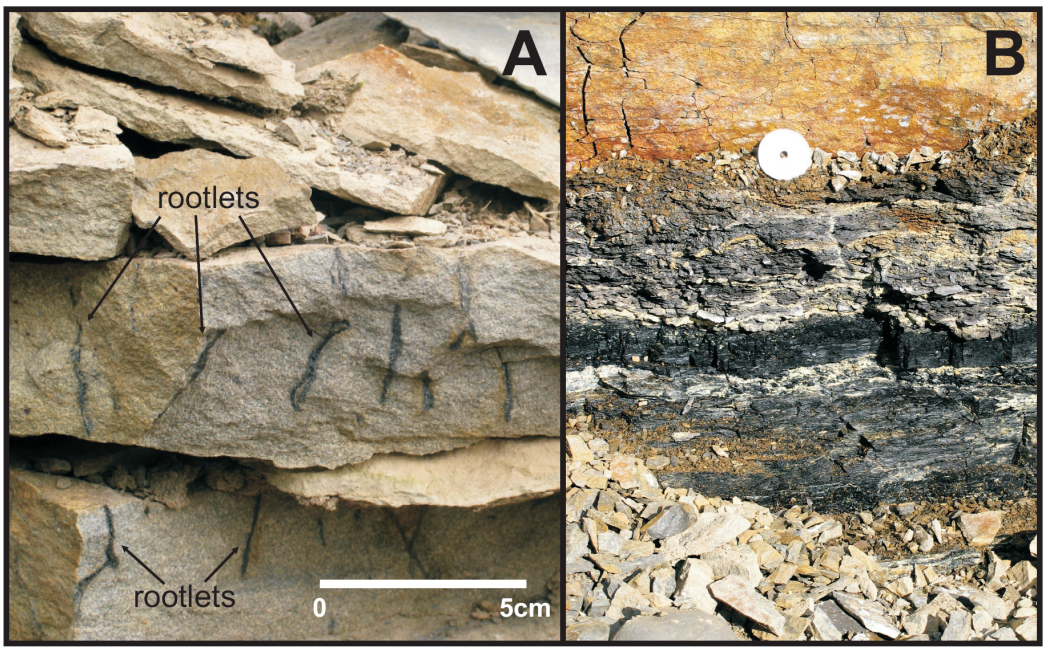

Figure 1.16: Top of the Hollendardalen Formation on Nordenskiöldfjellet (Longyearbyen section; see file A1.2, Appendix 1 for lithostratigraphic log). **A)** Rootlets extending through sandstone beds. **B)** Close up of ~10 cm coal horizon, at a laterally equivalent height to the rootlets shown in panel A. Coin for scale.

The geographical distribution and northwestern provenance of the Hollendardalen Formation represents the first significant clastic input derived from the rising West Spitsbergen Orogenic Belt (Steel *et al*. 1981; Müller and Spielhagen 1990). The Frysjaodden Formation can only be resolved into members in the northwestern parts of the basin where the Hollendardalen Formation is present (Dallman *et al*. 1999). The Hollendardalen splits the shales of the Frysjaodden Formation into the Marstranderbreen Member below and the Gilsonryggen Member above it respectively. The 250-500m thick prodeltaic mudstones of the Gilsonryggen Member are interrupted by the turbiditic sandstones and slump deposits of the Bjørnsonfjellet Member, which tapers eastwards from >10 m on the western basin margin to thin sandstone beds on the eastern margin (Steel *et al*. 1981; Helland-Hansen 1990).

The Frysjaodden Formation grades upwards into the shelf-margin delta succession of the Battfjellet Formation, which displays marked lateral facies variations within eastwardly prograding clinoforms, indicative of a shelf-slope-basin setting (Kellogg 1975; Mellere *et al*. 2002). Continued regression led to the deposition of the overlying non-marine clastic Aspelintoppen Formation which contains abundant plant debris, plant macrofossils, petrified wood and thin coal seams (Kellogg 1975; Helland-Hansen 1990; Dallman *et al*. 1999).

1.6.3 Age constraints

Robust age constraints for the Palaeogene stratigraphy of the Spitsbergen Central Basin are sparse, owing to a dearth of both macro- and micro-fossils in the sediments, and even when such fossils are found their preservation is poor (Manum *et al*. 1976; Manum and Throndsen 1986). The endemic nature of some macrofossil assemblages also means that they are of limited use as correlation tools (Manum and Throndsen 1986).

Early work attempting to date the formations focused on plant fossil assemblages, with both Heer (1868; 1870; 1876) and Nathorst (1910) inferring a Miocene age for the Firkanten and Aspelintoppen Formations. Conversely work on molluscs implied that the succession was Palaeogene in age, with Ravn (1922) suggesting Palaeocene and Eocene ages for the Grumantbyen and Battfjellet formations respectively. Subsequent studies agreed that the lower formations in the succession were Palaeocene in age, with Vonderbank (1970) assigning the Basilika Formation to this epoch. Livšic (1974) collated information from several fossil groups (molluscs, plant fossils, spores, pollen and foraminifera) and was also able to deduce a Palaeocene age for the Basilika Formation, and defined an Eocene age for the Grumantbyen to Battfjellet formations. Later work by Manum and Throndsen (1986) supported a Palaeocene age for the Basilika Formation based on dinoflagellate cysts. The same authors also carried out

palynological analyses of spot samples from the lower Gilsonryggen Member at several different localities, and documented the occurrence of the dinoflagellate cyst genus *Apectodinium*. This led Manum and Throndsen (1986) to conclude that the lower Gilsonryggen Member was latest Palaeocene in age (e.g. Luterbacher *et al*. 2004). However, as only spot samples were analysed the exact position of the Palaeocene-Eocene boundary was not constrained.

Fission track analysis of apatite crystals has resulted in additional constraints on the Central Basin's depositional history, indicating that deposition of the Firkanten Formation commenced ~64 ±2 Ma (Palaeocene: Danian) with the base of the Aspelintoppen being deposited ~49 ±2 Ma (Eocene: latest Ypresian - earliest Lutetian; Blythe and Kleinspehn 1998). Recent work by Harding *et al*. (2011) has built on the study of Manum and Throndsen (1986) by carrying out high resolution palynological analyses to constrain the position of the Palaeocene-Eocene boundary, and documents the environmental changes associated with the PETM. The position of the Palaeocene-Eocene boundary was located ~3 m above the top of the Hollendardalen Formation in the Longyearbyen area (Figure 1.12). Furthermore, palaeomagnetic analysis has indicated that the Gilsonryggen Member was deposited within Chron 24r, implying that ~250 m of sediment accumulated within ≤2 Myr, given recent estimates for the time between the onset of the PETM and the top of Chron 24r (Westerhold *et al*. 2007).

Chapter 2: constraints on the numerical age of the Palaeocene/Eocene boundary

This chapter is an exact copy of the article published in *Geochemistry Geophysics Geosystems* (Appendix file A2.2).

Citation: Charles, A.J., Daniel J. Condon, Ian C. Harding, Heiko Pälike, John E.A. Marshall, Ying Cui, Lee Kump and Ian W. Croudace (2011), Constraints on the numerical age of the Paleocene-Eocene boundary, *Geochem. Geophys. Geosyst.*, **12**, doi:10.1029/2010GC003426.

Author contributions: Adam J. Charles collected and analysed Fe and Mn XRF and palynological data, with guidance from Ian C. Harding, Heiko Pälike, John E.A. Marshall, Ying Cui, Lee Kump and Ian W. Croudace. Daniel J. Condon carried out radio-isotopic analysis of sample SB01-1. Adam J. Charles wrote the manuscript with contributions from Daniel J. Condon (sections 2.2.3 and 2.3.1, as well as a paragraph on radioisotopic dating in the introduction section).

Abstract

Here we present combined radio-isotopic dating (U-Pb zircon) and cyclostratigraphic analysis of the carbon isotope excursion at the Paleocene/Eocene (P/E) boundary in Spitsbergen, to determine the numerical age of the boundary. Incorporating the total uncertainty from both radio-isotopic and cyclostratigraphic datasets gives an age ranging from 55.728-55.964 Ma, within error of a recently proposed astronomical age of ~55.93 Ma. Combined with the assumption that the Paleocene Epoch spans twenty-five 405 kyr cycles, our new age for the boundary suggests an age of ~66 Ma for the Cretaceous/Paleogene (K/Pg) boundary. Furthermore, our P/E boundary age is consistent with the hypothesis that the onset of the Paleocene-Eocene thermal maximum (PETM) at the boundary occurred on the falling limb of a 405 kyr cycle, suggesting the event was initiated by a different mechanism to that which triggered the other early Eocene hyperthermals.

2.1 Introduction

The early Cenozoic was an interval of globally warm climate (e.g. Zachos *et al*. 2001, 2008; Pearson *et al*. 2007; Sluijs *et al*. 2008a; Bijl *et al*. 2009), punctuated by a series of short-term global-scale transient warming events known as hyperthermals (Kennett and Stott 1991; Zachos *et al*. 2001, 2008; Cramer *et al*. 2003; Lourens *et al*. 2005; Nicolo *et al*. 2007; Agnini *et al*. 2009; Galeotti *et al*. 2010). The most pronounced hyperthermal, the Paleocene-Eocene thermal maximum (PETM), reflects global-scale warming of both surface and bottom waters by ~5ºC (Kennett and Stott, 1991; Zachos *et al*. 2003; Tripati and Elderfield 2005; Sluijs *et al*. 2006). Negative carbon isotope excursions (CIEs) and carbonate dissolution horizons have been shown to be coeval with warming during both the PETM and other hyperthermals (Lourens *et al*. 2005; Zachos *et al*. 2005, 2010), implying that a significant quantity of isotopically light carbon was injected into the exogenic system to cause the observed warming (Dickens *et al*. 1995; 1997; Sluijs *et al*. 2007a; Panchuk *et al*. 2008; Zeebe *et al*. 2009). However, the trigger mechanism for carbon release at the PETM is controversial, with several hypotheses proposed (see Sluijs *et al*. [2007] for a review). Several authors have suggested that insolation maxima during the peak of 100 and 405 kyr eccentricity cycles resulted in warming of oceanic deep waters, causing the dissociation of methane hydrates, thus instigating the warming event(s) (Cramer *et al*. 2003; Lourens *et al*. 2005; Sluijs *et al*. 2007a). Conversely it has also been suggested that the methane and carbon dioxide which initiated the PETM were generated from contact metamorphism of organic-rich sediments around intrusions in North Atlantic sedimentary basins (Svensen *et al*. 2004, 2010; Storey *et al*. 2007); a trigger requiring no orbital forcing but coeval magmatism. An understanding of the causative mechanism(s) for the PETM and later Eocene hyperthermals therefore requires a precise and accurate temporal framework within which the various records can be integrated in order to assess potential drivers (geologic and/or astronomical). Much progress has been made through the construction of high-resolution proxy and lithologic records from various ODP and IODP sites (Zachos *et al*. 2001, 2003, 2005, 2008; Sluijs *et al*. 2007a, 2008), and the construction of orbitally-tuned timescales for these intervals have helped elucidate the relative timing/sequencing of different events (Lourens *et al*. 2005; Westerhold *et al*. 2007; 2009; Westerhold and Röhl, 2009; Galeotti *et al*. 2010). However, an outstanding issue relates to the numerical age of key events, such as the PETM, which are currently considered to be 'floating' – i.e. the age models contain only relative ages with respect to certain stratigraphic markers. This issue is the result of four factors: (1) the 'unstable' nature of the astronomical solutions in the early Paleogene, meaning that numerical ages derived from tuning geological datasets to astronomical solutions carry high uncertainty (Laskar *et al*.

2004); (2) a gap in cyclostratigraphic records in the middle Eocene, meaning composite cyclostratigraphic records for the entire Eocene cannot currently be constructed (Hilgen 2008; Pälike and Hilgen 2008); (3) disagreement surrounding the length of the Paleocene Epoch as derived from floating cyclostratigraphic timescales, with the presence of either twenty-four or twenty-five 405 kyr eccentricity cycles proposed (Kuiper *et al*. 2008; Westerhold *et al*. 2008; 2009; Hilgen *et al*. 2010), and (4) a lack of geologically well constrained radio-isotopic dates, for both the P/E and K/Pg boundaries and associated magneto-chrons. This is largely a result of uncertainty in the $^{40}Ar/^{39}Ar$ dating methods (Kuiper *et al*. 2008; Renne *et al*. 2010; Channell *et al*. 2010) that are used to underpin Cenozoic timescales (note this uncertainty also prevents the accurate determination of the number of 405 kyr cycles in the Paleocene).

The current astronomical solutions are unstable prior to ~40 Ma owing to the chaotic nature of the orbits (Laskar 1999; Varadi *et al*. 2003; Laskar *et al*. 2004; Pälike *et al*. 2004); therefore, unlike the Neogene timescale, construction of a numerical geologic timescale for the Paleogene relies on radio-isotopic dating (primarily $^{40}Ar/^{39}Ar$ and/or U-Pb) of minerals (sanidine and/or zircon) from volcanic ash layers (e.g. Wing *et al*. 2000; Luterbacher *et al*. 2004). Time-series analysis of various proxy records (colour, elemental, isotopic) permits identification of cyclicity within sedimentary records that can be attributed to orbital (Milankovitch) forcing, which has permitted the development of floating timescales for the early Paleogene (Lourens *et al*. 2005; Westerhold *et al*. 2007, 2008, 2009; Westerhold and Röhl, 2009; Galeotti *et al*. 2010). Such floating timescales can be constrained via radio-isotopic dating of minerals from volcanic layers, either directly or by correlation (using bio- and/or magento-stratigraphy). At present $^{40}Ar/^{39}Ar$ dates underpin much of the Cenozoic timescale. However the accuracy of these dates is relative to ages of the mineral standard used in their calibration - typically the Fish Canyon sanidine (FCs) standard, in addition to the potassium decay constants (Renne *et al*. 1998), both of which have been the focus of ongoing research. Attempts to calibrate the age of FCs using sanidines from multiple tuff layers with both $^{40}Ar/^{39}Ar$ and astronomical ages, has resulted in an age of 28.201 ±0.046 Ma (Renne *et al*. 1998; Kuiper *et al*. 2008). Renne *et al*. (2010) derive an age of 28.305 ±0.036 Ma for the FCs based upon a dataset of paired $^{238}U/^{206}Pb$ (zircon) and $^{40}Ar/^{39}Ar$ (sanidine and biotite) dates for rocks where the minerals should give equivalent dates. Furthermore, Channell *et al*. (2010) used astronomical ages for Quaternary magnetic reversals, also dated by $^{40}Ar/^{39}Ar$, to derive an age of ~27.93 Ma for FCs. These age estimates for the FCs do not overlap within their quoted uncertainties, and combined indicate that the accuracy of $^{40}Ar/^{39}Ar$ dates is (at present) limited to ~1 %. In contrast, the accuracy of U-Pb dates is relative to isotopic tracers which can be accurately calibrated to SI units, and the decay constants that are known

through counting experiments (Jaffey *et al*. 1971). Precise isotope ratio determinations can therefore result in $^{238}U/^{206}Pb$ (zircon) dates with total uncertainties of <0.2 % (Jaffey *et al*. 1971; Condon *et al*. 2007). Furthermore, transformation of mineral dates into eruption/stratigraphic dates requires interpretation of mineral date populations and consideration of petrology (i.e., magma chamber processes, mineral closure temperature for retention of isotopes systematics).

Compounding the problem of Paleogene timescale calibration is the issue that the geological context of radio-isotopically dated samples is somewhat uncertain with respect to the proxy records being constrained. As a result, recent numerical ages derived for the P/E boundary using the recalibrated $^{40}Ar/^{39}Ar$ radio-isotopic data and cyclostratigraphic datasets have yielded inconsistent ages for the boundary (Kuiper *et al*. 2008; Westerhold *et al*. 2008, 2009), preventing consensus on the duration of the Paleocene epoch and the exact temporal relationship of the PETM to potential geologic/orbital triggers (e.g. Svensen *et al*. 2004, 2010; Storey *et al*. 2007). More robust constraints on the numerical age of the P/E boundary are therefore required in order to (1) constrain the duration of the Paleocene Epoch, to ascertain the number of 405 kyr cycles within it and permit the accurate correlation of IODP, ODP and DSDP cores, (2) anchor currently floating cyclostratigraphic records, and (3) constrain the exact temporal relationship between the PETM and potential triggers.

The P/E boundary is defined at the base of the 2.5-6 ‰ negative CIE (Dupuis *et al*. 2003), coeval with the PETM. Typically, previous studies have only indirectly derived a numerical age for the P/E boundary (e.g. Wing *et al*. 2000; Luterbacher *et al*. 2004; Westerhold *et al*. 2007, 2008, 2009; Kuiper *et al*. 2008), owing to the absence of ash layers within the PETM CIE (the exception being Jaramillo *et al*. [2010]; see Section 2.4.1). Here we document a U-Pb (zircon) date from a bentonite layer *within* the PETM CIE from the Longyearbyen section in the Central Basin of Spitsbergen. We combine this date with cyclostratigraphic datasets, from both the Longyearbyen section (Harding *et al*. 2011) and core BH9/05 (drilled near Sveagruva, Spitsbergen; Dypvik *et al*. [2011]), to constrain the age of the P/E boundary.

2.2 Materials and methods

2.2.1 Geological succession

The study localities are situated in the Paleogene Central Basin of Spitsbergen, the largest island in the Svalbard Archipelago, situated on the NW corner of the Barents Shelf (Figure 2.1; Harland [1997]; Dallman *et al*. [1999]). Harland (1997; and references therein) provides a comprehensive overview of the stratigraphy of the Central Basin

and the other Paleogene successions on Spitsbergen. The stratigraphic nomenclature used in this report adheres to that proposed by Dallman *et al*. (1999). During the Paleogene Spitsbergen was situated at ~75˚N (Harland 1997), adjacent to the NE corner of Greenland, but with the progressive opening of the northern North Atlantic a predominantly transpressional dextral strike-slip motion between the two continental masses was initiated in the Paleocene (Figure 2.1; Bruhn and Steel [2003]). For the remainder of the Paleogene the Central Basin developed as a subsiding foreland basin (Kellogg 1975; Helland-Hansen 1990; Müller and Spielhagen 1990; Harland 1997), the sediment shed from the rising West Spitsbergen Orogenic Belt resulting in a thick sedimentary succession (up to 2.5 km: Helland-Hansen [1990]).

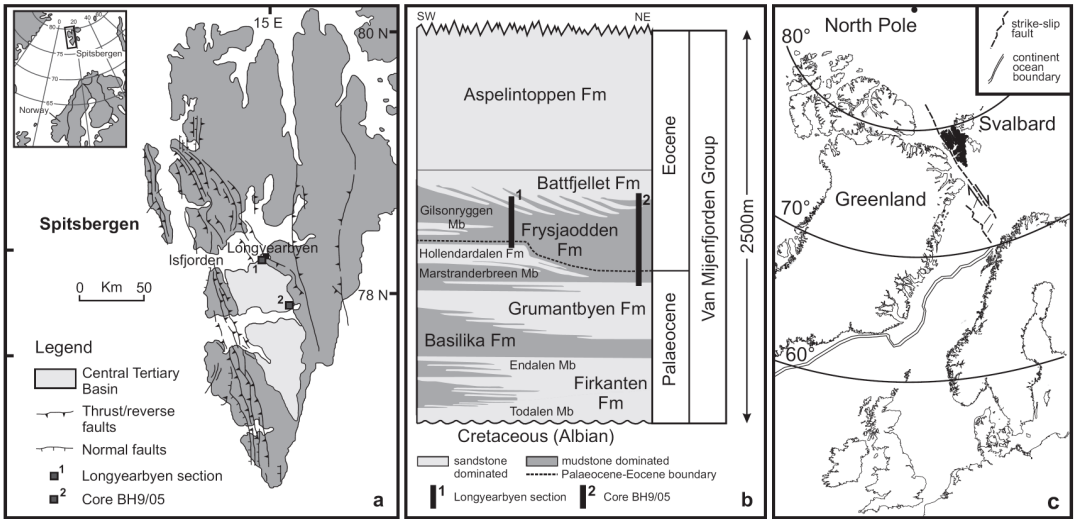

Figure 2.1: Study area. **a)** Map of Spitsbergen illustrating study localities (after Uroza and Steel [2008]; Blythe and Kleinspehn [1998]). **b)** The Paleogene stratigraphy of Spitsbergen illustrating the interval of the Frysjaodden Formation studied at each locality (after Uroza and Steel [2008]; Steel *et al*. [1985]). **c)** Paleogeographic reconstruction of Spitsbergen (in black) and the Svalbard archipelago in the Eocene (after Mosar *et al*. [2002]).

Two sections were studied: the Longyearbyen outcrop section and core BH9/05. At Longyearbyen the PETM lies within the Gilsonryggen Member of the Frysjaodden Formation (Harding *et al*. 2011), a unit of around 250 m of homogeneous mudstones. A -4 ‰ organic carbon isotope excursion ($\delta^{13}C_{TOC}$) is present between 3 and 28 m above the top of the Hollendardalen Formation, with the coeval presence of the PETM-diagnostic dinoflagellate cyst *Apectodinium augustum* (Harding *et al*. 2011). Two conspicuous bentonite horizons occur at 10.90 and 14.60 m above the top of the Hollendardalen Formation, within the PETM CIE (Figure 2.2).

The Frysjaodden Formation is identified from 551-110 m depth in core BH9/05 (Dypvik *et al*. 2011), drilled NW of the town of Sveagruva near Urdkollbreen. The cored succession cannot be divided into members due to the fine grained nature of the lithologies (Dallman *et al*. 1999). The mudstone-dominated succession is continuous across the upper Paleocene-lower Eocene interval, with only minor amounts of carbonate detected in XRD analyses (Dypvik *et al*. 2011). A ~4.2 ‰ organic carbon isotope ($\delta^{13}C_{TOC}$) excursion is present at the base of the Frysjaodden Formation in core BH9/05 (534-487 metres depth, see Figure 2.2; Cui [2010]), again coincident with two bentonite horizons lying at 517.20 and 511.10 metres depth respectively (Dypvik *et al*. 2011).

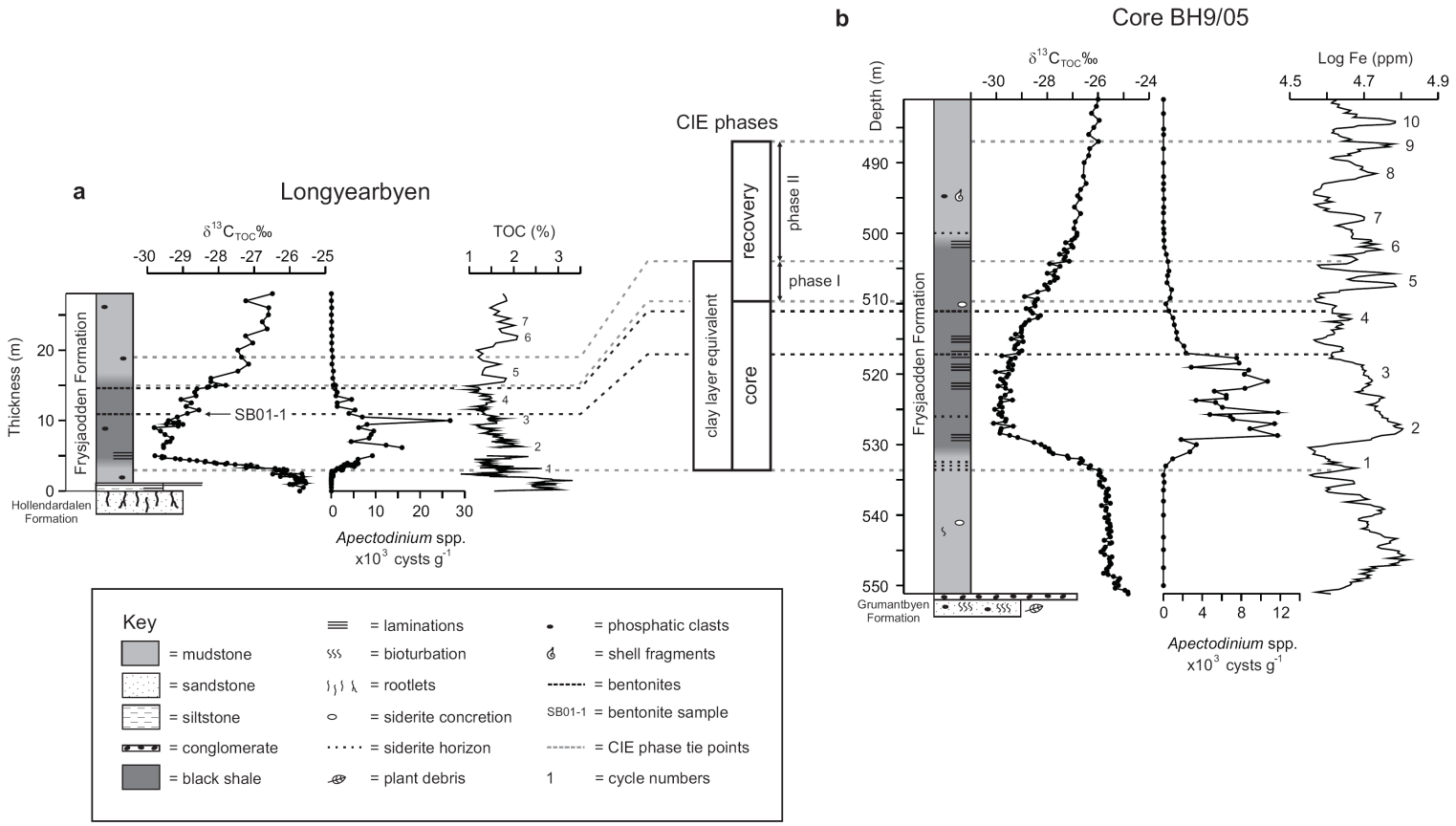

Figure 2.2: Lithological, dinocyst and geochemical (organic carbon isotope [$\delta^{13}C_{TOC}$‰]; TOC [%]; Log Fe [ppm]) datasets across the P/E boundary from **a)** the Longyearbyen outcrop section (Harding *et al*. 2011) and **b)** core BH9/05 (Log: Dypvik *et al*. 2011; $\delta^{13}C_{TOC}$: Cui 2010). Note the Hollendardalen Formation is absent in core BH9/05, due to pinch out south of the Longyearbyen section (e.g. Dallman *et al*. 1999). Cycle numbers and CIE phases adhere to those proposed by Röhl *et al*. (2007). Note that the heights/depths used to define the base and top of recovery phase I are based on analysis of both cyclostratigraphic and $\delta^{13}C_{TOC}$ records (as suggested by Röhl *et al*. [2007]), due to the asymptotic shape of CIE recovery interval in Spitsbergen.

2.2.2 Palynological processing

Sixty-six samples were processed in order to constrain the $\delta^{13}C_{TOC}$ excursion in core BH9/05 using dinoflagellate cyst (dinocyst) biostratigraphy. Sample processing methods were identical to those of Harding *et al*. (2011), with the exception that no samples were subject to ultrasonic treatment. Concentrations of dinocysts were generated by counting 300 specimens where possible, with normalisation against the out-of-count *Lycopodium* spike (Stockmarr 1971). Dinocyst taxonomy follows that of Fensome and Williams (2004). The appearance of the dinocyst *Apectodinium augustum* at the start of the $\delta^{13}C_{TOC}$ excursion firmly identifies the PETM in core BH9/05, illustrating that the bentonite horizons in both the Longyearbyen section and core BH9/05 are coeval (Figure 2.2). The PETM CIE from core BH9/05 is plotted in Figure 2.3 to illustrate the different phases of the CIE in Spitsbergen, with respect to ODP sites 690 and 1263.

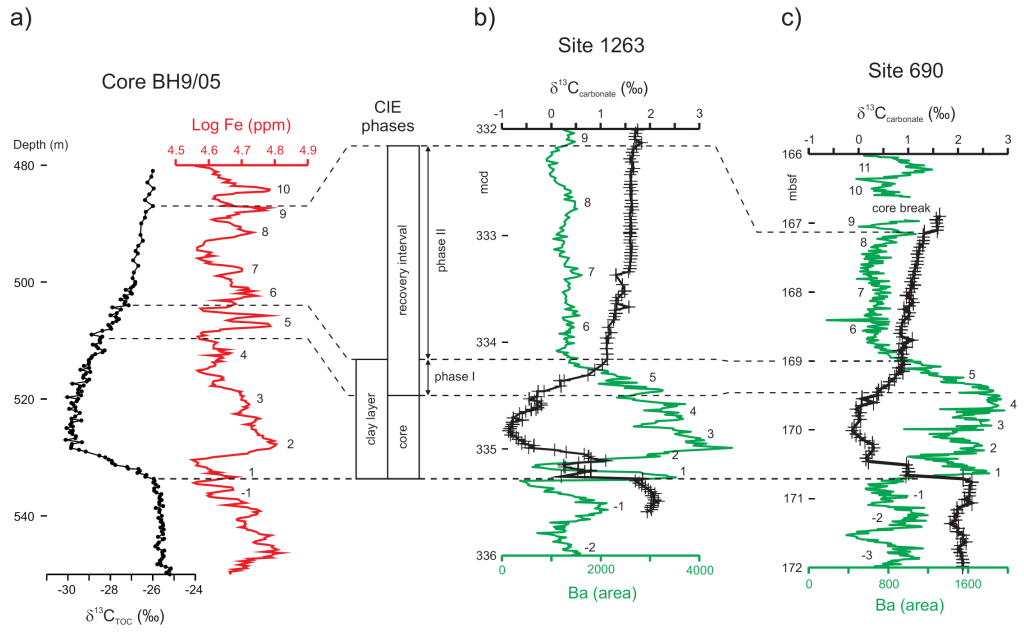

Figure 2. 3: Comparison of PETM CIE records from Spitsbergen and selected ODP sites. **a)** Core BH9/05, Spitsbergen, $\delta^{13}C_{TOC}$ (‰) record of Cui (2010; black), and Log Fe (ppm; this study). **b)** ODP Site 1263 (Leg 208, Walvis Ridge) $\delta^{13}C_{carbonate}$ (‰) record from Zachos *et al*. (2005; black), and Ba (area) records from Röhl *et al*. (2007; grey). **c)** ODP Site 690 (Leg 113, Weddell Sea) $\delta^{13}C_{carbonate}$ (‰) record from Bains *et al*. (1999; black) and Ba records from Röhl *et al*. (2007; grey). Panels **b)** and **c)** after Röhl *et al*. (2007). Cycle numbers and CIE phases adhere to those proposed by Röhl *et al*. (2007). Note that due to the asymptotic shape of CIE recovery interval in Spitsbergen, we identified the onset and end of recovery phase I using both the $\delta^{13}C_{TOC}$ and cyclostratigraphic records of core BH9/05, as suggested by Röhl *et al*. (2007).

2.2.3 Radio-isotopic dating

Analysis of the lower bentonite layer in the Longyearbyen section (sample SB01-1; Figure 2.2), was carried out at the NERC Isotope Geosciences Laboratory (NIGL), UK. Zircons were isolated from around 300 grams of sample SB01-1, using conventional mineral separation techniques. Prior to isotope dilution thermal ionization mass spectrometry (ID-TIMS) analyses zircons were subject to a modified version of the chemical abrasion technique (Mattinson 2005). For details of sample pre-treatment, dissolution and anion exchange chemistry at NIGL the reader is referred to Sláma *et al*. (2008). Our U-Pb ID-TIMS analyses utilized the EARTHTIME ^{205}Pb-^{233}U-^{235}U (ET535) tracer solution. Measurements at the NERC Isotope Geosciences Laboratory were performed on a Thermo Triton TIMS. Pb analyses were measured in dynamic mode on a MassCom SEM detector and corrected for 0.14 ±0.04 %/u. mass fractionation. Linearity and dead-time corrections on the SEM were monitored using repeated analyses of NBS 982, NBS 981 and U500. Uranium was measured in static Faraday mode on 10^{11} ohm resistors or for signal intensities <15 mV, in dynamic mode on the SEM detector. Uranium was run as the oxide and corrected for isobaric interferences with an ^{18}O/^{16}O composition of 0.00205 (IUPAC value and determined through direct measurement at NIGL). U-Pb dates and uncertainties were calculated using the algorithms of Schmitz and Schoene (2007), combined with a ^{235}U/^{205}Pb ratio of 100.18 and ^{233}U/^{235}U double spike ratio of 0.99464 for the ET535 tracer. All common Pb in the analyses was attributed to the blank and subtracted based on the isotopic composition and associated uncertainties analyzed over time. The ^{206}Pb/^{238}U ratios and dates were corrected for initial ^{230}Th disequilibrium using a $Th/U_{[magma]}$ of 4 ±1 applying the algorithms of Schärer (1984) resulting in an increase in the ^{206}Pb/^{238}U dates of ~100 kyrs and an additional uncertainty contribution of ~10 kyrs. Errors for U-Pb dates are reported in the following format: ±X(Y)[Z], where X is the internal or analytical uncertainty in the absence of all systematic error (tracer calibration and decay constants), Y includes the quadratic addition of tracer calibration error (using a conservative estimate of the 2σ standard deviation of 0.1% for the Pb/U ratio in the tracer), and Z includes the quadratic addition of both the tracer calibration error and additional ^{238}U decay constant errors of Jaffey *et al*. (1971). All analytical uncertainties are calculated at the 95% confidence interval. These ^{238}U/^{206}Pb dates are traceable back to SI units via the gravimetric calibration of the EARTHTIME U-Pb tracer and the determination of the ^{238}U decay constant (Jaffey *et al*. 1971; Condon *et al*. 2007).

2.2.4 XRF time-series

Fe and Mn time-series were generated for core BH9/05 using a Niton UK XL3t portable XRF scanner. Measurements (n=1195; Appendix 2) were taken every 20 cm throughout that part of the core section recording the $\delta^{13}C_{TOC}$ excursion (550 m to 480

m core depth) and every 40 cm outside this interval (Figure 2.4). Twelve samples were analyzed using wavelength dispersive (WD) XRF, to calibrate results from the Niton UK scanner. These samples were crushed to a fine powder and air dried at 105 ºC. The sample (0.5 g ±0.0003) was mixed with 5 ±0.003 g lithium tetraborate flux (Fluxana GmbH, Germany) and fused at ~1100 ºC using a Vulcan fusion system (HD Elektronik und Elektrotechnik GmbH, Germany) to provide a 1:10 glass bead. The glass beads were analysed using a Philips MAGIX-PRO automatic sequential wavelength dispersive X-ray fluorescence spectrometer fitted with a 4 kW Rh X-ray tube. Loss on ignition (LOI) was estimated from the function (100 %- Σ XRF oxides) since the original XRF major element calibration was constructed on this basis. We obtained correlation coefficients (r^2) between the WD XRF and the Niton UK scanner of 0.76 for Fe and 0.89 for Mn (Figure 2.5).

2.2.5 Time-series analysis

Both Fe and Mn time-series were first smoothed using a 5-point moving average in order to reduce noise. Log Fe and Mn values were used in order to stabilize cycle variance, with the data also normalized and detrended before spectral analysis (Weedon 2003). Gaussian filtering and tuning were carried out using Analyseries version 1.1 (Paillard *et al*. 1996). In order to generate both wavelet and multi-taper method power spectra, both Fe and Mn time-series were re-sampled using a constant sample spacing, *via* linear interpolation using Analyseries. Multi-taper method power spectra (Thompson 1982) were calculated using SSA-MTM toolkit (Dettinger *et al*. 1995; Ghil *et al*. 2002) with a red noise model to assess confidence levels. Wavelet spectra were calculated using the Matlab script of Torrence and Compo (1998). The time-series was zero padded to reduce edge effects, with a red noise model to assess confidence levels (Torrence and Compo 1998).

2.3 Results

2.3.1 Radio-isotopic dating

Zircons separated from bentonite sample SB01-1 were small (<50 μm) with aspect ratios of ~3 to ~7. Thirteen single grains were analyzed, and the resulting data are presented in Appendix 2. Three of the thirteen analysis produced discordant U-Pb data with Paleozoic $^{207}Pb/^{206}Pb$ dates. The remaining ten analyses yielded $^{206}Pb/^{238}U$ dates between 57.08 and 55.71 Ma (Figure 2.6). U-Pb ages for volcanic ash beds are determined by the interpretation of U-Pb dates from single zircon crystals. Utilization of the chemical abrasion pre-treatment technique (Mattinson 2005) for the effective elimination of Pb-loss means that we consider each zircon $^{206}Pb/^{238}U$ date accurate (i.e., they do not reflect post-crystallization Pb-loss). Detailed studies of zircons and other

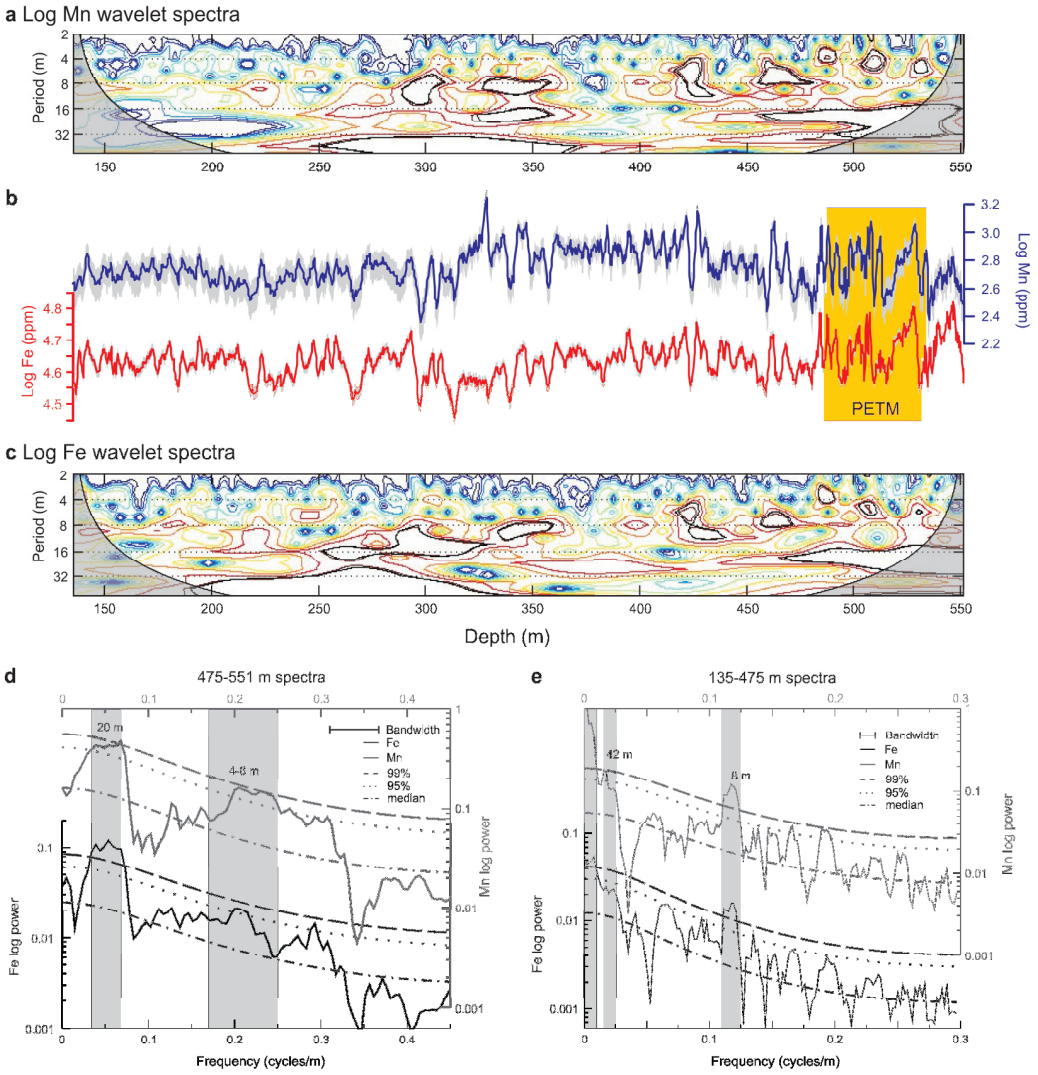

Figure 2.4: BH9/05 time-series in the depth domain. **a)** and **c)** Log Mn and Fe wavelet spectra respectively. Black lines indicate 95 % significance level. Shaded area indicates the 'cone of influence' where edge effects make recognition of cycles less confident (Torrence and Compo 1998). Warm (cold) colors indicate high (low) spectral power. **b)** Log Mn (blue) and Fe (red) time-series. Grey bands represent 2σ error values for the precision of the Niton UK XRF scanner, calculated using the standard deviation derived from repeat analyses of fifteen samples, each measured 10 times. Yellow box indicates stratigraphic thickness of PETM CIE. **d)** and **e)** Multi-taper method power spectra (Thompson 1982) for the intervals from 475-551 m and 135-475 m respectively. Grey bars illustrate the dominant cycles and their stratigraphic thickness. Note the wide bandwidth on panel d is the result of the short stratigraphic thickness of the time-series with respect to the cycle wavelengths being analyzed (which has the effect of smearing out the spectral peaks). Spectra were generated by re-sampling the time-series using a constant sample spacing (0.2 m, panel d; 0.5 m, panel **e)**, using 3 tapers. Red noise models were generated using SSA-MTM toolkit (Ghil *et al.* 2002) to calculate the confidence levels illustrated.

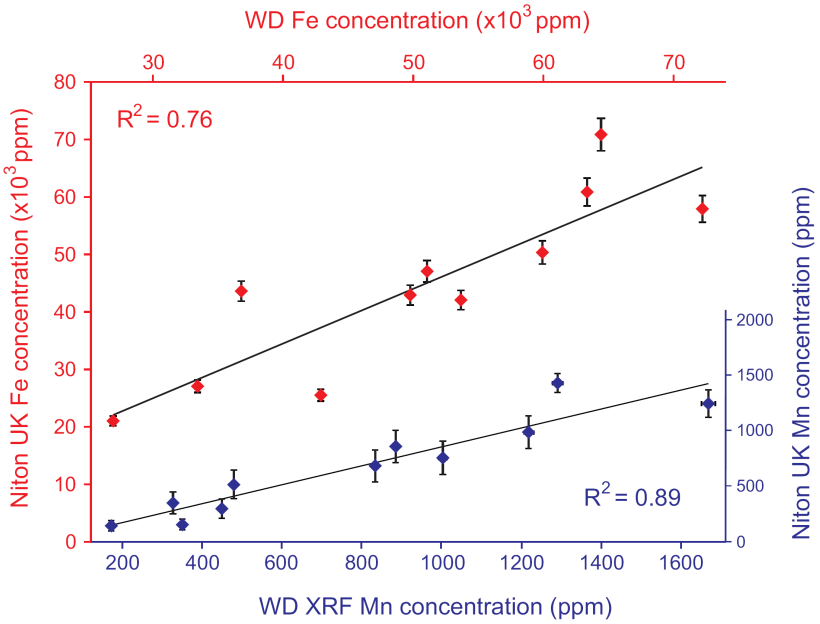

Figure 2.5: Calibration curve for the Niton UK portable XRF device to wavelength dispersive (WD) XRF.

minerals dateable by the U-Pb system often indicate a protracted interval of zircon crystallization in a magmatic system, demonstrating the possibility that some zircon in a given ash layer record ages of the eruption (i.e., those that crystallized immediately prior to eruption) and some older ages which reflect the pre-eruptive crystallization (and residence) of zircons (Schoene *et al*. 2010). In such samples the age of the youngest zircon (or zircon population) is considered to best approximate the age of the ash layers with older zircon dates reflecting pre-eruptive crystallization. Excluding obvious inheritance of Paleozoic zircon, we observe a range of zircon $^{206}Pb/^{238}U$ dates in sample SB01-1 from 57.08 ±0.06 to 55.71 ±0.14 Ma, with the five youngest analyses yielding a weighted mean $^{206}Pb/^{238}U$ date of 55.785 ±0.034(0.066)[0.086] Ma (MSWD = 0.88, calculated using Isoplot 3.0 [Ludwig 1991]) which is interpreted as being the best estimate for the zircons of this sample. We consider this date to best approximate the age of sample SB01-1 and the older zircon $^{206}Pb/^{238}U$ dates to reflect analyses of xenocrystic and/or zircons that have experienced pre-eruptive magma residence, with the single analysis precision of ~100 kyr permitting de-convolution of the mixed age population. An alternative to the conventional approach of taking a weighted mean date based upon a coherent population of youngest $^{206}Pb/^{238}U$ dates would be to interpret the single zircon dates. As the youngest five analyses form a coherent population this would have no discernable effect on the interpreted $^{206}Pb/^{238}U$ date for

SB01-1 and would increase the total uncertainty by an additional ~20 kyrs, and as such our proposed date for SB01-1 is insensitive to different approaches to zircon date interpretation.

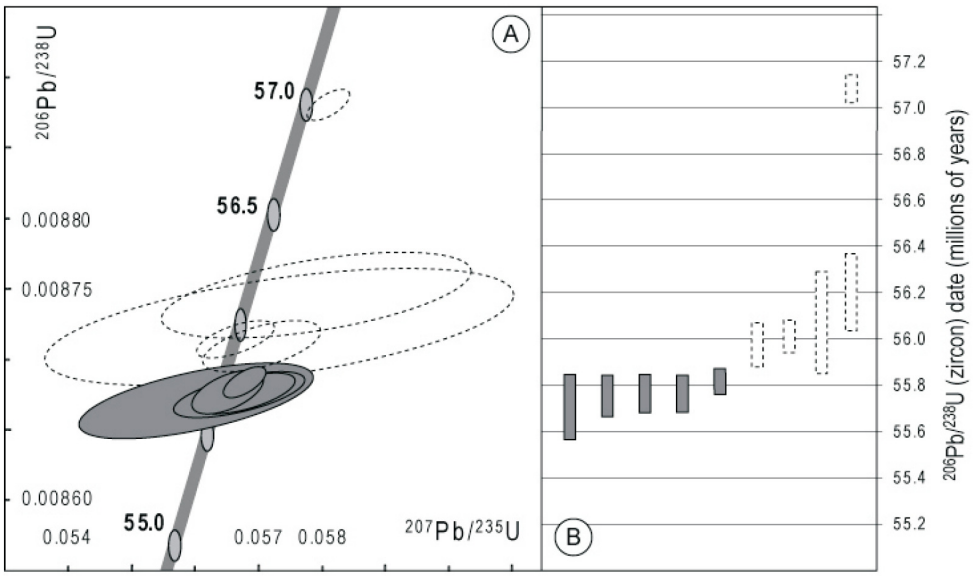

Figure 2.6: U-Pb data for sample SB01-1. **a)** conventional U-Pb concordia plot of zircons analysed from sample SB01-1. The grey band reflects the uncertainty in the ^{238}U and ^{235}U decay constants (Jaffey *et al*. 1971). **b)** plot of $^{238}U/^{206}Pb$ dates for single zircon crystals analyses (same data as in Figure 2.6a). Dashed ellipses/bars represent analyses of zircon that are considered to be xenocrysts and/or inherited crystals that are disregarded in calculation of final date, whereas as grey filled ellipses/bars represent the analyses used for calculation of the weighted mean final date (see text for discussion).

2.3.2 Cyclostratigraphic analysis

A detailed description of the cyclostratigraphic age model for the Longyearbyen section can be found in Harding *et al*. (2011, Appendix 1). Here, numerical ages from Longyearbyen (Harding *et al*. 2011) were corrected using the numerical age of the bentonite. However, we also generated Fe and Mn time-series from core BH9/05, with cyclostratigraphic analysis of this data discussed below.

2.3.2.1 Records in the depth domain

In order to build an orbital age model for core BH9/05, it was first necessary to ascertain if the cycles present in the time-series were derived from orbital forcing (Weedon 2003; Bailey 2009). Comparison of the Fe/Mn time-series of core BH9/05

with the TOC record from Longyearbyen illustrates that the same cycles are present in the depth domain in both different parameters and localities within Spitsbergen (Figure 2.2). This confirms the cycles present in the PETM are not predominantly the result of stochastic noise (Weedon 2003).

The BH9/05 time-series (Figure 2.4) illustrate a strong cyclicity within the interval from the base of the Frysjaodden Formation to the top of the PETM (551-487 m), with two dominant cycle lengths of 4-6 m (~0.2 cycles/m) and 20 m (0.05 cycles/m) above 95 % confidence level (Figure 2.4; note that the short stratigraphic thickness of this interval with respect to the cycle wavelengths being analyzed results in a wide bandwidth for the power spectra shown in Figure 2.4d, which has the effect of smearing out the spectral peaks). Above this interval the cycle wavelength increases, with components at 0.12 and 0.024 cycles/m representing 8 m and 42 m cycles respectively (Figure 2.4). The wavelet spectra therefore suggest that the sedimentation rate increases above the PETM (as cycle wavelength increases when sedimentation rates rise). This is in contrast to other PETM continental margin sections, which typically show an increase in sedimentation rates within the PETM (e.g. John *et al*. 2008; Sluijs *et al*. 2008a). However, the Central Basin lies adjacent to the West Spitsbergen Orogeny, and thus the high volume of sediment shed off the growing orogenic belt at this time (Harland 1997; Dallman 1999) probably overprinted any climatically induced changes in sedimentation. The increase in sedimentation rates above the PETM is also consistent with the gradual infilling of the basin through time, eventually leading to deposition of the overlying shelf margin delta and terrestrial formations (Battfjellet and Aspelintoppen Formations respectively [see Dallman 1999]).

In order to estimate the duration of the Fe and Mn cycles, an independent estimate of the sedimentation rate is required. Outside the PETM interval, no such constraints are currently available. Therefore, the rest of this study will focus on the interval between the base of the Frysjaodden Formation and the end of the PETM (551–487 m), where the PETM CIE acts as an external constraint on cycle durations. Note that the PETM CIE is a valid external constraint for the following reasons: (1) The CIE inflection points in $\delta^{13}C_{TOC}$ and $\delta^{13}C_{n\text{-}alkane}$ records in core BH9/05 are at stratigraphically equivalent heights (Cui 2010), indicating changes in organic matter assemblage did not alter the stratigraphic position of the CIE inflection points. (2) The abundance of reworked pre-Cenozoic palynomorphs is low throughout the lower Frysjaodden Formation (Harding *et al*. 2011), indicating reworking of such material did not significantly alter the $\delta^{13}C_{TOC}$ record. Furthermore the consistent stratigraphy between Spitsbergen sites (Figure 2.2), suggests localized reworking of Paleocene organic matter did not significantly affect

our records (as differential reworking of isotopically heavy pre-PETM material would alter the carbon isotope stratigraphy between sites; Harding *et al*. [2011]).

The stratigraphic thickness of the PETM CIE in core BH9/05 (onset to the end of recovery phase II: 533.66 m to 487.00 m) was combined with previously published data for the duration of this interval to calculate the sedimentation rate during the PETM. However, different estimates for the duration of the PETM CIE currently exist. Röhl *et al*. (2007) used cycles in Fe, Ca and Ba at ODP sites 1263 (Walvis Ridge) and 690 (Weddell Sea) to derive a PETM duration of 170 kyr (8.5 precession cycles), which is similar to cyclostratigraphic results from the Bighorn Basin (157 kyr, 7.5 precession cycles; Abdul Aziz *et al*. [2008]). A recent re-appraisal of the ^{3}He age model of Farley and Eltgroth (2003) led to estimates from 90 ±10 to 140 ±30 kyr for the duration of the PETM CIE at ODP Site 690 (Sluijs *et al*. 2007a), with the upper estimate consistent with recent cyclostratigraphic results. As similar durations for the PETM CIE have been derived from both low (Walvis Ridge), mid (Bighorn Basin) and high (Weddell Sea) latitudes it is reasonable to assume that the duration of the event would have been similar in the Arctic (170 kyr, *sensu* Röhl *et al*. [2007]). Given the 46.6 m thickness of the CIE (Figure 2.2) and assuming that its duration is 170 kyr yields a sedimentation rate of 27.4 cm/kyr (4660 cm/170 kyr). Using this sedimentation rate the 4-6 m and 20 m cycles within the PETM represent 15-22 kyr and 73 kyr cycles respectively.

However, recently Murphy *et al*. (2010) derived a duration of 217 +44/-31 kyr for the PETM CIE (onset to the end of recovery phase II) from ODP Site 1266 using an extraterrestrial ^{3}He age model. Potential reasons for the difference between this age model and that of Röhl *et al*. (2007) were previously discussed in Murphy *et al*. (2010). Using a duration of 217 kyr for the PETM CIE (onset to the end of recovery phase II) together with the stratigraphic thickness of the same interval from core BH9/05 gives sedimentation rates of 21.5 cm/kyr (4660 cm/ 217 kyr). In this scenario, the 4-6 m and 20 m cycles would have durations of 19-28 kyr and 93 kyr respectively. The duration of the 4-6 m cycles using either the Röhl *et al*. (2007) or Murphy *et al*. (2010) age models is therefore consistent with their derivation from precession forcing. The ratio between the 4-6 and 20 m cycles suggests the 20 m cycle represents the short eccentricity component (~100 kyr), consistent with the cycle duration derived using the Murphy *et al*. (2010) age model. The dominance of precession and eccentricity with a minor obliquity component in late Paleocene/early Eocene sediments is typical and has been observed at numerous sites on a global scale (e.g. Westerhold *et al*. 2007, 2008; Abdul Aziz *et al*. 2008; Sluijs *et al*. 2008a).

Because of the different age models for the duration of the PETM CIE, we present two options for the interpretation of the cycles within core BH9/05 (Section 2.3.2.2). We extracted the Gaussian filter outputs from the Fe and Mn time-series in the depth domain at wavelengths of 4.2 m (0.24 ±0.07 cycles/m), and 20 m (0.05 ±0.01 cycles/m; Figure 2.7). The 4.2 m and 20 m filters represent the precession and short eccentricity components respectively, with precession cycles numbered according to Röhl *et al*. (2007). Figure 2.7 shows that a minimum of 8.5 precession cycles are present within the PETM CIE (from onset to end of recovery phase II), consistent with the cyclostratigraphic age model of Röhl *et al*. (2007). If we consider the Röhl *et al*. (2007) age model to be the most accurate, the precession cycles labeled 1 to 3 in Figure 2.7 (i.e. excluding those marked with an asterisk) correspond to one short eccentricity (20 m) cycle. However, between 4-6 precession cycles (typically 5) should be present for every one short eccentricity cycle (e.g. Pälike 2005), and thus it is difficult to reconcile the two filter outputs in this interval. Furthermore, we identify three additional cycles with low amplitude in the time-series and filter outputs in the PETM interval (marked with asterisks) when compared to the Röhl *et al*. (2007) age model (Figure 2.7). If these cycles are interpreted as low-amplitude precession cycles, the duration of the PETM CIE is consistent with that obtained from the ^{3}He age model of Murphy *et al*. (2010; i.e. 11 precession cycles). Using this approach the short eccentricity:precession cycle ratio is 1:5, consistent with orbital cycle ratios (e.g. Pälike 2005). Two of the additional precession cycles occur within the interval between the PETM CIE onset and the end of recovery phase I (making a total of 7 cycles; Figure 2.7), which is equivalent to the clay layer interval in ODP Leg 208 sites (Figure 2.3). This is consistent with the hypothesis of Röhl *et al*. (2007), who argued that 5-7 precession cycles must be present within the clay layer interval of Leg 208 sites, in order to maintain the phase of the 405 kyr eccentricity cycle extracted from Site 1262.

2.3.2.2 Records in the time domain

Here we construct two separate cyclostratigraphic age models for core BH9/05 (from 551-487 m), each based on the different options for the duration of the PETM CIE from Röhl *et al*. (2007) and Murphy *et al*. (2010). Option A, matching the BH9/05 records to the Röhl *et al*. (2007) age model, was carried out by matching the Fe concentration record from BH9/05 to that of ODP Leg 208, Site 1263 (Westerhold *et al*. [2007]; corrected after Röhl *et al*. [2007]; Appendix 2), using the PETM CIE as an external constraint. The duration of the PETM CIE from the ^{3}He age model of Murphy *et al*. (2010) is longer than recent cyclostratigraphic estimates of the PETM CIE (e.g. Röhl *et al*. 2007; Abdul Aziz *et al*. 2008), and therefore tuning the BH9/05 record to another site consistent with this ^{3}He age model is currently not possible. Therefore, in order to build an age model for core BH9/05 consistent with the results of Murphy *et al*. (2010),

we assigned a 21 kyr duration to the interval between each precession cycle peak, for each cycle identified in the filter output of Figure 2.7c (following a similar approach by Westerhold *et al*. [2007] and Röhl *et al*. [2007]). Note that this approach assumes sedimentation rates remained constant between precession cycle peaks. Cycle peaks were assigned ages relative to cycle -1 in Figure 2.7c, with the resultant age model (Option B) shown in Appendix 2. However, we note that precession cyclicity is quasi-periodic, with cycle durations ranging from 19-24 kyr in duration (e.g. Pälike 2005). Therefore we estimate an error of ±3 kyr for each precession cycle peak utilized in age model Option B.

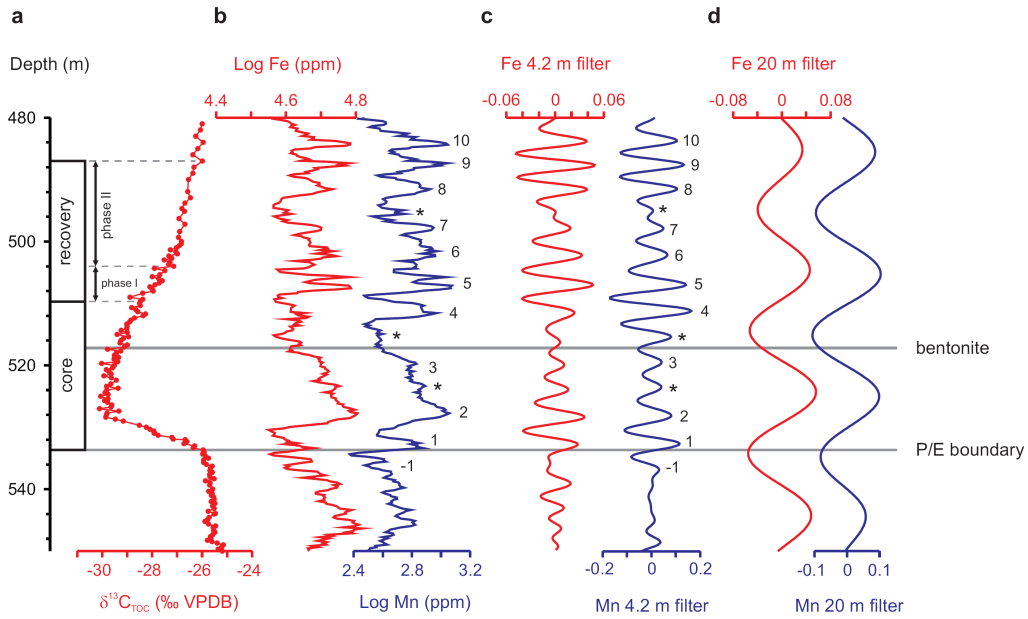

Figure 2.7: Filtered records of core BH9/05 in the depth domain. **a)** $\delta^{13}C_{TOC}$ (‰) from Cui (2010), illustrating the phases of the PETM CIE from Röhl *et al*. (2007). **b)** BH9/05 Log Fe (ppm; red) and Mn (ppm; blue) time-series. Cycle numbers adhere to those of Röhl *et al*. (2007), with potential additional cycles marked with an asterisk. **c)** Log Fe (red) and Log Mn (blue) 4.2 m (0.24 ±0.07 cycles/m) Gaussian filter output, representing the precession component of orbital forcing (cycle numbers as in panel b). **d)** Log Fe (red) and Log Mn (blue) 20 m (0.05 ±0.01 cycles/m) filter, representing the short eccentricity (~100 kyr) component of orbital forcing.

2.3.3 The numerical age of the Paleocene/Eocene boundary

The P/E boundary is defined as the base of the PETM CIE (Dupuis *et al*. 2003) and we therefore integrate the age of the bentonite with time-series datasets to constrain the age of the P/E boundary (and by inference the onset age for the PETM CIE). Numerical ages for both the cyclostratigraphic age models from Section 2.3.2.2 and the record from the Longyearbyen section (Harding *et al*. 2011) were corrected using the age of the bentonite. In order to constrain the age of the P/E boundary, the relative duration between the dated bentonite horizon and the onset of the PETM CIE is required. No grain size fluctuations or abrupt shifts in carbon isotope values were observed within this interval in either the Longyearbyen section or core BH9/05 (Figure 2.2), implying that sedimentation was continuous between the onset of the CIE and the lower bentonite horizon.

Figure 2.8 shows the duration between the bentonite and base of the PETM CIE using age model Option A for core BH9/05 together with the cyclostratigraphic age model from the Longyearbyen section (Harding *et al*. 2011). Cycle counting using the Gaussian filter output of precession illustrates a 40 and 45 kyr duration between the lower bentonite and the base of the PETM CIE in core BH9/05 and at Longyearbyen respectively; which results in numerical ages of 55.827 ±0.086 Ma (BH9/05) and 55.831 ±0.086 Ma (Longyearbyen) for the P/E boundary (Figure 2.8). As each section was tuned independently, the 5 kyr difference between the ages derived from each section partly represents the error associated with the tuning process. However, as the time-series from each section are constructed from different parameters (TOC% in Longyearbyen; Fe and Mn concentrations in core BH9/05), part of the 5 kyr offset may result from differences in how the individual parameters were incorporated into the sedimentary record. Therefore we incorporate the 5 kyr offset into the error for the age the P/E boundary. Further error results from tuning the cyclostratigraphic records from Spitsbergen to the Fe record of ODP Site 1263, because carbonate dissolution at the base of the PETM clay layer at Site 1263 results in a minor hiatus in this section (Zachos *et al*. 2005; McCarren *et al*. 2008). It is estimated that the duration of missing time owing to carbonate dissolution is on the order of 10 kyr (Röhl *et al*. 2007), which we incorporate into the error, producing an age of 55.829 ±0.101 Ma (Figure 2.8). Conversely, using age model Option B for core BH9/05 results in a duration of 81 kyr between the bentonite and the base of the PETM CIE (Figure 2.9), giving an age of 55.866 ±0.098 Ma for the P/E boundary. The error based on age model Option B includes ±0.086 Myr from U-Pb dating of bentonite SB01-1, and ±0.012 Myr error from cycle counting (4 precession cycles at ± 3 kyr per cycle; Section 2.3.2.2). Note that no error for carbonate dissolution is applied to Option B because this approach required no tuning to Site 1263, and the near absence of carbonate in the Frysjaodden

Formation (Dypvik *et al*. 2011; Harding *et al*. 2011) implies that carbonate dissolution did not alter the Spitsbergen PETM records. The difference between age model option A and B for the age of the P/E boundary is thus ~37 kyr, and both options are within error of one another because the accuracy of the radio-isotopic date dominates the uncertainty of our derived P/E boundary age. Therefore the age of the boundary inferred here is not significantly altered by large changes in the duration of the PETM CIE used to derive the respective age models. Taking into account both the cyclostratigraphic options and their uncertainty, together with the uncertainty from the radio-isotopic dating of sample of SB01-1, we derive an age range of 55.728-55.964 Ma for the P/E boundary (Figure 2.10).

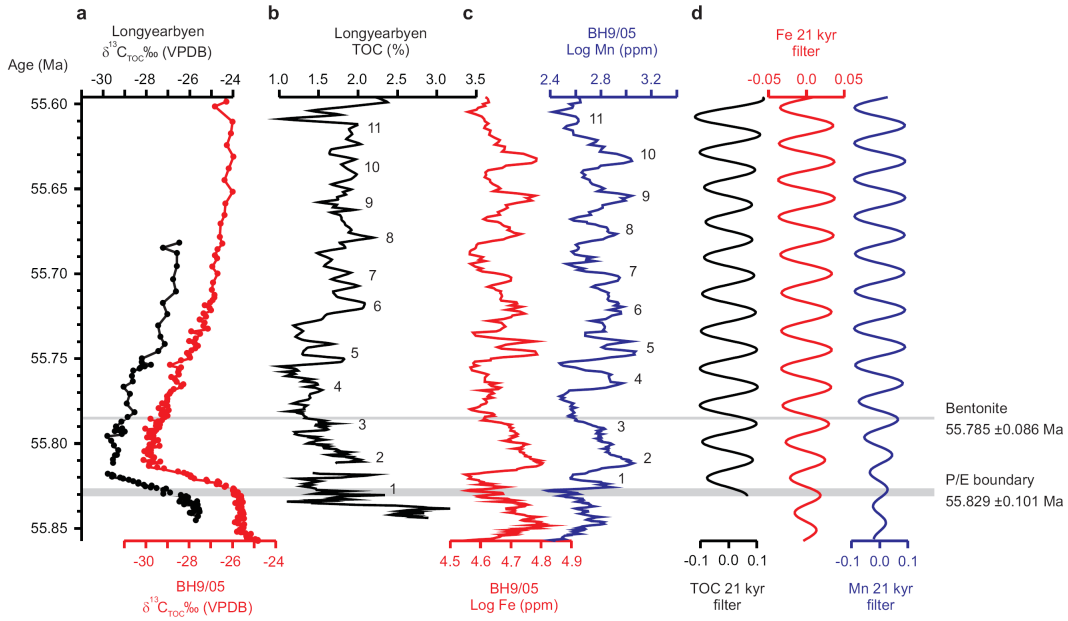

Figure 2.8: The age of the Paleocene/Eocene boundary in Spitsbergen, using cyclostratigraphic Option A. **a)** $\delta^{13}C_{TOC}$ (‰) from the Longyearbyen section (black) (Harding *et al*. 2011) and core BH9/05 (red) (Cui 2010). **b)** Longyearbyen TOC (%) (Harding *et al*. 2011). **c)** Core BH9/05 Log Fe (ppm, red) and Mn (ppm, blue). **d)** 21 kyr Gaussian filter outputs for TOC (black) Log Fe (red) and Log Mn (blue) respectively, illustrating an ~40 kyr duration between the onset of the PETM CIE and the bentonite layer.

2.4 Discussion

2.4.1 Comparison with recent age estimates for the P/E boundary

Owing to the lack of direct radio-isotopic dating of the P/E boundary (other than Jaramillo *et al*. [2010], see below), earlier studies have derived numerical ages indirectly using either astronomical solutions and/or cycle counting from stratigraphic horizons which are themselves constrained by radio-isotopic dating. Three different astronomical age options have recently been proposed for the P/E boundary (Westerhold *et al*. 2007, 2008). These options were derived by extracting the 405 kyr cycle from both Fe and a* records from ODP Site 1262 (Leg 208, Walvis Ridge; Westerhold *et al*. [2007]). Combined with broad radio-isotopic age constraints the correlation of the extracted 405 kyr cycle to astronomical solutions (Varadi *et al*. 2003; Laskar *et al*. 2004) yields three different options each separated by one 405 kyr cycle (option one: ~55.53 Ma; option two: ~55.93 Ma; option three: ~56.33 Ma). Note that three options were proposed due to the uncertainties associated with both astronomical solutions and $^{40}Ar/^{39}Ar$ radio-isotopic dating (Westerhold *et al*. 2007, 2008). The error associated with each option is ±20 kyr (Westerhold *et al*. 2007), derived from the error associated with the extremely stable 405 kyr eccentricity cycle as calculated from astronomical modeling (Laskar *et al*. 2004).

Recent ages for the P/E boundary derived *via* cycle counting from radio-isotopic horizons have utilized $^{40}Ar/^{39}Ar$ (sanidine) dating of the K/Pg boundary (Kuiper *et al*. 2008; Westerhold *et al*. 2008; Hilgen *et al*. 2010), and ash – 17 in the Fur Formation of Denmark (Storey *et al*. 2007; Westerhold *et al*. 2009). As outlined in Section 2.1, the ~1 % uncertainty in the age of the FCs, against which the $^{40}Ar/^{39}Ar$ dates are determined, has precluded a high accuracy (<0.2 %) age estimate for the P/E boundary using this method. Together with the uncertainty for the duration of the Paleocene Epoch from floating cyclostratigraphic timescales (Kuiper *et al*. 2008; Westerhold *et al*. 2008; Hilgen *et al*. 2010) this can therefore account for the difference between our age estimate and those recently derived utilizing $^{40}Ar/^{39}Ar$ dates (e.g. Westerhold *et al*. 2008, 2009).

Recently, Jaramillo *et al*. (2010) obtained a $^{238}U/^{206}Pb$ date of 56.09 ± 0.13 Ma (total uncertainty) on zircons from a felsic pyroclastic tuff from a coastal plain Late Paleocene – Early Eocene section in Venezuela (Riecito Mache section). This pyroclastic tuff is at a level that records a negative CIE that is inferred to represent the PETM, and therefore inferentially constrains the P/E boundary to ~56.3 Ma (Jaramillo *et al*. 2010). This date is ~400-500 kyr older than our age for the P/E boundary. The zircons utilized to derive this date were extracted from a sample described as tuffaceous sandstone

(Jaramillo *et al*. 2010; their Figure S3). It is therefore possible that fluvial reworking of detrital zircons from an eruption ~56.1 Ma could account for the discrepancy between the Spitsbergen and Venezuelan P/E boundary ages. In addition, the identification of the PETM CIE at the Riecito Mache section is complicated by $\delta^{13}C_{TOC}$ records with a high degree of scatter, and therefore an alternative explanation is that the dated tuffaceous sandstone was not deposited within the PETM CIE.

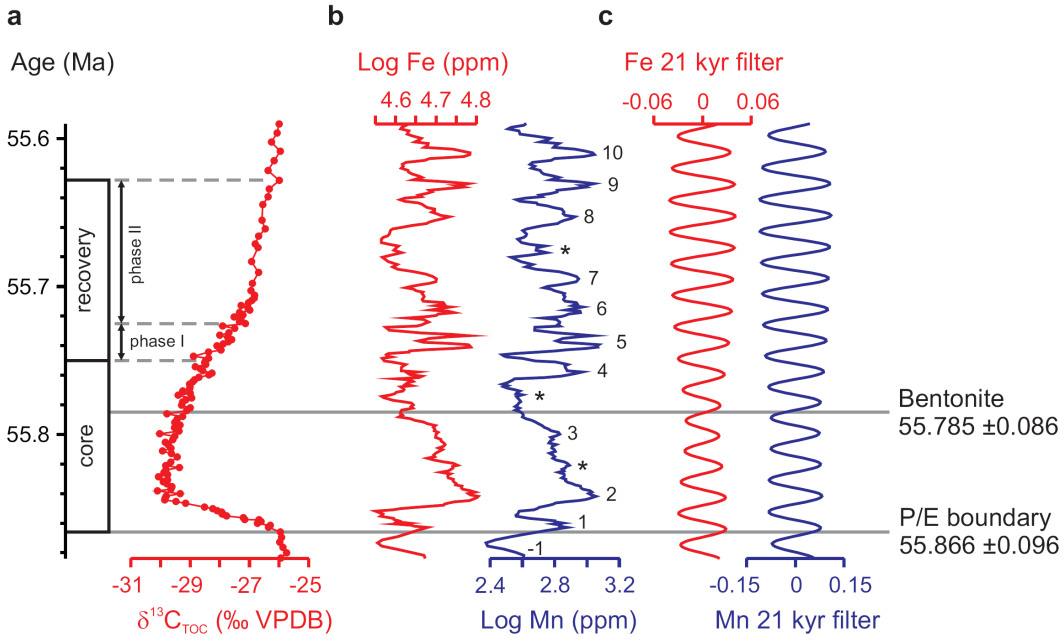

Figure 2.9: The age of the Paleocene/Eocene boundary in Spitsbergen, using cyclostratigraphic Option B. **a)** $\delta^{13}C_{TOC}$ (‰) from core BH9/05 (red; Cui 2010), illustrating the phases of the PETM CIE from Röhl *et al*. (2007). **b)** Core BH9/05 Log Fe (ppm, red) and Mn (ppm, blue). Cycle numbers adhere to those of Röhl *et al*. (2007), with potential additional cycles marked with an asterisk. **c)** 21 kyr Gaussian filter outputs for Log Fe (red) and Log Mn (blue) respectively, illustrating an ~80 kyr duration between the onset of the PETM CIE and the bentonite layer.

The PETM CIE in Spitsbergen is firmly identified by $\delta^{13}C_{TOC}$ records together with the *Apectodinium* acme (Figure 2.2; e.g. Crouch *et al*. [2001]; Sluijs and Brinkhuis [2009]), and dinocyst morphotype *Apectodinium augustum*, which only occurs within the PETM interval (e.g. Luterbacher *et al*. 2004). Given the accuracy of the U-Pb (zircon) system by isotope dilution, the context of the dated sample within the PETM CIE and the proximity of the dated horizon to the P/E boundary, we consider our age range of 55.728-55.964 Ma for the P/E boundary from Spitsbergen to be the most accurate radio-isotopic age estimate. Our age range for the boundary is within error of age

option 2 of Westerhold *et al*. (2007, 2008) for the same horizon. The numerical age for the P/E boundary (equivalent to the PETM onset) must fall within one of the age options proposed by Westerhold *et al*. (2007, 2008) in order to maintain the phase relationship of the 405 kyr eccentricity cycle between astronomical solutions and records of the same cycle extracted from ODP Site 1262 (Röhl *et al*. 2007; Westerhold *et al*. 2007, 2008). Therefore, our age for the P/E boundary substantiates age option 2 of Westerhold *et al*. (2007, 2008) as the correct option, giving a numerical age of ~55.93 Ma for the boundary.

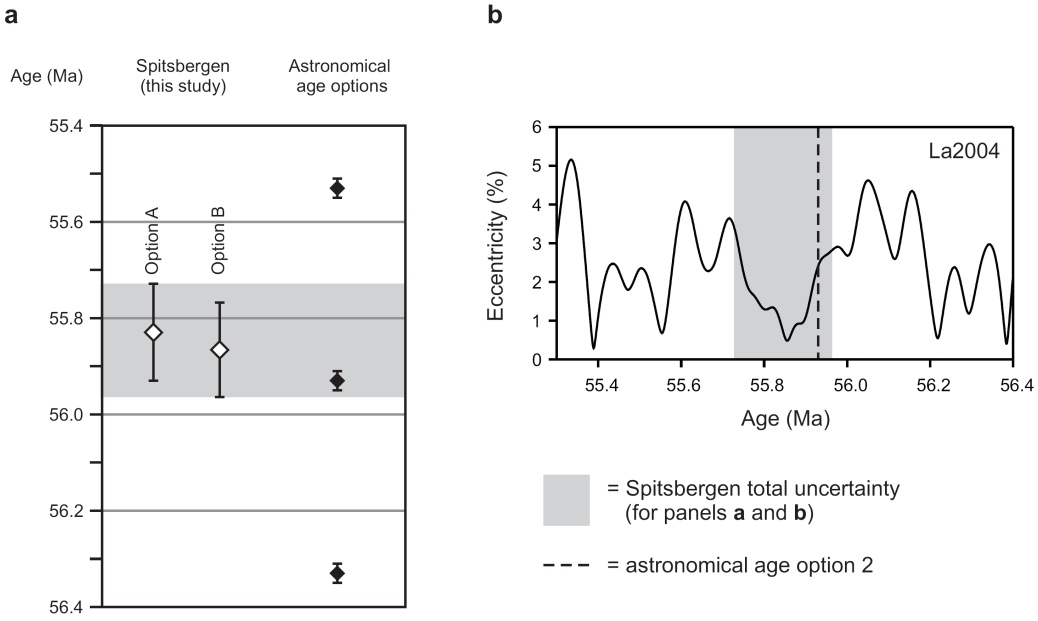

Figure 2.10: The position of the P/E boundary (equivalent to the PETM CIE onset) with respect to orbital forcing. **a)** comparison of P/E boundary ages determined from Spitsbergen with the astronomical age options of Westerhold *et al*. (2007, 2008). Note that both Spitsbergen age options are within error of astronomical age option 2 (55.93 Ma). **b)** total uncertainty for the age of the P/E boundary from Spitsbergen (grey shaded bar), plotted against the Laskar *et al*. (2004; La2004) orbital solution. Age option 2 of Westerhold *et al*. (2007, 2008) is plotted for comparison.

2.4.2 On the age of the K/Pg boundary

Radio-isotopic constraints at the K/Pg boundary (e.g., single crystal $^{40}Ar/^{39}Ar$ sanidine dates from the IrZ-Coal bentonite, Hell Creek Formation, Montana, [Swisher *et al*. 1993]) and immediately overlying the P/E boundary (Spitsbergen, this study) now bracket Paleocene time, constraining its duration. However, at present uncertainty in the numerical age of the monitor standards used in the $^{40}Ar/^{39}Ar$ studies that constrain the K/Pg boundary (see Section 2.1) result in uncertainties on the order of ~600 kyr or greater (Kuiper *et al*. 2008; Channell *et al*. 2010; Renne *et al*. 2010) which precludes the accurate determination of the number of 405 kyr cycles within the Paleocene. Given our high-precision and high-accuracy constraint for the P/E boundary we suggest that the uncertainty of the numerical age of the K/Pg boundary now represents the most substantial source of uncertainty for constraining the duration of the Paleocene. However, an alternative way to derive the age of the K/Pg boundary is to use our P/E boundary age together with the duration of the Paleocene Epoch derived from cyclostratigraphic studies.

Such cyclostratigraphic analyses of early Paleogene successions from ODP Legs 198 (Shatsky Rise, NW Pacific Ocean) and 208 (Walvis Ridge, SE Atlantic Ocean), together with ODP sites 1001 (Nicaragua Basin), 1051 (Blake Nose) and the Zumaia outcrop section (Basque Basin, Spain), led to the development of an age model for the Paleocene where the K/Pg and P/E boundaries were separated by twenty-four 405 kyr eccentricity cycles giving a duration of 9.720 Myr (Westerhold *et al*. 2008). However, recent analysis of the Zumaia outcrop section (Kuiper *et al*. 2008), implies that an additional 405 kyr eccentricity cycle (relative to Westerhold *et al*. [2008]) is present in the Paleocene epoch. A revised analysis of the Fe and magnetic susceptibility records from ODP Site 1263 has also suggested twenty-five 405 kyr eccentricity cycles are present in the Paleocene (Hilgen *et al*. 2010). If we assume that the most recent cyclostratigraphic studies for the duration of the Paleocene are accurate (twenty-five 405 kyr cycles [Kuiper *et al*. 2008; Hilgen *et al*. 2010]), this would indicate a duration of 10.125 Myr for the Paleocene epoch. This duration combined with our age range of 55.728-55.964 Ma for the P/E boundary predicts an age of ~66 Ma for the K/Pg boundary.

2.4.3 Implications for the PETM trigger mechanism

Our new age for the P/E boundary allows us to investigate the relationship between the PETM and potential forcing mechanisms. It has been proposed that insolation maxima during the peak of both short (~100 kyr) and long (405 kyr) eccentricity cycles may have resulted in warmer water conditions, triggering the dissociation of methane hydrates on the seafloor, and thus generating hyperthermal events such as the PETM

(Cramer *et al*. 2003; Lourens *et al*. 2005; Sluijs *et al*. 2007a). However, Westerhold *et al*. (2007) argued that the PETM occurred on the falling limb of a 405 kyr eccentricity cycle, based on records of this cycle extracted from ODP Site 1262. Here, we plot our age range of 55.728-55.964 Ma for the P/E boundary (equivalent to the PETM CIE onset) against the astronomical solution of Laskar *et al*. (2004) to illustrate the relationship between the PETM onset age and 405 kyr eccentricity forcing (Figure 2.10). Orbital models have illustrated that the 405 kyr eccentricity phase is stable over the entire Paleogene interval (Laskar *et al*. 2004), which validates our approach, although the relative cycle-to-cycle amplitude is less certain due to the chaotic nature of the solar system. The total uncertainty for the age of the PETM onset from Spitsbergen illustrates that the PETM was not initiated on the peak of a 405 kyr cycle (Figure 2.10). In addition, it has been argued that the PETM onset age must fall within one of the age options proposed by Westerhold *et al*. (2007, 2008) in order to maintain the phase relationship of the 405 kyr eccentricity cycle between astronomical solutions and records of the same cycle extracted from ODP Site 1262 (Röhl *et al*. 2007; Westerhold *et al*. 2007, 2008). Given our age range is within error of astronomical age option 2 (Figure 2.10), our results are consistent with the hypothesis that the onset of the PETM occurred on the falling limb of a 405 kyr eccentricity cycle (Westerhold *et al*. 2007). Conversely, cyclostratigraphic studies of geological datasets have consistently placed ETM2 (equivalent to the Elmo event of Lourens *et al*. [2005]; or event H1 of Cramer *et al*. [2003]), ETM3 (or the X event of Zachos *et al*. [2004]; event K of Cramer *et al*. [2003]) and other potential hyperthermals (negative CIEs of Cramer *et al*. [2003]) either on the maxima of both 100 and 405 kyr cycles (Lourens *et al*. 2005; Galeotti *et al*. 2010) or with ETM2 at a 100 kyr eccentricity peak on the rising limb of a 405 kyr eccentricity cycle (Westerhold *et al*. 2007; Westerhold and Röhl 2009; Zachos *et al*. 2010), consistent with orbital forcing as a common trigger mechanism. Therefore, the occurrence of the PETM on the falling limb of a 405 kyr eccentricity cycle supports the hypothesis that the event required a different trigger mechanism when compared to other early Eocene hyperthermals (Zachos *et al*. 2010).

It has also been proposed that the PETM may have been triggered by the injection of volcanic sills into organic-rich sediments in the North Atlantic, generating methane and/or carbon dioxide via contact metamorphism, with outgassing through hydrothermal vent systems (Svensen *et al*. 2004, 2010; Storey *et al*. 2007). If correct, it would be expected that the emplacement of these sills occurred immediately prior to the onset of the PETM. Recent estimates for the emplacement of sills on the Vøring Plateau (55.6 ±0.3 and 56.3 ±0.4 Ma; Svensen *et al*. [2010]) and for the eruption of mid-ocean ridge basalt-like flows in the North Atlantic (55.5 ±0.3 Ma; Storey *et al*. [2007]) are within error of our new age for the onset of the PETM. However, given the

low uncertainty on our age for the PETM onset, age estimates with equivalent uncertainties are required for igneous units in the North Atlantic, in order to fully test the hypothesis that volcanism was responsible for the release of the isotopically light carbon which gave rise to the PETM.

2.5 Conclusions

Our combined chemo- and bio-stratigraphic analysis enables the PETM to be recognized at two localities in the Central Basin of Spitsbergen, and demonstrates that two coeval bentonite layers occur within the PETM CIE at both localities. By integrating cyclostratigraphic datasets with radio-isotopic dating ($^{238}U/^{206}Pb$, zircon) of the PETM CIE, we derive similar numerical ages for the P/E boundary based on two different options for the interpretation of the cyclostratigraphic data. This approach yields a total uncertainty for the P/E boundary (equivalent to the PETM CIE onset age) between 55.728-55.964 Ma, which is within error of astronomical age option 2 (Westerhold *et al*. 2007, 2008). Combined with models of the duration of the Paleocene spanning twenty-five 405 kyr cycles (Kuiper *et al*. 2008; Hilgen *et al*. 2010), our new age range for the boundary predicts that the numerical age of the K/Pg boundary is ~66 Ma. Furthermore, the new age for the P/E boundary (PETM CIE onset age) provides additional constraints on the trigger mechanism for the PETM. Comparing our age range for the PETM CIE onset with the Laskar *et al*. (2004) orbital solution indicates that the event was not initiated on a 405 kyr eccentricity peak. Furthermore, our age range is within error of astronomical age option 2 of Westerhold *et al*. (2007, 2008), consistent with the hypothesis that the onset of the PETM occurred on the falling limb of a 405 kyr eccentricity cycle (Westerhold *et al*. 2007). Conversely, other early Eocene hyperthermals have been inferred to occur on eccentricity maxima (or with ETM2 on the rising limb of a 405 kyr cycle) consistent with orbital forcing as a common trigger mechanism. Our results thus suggest that the PETM was triggered by a mechanism different from that proposed for the later Eocene hyperthermals.

Chapter 3: A low salinity Arctic during the Palaeocene/Eocene thermal maximum: new evidence from dinoflagellate cysts

To be submitted

Co-authors: Ian C. Harding, John E.A. Marshall

Author contributions: Adam J. Charles collected and analysed the carbon isotope and dinofagellate cyst data presented, as well as writing the manuscript, under the supervision of Ian C. Harding and John E.A. Marshall. Sedimentary logging and geological mapping of the Bergmanfjellet section was carried out by Adam J. Charles and John E.A. Marshall in 2008.

Abstract

The Palaeocene-Eocene thermal maximum (PETM) ~56 Ma, provides an opportunity to study how the Arctic ecosystem responded to transient global warming. Previously published dinocyst data from Spitsbergen (Longyearbyen section) suggest maximum flooding and salinity changes around the peak of the PETM in the Arctic. Here we compare published results from Longyearbyen with data from two additional successions in Spitsbergen: core BH9/05 near Sveagruva and a new outcrop section at Bergmanfjellet. Changes in dinocyst assemblages from these localities demonstrate that peak abundances of fully marine taxa coincide with maximum dinocyst diversities across the basin, confirming the presence of a maximum flooding surface at the peak of the PETM. Later influxes of the taxon *Senegalinium,* tolerant of low salinity, indicate the presence of a surficial freshwater lens which decreased in influence from northeast to southwest across the Central Basin. This fresh water influx, combined with indicators of lowered oxygen conditions, confirm the establishment of salinity-driven water column stratification. Fluctuations in *Senegalinium* abundance indicate pronounced temporal variability in the intensity of terrestrial runoff and thus the hydrological cycle, and that maximum intensity was reached 40-60 kyr after the onset of the PETM.

3.1 Introduction

The Arctic region exerts a global influence on the modern Earth system, through its effect on planetary albedo and its influence on the salinity (and thus density) of surface waters at the sites of North Atlantic Deep Water formation (e.g. Ramstorf 2002; Peterson *et al*. 2006). However, recent studies of the region have observed elevated surface air temperatures (IPCC AR4 2007), enhanced freshwater runoff from fluvial systems (Peterson *et al*. 2002) and increased precipitation anomalies during intervals of high North Atlantic Oscillation (Peterson *et al*. 2002, 2006), indicating the Arctic is changing in response to modern anthropogenic warming. Despite this, there is a considerable degree of uncertainty associated with climate models which suggest the response of the region to global change. Although the models agree that Arctic surface air temperatures will rise further, estimates of mean temperature rise by the year 2100 range from +2.8ºC to +7.8ºC (mean ensemble value +5 ºC, A1B scenario; IPCC AR4 2007). These estimates are further complicated by the uncertainty associated with the quantity of fossil fuels that will be released by future generations, which alters the mean ensemble temperature increase depending on the quantity of fossil fuels incorporated in the model run (mean 5.2ºC increase in A2 scenario; 3.4ºC B2 scenario; IPCC AR4 2007).

Given the uncertainty inherent in the model results, one way to provide some empirical data demonstrating the response of Arctic climate to transient warming events is to generate climatic records of such events from the geological past. One such event, the Palaeocene-Eocene Thermal Maximum (PETM: Kennett and Stott 1991; Sluijs *et al*. 2007a), has been taken as an ancient analogue for anthropogenic global warming. Marking the Palaeocene/Eocene boundary ~56 Ma (Chapter 2), warming, climatic perturbations and the subsequent recovery of the Earth system occurred within <250 kyr (Röhl *et al*. 2007; Abdul-Aziz *et al*. 2008; Murphy *et al*. 2010). Multi-proxy datasets infer PETM sea surface temperature increases ranging from ~5ºC in the tropics (Zachos *et al*. 2003) up to ~8-9ºC at the mid-latitudes and poles (Kennett and Stott 1991; Sluijs *et al*. 2006; Zachos *et al*. 2006). Stable carbon isotope records ($\delta^{13}C$) through the PETM demonstrate a perturbation of the global carbon cycle coeval with warming, with a sharp (2.5-6 ‰) negative excursion recorded in organic and inorganic carbon in both marine and terrestrial settings (e.g. Kennett and Stott 1991; Koch *et al*. 1992; Bains *et al*. 1999; Handley *et al*. 2008). The pronounced carbon isotope excursion (CIE) is synchronous with a >2 km shoaling of the calcite compensation depth in the Atlantic (Zachos *et al*. 2005), resulting in carbonate dissolution and reduced sedimentation rates in bathyal settings (Farley and Eltgroth 2003; Zachos *et al*. 2005; Röhl *et al*. 2007; McCarren *et al*. 2008). Pacific and Southern Ocean sites are

less affected by carbonate dissolution (e.g. Zachos *et al*. 2003; Zeebe and Zachos 2007), with evidence that surface water carbonate production was unaffected (Gibbs *et al*. 2010; Robinson 2011). Together with the $\delta^{13}C$ excursion, the carbonate dissolution occurring at the PETM implies the injection of isotopically light carbon into the exogenic system, in the form of methane and/or carbon dioxide (Dickens *et al*. 1995; Kurtz *et al*. 2003; Svensen *et al*. 2004; Higgins and Schrag 2006). However the exact mechanism causing carbon release, and the quantities of carbon involved, remain controversial (Sluijs *et al*. 2007a; Panchuk *et al*. 2008; Zeebe *et al*. 2009; Cui *et al*. 2011).

Continental margin successions show an increase in sedimentation rates through the PETM, believed to be caused by enhanced terrestrial runoff and consequently resulting in increased mass accumulation rates of organic carbon (John *et al*. 2008; Sluijs *et al*. 2008a). This, together with increases in weathering intensity (Ravizza *et al*. 2001; Dallanave *et al*. 2010), precipitation (Schmitz and Pujalte 2007), and an enhanced deuterium flux to the high Arctic (Pagani *et al*. 2006), has been used as evidence for an intensification of the hydrological cycle initiated at the onset of the PETM. Marked floral/faunal migrations and increased taxonomic turnover also occur during the PETM (Koch *et al*. 1992; Kelly *et al*. 1996; Clyde and Gingerich 1998; Wing *et al*. 2005; Gibbs *et al*. 2006a), with the extinction of ~30-50 % of benthic foraminiferal species around the onset of the CIE (Kennet and Stott 1991; Thomas 1998; Takeda and Kaiho 2007). Surface water perturbations are also indicated by the extinction of up to 10 % of nannofossil taxa (Bown and Pearson 2009), as well as the global migration of the dinocyst genus *Apectodinium*, which may (at least partially) have been the result of increased sea surface temperatures during the event (Brinkhuis *et al*. 1994; Bujak and Brinkhuis 1998; Crouch *et al*. 2001; Egger *et al*. 2000; 2003; Sluijs and Brinkhuis 2009).

Although the PETM is well documented in low to mid-latitude sites, conditions in the high Arctic are poorly constrained, owing to the lack of modern continental land masses in the region, and the logistical constraints on both Arctic fieldwork and ocean drilling through Arctic sea ice. The pioneering Ocean Drilling Program (ODP) Leg 302 (usually referred to as the Arctic Coring Expedition [ACEX]) was the first to extract extensive Palaeogene core material in the Arctic Ocean (Moran *et al*. 2006). Leg 302 recovered sediments spanning the Palaeocene-Eocene boundary at Site 302-4A, but which regrettably contained core gaps through the PETM interval (e.g. Pagani *et al*. 2006; Sluijs *et al*. 2006). However, even taking such constraints into consideration, studies of the PETM at Site 302-4A have demonstrated Arctic sea surface temperatures that may have reached annual maxima of ~23ºC, and the influx of the PETM dinocyst

marker genus *Apectodinium* (Sluijs *et al*. 2006, 2008a). Development of photic zone euxinia (Sluijs *et al*. 2006; Stein *et al*. 2006; Weller and Stein 2008) and enhanced mass accumulation rates of organic carbon (Sluijs *et al*. 2008a) have also been documented across the PETM interval at Site 302-4A. These changes were probably caused by elevated freshwater runoff, leading to the development of low salinity surface water conditions, stratification and stagnation (Pagani *et al*. 2006; Sluijs *et al*. 2006, 2008a). Furthermore, elevated runoff would have increased siliciclastic sediment supply and the abundance of organic material delivered to the site, promoting organic carbon burial (Sluijs *et al*. 2008a).

More recently, work on the Palaeogene succession of the Spitsbergen Central Basin (Figure 3.1) has revealed that the PETM is recorded in marine mudstones in the Longyearbyen section (Harding *et al*. 2011) and core BH9/05 (Chapter 2; Cui *et al*. 2011). Both these PETM sections contain stratigraphically expanded CIEs (~30 m at Longyearbyen [Harding *et al*. 2011] and ~50 m in core BH9/05 [Cui *et al*. 2011]), which are thicker than the excursions in the majority of continental margin sections so far documented (e.g. Bolle *et al*. 2000; Sluijs *et al*. 2006; Guisberti *et al*. 2007; Handley *et al*. 2008), and an order of magnitude thicker than most deep water sites (e.g. Zachos *et al*. 2003; Röhl *et al*. 2007). Results from Longyearbyen indicate low salinity surface water conditions during the PETM similar to Site 302-4A (Harding *et al*. 2011). In addition, low bottom water oxygenation was typical during the PETM in Longyearbyen, although the presence of organic foraminiferal test linings may indicate short (perhaps seasonal) intervals of oxygenation (Harding *et al*. 2011). This contrasts with Site 302-4A, where euxinic conditions developed in the photic zone through the PETM (Sluijs *et al*. 2006; Stein *et al*. 2006). The magnitude of the CIE also differs between the Spitsbergen sections and Site 302-4A, (6 ‰ at Site 302-4A - Sluijs *et al*. 2006, 2008a; 4 ‰ in Spitsbergen – Cui *et al*. 2011; Harding *et al*. 2011), as does the abundance of angiosperm pollen (abundant at Site 302-4A but rare in the Longyearbyen section). Both the CIE and angiosperm pollen records may record predominantly local signals due to the proximal palaeoenvironmental settings of both Site 302-4A and the Longyearbyen section (Sluijs *et al*. 2008a; Harding *et al*. 2011). Significant differences between these localities therefore make it difficult to assess which (if either) was representative of the Arctic region during the PETM.

Dinoflagellate cyst (dinocyst) assemblage data in Longyearbyen indicate pronounced temporal changes in dinocyst assemblages, indicative of oceanographic changes within the 'core' of the PETM CIE (Harding *et al*. 2011). However, owing to the coring gaps around the peak of the CIE at Site 302-4A, the striking temporal changes observed in Longyearbyen cannot currently be assessed on a regional Arctic basis. Thus to provide

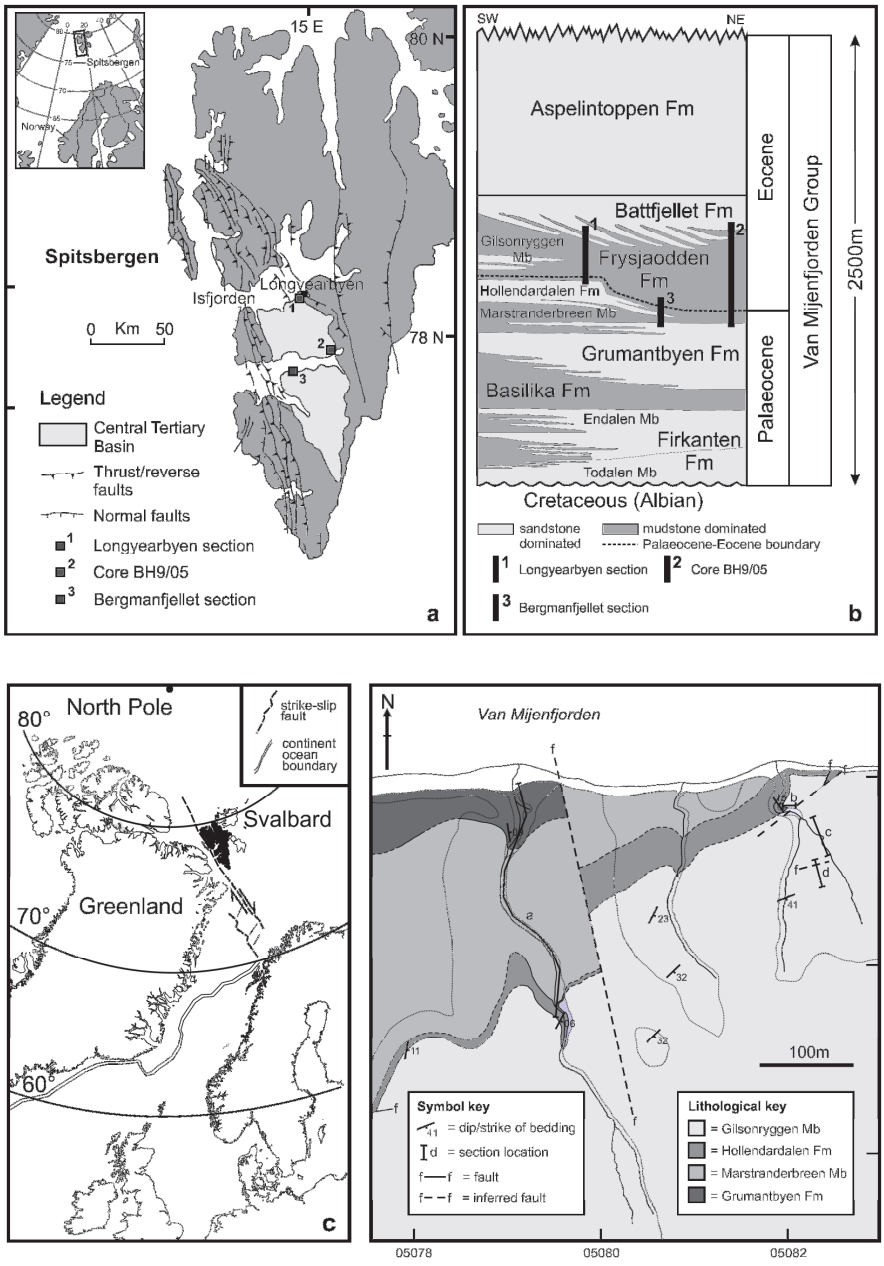

Figure 3.1: The study sections. **a)** Location map illustrating the position of the Central Basin, and the three study localities (after Uroza and Steel 2008; Blythe and Kleinspehn 1998). **b)** The Palaeogene stratigraphy of Spitsbergen, illustrating the stratigraphy spanned by the study localities (after Uroza and Steel 2008; Steel *et al*. 1985). **c)** Palaeogeographic reconstruction of the northern North Atlantic region during the early Eocene, illustrating the position of Spitsbergen in black (after Mosar *et al*. 2002). **d)** Geological map of the area around Bergmanfjellet, illustrating the position of sections (a to d) used to construct the composite Bergmanfjellet section. Note the Hollendardalen Formation was not previously recorded on published geological maps of this area

a wider geographical overview of Arctic palaeoceanography (i.e. across the Spitsbergen Central Basin) we compare published results from Longyearbyen with data from two additional successions, including a new PETM outcrop section from the southern coast of Van Mijenfjorden at Bergmanfjellet. We assess dinocyst assemblage changes across all three localities in order disentangle local and basin-scale biotic events, to assess temporal changes in oceanographic conditions across the PETM in a high Arctic setting.

3.1.1 Dinoflagellate cysts as proxies for sea surface conditions

Dinoflagellates are protists which have a unique nucleus (the dinokaryon; e.g. Fensome *et al*. 1999) and/or possess two dissimilar flagella (Evitt 1985; Fensome *et al*. 1999), enabling movement through the water column for some members of the group (Levandowsky and Kaneta 1987). The majority of dinoflagellates live in near-surface waters in aquatic settings (freshwater-oceanic; e.g. Dale 1996; Marret and Zonneveld 2003). Today, ~10-15 % of species produce resting cysts (dinocysts) which are geologically preservable as part of a two-stage life cycle (Evitt 1985). Owing to the dinoflagellates' habitat within surface waters, the cysts they produce are known to be sensitive indicators of surface water conditions in both modern and ancient sediments (Wall *et al*. 1977; Brinkhuis 1994; Dale 1996; Marret and Zonneveld 2003; Sluijs *et al*. 2005). However, certain types of dinocysts (peridinioids) are preferentially susceptible to syn/post depositional oxidation (e.g. Zonneveld *et al*. 2001, 2008), therefore redox conditions need to be assessed before making palaeoceanographic interpretations. In modern and Quaternary sediments, four main ecological signals can be determined by examining the composition of dinocyst assemblages: distance from the shore, using a parameter known as the neritic/oceanic signal; nutrient availability, or the productivity signal; salinity and lastly sea surface temperature (e.g. Wall and Dale 1973; Wall *et al*. 1977; Lewis *et al*. 1990; Dale 1996; deVernal *et al*. 1997; Devillers and de Vernal 2000; Kouli *et al*. 2001; Mudie *et al*. 2001; Marret and Zonneveld 2003; Zonneveld *et al*. 2009). Although most dinocyst genera studied in the Palaeogene are extinct, multiple studies of fossil cyst assemblages have also illustrated the same variations in palaeoecological conditions resulted in marked assemblage changes, as corroborated by proxy records (see review in Sluijs *et al*. 2005).

For example, Sluijs *et al*. (2008b) used the ratio of more offshore taxon *Spiniferites* to the inner neritic taxon *Areoligera* (*Spiniferites* – *Areoligera* ratio), together with a drop in the >63 μm sediment fraction to infer a relative sea level rise occurred during the PETM on the New Jersey shelf. These changes were followed by successive acmes of the low-salinity tolerant taxon *Senegalinium*, implying elevated terrestrial runoff and nutrient concentrations on the New Jersey margin during the PETM (Sluijs and Brinkhuis

2009). Other examples of salinity changes include the Oligocene Rhine Graben in Germany, where alterations between assemblages dominated by *Homotryblium tenuispinosum* and *Thalassiphora pelagica* were interpreted as fluctuations between a humid and dry climate state (Pross and Schmiedl 2002). Major climatic perturbations in the Palaeogene also resulted in marked dinocyst assemblage changes, such as the southern migration of the cold water taxon *Svalbardella* during the Oi-2b glaciation event in the Oligocene (Van Simaeys *et al*. 2005), and the *Apectodinium* acme during the PETM (e.g. Bujak and Brinkhuis 1998; Crouch *et al*. 2001). Finally, the ratio between abundances of peridinioid (P) and gonyaulacoid (G) dinocysts (known as the P/G ratio, modified from the original concept of Harland [1973]), is typically used to infer changes in Palaeogene productivity (e.g. Sluijs *et al*. 2005; Bijl *et al*. 2010). This is based on the assumption that the majority of peridinioid (P) cysts in the Palaeogene would have been heterotrophic taxa which thrive in nutrient-rich settings, compared to the autotrophic gonyaulacoid (G) cysts (Sluijs *et al*. 2005). Elevated abundances of peridinioids during the PETM in New Zealand have thus been used to infer higher productivity during the event (Crouch and Brinkhuis 2005). The discussion above therefore indicates that dinocysts are powerful tools for reconstructing sea surface conditions during the PETM and other intervals of the Palaeogene, and are therefore applicable for such reconstructions within the Spitsbergen succession.

3.2 Material and Methods

3.2.1 Geological setting

The three study localities all lie within the Palaeogene Central Basin of Spitsbergen, the largest island of the Svalbard archipelago (Figure 3.1). The palaeolatitude of Svalbard has changed little since the Palaeogene, when it was located ~75°N (Harland 1997), and the initiation of sea-floor spreading in the present day northern North Atlantic resulted in a dextral strike-slip movement between Svalbard and Greenland (Müller and Spielhagen 1990; Harland 1997). This resulted in the development of a transpressive tectonic regime by the latest Palaeocene (Müller and Spielhagen 1990; Bruhn and Steel 2003), eventually leading to the separation of Svalbard from Greenland to its present day position (Müller and Spielhagen 1990). Transpression resulted in uplift of the West Spitsbergen orogenic belt from the Palaeocene to the Eocene-Oligocene boundary (Harland 1997; Blythe and Kleinsphene 1998), leading to the deposition of a stratigraphically expanded Palaeogene succession within a foreland basin (~2500 m; Helland-Hansen [1990]). Owing to orogenic loading, higher subsidence on the western margin of the basin together with a high sediment supply resulted in a marked westward thickening of the Eocene stratigraphy (Kellogg 1975; Helland-Hansen 1990). For example, using the stratigraphic nomenclature of Dallman *et al*. (1999: which we

employ here), the thickness of the Gilsonryggen Member (in which the PETM resides), increases from 300 to 600 m from east to west (Helland-Hansen 1990).

The palaeogeography of the Central Basin in the Eocene is constrained by the growing orogenic belt to the west (Helland-Hansen 1990; Müller and Spielhagen 1990; Harland 1997), and by the distribution of Permian strata to the northeast (phosphatic clasts from these strata were eroded and rafted into the basin during deposition of the Frysjaodden Formation: Bikenmajer *et al*. [1972]; Dalland [1977]). There is consensus that at this time the southern margin of the Central Basin was open, with a marine connection to the opening North Atlantic (Livšic 1974; Müller and Spielhagen 1990; Harland 1997). However, the position of the eastern margin of the basin is poorly constrained. Livšic (1974) suggested a restricted basin predominantly closed to the east based on bivalve assemblages, which are comprised entirely of euryhaline taxa. Conversely, Helland-Hansen (1990) argued that the predominance of wave- and storm-generated sedimentary structures coupled with the sedimentary architecture suggested a basin open to both the south and the east.

Here we document results from three mudstone-dominated sections from across the Central Basin: the Longyearbyen section, core BH9/05, and a new outcrop section at Bergmanfjellet (Figure 3.1). Detailed lithological, geochemical and dinocyst assemblage data from the Longyearbyen section have previously shown that the PETM is present within the Gilsonryggen Member of the Frysjaodden Formation, represented by a -4 ‰ $\delta^{13}C_{TOC}$ excursion coeval with the appearance of PETM-diagnostic dinoflagellate cyst *Apectodinium augustum* (Harding *et al*. 2011). Terrestrial deposition immediately preceded the PETM at Longyearbyen (Harding *et al*. 2011), but coeval marine sediments occur in both core BH9/05 and the Bergmanfjellet locality, indicating that the Longyearbyen section is the most proximal of the localities studied here. The presence of *A. augustum* coincident with a -4 ‰ $\delta^{13}C_{TOC}$ excursion also identifies the PETM in core BH9/05 (Chapter 2); carbon isotope stratigraphy and a detailed lithological description for the core have been provided by Cui *et al*. (2011) and Riber (2009) respectively. In contrast to the Longyearbyen section and core BH9/05, the Bergmanfjellet outcrop section on the southern margin of Van Mijenfjorden is located close to the western margin of the preserved Central Basin deposits, adjacent to the West Spitsbergen orogenic belt. Owing to the growth of the orogenic belt in the Palaeogene, and the thickening of stratigraphy to the west, it has been inferred that deposition on the western margin of the basin occurred within a foredeep setting with high subsidence (Helland-Hansen 1990). However, our geological mapping of the area has illustrated that the Palaeogene stratigraphy at Bergmanfjellet is divided up into faulted blocks (Figure 3.1d). Therefore we

constructed a composite section from the Grumantbyen Formation to the Gilsonryggen Member of the Frysjaodden Formation (Figure 3.2).

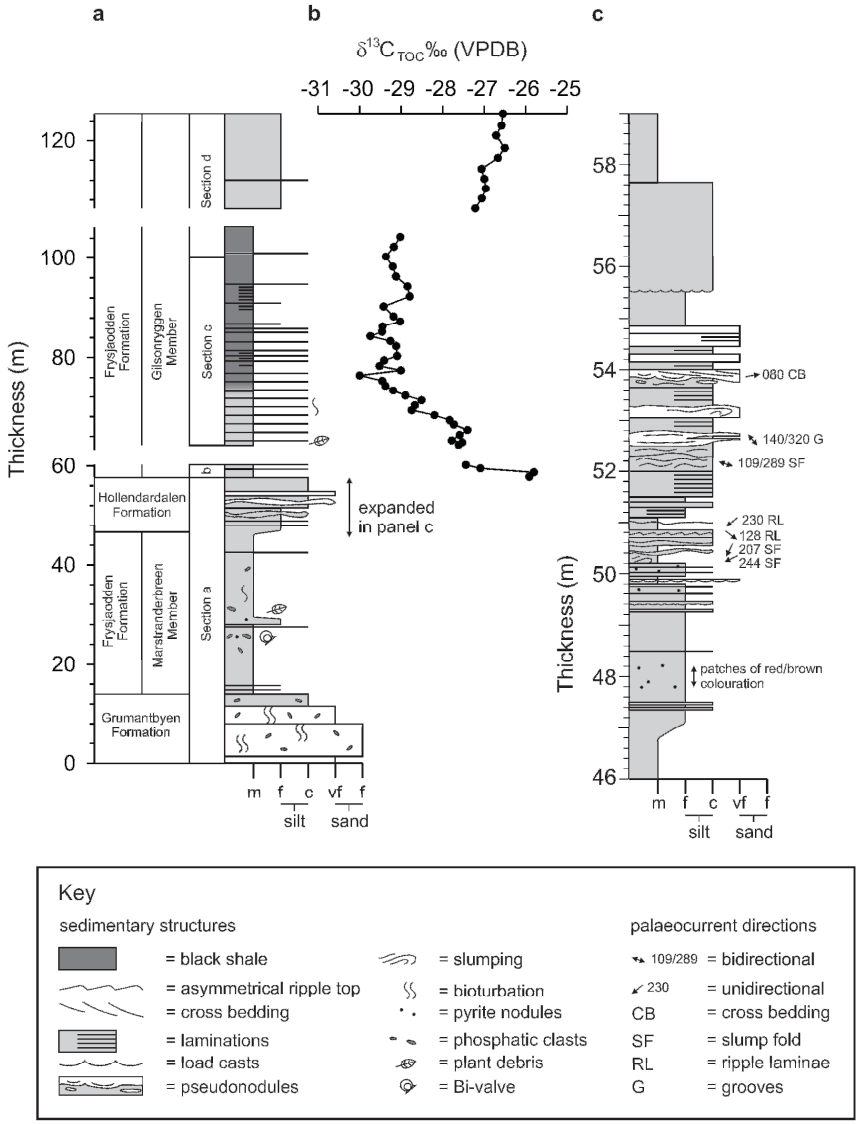

Figure 3.2: The Bergmanfjellet section. **a)** Composite sedimentary log. Positions of sections (a to d) are illustrated in Figure 3.1. **b)** Bulk organic carbon isotope record ($\delta^{13}C_{TOC}$ ‰ VPDB). **c)** Expanded view of the Hollendardalen Formation, illustrating palaeocurrent directions.

3.2.2 Organic carbon isotopes

In order to locate the PETM in the Bergmanfjellet section, 49 samples were analysed to construct a bulk organic carbon isotope record ($\delta^{13}C_{TOC}$) through the Gilsonryggen Member of the Frysjaodden Formation. Samples were crushed to a fine powder using an agate pestle and mortar before the removal of inorganic carbon *via* addition of Analar HCl (37 %). Samples were left overnight before dilution with Milli-Q water, and subsequently left to settle before being decanted and subjected to further dilution. Once neutralized, samples were oven dried at ~60ºC, before further crushing. Around three milligrams of sample was used to measure total organic carbon percentages (TOC %) using a Carlo Erba EA1108 elemental analyzer. Decarbonated TOC % data (not shown) was used to calculate the weight of sample required for isotopic analysis so each sample had a roughly constant carbon content (~30 μg C). Samples were run on a Euro EA elemental analyzer linked to an Iso Prime mass spectrometer, using an EMA soil low organic carbon standard for calibration (TOC: 1.65 %; $\delta^{13}C$: -27.46 ‰). Analytical precision based on standard reproducibility was 0.15 ‰.

3.2.3 Palynological processing

Standard palynological processing techniques as outlined in Wood *et al*. (1996) were used. Some 5-10 g of sample was crushed to millimetre sized chips, before being bathed overnight in hydrochloric acid (32%) to dissolve carbonates. Samples were subsequently diluted with water, left to settle and then decanted, repeated multiple times until neutralised. The silicate fraction was dissolved by subjecting the samples to HF (60 %) over 48 hours before dilution and neutralisation as above. A known quantity of exotic *Lycopodium* spores were added to the samples during the second HF dilution, in order to calculate the absolute abundance of dinocysts (Benninghoff 1962; Stockmarr 1971). Samples were passed through a 10 μm nylon sieve in order to remove the solute, with inert organic components remaining in the sieve. Samples were then boiled in HCl (32 %) in order to dissolve neo-formed fluorides from the HF stage, rapidly diluted with ~250 ml of water, and sieved again. Samples with high abundances of pyrite framboids and amorphous organic matter (AOM) were subjected to flash oxidation (5 minutes in 70% nitric acid) in order to dissolve/break up these components, before rapid dilution with ~250 ml of water and subsequent sieving. Where possible, 300 dinocysts were counted per slide, with the abundance of the out-of-count *Lycopodium* spike used to calculate the absolute abundance of cysts. Dinoflagellate cyst nomenclature follows that of Fensome and Williams (2004; see Appendix 6 for representative images of key taxa). In order to assess generic diversity, the Shannon-Weaver Index or H(G) of Shannon (1948) was used, calculated using the statistics package Primer, version 6.1.6. The slides utilized to generate the above data are deposited in the collection of the University of Southamton, UK.

3.3 Results

3.3.1 Bergmanfjellet carbon isotope record

A 4.2 ‰ negative carbon isotope excursion is observed in the bulk organic carbon ($\delta^{13}C_{TOC}$) record from the Bergmanfjellet section (Figure 3.2, Appendix 3), coincident with an acme of the dinocyst genus *Apectodinium*, including PETM-diagnostic species *A. augustum*. The onset of the $\delta^{13}C_{TOC}$ excursion occurs immediately above the base of the Gilsonryggen Member of the Frysjaodden Formation, the same point in the stratigraphy as the previously documented PETM section in Longyearbyen (Harding *et al*. 2011). The -4.2 ‰ magnitude of the CIE in Bergmanfjellet is similar to that from the PETM intervals in both the Longyearbyen section (Harding *et al*. 2011) and core BH9/05 (Cui *et al*. 2011). These constraints therefore confirm the presence of the PETM in the Bergmanfjellet section. Unfortunately however, structural disturbance has led to stratigraphic gaps within the PETM interval at this locality. A minor fault was observed during sedimentary logging of the section, occurring immediately above the onset of the $\delta^{13}C_{TOC}$ excursion and the first appearance datum of *A. augustum*. The absence of bentonite layers in the Bergmanfjellet section (observed in the PETM CIE in both the other Spitsbergen localities: Figure 3.3) together with abrupt changes in lithology, dinocyst assemblages and a ~2 ‰ jump in $\delta^{13}C_{TOC}$ values, also indicates the presence of a second fault in the upper part of the section (Figure 3.3). The absence of an exponential return of isotopic values to more positive values suggests recovery phase I of the PETM CIE has been removed by the upper fault at this site.

3.3.2 Dinocyst assemblages

This section describes the dinocyst assemblage record through both core BH9/05 and the Bergmanfjellet section, and defines acme events which are present in both absolute and relative abundance data (Figures 3.4-3.5 and Appendix 3) unless otherwise stated.

3.3.2.1 Core BH9/05

Fluctuations in the abundance of dinocyst genera in core BH9/05 are displayed in Figure 3.4. Total dinocyst abundance is low between 550-531 m (typically <2500 cysts g^{-1}) and from 510-481 m (typically <3300 cysts g^{-1}; Figures 3.3 and 3.4). Although assemblages in these intervals are dominated by *Spiniferites* spp. and other taxa present in very low numbers, the low recovery meant that less than 300 dinocysts were counted per sample. Therefore the assemblages from these intervals are not considered statistically significant, and environmental interpretations cannot be drawn. The PETM CIE is the only interval in >400 m of the Frysjaodden Formation in core BH9/05 where >300 dinocysts per sample were consistently observed (between 530 m to 511 m). Therefore discussion of dinocyst assemblages will focus on this interval.

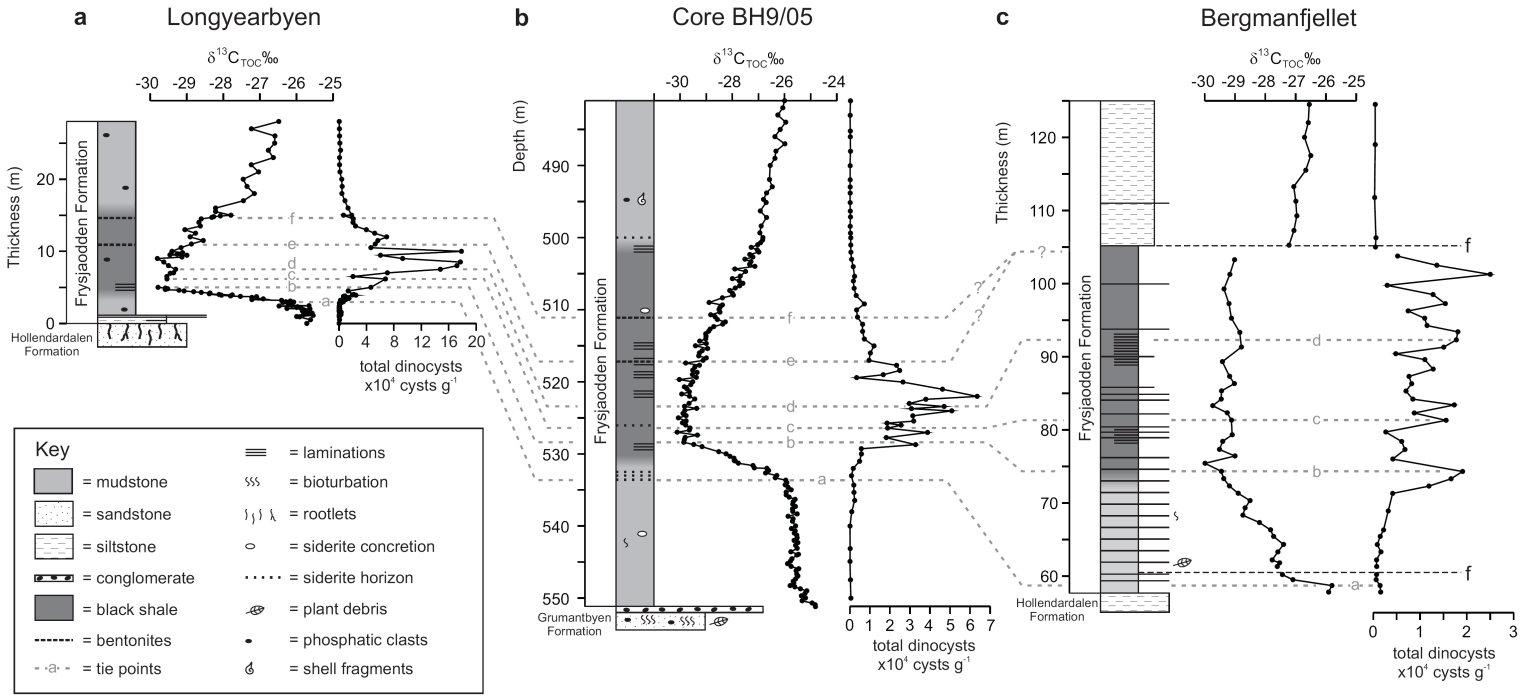

Figure 3.3: Comparison of Spitsbergen PETM sections in the depth domain. Sedimentary logs, $\delta^{13}C_{TOC}$ (‰ VPDB) and total dinocyst abundances are plotted against the same depth scale for **a)** the Longyearbyen section [Harding *et al*. 2011] **b)** core BH9/05 and [Cui *et al*. 2011; Dypvik *et al*. 2011] **c)** the Bergmanfjellet section [this study]. Tie points used to transfer the BH9/05 age model to the other two sections are illustrated as dashed lines (a to e; see text for discussion). Dashed lines marked with the letter 'f' in panel c represent faults in the Bergmanfjellet section. Note that the Hollendardalen Formation is not present in core BH9/05 due to southeastern thinning and pinch out of this formation (Dallman *et al*. 1999).

Total dinocyst abundances between 530 to 529 m reach ~6000 cysts g^{-1}, before increasing to ~63,000 cysts g^{-1} from 529-522 m (Figures 3.3 and 3.4). Concomitant increases in the abundances of *Apectodinium* spp., *Lentinia/Spinidinium* spp. and *Senegalinium* spp. account for the initial increase (from 528.73 to 524.73 m), with *Apectodinium* (~12,000 cyst g^{-1}; 26-49 % of the assemblage) slightly more abundant than *Lentinia/Spinidinium* (~8,000 cysts g^{-1}; 10-28 %) and *Senegalinium* (~8,000 cysts g^{-1}; 9-33 %; Figure 3.4). The acme in *Lentinia/Spinidinium* in this interval of the CIE in BH9/05 is not present in either the Longyearbyen (Harding *et al*. 2011) or Bergmanfjellet sections, and therefore represents a local acme. Peak abundances of the gonyaulacoid cysts *Hystrichokolpoma* spp., *Muratodinium* spp. and *Glaphyrocysta/Areoligera* spp. also occur during this interval, with maximum abundance of all these genera at ~526 m (tie point c; Figure 3.4), immediately above the peak CIE.

These gonyaulacoid cysts start to decline above 525 m and a pronounced acme in the hexa-peridinioid *Cerodinium/Deflandrea* spp. is observed at 523.43 m (~4000 cysts g^{-1}; 12 % of the assemblage). However, the increase in total dinocyst abundance across the 525-522 m interval is predominantly the result of an influx of the dinocyst *Senegalinium* spp., which accounts for around 70 % of dinocysts observed at its maximum abundance (~46,000 cysts g^{-1}; Figure 3.4). From 522-520 m the decline in *Senegalinium* spp. abundance drives the sharp decrease in total dinocyst abundance. A more gradual decline in total dinocyst abundance is observed from 520-511 m, marked by lower abundances of *Apectodinium* spp. and *Senegalinium* spp., although the abundance of *Spiniferites* spp. remains constant.

3.3.2.2 Bergmanfjellet

Dinocyst assemblage data for the Bergmanfjellet section are displayed in Figure 3.5 and Appendix 3. In a similar manner to both the Longyearbyen section (Harding *et al*. 2011) and core BH9/05, dinocyst abundances are low outside the PETM CIE (<1,600 cysts g^{-1}; Figure 3.5), with <300 dinocysts counted per sample. Again, the only interval with abundant dinocysts (>300 per count) lies within the main body of the PETM CIE (68.90 m to 103.75 m; Figures 3.3 and 3.5). Total dinocyst abundance increases from ~3,000 cysts g^{-1} at 68.90 m to ~19,000 cysts g^{-1} at 74.30 m. This increase is driven by elevated abundances of both *Apectodinium* spp. (~8,000 cysts g^{-1}; 22-48 %) and *Glaphyrocysta/Areoligera* spp. (~8,000 cysts g^{-1}; 14-46 %), which dominate assemblages in this interval (Figure 3.5). The absolute abundance of *Senegalinium* spp. also increases around 72 m (~3,000 cysts g^{-1}, although such an increase is not evident in the relative abundances), and thereafter fluctuates between 300-2000 cysts g^{-1} (2-25 %) from 76.00-90.40 m. However, *Senegalinium* spp. remains subordinate to

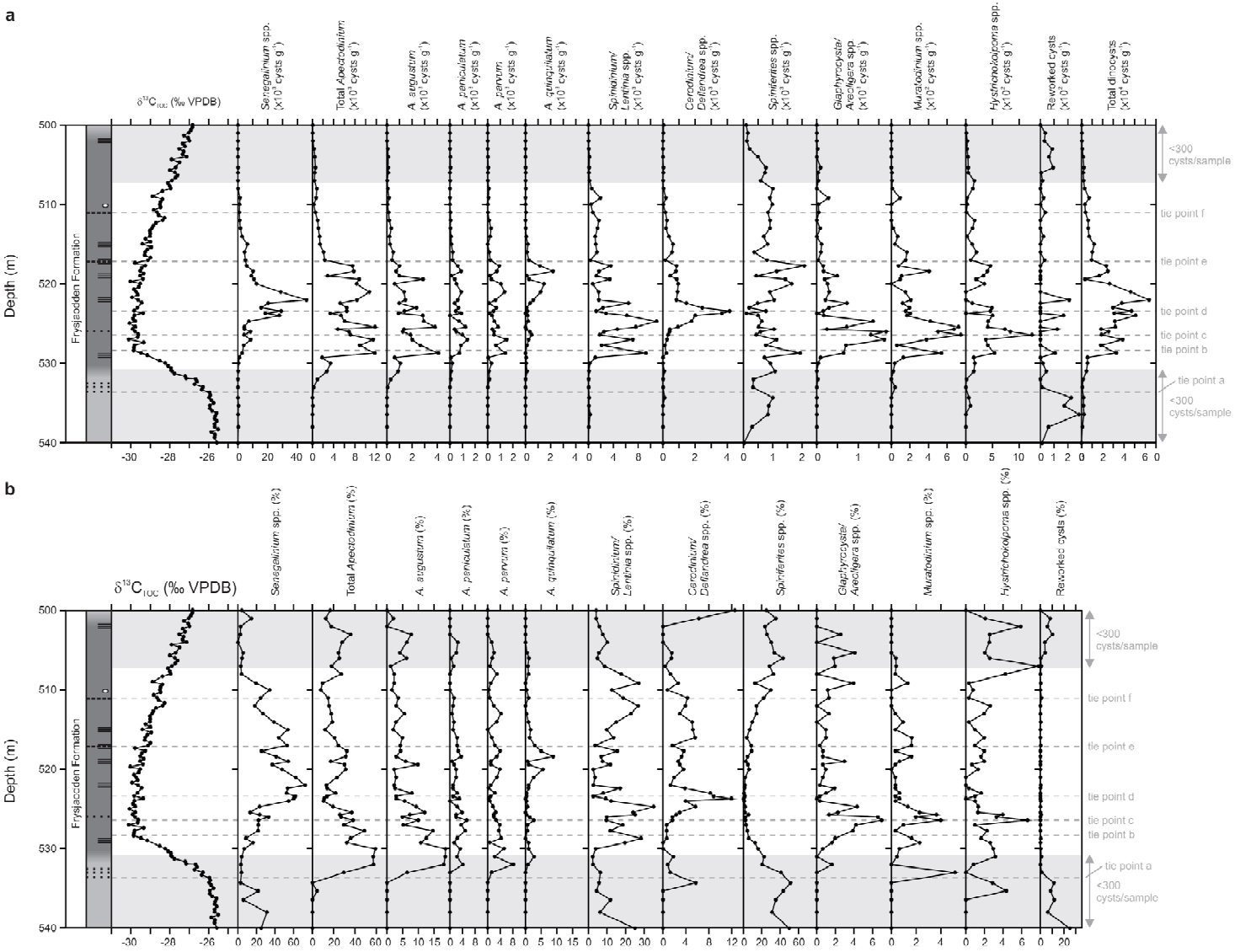
a
b
Depth (m)
Frysjaodden Formation
δ13CIOC (‰ VPDB)
Senegalinium spp. (x10³ cysts g⁻¹)
Total Apectodinium (x10³ cysts g⁻¹)
A. augustum (x10³ cysts g⁻¹)
A. paniculatum (x10³ cysts g⁻¹)
A. parvum (x10³ cysts g⁻¹)
A. quinquilatum (x10³ cysts g⁻¹)
Spiniferites spp. (x10³ cysts g⁻¹)
Glaphyrocysta/ Areoligera spp. (x10³ cysts g⁻¹)
Muratodinium spp. (x10³ cysts g⁻¹)
Hystrichokolpoma spp. (x10³ cysts g⁻¹)
Reworked cysts (x10³ cysts g⁻¹)
Total dinocysts (x10³ cysts g⁻¹)
Senegalinium spp. (%)
Total Apectodinium (%)
A. augustum (%)
A. paniculatum (%)
A. parvum (%)
A. quinquilatum (%)
Spiniferites spp. (%)
Glaphyrocysta/ Areoligera spp. (%)
Muratodinium spp. (%)
Hystrichokolpoma spp. (%)
Reworked cysts (%)
<300 cysts/sample
tie point f
tie point e
tie point d
tie point c
tie point b
tie point a

Apectodinium spp. from 76.00-90.40 m, with the latter genus dominating assemblages in this interval (~4,000 cysts g^{-1}; 32-75 %). Similar to core BH9/05, a pronounced acme in *Muratodinium* spp. (~1,000 cysts g^{-1}; 7 %) occurs immediately after the peak CIE at 81.30 m, within the interval dominated by *Apectodinium* spp. (Figure 3.5).

Elevated abundances of *Senegalinium* spp. are observed from 91.30-103.75 m (~6,000 cysts g^{-1}; 23-43 %), with abundances of *Apectodinium* spp. remaining relatively constant (~4,000 cysts g^{-1}; 21-55 % [relative abundances decrease slightly due to the closed sum problem]). A marked acme in the hexa-peridinioids *Cerodinium/Deflandrea* is observed at around 92 m (~2,000 cysts g^{-1}: 12 %), coeval with the increase in *Senegalinium* abundance. In contrast to the Longyearbyen section and core BH9/05, near-monotypic assemblages of *Senegalinium* immediately after the *Cerodinium/Deflandrea* acme are not observed in Bergmanfjellet. Above the fault at 103.75 m there is a return to low dinocyst abundances with assemblages dominated by *Spiniferites* spp. (Figure 3.5).

3.3.3 Redox conditions

Dinocyst assemblages are known to be affected by redox conditions, with oxic syn- or post-depositional conditions leading to the preferential removal of certain types of cysts (peridinioids), biasing the assemblage and therefore potentially the environmental interpretations drawn from it (e.g. Zonneveld *et al*. 2001, 2008). Conversely, anoxic conditions will preserve the original species composition of dinocyst assemblages (Zonneveld *et al*. 2001, 2008). Therefore, in order to be able to detect environmental signals recorded in the Svalbard dinocyst assemblages, it is first necessary to assess redox conditions within the Palaeogene Central Basin. Here we assess temporal redox changes in core BH9/05 by comparing the Th/U ratio from Dypvik *et al*. (2011), with the abundance of labile Amorphous Organic Matter (AOM; Figure 3.6). From 551-529 m depth, the Th/U ratios are >3, AOM concentrations are low, and laminations are rare within the sediment (Figure 3.6). Together with the presence of a relatively high diversity agglutinated foraminiferal assemblage (Nagy *pers comm*. 2010), this suggests that bottom and pore waters were oxic within this interval. From 529-516 m depth, an elevated abundance of pyrite framboids is

Figure 3.4: Absolute **a)** and relative **b)** abundances of dinocysts from core BH9/05, plotted against depth. Grey dashed lines indicate the position of age model tie points discussed in the text. Shaded areas indicate samples where <300 dinocysts per sample were observed, making dinocyst data more imprecise. Note that this diagram shows an expanded view of the PETM in order to illustrate the dinocyst acmes, the PETM recovery interval (500-487 m) is not shown.

observed in palynological preparations, with increased concentrations also derived from XRD analyses (Riber 2009; Dypvik *et al*. 2011). This together with lower Th/U ratios (<3; Dypvik *et al*. 2011), high concentrations of AOM and laminated sediments implies that conditions within the sediment were anoxic during this interval. Furthermore, a decline in the agglutinated foraminiferal diversity suggests that bottom water oxygenation may have declined (Nagy *pers comm*. 2010). Above 516 m, decreasing abundances of pyrite and AOM, together with a gradual increase in Th/U ratios and foraminiferal diversity implies a gradual transition back to oxic bottom waters. Similar features are observed at both Longyearbyen and Bergmanfjellet. Harding *et al*. (2011) observed elevated pyrite and AOM concentrations within the PETM CIE at the Longyearbyen outcrop section. At Bergmanfjellet, elevated abundances of pyrite and AOM are also observed in palynological residues within the 'core' of the PETM CIE, together with pronounced laminations. Taken together, these independent lines of evidence from all three sections suggest a decline in oxygen levels within the PETM CIE, implying low bottom water oxygenation across the basin and anoxic conditions within the sediment. Therefore, by determining low bottom water oxygen levels it is possible to deduce that the dinocyst assemblages in the 'core' of the CIE are not biased by oxidation, and these assemblages can be used to assess palaeoceanographic conditions in this interval. Conversely, the low abundance of labile peridinioids outside the core of the PETM CIE (Figure 3.6), is consistent with the preferential oxidation of these taxa, resulting in the low diversity and abundance of dinocysts observed, dominated by the more refractory taxon *Spiniferites* (Figures 3.4 and 3.5).

3.3.4 Age model

Cyclostratigraphic age models have previously been constructed for the Longyearbyen section (Harding *et al*. 2011) and core BH9/05 (Chapter 2). However, in order to prevent artefacts between the different age models biasing interpretations and accurately assess dinocyst assemblage changes in a temporal context, it is necessary to compare each section against the same age model (i.e. Independent tuning of both Spitsbergen localities to the Log Fe record of Site 1263 illustrates a ~5 kyr age model offset between sites: Chapter 2). Here, we use litho-, chemo- and biostratigraphic tie points to export age model Option B from core BH9/05 (Chapter 2), to both the Longyearbyen and Bergmanfjellet sections (Figure 3.3). Core BH9/05 was used because the age model is based upon cyclostratigraphic data with a higher temporal resolution than the age model of the Longyearbyen section. Option B of this age model was constructed by assigning a 21 kyr duration to each precession cycle identified in the depth domain, and is consistent with the Murphy *et al*. (2010) ^{3}He age model from ODP Site 1266 (Chapter 2).

The tie points utilized are listed below in stratigraphic order. The stratigraphically lowest tie points are the inflection points marking the onset of the CIE (tie point **a**) and around the peak of the CIE, where a steady negative decline in carbon isotope values is replaced by a flat trajectory of values which fluctuate around a mean (tie point **b**, Figure 3.3). Furthermore, successive acmes in *Muratodinium* spp. and *Cerodinium/Deflandrea* spp. occur immediately above the peak of the PETM CIE in all three localities. Given the pronounced stratigraphically restricted nature of these acmes, and their consistent position with respect to the PETM CIE, we assume these events were coeval and use them as a further tie points (tie points **c** and **d**, Figures 3.3, 3.4 and 3.5).

Finally, two conspicuous bentonite layers are recorded within the PETM CIE in both the Longyearbyen section and core BH9/05 (Chapter 2), which are inferred to be coeval based on their position with respect to $\delta^{13}C_{TOC}$ records, and are therefore included as the highest stratigraphic tie points (tie points **e** and **f**, Figure 3.3). However, no bentonites have been discovered within the Bergmanfjellet section, which suggests they have been removed by the faulting towards the top of the study interval. In both the Longyearbyen section and core BH9/05, the highest abundance and diversity of dinocysts occurs below these bentonite layers. Therefore, the absence of bentonites within the Bergmanfjellet section, coupled with the depleted $\delta^{13}C_{TOC}$ values and the relatively high abundance and diversity of dinocysts directly below the fault implies that the >40 m of stratigraphy between the two faults must have been deposited during the 'core' of the PETM CIE (as defined by Röhl *et al*. 2007).

3.4 Discussion

3.4.1 Basin-scale versus local events

Here we compare dinocyst assemblages from the Bergmafjellet section and core BH9/05 with those previously documented from the Longyearbyen section (Harding *et al*. 2011), in order to distinguish basin-scale events from local events in the Central Basin throughout the 'core' of the PETM CIE (where anoxic conditions preserve original cyst assemblages). We define basin-scale events as dinocyst acmes occurring within all three localities, whilst local events occur in only a single locality.

3.4.1.1 Basin-scale temporal changes

Low abundance assemblages dominated by the gonyaulacoid taxon *Spiniferites* spp. are present at all three localities in pre- and post-PETM sediments. In modern settings *Spiniferites* spp. typically occurs in sediments underlying open marine water masses

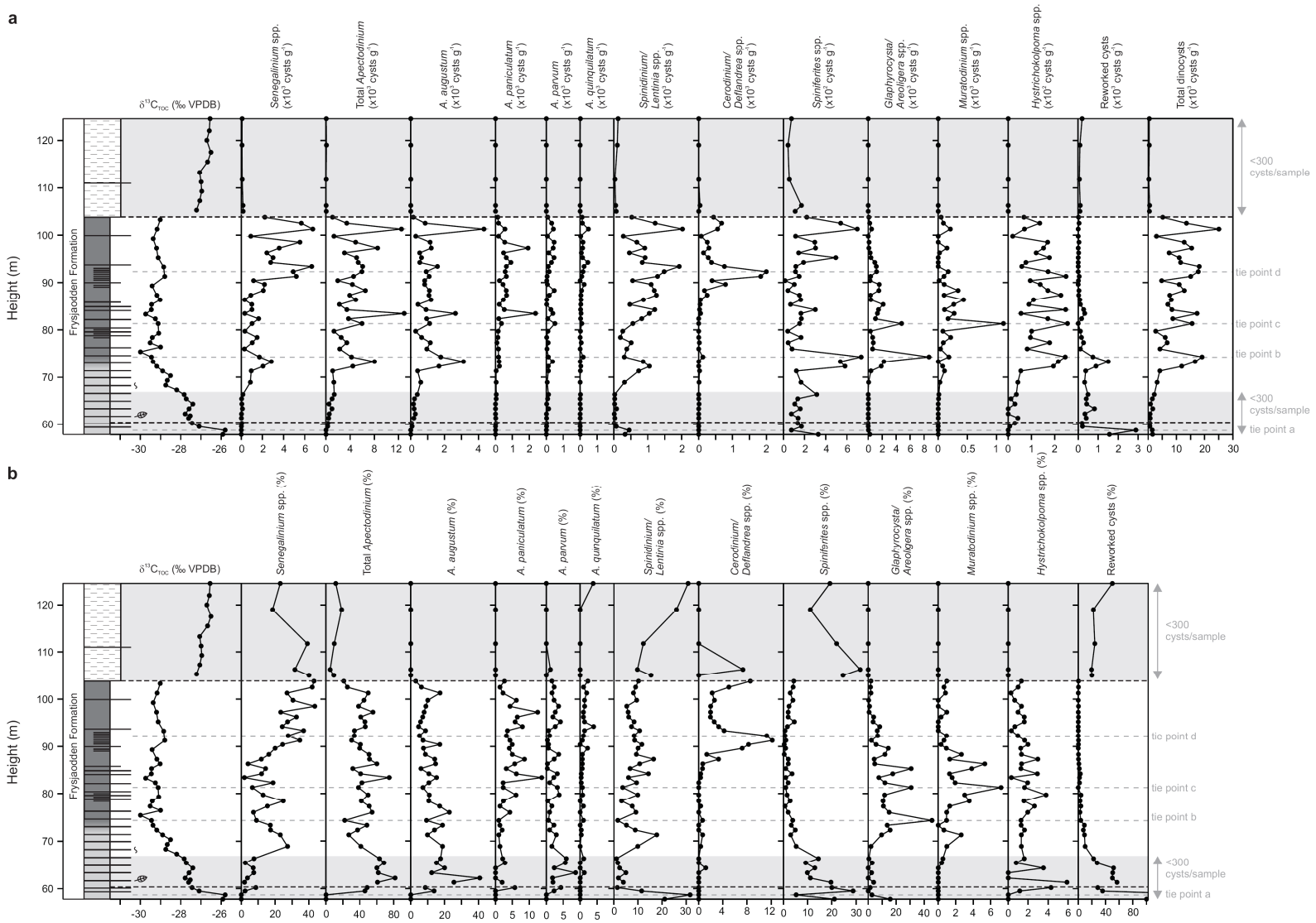
a
b
Height (m)
Frysjaodden Formation
δ13Croc (‰ VPDB)
Senegalinium spp. (x10³ cysts g⁻¹)
Total Apectodinium (x10³ cysts g⁻¹)
A. augustum (x10³ cysts g⁻¹)
A. paniculatum (x10³ cysts g⁻¹)
A. parvum (x10³ cysts g⁻¹)
A. quinquilatum (x10³ cysts g⁻¹)
Spinidinium/ Lentinia spp. (x10³ cysts g⁻¹)
Cerodinium/ Deflandrea spp. (x10³ cysts g⁻¹)
Spiniferites spp. (x10³ cysts g⁻¹)
Glaphyrocysta/ Areoligera spp. (x10³ cysts g⁻¹)
Muratodinium spp. (x10³ cysts g⁻¹)
Hystrichokolpoma spp. (x10³ cysts g⁻¹)
Reworked cysts (x10³ cysts g⁻¹)
Total dinocysts (x10³ cysts g⁻¹)
Senegalinium spp. (%)
Total Apectodinium (%)
A. augustum (%)
A. paniculatum (%)
A. parvum (%)
A. qunquilatum (%)
Spinidinium/ Lentinia spp. (%)
Cerodinium/ Deflandrea spp. (%)
Spiniferites spp. (%)
Glaphyrocysta/ Areoligera spp. (%)
Muratodinium spp. (%)
Hystrichokolpoma spp. (%)
Reworked cysts (%)
<300 cysts/sample
tie point d
tie point c
tie point b
tie point a

(Marret and Zonneveld 2003). Although pre- and post-PETM sediments are potentially biased by oxidation (Section 3.3.3), gonyaulacoids are known to be more refractory taxa (e.g. Zonneveld *et al*. 2008), and their abundance is therefore more unlikely to have been altered. Together with the low abundance/absence of other marine gonyaulacoids (e.g. *Muratodinium* and *Glaphyrocysta* spp.), the low abundance assemblages dominated by *Spiniferites* in pre- and post-PETM sediments suggests that fully marine conditions did not occur within the Central Basin preceding and post-dating the PETM.

At the onset (or immediately preceding the PETM CIE), the first occurrence of *Apectodinium* is recorded at all three localities. Just before the peak CIE dramatic increases in *Apectodinium* abundance mark its acme across the basin (Figure 3.7). The abundance of the genus remains high throughout the interval in which dinocyst assemblages are unaffected by oxidation. Such a PETM-*Apectodinium* acme has been widely recorded (e.g. Bujak and Brinkhuis 1998; Egger *et al*. 2000; Crouch *et al*. 2001; Sluijs *et al*. 2007a), and the global migration of this genus is thus far a unique event in the entire dinocyst record (Mid Triassic – Holocene). Typically limited to low latitude regions during the Palaeocene (Bujak and Brinkhuis 1998), the global migration of *Apectodinium* has been interpreted to be (at least partially) the result of globally warmer waters at the onset of (or immediately preceding) the PETM (Brinkhuis *et al*. 1994; Bujak and Brinkhuis 1998; Crouch *et al*. 2001; Sluijs *et al*. 2007b; Sluijs and Brinkhuis 2009). However, temperature may not have been the only limiting factor affecting the distribution of this taxon. The high percentage of peridinioids at all three Spitsbergen localities within the PETM CIE suggests nutrient-rich surface waters with high productivity during the PETM (Figure 3.7). The coeval acme in *Apectodinium* indicates the genus thrived in such conditions. This is consistent with results from previous studies, which have documented the *Apectodinium* acme in localities also inferred to have received high nutrient supplies (Crouch and Brinkhuis 2005; Sluijs and Brinkhuis 2009). However, warm water, nutrient-rich conditions in continental margin settings are not restricted to the PETM, thus some other (as yet unknown) factor must have contributed to initiate this unique event (Sluijs and Brinkhuis 2009).

Figure 3.5: Absolute **a)** and relative **b)** abundance of dinocysts from the Bergmanfjellet outcrop section, plotted against depth. Grey dashed lines indicate the position of age model tie points discussed in the text. Shaded areas indicate samples where <300 dinocysts per sample were observed, making dinocyst data more imprecise. Dashed lines indicate the position of two faults in the section.

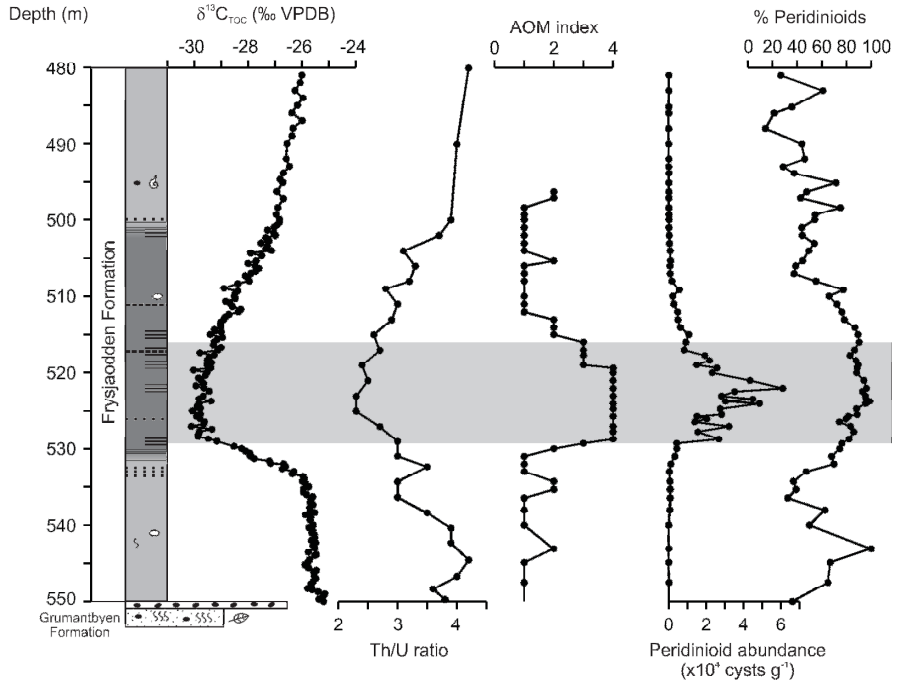

Figure 3.6: redox indicators in core BH/905 through the PETM interval. Sedimentatry log and Th/U ratio are from Dypvik *et al*. (2011), with $\delta^{13}C_{TOC}$ from Cui *et al*. (2011). Grey shaded bar indicates the interval where sedimentary anoxia is inferred. Amorphous Organic Matter (AOM) index is based on visual estimation of the abundance of AOM within palynological preparations. 0 = absent within the entire slide, 1= typically present in a 40 μm field of view, 2= common, <30 %, 3 = abundant, between 30-60 % of the assemblage, 4 = highly abundant, >60 % of the assemblage. Relative and absolute abundance of labile peridinioid dinocysts are plotted for comparison.

Coeval to the increases in *Apectodinium* abundance, elevated abundances of *Glaphyrocysta/Areoligera* are also observed across the basin (Figure 3.7). A *Glaphyrocysta/Areoligera* acme occurs in all three sections around the peak of the PETM CIE, coeval with a more temporally restricted acme in *Muratodinium*, immediately after the peak CIE (~30 kyr after the CIE onset using age model Option B from Chapter 2; ~18 kyr using Option A; tie point **c**; Figure 3.7). *Glaphyrocysta/Areoligera* and *Muratodinium* have previously been observed within inner-neritic normal marine settings (Brinkhuis 1994; Powell *et al*. 1996; Pross and Brinkhuis 2005; Sluijs *et al*. 2005), and therefore their peak abundance around the peak CIE implies the most saline waters were recorded in the Central Basin at this time. Together with the relatively high generic diversity and low dominance of dinocysts across the basin in this interval (Figure 3.7), this confirms the hypothesis of Harding *et al*. (2011) that the peak CIE is coincident with a maximum flooding surface within the basin.

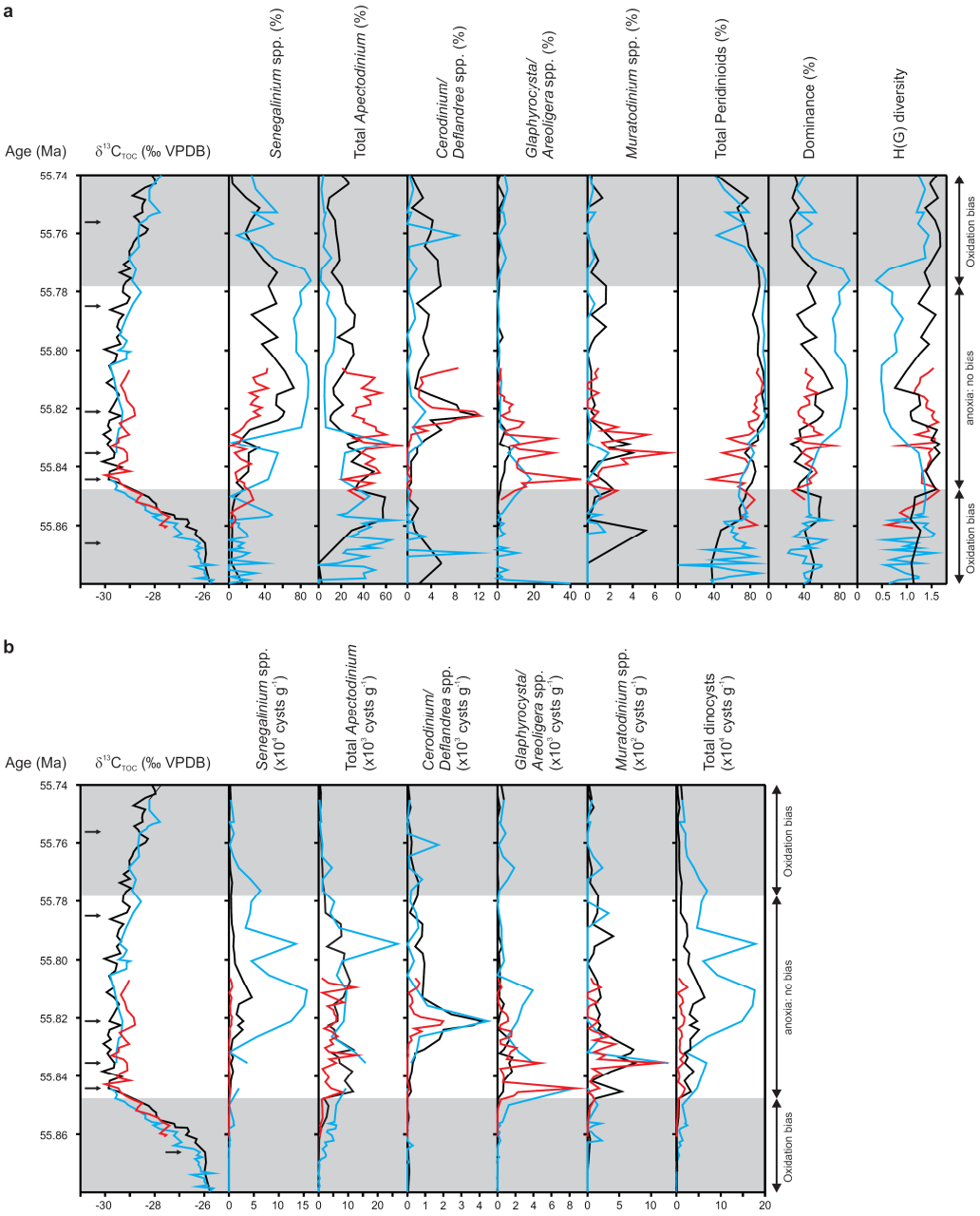

Figure 3.7: Comparison of **a)** relative and **b)** absolute dinocyst abundance data across the Central Basin, plotted against age model Option B of core BH9/05 (Chapter 2). Data from core BH9/05 (black), Longyearbyen (blue) and Bergmanfjellet (red) is plotted in each panel. Black arrows indicate the position of tie points (**a** to **e**, from Figure 3.3) used to transfer BH9/05 age model Option B to the Longyearbyen and Bergmanfjellet sections. Grey shaded areas indicate the intervals where dinocysts are potentially biased by oxidation, defined by analysis of redox conditions in core BH9/05 (Figure 3.6).

However, coeval with the *Glaphyrocysta/Areoligera* acme, increased abundances of *Senegalinium* are also observed. *Senegalinium* has previously been demonstrated as a taxon which thrived within low-salinity nutrient-rich settings, caused by high terrestrial runoff (Sluijs *et al*. 2008a; Sluijs and Brinkhuis 2009; Barke *et al*. 2011). Harding *et al*. (2011) concluded that the co-occurrence of abundant low-salinity tolerant and normal marine salinity dinocysts in the Longyearbyen section was the result of salinity-driven stratification, with *Senegalinium* inhabiting a fresh water cap overlying higher salinity waters with more normal marine dinocysts (Figure 3.8a). The increase in low-oxygen indicators throughout the basin during the PETM, together with the coeval increase in low-salinity dinocysts in all three sections, is consistent with the development of stratification across the entire Central Basin by the peak of the CIE.

Subsequently, *Senegalinium* abundance continues to increase across the basin, with the coeval decline in the abundance of the more normal marine taxa (*Glaphyrocysta/Areoligera* and *Muratodinium*). From 40-60 kyr after the onset of the PETM (23-33 kyr using age model Option A), maximum abundances of *Senegalinium* are reached in all three localities, with low abundances of marine dinocysts (Figure 3.7). This suggests that maximum fresh water input and stratification was reached in the basin at this time (Figure 3.8b and 3.9). Two possible explanations for the *Senegalinium* acme exist. The first is that relative sea level fall immediately after the peak of the PETM CIE would have resulted in all localities being closer to the coast and therefore the sources of runoff, causing relative increases in freshwater content across the basin. However, no sedimentary evidence for regression is observed in any of the sections in this interval (e.g. no regressive facies shifts [Figure 3.3; Dypvik *et al*. 2011; Harding *et al*. 2011]). Therefore, a more probable cause of the *Senegalinium* acme is increased freshwater input from enhanced terrestrial runoff. This has been inferred at other PETM localities including Site 302-4A (e.g. Guisberti *et al*. 2007; John *et al*. 2008; Sluijs *et al*. 2008a), as a result of an enhanced hydrological cycle (Ravizza *et al*. 2001; Pagani *et al*. 2006; Schmitz and Pujate 2007). An intensified hydrological cycle would result in enhanced precipitation at high latitudes (Pagani *et al*. 2006), consistent with elevated terrestrial runoff and the development of a freshwater cap across the Spitsbergen Central Basin during the PETM. Peak abundances of *Senegalinium* are reached 40-60 kyr after the onset of the CIE in Spitsbergen (Figure 3.7 and 3.8). Sluijs and Brinkhuis (2009) also observed the influx of *Senegalinium* lagged the onset of the PETM on the New Jersey margin, and suggested the onset of freshwater forcing lagged the CIE onset. Therefore, the 40-60 kyr lag between the onset CIE and the peak of the *Senegalinium* acme in Spitsbergen may provide further evidence for the delayed onset of freshwater forcing in continental margin settings during the PETM.

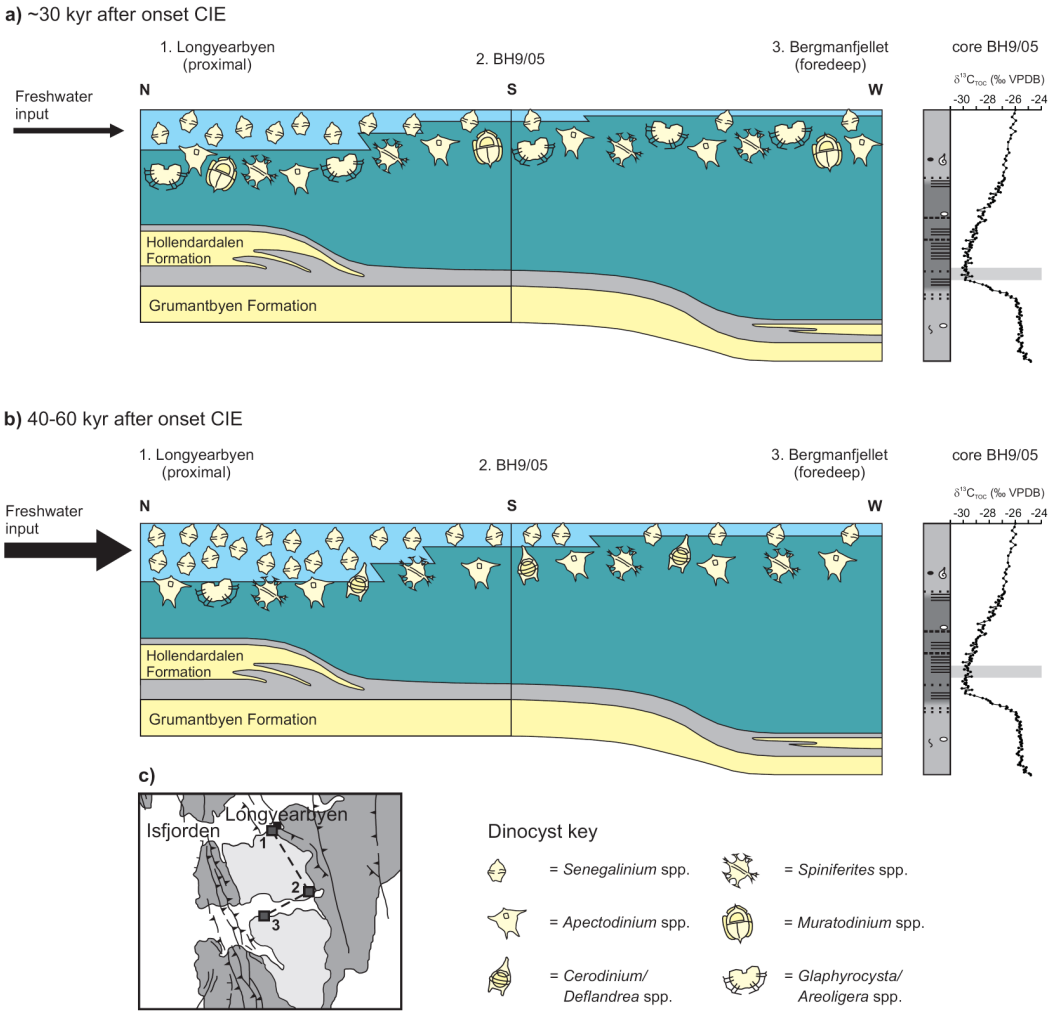

Figure 3.8: Schematic diagram illustrating palaeoceanographic changes in the Central basin during the PETM, and their affect on dinocyst assemblages. Note the dog-leg in the diagram between core BH9/05 and Bergmanfjellet. Section numbers correspond to numbers in panel c. **a)** ~30 kyr after onset CIE using Age model Option B of Chapter 2 (~18 kyr after onset CIE using age model Option A). **b)** 40-60 kyr after onset CIE using Age model Option B of Chapter 2 (23-33 kyr using age model Option A). The position of the reconstruction with respect to the $\delta^{13}C_{TOC}$ record of core BH9/05 is shown on the right. See Figure 3.3 for lithological key. **c)** Location map illustrating the position of the three study localities and the cross section for panels a and b (dashed line). See Figure 3.1 for key.

However, the perturbation of hydrogen isotopic values (Pagani *et al*. 2006; Tipple *et al*. 2011) and the deposition of a fluvial megafan in the Spanish Pyrenees (Schmitz and Pujate 2007), occurred at (or preceeded) the onset of the CIE (Figure 3.9). Most proxy data thus support the contention that hydrological cycle intensification began around the CIE onset, consistent with results from climate models (e.g. Figure 3.9; Pagani *et al*. 2006). Therefore an alternative explanation for the apparent lag between the CIE onset and maximum freshwater forcing in the Central Basin is that rising sea levels around the CIE onset suppressed the influence of runoff. Conversely, the lag in maximum freshwater flux could imply that peak hydrological cycle intensity was only reached some 40-60 kyr after the CIE onset (at least locally).

Within the *Senegalinium* acme, a pronounced temporally-restricted basin-scale acme in the hexa-peridinioid dinocysts *Cerodinium/Deflandrea* is also observed (occurring within ≤5 kyr using age model Option B; ≤2.5 kyr using Option A; tie point **d**; Figure 3.7). The acme in *Cerodinium/Deflandrea* and the presence of other hexa-peridinioids (such as *Lentinia/Spinidinium*) within the interval of high *Senegalinium* abundance confirms that Palaeogene hexa-peridinioids could tolerate low-salinities and thrived in high nutrient settings, as proposed previously (Brinkhuis *et al*. 1992; Sluijs and Brinkhuis 2009). However, temporal offsets between the acmes of different hexa-peridinioid genera (e.g. *Senegalinium* and *Cerodinium/Deflandrea*), suggests optimal salinities/nutrient contents were different for each genus.

To summarise, the dinocyst assemblages throughout the PETM can be used to infer the depositional setting of the basin during the PETM. High abundances of neritic taxa (predominantly peridinioids and *Glaphyrocysta/Areoligera*, *Muratodinium*) and high nutrient, warm water taxon *Apectodinium* occur around the peak of the CIE (Figure 3.7, 3.8 and 3.9). Subsequently, elevated abundances of high nutrient, low salinity taxon *Senegalinium* are encountered, with similar *Apectodinium* concentrations (Figure 3.7 and 3.8). Overall, this implies that deposition took place in a neritic, high nutrient setting throughout the PETM, with relatively warm sea surface temperatures.

3.4.1.2 Spatial changes within basin-scale events

Although the *Senegalinium* acme mentioned in Section 3.4.1.1 occurs across the basin, changes in *Senegalinium* abundances occur between each locality, indicative of spatial oceanographic changes in the Central Basin. The concentration of *Senegalinium* is markedly different between each locality within the acme in terms of both relative and absolute abundances (Figure 3.7). In Longyearbyen, ~90 % of the dinocyst assemblage is composed of the genus at its acme, compared to 72 % and 43 % in core BH9/05 and Bergmanfjellet respectively. If *Senegalinium* lived in a surficial freshwater cap (Section

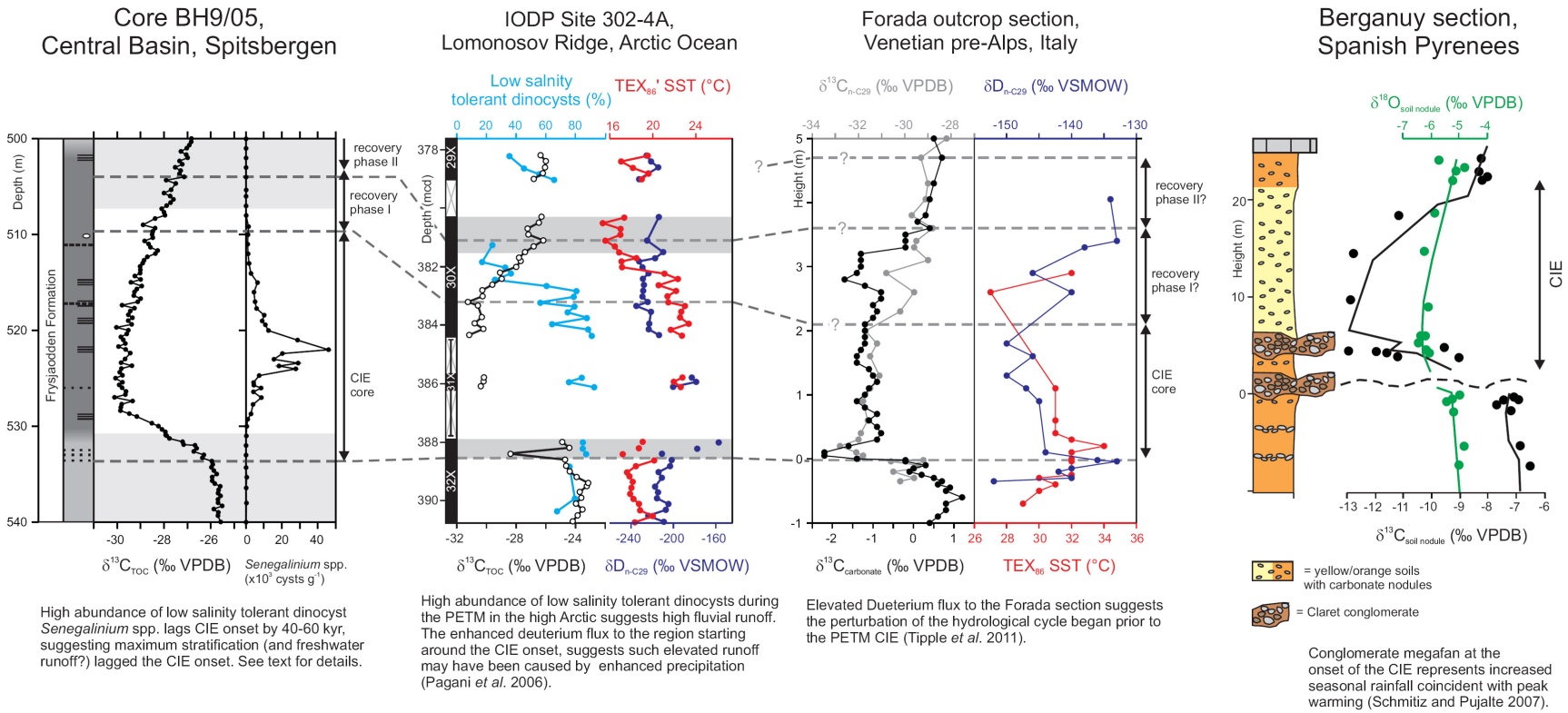

Figure 3.9: Comparison of the *Senegalinium* spp. acme (Spitsbergen) with proxies typically used to infer changes in hydrology. Core BH9/05 record of *Senegalinium* spp. abundance is considered representative of the Spitsbergen PETM. Shaded areas in core BH9/05 indicate samples where <300 dinocysts per sample were observed, making dinocyst data more imprecise. Note the top of the CIE (recovery phase II) has been truncated to show the details of the *Senegalinium* acme. Data from the Berganuy and Forada sections from Schmitz and Pujalte (2007) and Tipple *et al.* (2011), respectively. Black and Green solid lines in the Berganuy section represent 3pt running average of soil nodule data. Note the CIE phases are not defined at Berganuy owing to the low resolution $\delta^{13}C$ record. IODP Site 302-4A data from Sluijs *et al.* (2006), other than hydrogen isotopic data (from Pagani *et al.* 2006). Grey shaded areas at Site 302-4A indicate regions of drilling disturbance. Note the most enriched hydrogen isotopic values and the occurrence of a fluvial megafan occur at (or preceeding) the onset of the PETM CIE, in contrast to Spitsbergen, where the *Senegalinium* acme lags the CIE onset.

3.4.1.1), its decreasing abundance away from the most proximal section in the northeast (Longyearbyen) suggests the declining influence of freshwater away from its source (Figure 3.8). This is consistent with the fluvial input of freshwater (and nutrients) from the northeastern margin of the basin. In addition, it is notable that *Apectodinium* abundance remains relatively constant through the *Senegalinium* acme at all three sites (Figure 3.7), suggesting *Apectodinium* could tolerate euryhaline conditions and high nutrient supplies, which is consistent with previous results (e.g. Sluijs and Brinkhuis 2009).

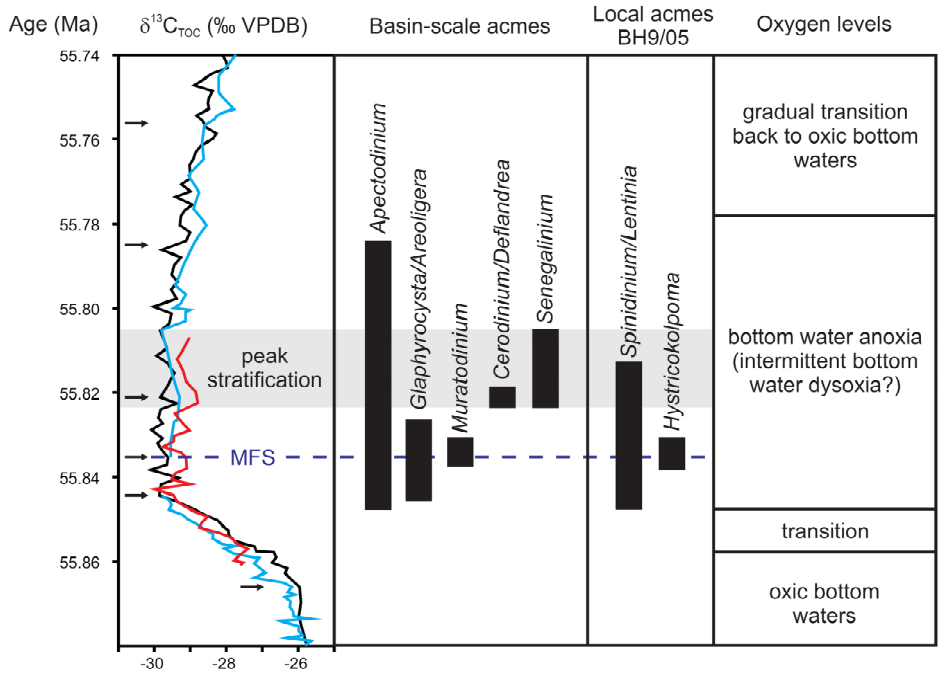

Figure 3.10: Summary diagram of biotic and palaeoceanographic events across the Central Basin during the PETM, plotted against age model Option B of Chapter 2. correlated $\delta^{13}C_{TOC}$ records from core BH9/05 (black), Longyearbyen (blue) and Bergmanfjellet (red). Black arrows indicate the position of tie points (**a** to **e**, from Figure 3.3) used to transfer the BH9/05 age model to the other sections. MFS = maximum flooding surface.

3.4.1.3 Local acmes

Two localized acmes are observed in core BH9/05 within the interval of sedimentary anoxia. We refrain from interpreting other localised acmes which occur outside the anoxic interval (in other words within intervals of low dinocyst abundance: <300 cysts per sample), as such events may be artefacts of differential preservation between localities, or the low number of cysts counted. In core BH9/05, a broad localized acme

in the hexa-peridinioid cysts *Lentinia/Spinidinium* occurs around the peak of the CIE (Figures 3.4 and 3.9). As noted above, hexa-peridinioids such as *Lentinia/Spinidinium* are believed to have inhabited low-salinity high nutrient settings (Sluijs and Brinkhuis 2009). Here we propose that optimal salinity/nutrient conditions were different for individual hexa-peridinioid genera in the Palaeogene (Section 3.4.1.1). If correct, the localized acme in *Lentinia/Spinidinium* would suggest that absolute nutrient concentrations and/or salinities were different between core BH9/05 and the other localities, consistent with the inference of the waning influence of runoff from proximal to distal settings (Section 3.4.1.2). A temporally-restricted acme in *Hystrichokolpoma* also occurs in core BH9/05 (Figures 3.4 and 3.9), coeval with peak *Muratodinium* and *Glaphyrocysta/Areoligera* abundances in this section. *Hystrichokolpoma* is considered to be an open marine dinocyst taxon (Pross and Brinkhuis 2005), and thus its peak occurrence coeval to the highest abundances of other marine taxa in core BH9/05 can in part be explained as response to the highest salinity conditions in the basin at this time. The acme may not be present within other parts of the basin owing to potential salinity and/or nutrient concentration gradients between sites, as described above for *Lentinia/Spinidinium*.

3.4.2 A low-salinity Arctic during the PETM

Four marginal marine sections now document the PETM in the high Arctic (Sluijs *et al*. 2006, 2008a; Harding *et al*. 2011; this study). Comparison of all four sites therefore permits a tentative interpretation of the temporal succession of events occurring across the region during the PETM. Sedimentological data from the Longyearbyen section suggest that the onset of sea level rise preceded the CIE onset in the Arctic (Harding *et al*. 2011), with data from all three Spitsbergen localities indicating that maximum flooding around the peak of the CIE. This interval is not documented at Site 302-4A owing to coring gaps. However, deuterium isotopic data from Site 302-4A implies enhanced moisture transport and precipitation in the Arctic during the PETM (Pagani *et al*. 2006). Elevated precipitation resulted in high runoff, leading to low salinity surface waters, salinity driven stratification, and a high abundances of the low-salinity tolerant *Senegalinium* at the Spitsbergen localities and Site 302-4A (Sluijs *et al*. 2006; 2008a; Harding *et al*. 2011; this study). This, together with the warming of surface waters (Sluijs *et al*. 2006) and sea level rise (Sluijs *et al*. 2008a; Harding *et al*. 2011), resulted in the low bottom water oxygen levels at both sites (Sluijs *et al*. 2006; Stein *et al*. 2006; Weller and Stein 2008; Dypvik *et al*. 2011; Harding *et al*. 2011), with euxinia in the water column at site 302-4A (Sluijs *et al*. 2006; Weller and Stein 2008).

3.5 Conclusions

During the PETM in Spitsbergen, dinocyst assemblages illustrate that deposition took place in a neritic setting with a high nutrient supply and relatively warm sea surface temperatures. Sedimentary laminations, together with elevated pyrite and labile AOM abundances, are documented within the PETM CIE from all three sections across the basin. Together with decreased Th/U ratios and a decreased diversity of benthic foraminifera in core BH9/05, these observations imply a decrease in oxygen levels during the PETM, with low bottom water oxygenation across the basin. When considered together with the euxinic conditions within the photic zone at Site 302-4A, it is possible that oxygen levels decreased across the Arctic region in continental margin settings during the PETM.

Furthermore, dinocyst assemblages across the Central Basin confirm previous conclusions from the Longyearbyen section (Harding *et al*. 2011) that the peak of the PETM CIE is coincident with a maximum flooding surface, with the most saline waters documented in the basin at this time. *Senegalinium* concentrations imply the presence of a freshwater cap above these higher salinity waters during the peak of the CIE, with the abundance of freshwater decreasing from northeast to southwest, consistent with the declining influence of fluvial runoff into the basin from the northeast. Subsequently, elevated abundances of *Senegalinium* in all three sections imply maximum freshwater input and stratification around 40-60 kyr after the CIE onset, probably reflecting peak terrestrial runoff as a result of an intensified hydrological cycle. Recent studies of the Arctic have recorded enhanced freshwater runoff from fluvial systems (Peterson *et al*. 2002) and increased precipitation anomalies during intervals of positive North Atlantic Oscillation (which acts to increase precipitation over Scandinavia and Siberia; Peterson *et al*. 2002, 2006). The enhanced freshwater forcing observed during modern anthropogenic warming in the Arctic thus suggests that the region is already starting to respond in a manner similar to the response documented here during the PETM.

Chapter 4: Reconstructing basin-scale carbon burial during the Palaeocene/Eocene thermal maximum in Arctic Spitsbergen

To be submitted

Co-authors: Ian C. Harding, John E.A. Marshall, Rebecca Hodgkinson, Marcus Badger and Richard Pancost

Author contributions: Adam J. Charles collected total organic carbon and palynological data, as well as calculating mass accumulation rates, under the supervison of Ian C. Harding and John E.A. Marshall. Rebecca Hodgkinson, Marcus Badger and Richard Pancost collected and interpreted the organic geochemical data. Adam J. Charles wrote the manuscript, apart from sections 4.2.4 and 4.3.4, which were written by Marcus Badger.

Abstract

The sequestration of organic carbon has been proposed as a mechanism driving the recovery from the transient climatic warming event known as the Paleocene/Eocene thermal maximum (PETM). Given that the Arctic has been proposed as substantial carbon sink during the Paleogene, constraining the mechanisms and quantities of carbon sequestered in the region during the PETM is therefore essential to evaluate this mechanism. Here, we study the composition, mass accumulation rate (MAR) and total burial of organic carbon across three PETM localities in the Central Basin, Spitsbergen, in order to assess the potential of the Arctic as a carbon sink during the PETM. MARs and total organic carbon burial indicate the rapid accumulation of large quantities of organic carbon (10s of Gt) in this foreland basin setting, illustrating the potential of such basins to drawdown significant quantities of carbon on geologically transient timescales (<250 kyr). Furthermore, a switch from predominantly terrestrial to marine organic matter deposition was caused by a combination of enhanced marine productivity and anoxia, in turn driven by eustatic sea-level rise and enhanced moisture transport to the Arctic. Given the regional influence of the latter two factors, marine-dominated organic carbon burial probably occurred across continental margin settings over the entire Arctic. This change in carbon drawdown on a regional scale would imply the majority of carbon sequestered in Arctic continental margins was withdrawn directly from the exogenic system, and that the Arctic was a significant carbon sink during the PETM.

4.1 Introduction

The globally-warm background climates of the early Palaeogene (e.g. Pearson *et al*. 2007; Zachos *et al*. 2008; Bijl *et al*. 2009) were periodically interrupted by a series of transient warming events known as hyperthermals (Cramer *et al*. 2003; Lourens *et al*. 2005; Nicolo *et al*. 2007; Agnini *et al*. 2009; Galeotti *et al*. 2010; Stap *et al*. 2010; Zachos *et al*. 2010; Sexton *et al*. 2011). Although several hyperthermals are now documented from the late Palaeocene to the onset of the middle Eocene (Cramer *et al*. 2003; Zachos *et al*. 2010; Sexton *et al*. 2011), one particular event, known as the Paleocene/Eocene thermal maximum (PETM: Kennet and Stott 1991), is significantly amplified with respect to those both preceding and post-dating it (e.g. Cramer *et al*. 2003; Zachos *et al*. 2010). Documented at numerous localities on a global-scale (e.g. Sluijs *et al*. 2007a), the PETM is defined by negative oxygen and carbon isotopic excursions in both marine and terrestrial settings (Kennett and Stott 1991; Koch *et al*. 1992; Sluijs *et al*. 2007a). Surface and deep waters warmed by ~5°C on a global-scale (Kennett and Stott 1991; Zachos *et al*. 2003; 2006; Tripati and Elderfield 2005; Sluijs *et al*. 2006; 2007a), with warming driving high taxonomic turnover and poleward migrations of both terrestrial and marine flora and fauna (Kelly *et al*. 1996; Bujak and Brinkhuis 1998; Clyde and Gingerich 1998; Wing *et al*. 2005; Gibbs *et al*. 2006a; Bown and Pearson 2009; Jaramillo *et al*. 2010). Furthermore, evidence for elevated weathering (Ravizza *et al*. 2001) and precipitation (Schmitz and Pujalte 2007), together with an enhanced moisture flux to the high Arctic (Pagani *et al*. 2006), illustrate an enhanced hydrological cycle during the PETM.

Transient warming was accompanied by a ~2.5-6 ‰ negative carbon isotope excursion (CIE), which together with widespread coeval carbonate dissolution in bathyl settings (e.g. Zachos *et al*. 2005; McCarren *et al*. 2008) implies the injection of isotopically light carbon into the exogenic system. However, although several different carbon-injection scenarios have been proposed, including the dissociation of methane hydrates from continental margin sediments (Dickens *et al*. 1995; Kurtz *et al*. 2003; Svensen *et al*. 2004; Higgins and Schrag 2006), the PETM trigger mechanism remains contentious. In turn, the subsequent exponential recovery of carbon isotopic values (Bowen and Zachos 2010), together with the transition back to carbonate-rich sediments (Kelly *et al*. 2005; 2010; Zachos *et al*. 2005), indicates carbon was subsequently removed from the exogenic system at a slower rate than it had been injected. Three hypotheses have been proposed to explain the recovery of the Earth system following the PETM carbon injection:

1. Enhanced continental weathering driven by transient warming would lead to elevated inorganic carbon burial in marine settings (although only carbonate weathering would alter oceanic $\delta^{13}C$ values; e.g. Walker *et al*. 1981; Ravizza *et al*. 2001; Kelly *et al*. 2005). Evidence for enhanced weathering is documented by osmium isotopes (Ravizza *et al*. 2001), with elevated carbonate burial in the recovery interval of the PETM (Kelly *et al*. 2005; 2010; Zachos *et al*. 2005). However, current constraints on the duration of the CIE recovery interval imply that continental weathering alone cannot account for the rate of $\delta^{13}C$ recovery observed (Bowen and Zachos 2010; Cui *et al*. 2011). Thus, although weathering would have contributed to carbon drawdown and sequestration in marine reservoirs, additional mechanisms are required to explain the rate of $\delta^{13}C$ recovery.

2. Excess atmospheric carbon was drawn down and sequestered within the terrestrial biosphere. Beerling (2000) proposed that the PETM warming led to a significant expansion of the terrestrial carbon reservoir, predominantly through increased forest growth and carbon storage within terrestrial biomass. Conversely, Bowen and Zachos (2010) argued that elevated tropical temperatures and seasonal aridity during the PETM resulted in the enhanced oxidation of carbon stocks in the terrestrial biosphere, releasing carbon during peak warming, with the subsequent replenishment of these reservoirs contributing to the $\delta^{13}C$ recovery. This mechanism dictates that tropical terrestrial flora would have experienced severe disturbance during the PETM. However, whilst floral studies from North America have documented a decline in taxonomic diversity (Harrington and Jaramillo 2007), peak floral diversity is recorded in the South American tropics (Jaramillo *et al*. 2010). Thus, given the conflicting evidence from these localities, as well as modelling studies, the terrestrial carbon storage hypothesis remains contentious.

3. Excess organic carbon burial may have resulted in the preferential removal of isotopically-light carbon from the exogenic system (Dickens 2001; John *et al*. 2008; Sluijs *et al*. 2008a). Given that a supply of organic carbon is required to generate methane hydrates, such a mechanism could be related to the recharge of a dynamic gas hydrate capacitor (e.g. Dickens 2003; 2011), if methane hydrates were released from the continental margins during the PETM (Dickens *et al*. 1995). Excess burial of organic carbon has been documented from both the New Jersey and Californian margins as well as the Arctic, and has been interpreted to be the result of elevated primary productivity and preservation in continental margin settings (John *et al*. 2008; Sluijs *et al*. 2008a). Given the majority of organic carbon in the marine realm is sequestered on the continental margins (Tyson 1995), an understanding of the magnitude and rate of carbon burial, as well as the composition of carbon sequestered

in such localities is essential to evaluate the merits of this hypothesis for potential carbon sinks. Whilst the Arctic basin is relatively small with respect to other ocean basins, the region is unique in that >50 % of the basin is continental shelf (e.g. Huntington *et al*. 2005), a proportion which would have probably been higher during the Palaoegene (the initiation of seafloor spreading forming the Eurasia Basin only occurred in the late Palaeocene [~Chron 24r: e.g. Harland *et al*. 1984). It is therefore possible that substantial quantities of organic carbon were sequestered in the region during the PETM, and other intervals of the Palaeogene (e.g. Sluijs *et al*. 2008a).

However, owing to the paucity of Arctic PETM localities, analysis of the organic matter sequestered has only been undertaken at two localities to date, IODP Site 302-4A (Lomonosov Ridge), and Longyearbyen (Spitsbergen). Sluijs *et al*. (2006) used the percentage of terrestrial palynomorphs and dinocysts together with the Branched Index of Tetraethers (BIT index: Hopmans *et al*. 2004) to illustrate an influx of marine organic matter during the PETM at Site 302-4A. Similarly, Harding *et al*. (2011) observed a switch from terrestrially-derived phytoclasts to marine dinocysts and amorphous organic matter during the PETM in Longyearbyen, coincident with elevated Hydrogen/Carbon (H/C) values. The switch from terrestrial to marine organic matter deposition at both the above localities has been attributed in part to eustatic sea level rise at the Paleocene/Eocene boundary (Sluijs *et al*. 2006, 2008b; Harding *et al*. 2011). Furthermore, mass accumulation rates of organic carbon (MARs C_{org}) of 0.18 g cm^{-2} kyr^{-1} have been calculated for the PETM interval at Site 302-4A (Sluijs *et al*. 2008a), but these have been the only Arctic estimates to date. Here we analyze the rate, magnitude and composition of carbon buried across the PETM in three localities across the Central Basin, Spitsbergen, in order to constrain the quantity and mechanisms of organic carbon burial, with implications for Arctic carbon drawdown on a regional-scale.

4.2 Material and methods

4.2.1 Geological setting

Spitsbergen, the largest and westernmost island of the Svalbard archipelago, resides on the northwest corner of the Barents Shelf. In the Palaeogene, rifting in the Labrador Sea resulted in the counter-clockwise rotation of Greenland, which together with the opening of the northernmost north Atlantic drove a transpressive dextral strike-slip regime between Svalbard and Greenland (Harland *et al*. 1984; Müller and Speilhagen 1990). This tectonic scenario led to orogenesis on the western margin of Spitsbergen, creating the West Spitsbergen Orogen and the adjacent foreland basin, the Central Basin (Harland 1997, and references therein). The PETM has now been identified within

three localities within the Central Basin (Harding *et al*. 2011; Cui *et al*. 2011; Chapters 2 and 3), which had a paleolatitude of ~75˚N.

The three localities studied are the Longyearbyen section (Harding *et al*. 2011), core BH9/05 (Dypvik *et al*. 2011; Cui *et al*. 2011; Chapters 2 and 3) drilled near Sveagruva, and the Bergmanfjellet section on the southern margin of Van Mijenfjorden (Chapter 3). The Longyearbyen and core BH9/05 localities are adjacent to the northern and eastern margins of the preserved basin deposits, with the Bergmanfjellet section located on the west, within the foredeep of the basin (Figure 4.1). Utilizing the stratigraphic nomenclature of Dallman *et al*. (1999), the PETM is located within the homogeneous mudstones of the Frysjaodden Formation at all three localities (≤5 cm coarse siltstone interbeds interrupt mudstone deposition at Bergmanfjellet; Figure 4.2). The PETM is identified a ~4 ‰ negative organic carbon isotope excursion ($\delta^{13}C_{TOC}$) together with PETM diagnostic dinoflagellate cyst species *Apectodinium augustum* (Figure 4.2; Harding *et al*. 2011; Cui *et al*. 2011; Chapters 2 and 3).

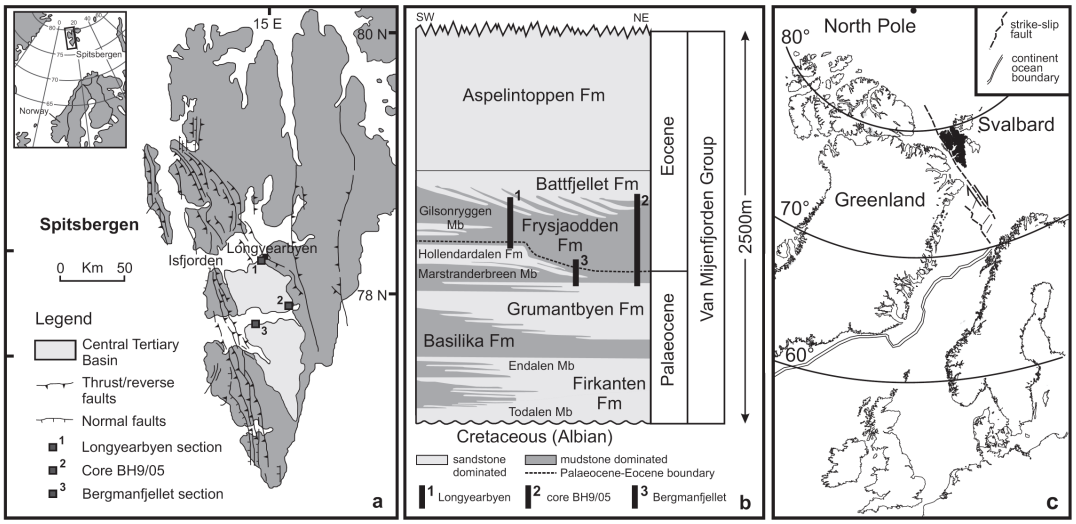

Figure 4. 1: The study sections. **a)** Location map illustrating the position of the Central Basin, and the three study localities (after Uroza and Steel 2008; Blythe and Kleinspehn 1998). **b)** The Palaeogene stratigraphy of Spitsbergen, illustrating the stratigraphy spanned by the study localities (after Uroza and Steel 2008; Steel *et al*. 1985). **c)** Palaeogeographic reconstruction of the northern North Atlantic region during the early Eocene, illustrating the position of Spitsbergen in black (after Mosar et al. 2002).

4.2.2 Mass accumulation rates and carbon burial

We have calculated values for dry bulk density and total organic carbon in order to derive the quantity of carbon sequestered in the Central Basin. In addition, we have determined linear sedimentation rates in order to calculate the mass accumulation rate

of organic carbon (MAR C_{org}) for the Spitsbergen PETM localities. Each of these parameters has been derived as detailed in the following sections.

4.2.2.1 Dry bulk density

In order to derive dry bulk density, we first calculated grain density (ρ), by measuring the dry weight (w) and volume (v) of 93 samples from the lower Frysjaodden Formation across all three Spitsbergen localities (ρ=w/v). Samples were washed in deionised water and then dried at ~60˚C overnight to drive off water, before weighing. Subsequently, samples were submerged in ~50 ml of water, with the measured volume of water displaced equalling the sample volume. The resultant grain density values were averaged, yielding a mean of 2.58 g cm^{-3} (n=93; Standard deviation 0.21 g cm^{-3}). Grain densities of ~2.6 g cm^{-3} for the lower Frysjaodden Formation have also been measured from a core drilled in Sysselmannbreen (Elvebakk *pers comm.* 2011), illustrating our average grain density determination is robust. Together with measured porosity values of the lower Frysjaodden Formation from the Sysselmannbreen core (Elvebakk *pers comm.* 2011), a grain density of 2.58 g cm^{-3} results in a dry bulk density of 2.42 g cm^{-3} ±0.20, which we take as representative of the Spitsbergen samples, and use throughout our calculations.

4.2.2.2 Sedimentation rates

Derivation of accurate linear sedimentation rates for the PETM is complicated by the fact that different age models have been proposed for the duration of the CIE (Abdul-Aziz *et al*. 2008; Farley and Eltgroth 2003; Murphy *et al*. 2010; Röhl *et al*. 2007). Cyclostratigraphic analysis has yielded durations of 170 kyr for the PETM CIE (onset-end recovery phase II) from ODP sites 690 and 1263 (Röhl *et al*. 2007), and 157 kyr from the Bighorn Basin (Abdul-Aziz *et al*. 2008). Conversely, extraterrestrial ^{3}He age models include a <120 kyr duration from ODP Site 690 (Farley and Eltgroth 2003), although this model has been challenged by Sluijs *et al*. (2007a). Furthermore, Murphy *et al*. (2010) derive a duration of 217 $^{+44}/_{-31}$ kyr from ODP Site 1266. Here we utilize three different age model end members to calculate MARs C_{org}, to account for the uncertainty associated with the duration of the PETM CIE. Chapter 2 documents two different age models for the PETM in core BH9/05, Options A and B, consistent with the Röhl *et al*. (2007) cyclostratigraphic age model and the extraterrestrial ^{3}He age model of Murphy *et al*. (2010) respectively. Here we also construct a third age model (Option C) for core BH9/05 consistent with the ^{3}He age model of Farley and Eltgroth (2003). In order to construct this age model, we assigned a 120 kyr duration to the PETM CIE (from the onset to the end of recovery phase II; 533.66 - 487.00 m), with a 90 kyr duration for the core interval of the CIE (533.66 - 509.70 m), and 30 kyr for the recovery (509.70 – 487.00 m). This approach assumes that sedimentation rates were

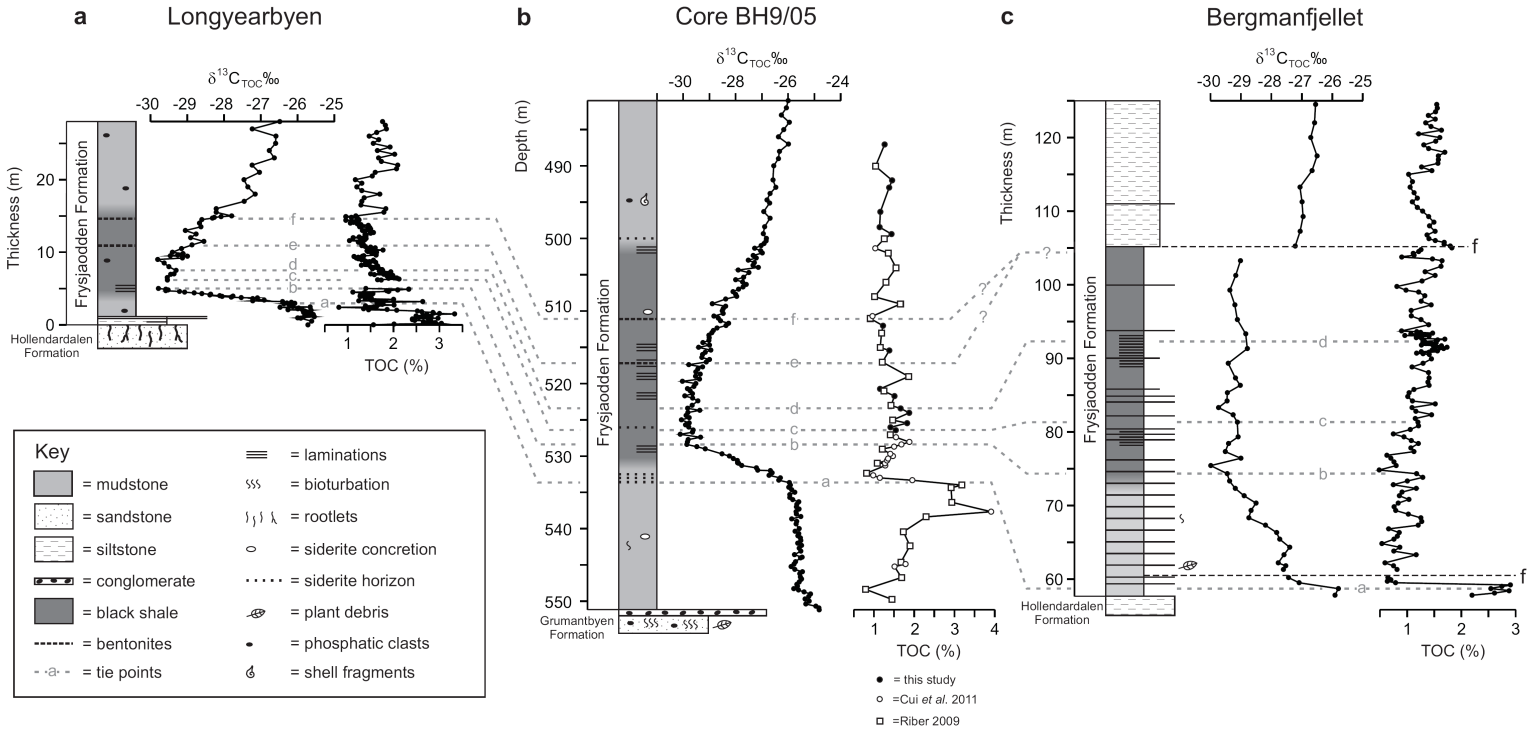

Figure 4.2: Lithological, organic carbon isotope ($\delta^{13}C_{TOC}$ [‰ VPDB]) and TOC (%) records through the PETM on Spitsbergen. **a)** The Longyearbyen section (after Harding *et al*. 2011). **b)** core BH9/05 (Log: Dypvik *et al*. 2011; $\delta^{13}C_{TOC}$: Cui *et al*. 2011). Note the TOC (%) curve is a synthetic curve derived by combining results from Riber (2009), Cui *et al*. 2011, and this study. **c)** The Bergmanfjellet section (Log and $\delta^{13}C_{TOC}$ from Chapter 3).

constant between these tie points. In order to derive sedimentation rates using the same age model for each Spitsbergen locality, we utilize these age model end members for core BH9/05, and export them to the Longyearbyen and Bergmanfjellet sections using the tie points described in Chapter 3.

4.2.2.3 Total organic carbon

Total organic carbon (TOC %) measurements have previously been undertaken on samples from the Longyearbyen section (Harding *et al*. 2011), core BH9/05 (Cui *et al*. 2011; Riber 2009) and Bergmanfjellet (Chapter 3). Here, we augment the TOC % records from these studies through analysis of 15 additional samples from core BH9/05, and 109 samples from Bergmanfjellet (Figure 4.2, Appendix 4). Samples were prepared using the methodology documented in Chapter 3, with around three milligrams of sample run using a Carlo Erba EA1108 elemental analyzer, with an analytical precision of 0.03 % based on standard reproducibility.

4.2.3 Palynology

In order to assess the composition of the organic matter being buried across the PETM interval in Spitsbergen, we carried out palynofacies and UV fluorescence analyses on samples from core BH9/05. Palynological sample processing for the samples analyzed here has been described in Chapter 3, and follows standard palynological processing methods. Fluorescence microscopy was carried out in incident light using a Zeiss Universal Microspectrophotometer 50 (UMSP 50; excitation filter 450-490 nm; long pass filter 520 nm; beam splitter 510 nm). Palynofacies analysis was carried out by counting a minimum of 300 palynomacerals for an individual sample. Amorphous organic matter (AOM: non-particulate) was not included in the count. We utilize the ratio between dinoflagellate cysts (dinocysts: marine) and terrestrial phytoclasts (brown + opaque phytoclasts excluding cuticle) together with the absolute abundance of dinocysts (from Chapter 3, Appendix 3) to document temporal changes in the relative abundance of marine organic matter being sequestered. Furthermore, we use the ratio of opaque:brown phytoclasts (excluding cuticle, see Appendix 4) to look at potential changes in the abundance of oxidized phytoclasts (opaque) through the PETM (e.g. Tyson 1995), as such changes could be indicative of terrestrial biosphere perturbation.

4.2.4 Organic geochemistry

Here we analyze the C_{29}/C_{27} diasterane ratio in core BH9/05, to further elucidate changes in organic matter composition across the PETM. Diasteranes are saturated tetracyclic compounds derived from the steroids and sterol membrane lipids and hormonal components of eukaryotes during diagenesis. The most common steranes in

ancient sediments are those with between 27 and 29 carbons (C_{27} – C_{29}). Although C_{27} – C_{29} diasteranes are derived from a wide variety of eukaryotes, C_{29} diasteranes are frequently associated with terrestrial higher plant organic matter, whereas C_{27} diasteranes predominate in marine settings (Huang and Meinschein 1976). The C_{29}/C_{27} diasterane ratio can therefore be used as an indicator of organic matter source variations. However as some marine algae have also been shown to produce the C_{29} sterols from which C_{29} diasteranes are derived (Volkman 1986, 1988) caution much be used when applying the proxy. Nevertherless when used in combination with other source material indicators diasteranes have been shown to be useful biomarkers for changing source contributions.

35 subsamples were ground to fine powder using a milling machine, and extracted ultrasonically with, sequentially, methanol (MeOH), MeOH:Dichloromethane (DCM; 1:1, v:v) and DCM. Supernatants were collected and combined, then reduced by rotary evaporation before being evaporated to dryness under a stream of nitrogen. Samples were split into non-polar and polar fractions over small (4 cm) columns of silica gel eluted with n-hexane and DCM:MeOH (3:1, v:v) respectively. Samples were analysed by Gas Chromatography Mass Spectometry (GC-MS) on a ThermoQuest Trace MS at the Organic Geochemistry Unit, University of Bristol fitted with a fused capillary column (50 m × 0.32 mm) coated with a 0.12 μm dimethylpolysiloxane film (Agilent Technologies CP-Sil 5 CB). Helium carrier gas was used and the oven programmed to increase from an initial temperature of 70°C to 130°C at 20°Cmin^{-1}, then to 300°C at 4°Cmin^{-1}, finally remaining isothermal for 25 mins. Compound peaks (equation 4.1) were integrated in TIC mode, or, where impossible due to co-eluting compounds, using characteristic ions (m/z=217 for diasteranes).

C_{29}/C_{27}=([diastigmastane 20S+diastimastane 20R])/([diacholestane 20S+diacholestane 20R]) Equation 4.1

4.3 Results

4.3.1 Mass accumulation rates

Here we utilize two different approaches to calculate both the MAR C_{org} throughout the PETM, and at individual localities. In order to derive the MAR C_{org} for the entire PETM, we calculate the mean MAR C_{org} from the CIE onset to the end of recovery phase II (mean MARs C_{org} for the core and recovery intervals were also calculated separately). Owing to the faulting within the Bergmanfjellet section, and the uncertainty associated with the position of the top of CIE recovery phase II in Longyearbyen, MARs C_{org} for the

entire PETM interval were only calculated for core BH9/05. Average values for the sedimentation rate and TOC were utilized in order to calculate representative rates. Table 4.1 illustrates the MARs C_{org} for core BH9/05 using the different age model end-members. Given the potential age model options for the duration of the PETM CIE, MARs C_{org} range from 0.64 ±0.11 to 1.27 ±0.21 g cm^{-2} kyr^{-1} (onset to end recovery phase II).

Table 4.1: MARs C_{org} for core BH9/05 derived using different age model options

Interval	Duration (kyr)	Mean TOC (%)	Dry bulk density (g cm^{-3})	Sedimentation rate (cm kyr^{-1})	MAR C_{org} (g cm^{-2} kyr^{-1})
Option A:					
Core	70	1.38 ±0.1	2.42 ±0.2	34.33	1.15 ±0.18
Recovery	105	1.27 ±0.1	2.42 ±0.2	21.64	0.67 ±0.11
Entire PETM	175	1.35 ±0.1	2.42 ±0.2	26.71	0.87 ±0.14
Option B:					
Core	116	1.38 ±0.1	2.42 ±0.2	20.66	0.69 ±0.11
Recovery	122	1.27 ±0.1	2.42 ±0.2	18.64	0.57 ±0.10
Entire PETM	238	1.35 ±0.1	2.42 ±0.2	19.62	0.64 ±0.11
Option C:					
Core	90	1.38 ±0.1	2.42 ±0.2	26.62	0.89 ±0.14
Recovery	30	1.27 ±0.1	2.42 ±0.2	75.67	2.33 ±0.39
Entire PETM	120	1.35 ±0.1	2.42 ±0.2	38.88	1.27 ±0.21

In order to compare rates of organic carbon burial between sites, MARs of C_{org} were also calculated for the core interval of the PETM CIE at each individual locality, by exporting age model options A-C from core BH9/05 to the Longyearbyen and Bergmanfjellet sections using tie points (Table 4.2; MARs of C_{org} were only calculated for the CIE core interval due to the absence of tie points in the CIE recovery). Mean TOC values were calculated for each interval, with sedimentation rates derived by assuming that rates were constant between tie points. Figure 4.3 shows the MARs C_{org} for the individual Spitsbergen localities, plotted against the different age model options. The lowest MARs C_{org} are found in the Longyearbyen section, with elevated rates in core BH9/05, and the highest rates at Bergmanfjellet (Table 4.2; Figure 4.3). Thus, the different MARs C_{org} between sites indicate the rate of carbon burial in the Spitsbergen Central Basin increased towards both the south and west. This pattern is replicated with each age model utilized, illustrating the differential rates of carbon burial between sites are insensitive to the age model used to derive the MARs. By utilizing the MARs C_{org} together with the duration of each interval, the total quantity of carbon buried

Table 4.2: MARs C_{org} and total carbon accumulated for individual Spitsbergen PETM localities, within the 'core' interval of the CIE.

Interval	Mean TOC (%)	Dry bulk density (g cm^{-3})	Sedimentation rate (cm kyr^{-1})			MAR C_{org} (g cm^{-2} kyr^{-1})			Carbon accumulated (t km^{-2} x10^3)
			Option A	Option B	Option C	Option A	Option B	Option C	
Longyearbyen:									
a-b	1.61 ±0.2	2.42 ±0.2	14.29	8.72	9.62	0.56 ±0.12	0.34 ±0.07	0.37 ±0.09	73.85
b-c	1.56 ±0.2	2.42 ±0.2	23.00	12.92	15.54	0.87 ±0.19	0.49 ±0.11	0.59 ±0.13	43.48
c-d	1.85 ±0.2	2.42 ±0.2	17.76	9.44	11.98	0.79 ±0.16	0.42 ±0.09	0.54 ±0.10	60.40
d-e	1.48 ±0.2	2.42 ±0.2	21.79	9.42	14.53	0.78 ±0.18	0.34 ±0.07	0.52 ±0.12	121.68
e-f	1.32 ±0.2	2.42 ±0.2	16.51	12.75	16.15	0.53 ±0.13	0.41 ±0.10	0.51 ±0.13	117.91
BH9/05:									
a-b	1.29 ±0.1	2.42 ±0.2	39.55	24.13	26.62	1.24	0.75	0.83	164.34
b-c	1.63 ±0.1	2.42 ±0.2	39.40	22.13	26.62	1.55	0.87	1.05	77.65
c-d	1.62 ±0.1	2.42 ±0.2	39.47	20.98	26.62	1.55	0.82	1.05	117.89
d-e	1.48 ±0.1	2.42 ±0.2	39.94	17.26	26.62	1.43	0.62	0.95	222.76
e-f	1.23 ±0.1	2.42 ±0.2	27.22	21.02	26.62	0.81	0.63	0.79	181.96
Bergmanfjellet:									
a-b	0.93 ±0.03	2.42 ±0.2	140.00*	78.65*	94.59*	3.16	1.77	2.13	419.72
b-c	0.92 ±0.03	2.42 ±0.2	140.00	78.65	94.59	3.13	1.76	2.12	156.56
c-d	1.35 ±0.03	2.42 ±0.2	144.74	76.92	97.61	4.73	2.51	3.19	359.39
d-e	1.28 ±0.03	2.42 ±0.2	144.74*	76.92*	97.61*	4.47	2.38	3.02	697.73
e-f	N/A	N/A	N/A	N/A	N/A	N/A	N/A	N/A	N/A

within each interval can be calculated (Table 4.2). Owing to the gradient of MARs C_{org} across the basin, the total amount of carbon accumulated increases both toward the south and the west, for any given interval within the core of the PETM CIE (Table 4.2). Given, the Bergamnfjellet section in the west is adjacent to the West Spitsbergen Orogenic Belt, this indicates that organic carbon sequestration increased towards the foredeep of the basin.

4.3.2 Total carbon burial

Here we calculate the total amount of organic carbon buried at each Spitsbergen locality and across the Central Basin, using the stratigraphic thickness of the PETM localities studied and their organic carbon content, where:

$$\text{Carbon buried} = \rho\, t\, (TOC/100) \qquad \text{Equation 4.2}$$

Where ρ is the dry bulk density in g cm^{-3}, t is the stratigraphic thickness in cm, and TOC is the total organic carbon content in %. The resultant quantity of carbon sequestered can be used to calculate an estimate of the total carbon buried within the Spitsbergen Central Basin, assuming a basin area of 12,000 km^2 (200 x 60 km, following Steel *et al*. 1981; 1985). Table 4.3 shows the amount of carbon buried across the Central Basin calculated from each individual PETM locality. Extrapolating the results from the Longyearbyen section across the Central Basin gives a figure of 10.9 ±2.5 Gt of sequestered carbon, whereas this figure rises to 18.3 ±3.0 Gt if results from core BH9/05 are utilized. Owing to the faulting within the Bergmanfjellet section, estimates could only be calculated for the core interval of the CIE, with 14.8 ±1.6 Gt of carbon buried across the basin if results from this section are considered representative. However, the incomplete nature of the Bergmanfjellet section implies the total amount of carbon sequestered over the entire CIE is underestimated. Within the CIE core interval the MARs C_{org} and total quantities of carbon buried are greatest at Bergmanfjellet (Tables 4.2 and 4.3), suggesting the total quantity buried at this site throughout the entire PETM was probably higher than the other two localities. Thus, given the increasing quantity of carbon buried towards both the south and the west (Section 4.3.1), we consider the Bergmanfjellet section in the west and the Longyearbyen section in the north to represent high and low end member scenarios of sequestration respectively (the quantity of carbon buried in the Longyearbyen section may also be slightly underestimated owing to the uncertain position of the top of the PETM CIE recovery phase II in this locality). Therefore, we consider that core BH9/05 is the most representative study locality, and that 18.3 ±3.0 Gt is the best estimate of the quantity of carbon sequestered during the PETM CIE within the Central Basin. However, significant uncertainties exist when calculating

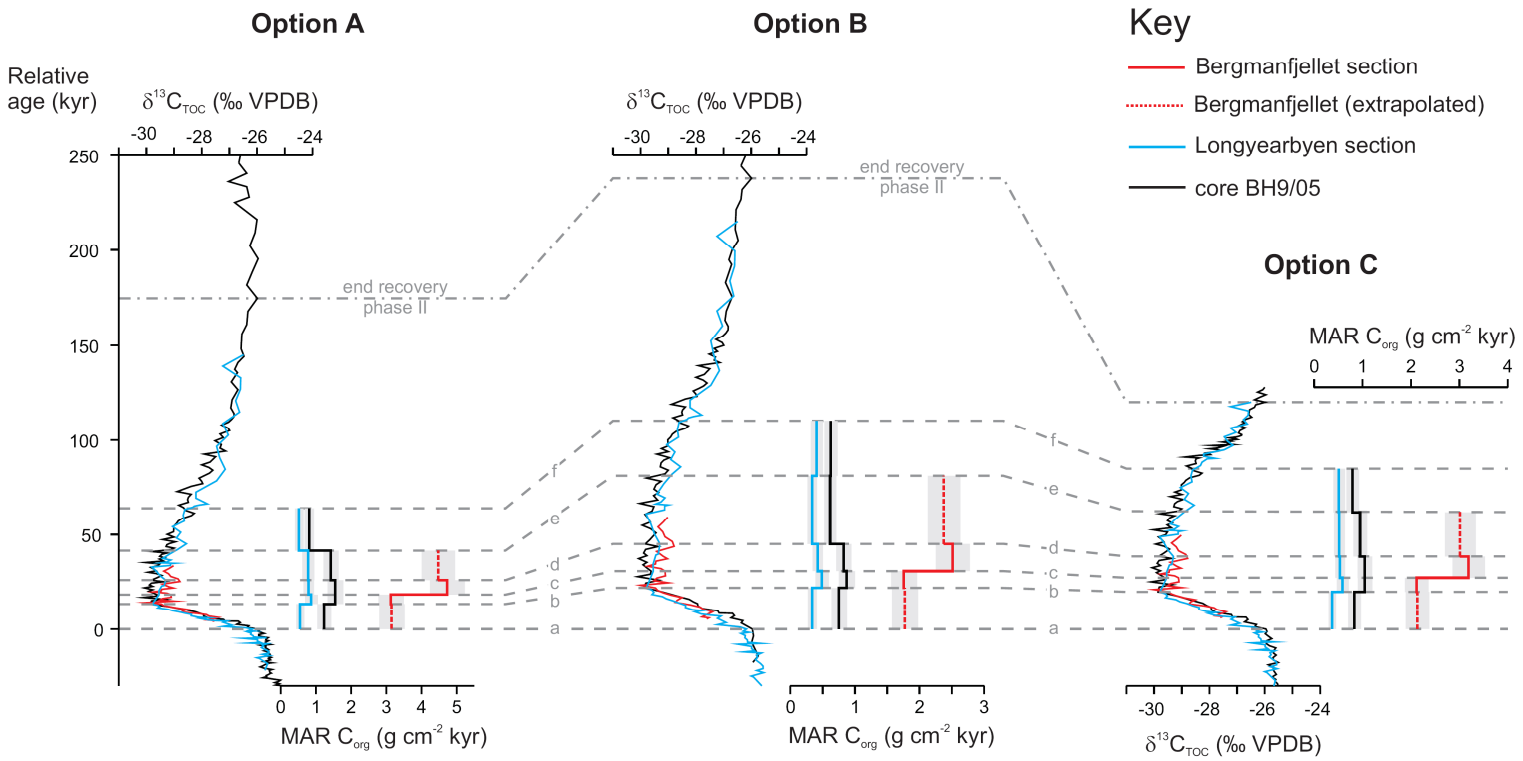

Figure 4.3: MAR C_{org} plotted against different PETM age model options. Option A (from Chapter 2), tuned to the Röhl *et al*. (2007) PETM age model of ODP Site 1263. Option B (from Chapter 2), consistent with the extraterrestrial ^{3}He age model of ODP Site 1266 (Murphy *et al*. 2010). Option C, plotted against the ^{3}He age model for ODP Site 690 (Farley and Eltgroth 2003). Errors were derived by propagating the error for both the dry bulk density (±0.2 g cm^{-2}), and the TOC measurements for each locality (±0.2 % longyearbyen; ±0.1 % core BH9/05; ±0.03 % Bergmanfjellet). Dashed line in Bergmanfjellet represent the MAR C_{org} assuming sedimentation rates between points a-b and d-e remained the same as those directly above/below these intervals respectively.

the total quantity of carbon accumulated within a basin (e.g. John *et al*. 2008; Sluijs *et al*. 2008a). Factors such as localised changes in TOC content, the accuracy of the calculation of basin area, and the assumption that the PETM thickness in core BH9/05 is representative across the basin, all add uncertainty to our estimate of basin carbon accumulation (e.g. John *et al*. 2008; Sluijs *et al*. 2008a). Therefore the uncertainty associated with our 18.3 Gt estimate is probably greater than the ±3.0 Gt calculated above from error propagation alone. Despite this, the estimates of carbon accumulation from all three Spitsbergen localities indicate that the quantity of carbon accumulated would be on the order of 10s of gigatonnes, thus indicating our estimate is accurate within an order of magnitude.

4.3.3 Palynology

Figure 4.4 illustrates the absolute abundance of dinocysts (Chapter 3), and the ratio of dinocysts (marine) to phytoclasts (terrestrial) through the lower Frysjaodden Formation in core BH9/05. Before the PETM CIE onset (below 533.66 m) both these parameters illustrate that dinocyst abundance is low, consistent with previous results from all three PETM localities across the basin (Harding *et al*. 2011; Chapter 3). The low abundance of dinocysts and amorphous organic matter (AOM: Figure 4.5) in this interval illustrate the assemblages are dominated by terrestrial organic matter (specifically phytoclasts: Figures 4.4 and 4.5). The opaque to brown phytoclast ratio illustrates that ~20-30 % of the phytoclasts transported into the basin at this time were oxidized. A gradual increase in the abundance of dinocysts is observed in both absolute and relative abundance from ~534-529 m, followed by a pronounced rise at 528.73 m. (Figure 4.4).

The abundance of dinocysts to phytoclasts is relatively high from 528.73 m to ~519 m (ranging between 0.22-0.62), reflecting the elevated absolute abundance of dinocysts in the core of the PETM CIE (Figure 4.4). However, organic matter assemblages within this interval are dominated by amorphous organic matter (AOM; Figure 4.5). Fluorescence microscopy demonstrates that the AOM has a low fluorescence, consistent with the thermal maturity of the samples (vitrinite reflectance values of ~1 % have been derived from the lower Frysjaodden Formation in Longyearbyen: Harding *et al*. 2011). Numerous framboidal inclusions reside within the AOM, which exhibit specular scatter under fluorescence (Figure 4.6), and are opaque under transmitted light (Figure 4.5). These characteristics are consistent with a pyritic composition for the framboids, a contention substantiated by the elevated XRD percentages of this mineral from the PETM interval of core BH9/05 (Riber 2009). Furthermore, the AOM contains highly fluorescent inclusions, such as fragments or entire specimens of dinocysts, such as *Apectodinium* (Figure 4.6). In order to contain inclusions of *Apectodinium*, the AOM

Table 4.3: Estimates of total carbon burial within the Spitsbergen Central Basin, based on data from individual PETM localities. Basin-scale burial estimates assume an area of 12,000 km^2 for the Central Basin (following Steel *et al*. 1981, 1985). Note that faulting within the Bergmanfjellet section prevents an estimate of carbon sequestered within the recovery interval at this localitiy.

Interval	Height/depth (m)	Interval thickness (cm)	Mean TOC (%)	Dry bulk density (g cm^{-3})	C accumulated (g cm^{-2})	C accumulated (t km^{-2} x10^6)	Basin carbon accumulation (Gt)
Longyearbyen:							
Core	3.10 - 14.90	1180	1.49 ±0.2	2.42 ±0.2	42.55 ±10	0.426 ±0.10	5.1 ±1.2
Recovery	14.90 - 28.00	1310	1.61 ±0.2	2.42 ±0.2	51.04 ±11	0.510 ±0.11	6.1 ±1.3
Entire PETM	3.10 - 28.00	2490	1.51 ±0.2	2.42 ±0.2	90.99 ±21	0.910 ±0.21	10.9 ±2.5
BH9/05:							
Core	533.66 - 509.70	2396	1.38 ±0.1	2.42 ±0.2	80.02 ±13	0.800 ±0.13	9.6 ±1.5
Recovery	509.70 - 487.00	2270	1.27 ±0.1	2.42 ±0.2	69.77 ±12	0.698 ±0.12	8.4 ±1.4
Entire PETM	533.66 – 487.00	4666	1.35 ±0.1	2.42 ±0.2	152.44 ±25	1.524 ±0.25	18.3 ±3.0
Bergmanfjellet:							
Core	61.25 – 104.75	4350	1.17 ±0.03	2.42 ±0.2	122.96 ±14	1.230 ±0.14	14.8 ±1.6
Recovery	NA	NA	NA	NA	NA	NA	NA
Entire PETM	61.25 – 104.75	4350	1.17 ±0.03	2.42 ±0.2	122.96 ±14	1.230 ±0.14	14.8 ±1.6

must have been generated within the marine realm, and during the PETM, and thus represents contemporaneous and not reworked AOM. A slight decrease in the proportion of opaque phytoclasts is also observed in this interval, with values ranging from 0.09-0.26. The decline of opaque phytoclasts during the PETM may indicate the terrestrial biosphere in the Arctic was not subjected to increased oxidation during the event, although the changes in sea level and runoff (Harding *et al*. 2011; Chapter 3) could also alter the ratio (Tyson 1995). Above 519 m, a gradual decline in the abundance of dinocysts and AOM is observed (Figure 4.4), together with a slight increase in the proportion of opaque phytoclasts (ranging from 0.15-0.47). Above 503 m the abundance of dinocysts remains low until the termination of the PETM CIE at 487 m, with the low AOM content and dinocyst to phytoclast ratio indicating a return to assemblages dominated by terrestrial organic matter (Figure 4.4).

4.3.4 Organic geochemistry

The C_{29}/C_{27} diasterane ratio is illustrated in Figure 4.4. Diasterane ratios of ~2 are recorded from 536-534 m, below the onset of the $\delta^{13}C_{TOC}$ excursion. From 534-528 m values decline from ~2 to ~1, coincident with the negative transition of $\delta^{13}C_{TOC}$ values marking the onset of the PETM. However, a sharp increase in the ratio is superimposed on this trend (up to 2.8, from 532-531 m). Diasterane ratios fluctuate between 0.6 and 1.4 from 527-520 m, before a gradual increase back to values ~2 at the end of the CIE recovery interval. Although the interpretation of the diasterane ratio is complex (Section 4.2.4), the decline in values during the core interval of the PETM CIE supports a shift to less terrestrially-derived organic matter reaching the site. Furthermore, fluctuations in the ratio during the PETM onset, together with other biomarker proxy data from core BH9/05 (Badger *et al*., *in prep*), indicate significant variability in the material deposited at this time. Such changes may suggest increasing distance from land (i.e. relative sea level rise) or changes in runoff (Badger *et al*., *in prep*). In addition, changes in the contribution of terrestrial and marine organic matter to the site during the PETM would have influenced $\delta^{13}C_{TOC}$ values, and caution is therefore required when interpreting the magnitude of the $\delta^{13}C_{TOC}$ change over the PETM.

4.4 Discussion

4.4.1 Carbon burial within the Central Basin

Mass accumulation rates of organic carbon have now been calculated for six separate localities during the PETM, for the NW Atlantic and NE Pacific margins (John *et al*. 2008), and within the Arctic (Sluijs *et al*. 2008a; this chapter). MARs C_{org} from the New Jersey and Californian margins, as well as Site 302-4A on the Lomonosov Ridge, range from 0.02 – 0.18 g cm^{-2} kyr^{-1} (New Jersey: 0.02-0.12 g cm^{-2} kyr^{-1}; California: 0.02-0.06 g

cm^{-2} kyr^{-1} [John *et al*. 2008]; Site 302-4A: 0.18 g cm^{-2} kyr^{-1} [Sluijs *et al*. 2008a]). By comparison, MARs C_{org} for the entire PETM CIE from core BH9/05, Spitsbergen, range from 0.64 to 1.27 g cm^{-2} kyr^{-1} (Table 4.1).

However, direct comparison of MARs from Spitsbergen to those from other localities is complicated by age model uncertainties. John *et al*. (2008) derived MARs from New Jersey and California by correlating the age model of Röhl *et al*. (2000; PETM duration of 220 kyr) to their study sites. The MARs C_{org} from North America (0.02 – 0.12 g cm^{-2} kyr^{-1}) are thus most comparable to those derived using age Option B of Spitsbergen (0.64 ±0.11 g cm^{-2} kyr^{-1}, PETM duration 238 kyr). By contrast, Sluijs *et al*. (2008a) assumed a PETM duration of 170 kyr to calculate C_{org} for Site 302-4A (following Röhl *et al*. 2007), and thus their MARs C_{org} (0.18 g cm^{-2} kyr^{-1}) are comparable to those obtained using age Option A from core BH9/05 (0.87 ±0.14 g cm^{-2} kyr^{-1}). After accounting for age model uncertainties, the MARs C_{org} from Spitsbergen are considerably higher than those calculated from previous studies.

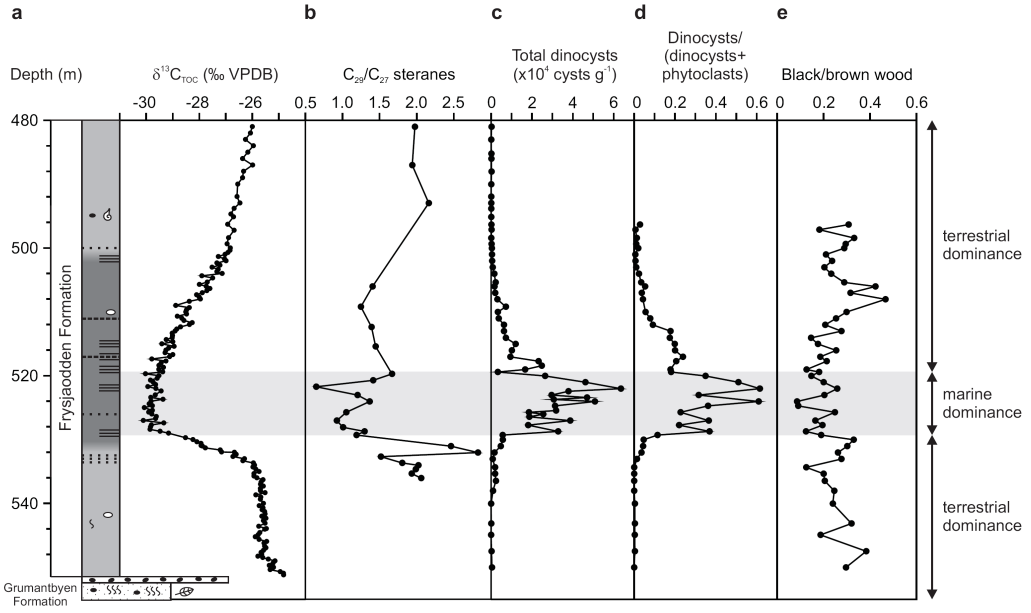

Figure 4.4: Organic matter source variations during the PETM in core BH9/05. **a)** Sedimentary log and $\delta^{13}C_{TOC}$ (‰ VPDB) from Dypvik *et al*. (2011) and Cui *et al*. (2011) respectively. **b)** Ratio of terrestrial (C_{27}) to marine (C_{29}) diasteranes. **c)** Total dinocyst concentration from Chapter 3. **d)** Ratio of dinocysts to phytoclasts (excluding cuticle). **e)** Ratio of opaque (oxidized) to brown (unoxidized) phytoclasts (excluding cuticle).

However, Site 302-4A and the North American localities reside on passive margins (John *et al*. 2008; Sluijs *et al*. 2008a), whereas deposition in Spitsbergen took place in a foreland basin. In Spitsbergen the interval from the PETM onset to top of Chron 24r has a stratigraphic thickness of ~250 m in the Longyearbyen section (Harding *et al*. 2011). Using the estimated ~2 Myr duration of this interval (Westerhold *et al*. 2007) gives minimum background sedimentation rates of ~13 cm/kyr. Thus, a high subsidence, high sedimentation regime in the Spitsbergen Central Basin led to the rapid sequestration of carbon in this foreland basin setting, dwarfing that occurring on the passive margins. Given the total quantity of carbon accumulated would have been on the order of 10s of gigatonnes, the Spitsbergen Central Basin illustrates the potential of small foreland basins to sequester vast quantities of carbon on geologically transient timescales (<240 kyr).

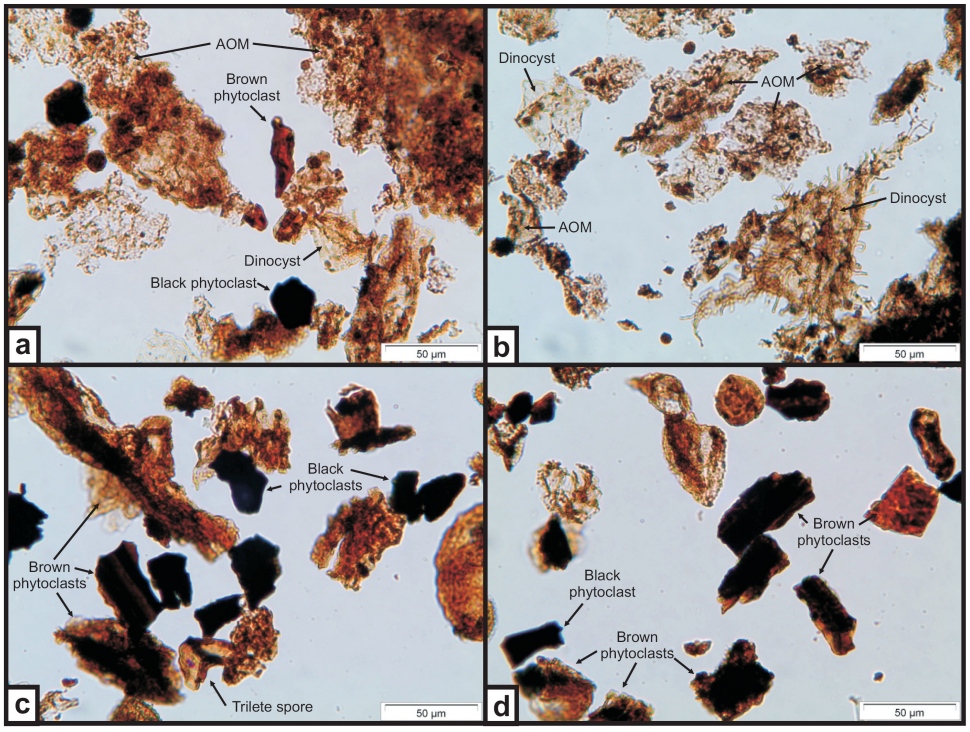

Figure 4.5: Light micrographs of palynological preparations from core BH9/05. **a)** and **b)** represent organic matter from the 'core' interval of the PETM CIE, from depths of 527.75 m and 523.43 m respectively. **c)** and **d)** organic matter assemblages from the pre-PETM interval (543.14 m) and PETM CIE recovery interval (490.03 m) respectively. All micrographs taken at x200 magnification.

4.4.2 Organic matter source variations through the PETM in the Arctic

Preceding the PETM CIE, the low dinocyst:phytoclast values, low abundance of dinocysts and AOM, together with relatively high C_{29}/C_{27} diasterane ratios all indicate a predominance of terrestrial organic matter. Conversely, within the core interval of the CIE, the elevated dinocyst:phytoclast values, high abundance of dinocysts and marine AOM together with low C_{29}/C_{27} diasterane ratios all indicate a switch to assemblages dominated by marine organic carbon. The subsequent decline in dinocyst and AOM abundance and return to high C_{29}/C_{27} diasterane ratios is indicative of a return back to terrestrially-dominated assemblages within the CIE recovery interval. The change from terrestrial- to marine-dominated organic matter within the core of the CIE in core BH9/05 is consistent with previous results from both the Longyearbyen and Bergmanfjellet sections, where elevated dinocyst abundances are documented within the core of the PETM CIE (Harding *et al*. 2011; Chapter 3). Elevated Hydrogen/Carbon ratios and a decline in the relative abundance of terrestrially-derived phytoclasts were also observed in the core of the CIE in the Longyearbyen section (Harding *et al*. 2011). All the above evidence therefore indicates that the switch from predominantly terrestrial to marine organic matter sequestration occurred across the entire Central Basin during the PETM CIE. Furthermore, a decline in the BIT index, together with decreased abundances of terrestrial palynomorphs and Osmundacae spores during the PETM at Site 302-4A (Sluijs *et al*. 2006, 2008a) indicate the switch from terrestrial to marine carbon sequestration was not restricted to the Spitsbergen Central Basin.

The switch in organic carbon composition in both Spitsbergen and Site 302-4A during the PETM was caused by the interaction of a number of different factors. Relative sea level rise at both localities (Sluijs *et al*. 2006, 2008a; Harding *et al*. 2011), would have acted to decrease the flux of terrestrial organic matter transported to the sites of deposition. Furthermore, evidence for enhanced moisture transport to the Arctic (Pagani *et al*. 2006), as well as low-salinity surface waters during the PETM suggest elevated runoff (Sluijs *et al*. 2006, 2008a; Harding *et al*. 2011). Whilst enhanced runoff would have increased the flux of terrestrial organic matter to the sites of deposition, such changes would have been offset by the elevated marine productivity associated with the high nutrient input from enhanced runoff. Evidence for such high productivity surface waters is provided from dinocyst assemblages at both Spitsbergen and Site 302-4A during the PETM (Sluijs *et al*. 2008a; Chapter 3). High surface water productivity would have increased the flux of dinocysts and other organic particles through the water column, whilst increasing biological oxygen demand (BOD). Elevated BOD, together with sea level rise and the warmer Arctic waters during the PETM resulted in sedimentary anoxia in Spitsbergen and euxinia in the photic zone at Site 302-4A (Sluijs *et al*. 2006; Stein *et al*. 2006; Weller and Stein 2008; Chapter 3). Such

low oxygen conditions would have acted to increase the preservation potential of labile marine organic matter, further elevating marine organic carbon burial. Given the switch from terrestrial to marine carbon during the PETM CIE, the net effect of sea level rise, runoff and anoxia in Spitsbergen and Site 302-4A was to increase the fraction of marine to terrestrial carbon buried. As Arctic sea level rise is inferred to be driven by eustatic change (Sluijs *et al*. 2008b; Harding *et al*. 2011), with elevated runoff caused by an enhanced hydrological cycle (Pagani *et al*. 2006; Sluijs *et al*. 2008a), it is probable that both these factors would affect the Arctic region. Given that the driving mechanisms for enhanced marine carbon burial in Spitsbergen and Site 302-4A would probably have acted across the entire Arctic during the PETM, we suggest this switch in organic matter composition may be a pan-Arctic phenomenon in proximal settings.

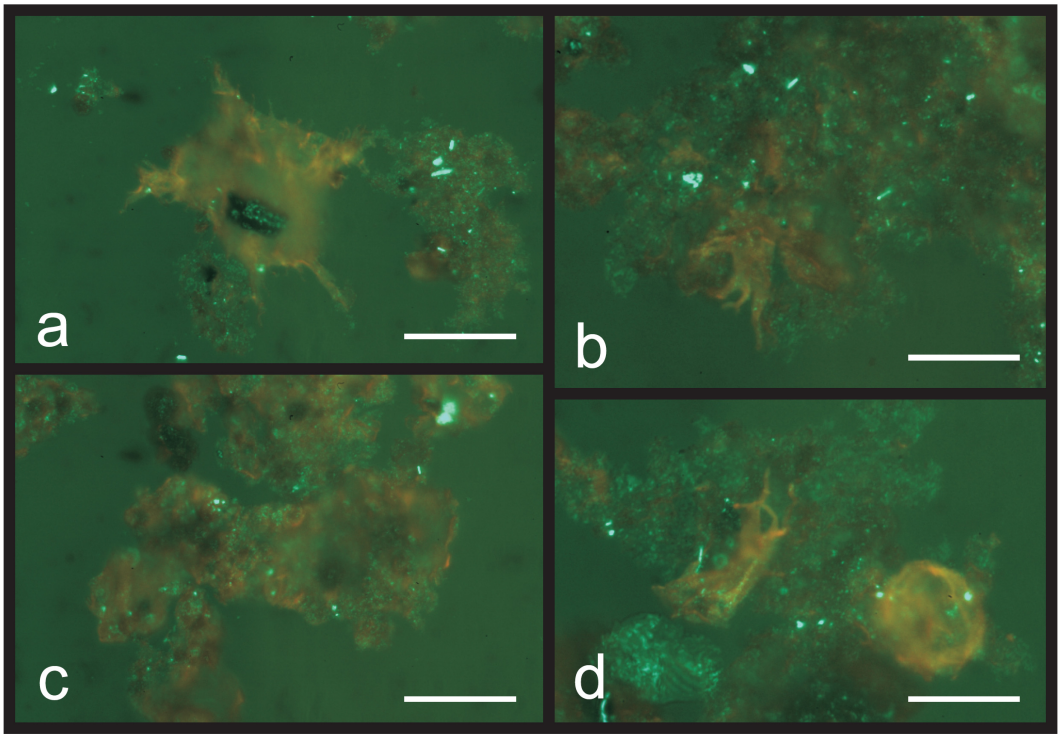

Figure 4.6: Fluorescence micrographs from core BH9/05. **a)** Fluoresence properties of marine algal material as illustrated by *Apectodinium* spp. **b)** and **d)** Fragments of *Apectodinium* spp. as inclusions within Amorphous Organic Matter (AOM). **c)** Fluoresence properties of AOM in the PETM. Note the inclusions of highly-fluorescent material and framboids exhibiting specular scatter (also present within the AOM in panels a, b and d). All micrographs taken at x400 magnification, 527.75 m depth. Scale bar, 50 μm.

4.4.3 The Arctic as a carbon sink during the PETM

Sluijs *et al*. (2008a) estimated that the excess (above background) quantity of organic carbon buried in the Arctic during the PETM was on the order of hundreds of gigatonnes, and the Arctic may have therefore played a significant part in carbon drawdown during the PETM. However the role of the Arctic as a carbon sink is dependant upon the assumption that the excess carbon sequestered was produced within the PETM, and did not consist of reworked organic matter washed into the basin. Within the CIE interval, the PETM dinoflagellate cyst assemblages are present across the Central Basin (with a low percentage of reworked cysts; Chapter 3). Together with the AOM with *Apectodinium* inclusions (Figure 4.6), this indicates the marine organic carbon buried was formed contemporaneously and would have withdrawn carbon directly from the exogenic system. Conversely, the fraction of reworked terrestrial organic carbon is more difficult to quantify, and will consist of a mixture of carbon synthesized during the PETM, and recycled by reworking.

Analysis of both the Spitsbergen PETM localities and Site 302-4A has illustrated that a switch from terrestrial to marine organic carbon deposition occurred in Arctic continental margin settings during the PETM, with a subsequent return to terrestrial-dominated organic carbon assemblages in the recovery interval (Sluijs *et al*. 2006, 2008a; this chapter). Given the regional-scale factors driving this change, this switch in organic matter composition probably affected pan-Arctic continental margin settings (Section 4.4.2). If correct, the burial of predominantly contemporaneous marine organic carbon produced during the CIE in the Arctic implies the excess carbon buried in this interval was not recycled, but withdrawn from the exogenic system. This suggests that within the core interval of the CIE, the Arctic would have been a significant carbon sink during the PETM.

However, within the recovery interval of the PETM CIE, a return to terrestrially dominated organic assemblages occurs in both Spitsbergen and at Site 302-4A (Sluijs *et al*. 2006, 2008a). Given that the transient climatic conditions driving the switch to marine organic carbon composition would have gradually abated on a regional-scale within the CIE recovery, the return to predominantly terrestrial organic carbon assemblages in marginal marine sites may have also been a pan-Arctic phenomenon. The significance of Arctic marginal settings as a carbon sink in the recovery interval of the PETM therefore depends upon the fraction of reworked terrestrial organic carbon, as such material does not involve the removal of carbon from the exogenic system. Unfortunately, the amount of reworking is likely to be highly variable on a spatial scale (owing to the spatial variability of fluvial inputs and the quantity of carbon such systems are reworking from the terrestrial stratigraphy exposed at the time). Assessing

the significance of the Arctic as a carbon sink in the recovery interval therefore requires a spatial resolution of localities not presently available. Despite this, a certain fraction of the terrestrial organic carbon incorporated into the marginal marine settings will have been synthesized in the biosphere during the PETM, transported and buried within marginal marine sites, withdrawing carbon directly from the exogenic system. Thus, current evidence suggests that any excess carbon removed from the exogenic system during the Arctic PETM was drawn down through the marine biosphere in the CIE core interval, with further localities required to assess the potential contribution of organic carbon burial in the recovery.

4.5 Conclusions

Analysis of three localities across the Central Basin of Spitsbergen now constrains the rate, magnitude and composition of carbon burial in this Arctic foreland basin setting during the PETM. Comparison of MARs C_{org} across all three sites indicates a gradient of carbon burial, with the rate and quantity of carbon buried increasing towards the foredeep of the basin. Estimates of the total quantity of carbon buried within the basin during the PETM are on the order of 10s of gigatonnes, consistent with a regime of high subsidence and sedimentation. The magnitude and rates of carbon burial therefore indicate that foreland basins can rapidly sequester large quantities of organic carbon on geologically transient timescales (<240 kyr), even in relatively small basins (~12,000 km^2).

Furthermore, analysis of the organic matter composition from core BH9/05 confirms previous results from the Longyearbyen section that a switch from terrestrially-dominated to marine-dominated organic matter sequestration occurred across the Central Basin during the PETM, and a similar scenario is known at Site 302-4A. This switch in organic carbon composition is the result of the interplay of several factors: elevated runoff in both Spitsbergen and Site 302-4A led to elevated primary productivity, which together with sea level rise and the warmer waters during the PETM, resulted in sedimentary anoxia and a net increase in the amount of marine organic carbon buried. Such transient changes were driven by the enhanced hydrological cycle and eustatic rise at the PETM, which would have affected the entire Arctic region. Given the regional nature of the driving mechanisms, it is probable that continental margin settings across the Arctic were subjected to similar switches in the nature of carbon being buried, resulting in a substantial drawdown of excess carbon from the exogenic system *via* the marine biosphere.

Chapter 5: Discussion, conclusions and future work

A brief discussion of some key questions arising from the work in Chapters 2-4 is given below (Section 5.1), followed by a synthesis of the major conclusions from this study (Section 5.2). Finally, Section 5.3 details how the findings and hypotheses proposed could be tested through further research.

5.1 Key questions

5.1.1 Is the PETM stratigraphically complete in core BH9/05?

Owing to the proximal depositional setting of the material studied in this work, it is pertinent to explore the possibility that unconformities may be present within the PETM CIE of core BH9/05. The onset of the CIE is marked by a pronounced negative shift in $\delta^{13}C$ values on a global scale (e.g. Sluijs *et al*. 2007a). Thus any unconformities within this interval should be manifested as steps in the $\delta^{13}C$ curve. For example, this type of step-like response is observed in the deep water records of the Walvis Ridge PETM owing to carbonate dissolution at the onset of the CIE (e.g. Zachos *et al*. 2005; McCarren *et al*. 2008). In Spitsbergen, we have recorded multiple transitional values to the most negative $\delta^{13}C$ values after the onset of the CIE onset in core BH9/05. This suggests that if unconformities are present within the CIE onset, they are stratigraphically restricted to intervals below the resolution of the $\delta^{13}C_{TOC}$ record, i.e. <30 cm. It is currently not possible to determine the presence of such small-scale unconformities, but note that such phenomena would lengthen the duration of the CIE onset, further lowering the carbon injection rates derived by Cui *et al*. (2011, Appendix 5).

Within the core of the PETM CIE in BH9/05 there is a notable transition to darker laminated mudstones with elevated concentrations of pyrite (Riber 2009; Dypvik *et al*. 2011; Chapters 3 and 4). The inferred development of water column stratification during the core of the PETM CIE in Spitsbergen (Harding *et al*. 2011; Chapter 3), together with sea level rise and the warmer waters during the PETM (Sluijs *et al*. 2006) resulted in anoxic conditions within the sediment (Chapter 3). A decline in diversity is also observed in agglutinated foraminiferal assemblages in core BH9/05, consistent with low bottom water oxygen (Nagy *pers comm*. 2011). Thus, rather than the erosive tractional currents required to generate unconformities on a scale that could bias

cyclostratigraphic interpretations, the site of deposition demonstrates evidence for low bottom water oxygen conditions and thus low bottom water current velocities (a non-depositional hiatus is extremely unlikely in this foreland basin setting). Conversely, in the recovery interval of the BH9/05 PETM CIE, indicators of anoxia within the sediment decline. Thus, it is currently not possible to rule out the presence of small-scale unconformities within this interval, although no sedimentological indicators support such a contention.

5.1.2 Was the BH9/05 time-series altered by short-lived changes in sedimentation rate, or overprinting from a non-orbital influence?

Comparison of Fe/Mn records from core BH9/05 with TOC (%) time-series records from the Longyearbyen section (Harding *et al*. 2011) has illustrated that the same cycles are present at both sites, indicating the cycles in the time-series are not result of stochastic noise or site-specific processes (Chapter 2). However, the BH9/05 time-series record the presence of three additional cycles within the PETM interval, compared to the Röhl *et al*. (2007) age model. If these cycles are interpreted as precession cycles, then the duration of the PETM is consistent with that proposed by Murphy *et al*. (2010).

It is thus necessary to explore the possibility that rapid changes in sedimentation rate, or non-orbital influences altered the time-series records, producing additional cycles. Cycle frequencies from 4-6 m are present in the Fe/Mn time-series records from core BH9/05, which are interpreted as precession cycles (Chapter 2). Analysis of the time-series illustrates that ~5 m cycles are predominant in the interval from 530.42-498.95 m, whereas ~4 m cycles predominate in the interval 498.95-485.75 m (Figure 5.1), as illustrated in the wavelet spectra from these records (Figure 2.4). Thus the range of cycle frequencies for the inferred precession cycles (excluding those marked with an asterisk) can be explained by a small change in sedimentation rate at ~500 m, with more condensed sedimentation in recovery phase II of the PETM. The consistent cycle thickness within these two respective intervals (Figure 5.1) is consistent with quasi-periodic changes in insolation associated with orbital forcing (excluding the cycles marked with an asterisk). Recent age models constraining the duration of the CIE (Röhl *et al*. 2007; Murphy *et al*. 2010) suggest the 4-6 m and 20 m cycles are derived from precession and eccentricity forcing respectively, consistent with the cycle ratio observed between these two components (Chapter 2).

Conversely, the three ~2 m low amplitude cycles marked with an asterisk are stratigraphically thinner than the 4-6 m cycles discussed above (Figure 5.1). The difference in cycle thickness may suggest these three cycles have a different

derivation, such as non-orbital influences on the time-series. Alternatively, intervals of relatively condensed sedimentation could also result in precession cycles with a reduced stratigraphic thickness. The ambiguous origin of these cycles therefore substantiates the need for two different cyclostratigraphic age options (Chapter 2), to account for this uncertainty.

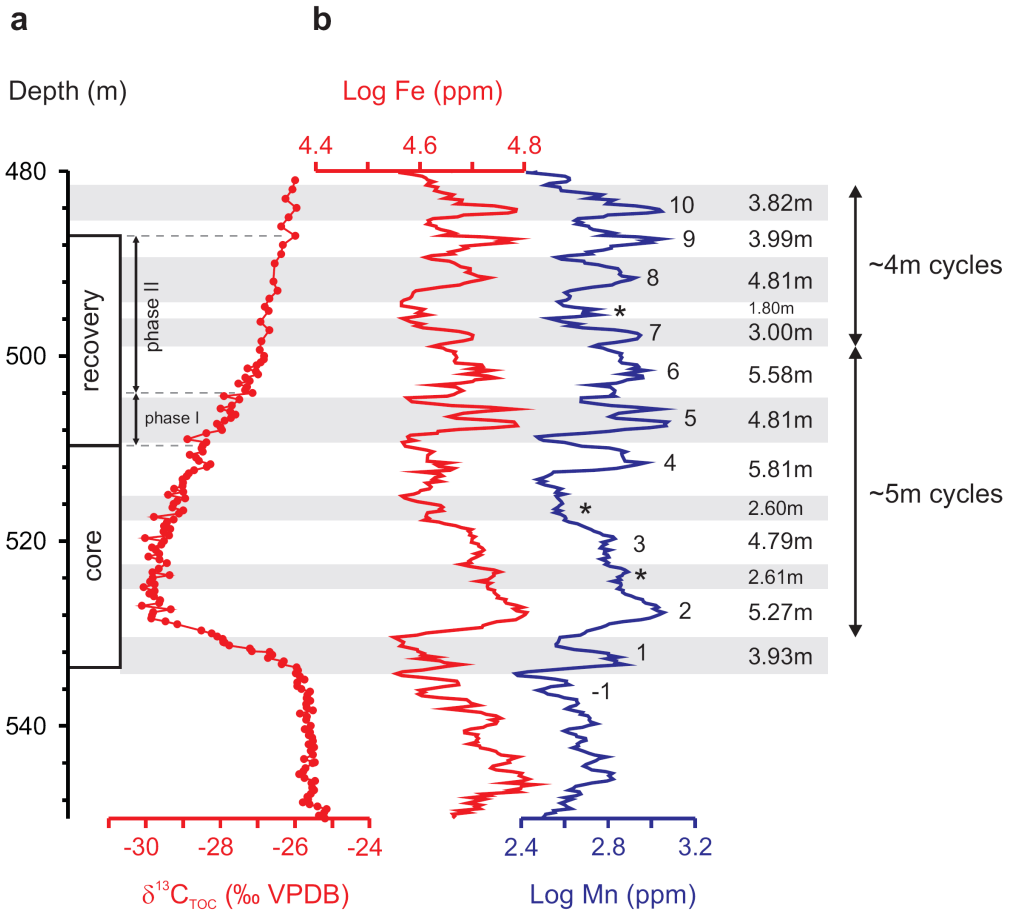

Figure 5.1: Stratigraphic thickness of inferred precession cycles from core BH9/05 during the PETM interval. **a)** $\delta^{13}C_{TOC}$ (Cui *et al.* 2011) showing phases of the PETM CIE as defined by Röhl *et al.* (2007). **b)** Log Fe and Mn time-series, illustrating the stratigraphic thickness of inferred precession cycles. Cycle numbers are after Röhl *et al.* (2007), with potential additional precession cycles labeled with an asterisk (see Chapter 2 for details).

5.1.3 How does the stratigraphic thickness of the PETM interval relate to fluvial runoff?

During the PETM interval in Spitsbergen, increased terrestrial runoff is inferred to have resulted in low salinity surface waters, leading to elevated abundances of the dinoflagellate cyst taxon *Senegalinium* spp. (Chapter 3). Abundances of *Senegalinium* decline from the northeast (Longyearbyen section) to the southwest (Bergmanfjellet),

suggesting the declining influence of fluvial runoff from a northeastern source (Chapter 3). However, whilst the influence of runoff is inferred to have declined towards the southwest, the stratigraphic thickness of the PETM CIE increases in the same direction. It might be expected that the stratigraphic thickness of the PETM interval should decline with the waning influence of runoff as sedimentation becomes more condensed, in a way similar to other passive margin settings such as the New Jersey margin (e.g. John *et al*. 2008). The apparent increase in stratigraphic thickness with the declining influence of runoff in Spitsbergen therefore appears paradoxical.

However, the Spitsbergen Central Basin is a foreland basin, with the uplift of the West Spitsbergen Orogenic Belt being contemporary with the deposition of the PETM sediments (Kellogg 1975; Steel *et al*. 1981; 1985; Müller and Spielhagen 1990; Harland 1997). Palaeocurrent directions and the eastern pinch-out of sandstone units indicate a western sediment source for the late Palaeocene-early Eocene sediments, consistent with a clastic sediment supply derived from the orogenic belt at this time (Kellogg 1975; Steel *et al*. 1981; Helland-Hansen 1990; Dallmann *et al*. 1999). Furthermore, the stratigraphic thickness of the Frysjaodden Formation containing the PETM thickens westward (Kellogg 1975; Helland-Hansen 1990; Dallmann 1999), indicating the sediment shed from the orogenic belt was the primary control on stratigraphic thickness at this time. Thus the increasing stratigraphic thickness of the CIE towards the west can be explained by the increasing proximity of the depositional localities to the clastic sediment supply from the growing West Spitsbergen Orogenic Belt (Figure 5.2).

In addition, however, erratic clasts including pebbles of diabase dolerite and granite were also deposited within the Frysjaodden Formation (Birkenmajer and Narebski 1963; Birkenmajer *et al*. 1972). The present day exposures of these lithologies illustrate that they were derived from a north or northeastern source area (Birkenmajer *et al*. 1972). Together with dinocyst evidence for fluvial input from the northeast (Chapter 3), this suggests the presence of two sources of runoff into the Central Basin during deposition (Figure 5.2). The increasing stratigraphic thickness of the PETM CIE toward the west suggests that the clastic sediment supply from the orogenic belt dwarfed sediment supply from the northeastern fluvial source, leading to the expanded CIE towards the west. Whilst the Bergmanjellet section lies adjacent to the West Spitsbergen Orogenic Belt today, it is believed that the orogenic belt was on the order of 20 km further to the west during the Paleogene (Steel *et al*. 1985). Thus, the Bergmanfjellet section would have been relatively distal to the freshwater input from the western margin of the basin, leading to the lower abundances of low-salinity tolerant dinocysts observed at this site.

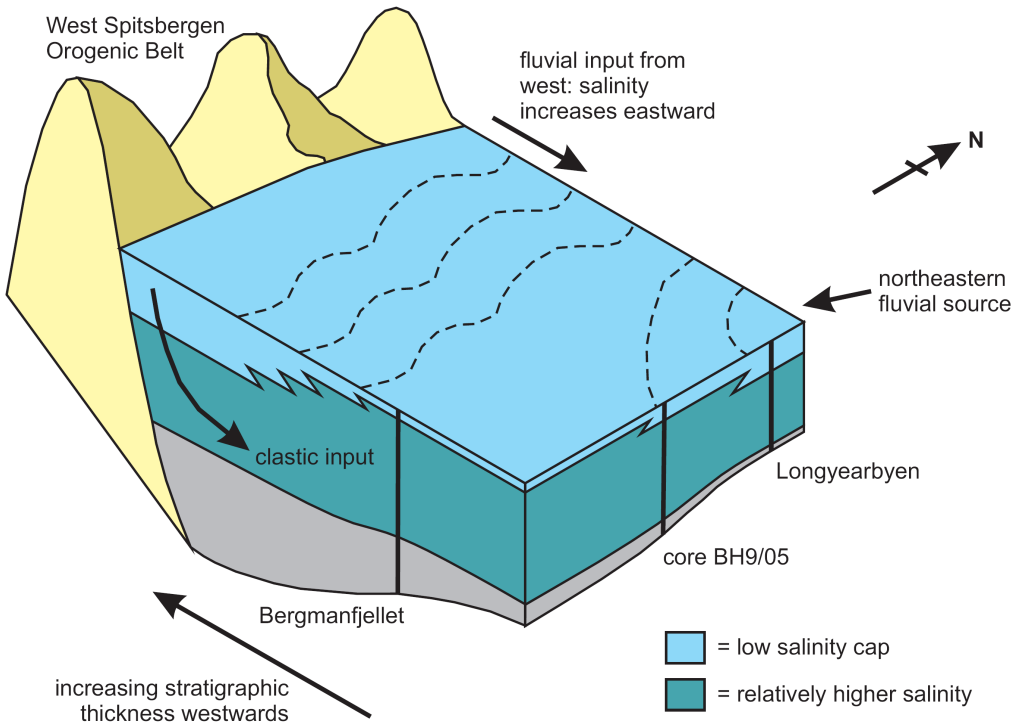

Figure 5.2: Schematic representation of the palaeoceanographic regime in Spitsbergen during the PETM, resulting in the declining influence of freshwater runoff from northeast to southwest, and yet increasing stratigraphic thickness in the same direction.

Given the position of the Longyearbyen section and core BH9/05 on the eastern margin of the basin, it is therefore likely that these sites were predominantly influenced by the freshwater influx from the northeastern fluvial source, whilst stratigraphic thickness was controlled primarily from sediment supplied from the west (Figure 5.2). Such a scenario can therefore account for the declining influence of salinity from northeast to southwest, and increasing stratigraphic thickness of the CIE observed in the Spitsbergen localities.

5.2 Synthesis of major conclusions

5.2.1 Links between Arctic hydrology, the marine biosphere and carbon burial

Arctic PETM localities have now been documented from the Lomonosov Ridge (IODP Site 302-4A: e.g. Backman *et al*. 2006; Moran *et al*. 2006) and from Spitsbergen (Harding *et al*. 2011; Cui *et al*. 2011; this study). Despite the different depositional settings of these localities (Site 302-4A: passive margin; Spitsbergen: foreland basin),

each provides evidence supporting relative sea level rise, low-salinity surface waters, and decreased oxygenation (Table 5.1). The following sequence of events illustrating how the PETM developed in the Arctic is consistent with the evidence provided by all of the localities studied.

5.2.1.1 Arctic sea level rise

Several lines of evidence suggest sea level rise in the Arctic region (Table 5.1). A pre-PETM change from terrestrial- to marine-influenced deposition in the Longyearbyen section (Spitsbergen) suggests that sea level rise preceded the onset of the CIE (Harding *et al*. 2011, Appendix 1). At all three Spitsbergen localities, the highest abundance of marine dinocysts indicates maximum flooding around the peak of the CIE (Harding *et al*. 2011; Chapter 3, Appendix 3). Elevated sea surface temperatures at Site 302-4A (Sluijs *et al*. 2006) indicate that Arctic sea level rise may have been (at least in part) driven by the thermal expansion of seawater, although melting of small-scale Antarctic alpine glaciers and/or changes in basin volume (associated with the North Atlantic Igneous province) may also have contributed (Sluijs *et al*. 2008b).

5.2.1.2 Enhanced hydrology, runoff and stratification

An enhanced deuterium flux to Site 302-4A has been used as evidence for elevated moisture transport to the Arctic, which would in turn result in increased precipitation (Pagani *et al*. 2006). Such elevated precipitation would have resulted in high runoff in continental margin settings such as the Spitsbergen Central Basin and Site 302-4A (e.g. Sluijs *et al*. 2008a; Weller and Stein 2008; Chapter 3), leading to low salinity, nutrient-rich surface waters (Table 5.1). This in turn resulted in a stratified water column, enabling the proliferation of freshwater tolerant dinoflagellates such as *Senegalinium* spp. in a surficial low salinity lens, with genera typically associated with open marine conditions inhabiting higher salinity waters below (Chapter 3). The pronounced acme in *Senegalinium* has been shown to lag the CIE onset by 23-60 kyr (a value incorporating total age model uncertainty), which indicates that maximum freshwater input and stratification lagged the CIE onset, at least in Spitsbergen (Chapter 3).

5.2.1.3 Anoxia, productivity and carbon burial

Warmer Arctic waters (Sluijs *et al*. 2006) and salinity stratification during the Arctic PETM drove a decline in oxygen levels, leading to sedimentary anoxia in Spitsbergen (Harding *et al*. 2011; Chapter 3) and photic zone euxinia at Site 302-4A (Sluijs *et al*. 2006; Stein *et al*. 2006; Weller and Stein 2008). Anoxia, sea level rise, and the enhanced marine productivity driven by high runoff (Table 5.1), resulted in a net increase in the fraction of marine carbon being buried in the Arctic during the PETM

Table 5.1: Evidence for palaeoceanographic changes in the Arctic region during the PETM

Change during PETM	Spitsbergen		Site 302-4A	
	Evidence	**References**	**Evidence**	**References**
Relative sea level rise	Longyearbyen: change from terrestrial to marine deposition, decreased quartz abundance, elevated H/C ratios. Elevated abundance of marine dinocysts at all sites. BH9/05: decline in C_{29}/C_{27} diasterane ratio and rise in dinocyst:wood ratio	Harding *et al*. (2011); Chapters 3 and 4	Decline in BIT index, and relative percentage of terrestrial palynomorphs and Osmundacae spores. Increased abundance of marine dinocysts, marine biomarkers, and aquatic organic matter. Elevated HI values.	Sluijs *et al*. (2006, 2008a); Weller and Stein (2008); Boucsein and Stein (2009).
Elevated sea surface temperatures	-	-	TEX_{86}' palaeotemperature proxy	Sluijs *et al*. (2006)
Enhanced moisture transport	-	-	Enhanced deuterium flux	Pagani *et al*. (2006)
Increased runoff	Increased concentration of terrestrial n-alkanes (with odd chain lengths $>C_{24}$) during the PETM	Cui (2010)	Elevated concentrations of terrestrial palynomorphs – despite increased dilution from elevated sedimentation rates. Maximum terrestrial n-alkane concentrations	Sluijs *et al*. (2008a); Weller and Stein (2008)
High productivity	Predominance of peridinioid dinocysts at all three sites – including presence of presumed high-nutrient taxon *Apectodinium*	Harding *et al*. (2011); Chapter 3	Predominance of peridinioid dinocysts – including presence of high presumed high-nutrient taxon *Apectodinium*	Sluijs *et al*. (2006, 2008a)
Low salinity surface waters	*Senegalinium* acme at all three sites	Harding *et al*. (2011); Chapter 3	*Senegalinium* acme. $\delta^{18}O$ and $^{87}Sr/^{86}Sr$ analysis of fish bones indicate low salinities, but may not represent the full extent of freshening due to the uncertain depth habitat of the specimens.	Sluijs *et al*. (2006, 2008a); Waddell and Moore (2008); Gleason *et al*. (2009)
Low oxygen conditions	Laminated sediments and elevated pyrite content across the basin.	Riber (2009); Dypvik *et al*. (2011); Harding *et al*. (2011); Chapter 3	Laminated sediments and absence of foraminiferal test linings. Elevated TOC concentrations. Presence of the bacterial biomarker isorenieratane and abundant <5 μm pyrite framboids. C/S ratios <1. Elevated concentrations of S and redox sensitive elements indicated by XRF.	Sluijs *et al*. (2006, 2008a); Stein *et al*. (2006); Weller and Stein (2008); Boucsein and Stein (2009); März *et al*. (2010)

(Chapter 4). The predominance of marine carbon burial within the PETM CIE implies that the sequestered carbon was synthesized during the PETM and would have thus drawn down carbon directly from the exogenic system, implying that the Arctic would have been a significant carbon sink during the PETM (Chapter 4).

5.2.2 Constraints on the numerical age and trigger mechanism for the PETM

Combining radio-isotopic dating of one of the bentonite layers within the Spitsbergen PETM CIE together with cyclostratigraphic analysis of Fe and Mn time-series, has constrained the numerical age of the Palaeocene-Eocene boundary (onset PETM CIE) to between 55.728-55.964 Ma (Chapter 2, Appendix 2), consistent with the recently proposed astronomical age of 55.93 Ma (Option 2 of Westerhold *et al*. 2007, 2008). The numerical age of the boundary has to fall on one of the astronomical age options of Westerhold *et al*. (2007, 2008), in order to maintain the phase relationship between records of the 405 kyr cycle extracted from ODP Site 1262 (ODP Leg 208 Walvis Ridge) and the same component of the astronomical solutions (Laskar *et al*. 2004). Thus, these findings substantiate an age of 55.93 Ma (Option 2 of Westerhold *et al*. 2007, 2008) for the Palaeocene-Eocene boundary, equivalent to the onset age of the PETM CIE. When compared to the orbital solution of Laskar *et al*. (2004) this indicates the onset of the CIE occurred on the falling limb of 405 kyr eccentricity cycle. Given that other early Eocene hyperthermals are consistently found on eccentricity peaks or the rising limb of such cycles (Westerhold *et al*. 2007; Westerhold and Röhl 2009; Zachos *et al*. 2010; Sexton *et al*. 2011), this suggests the PETM was driven by a different trigger mechanism when compared to the other hyperthermals.

5.3 Further research

5.3.1 Testing the numerical age of the Palaeocene-Eocene boundary

The combined radio-isotopic and cyclostratigraphic analysis of the PETM in Spitsbergen has permitted the derivation of a precise age estimate for the Palaeocene-Eocene boundary (Chapter 2). Further research should aim to test the proposed age range for the boundary by combining radio-isotopic and cyclostratigraphic methodologies. This could be achieved by the radio-isotopic dating of ash layers within other sedimentary successions, and then ascertaining the duration between a given ash layer and the onset of the PETM CIE (e.g. Westerhold *et al*. 2009). Given that the errors associated with $^{40}Ar/^{39}Ar$ radioisotopic dating are currently ~1 % (e.g. Renne *et al*. 1998; 2010; Kuiper *et al*. 2008; Channell *et al*. 2010), U-Pb dating of ash layers is required for this purpose in order to accurately assess the age of Paleocene-Eocene boundary.

5.3.2 Towards a robust age model for the PETM

In Chapter 2, cyclostratigraphic analysis of Fe and Mn time-series from core BH9/05 has yielded two possible age model options for the PETM interval. Option A adheres to the cyclostratigraphic age model proposed by Röhl *et al*. (2007), with Option B consistent with the extraterrestrial ^{3}He age model of Murphy *et al*. (2010). However, precession cycles 1-3 in age model Option A correspond to one 100 kyr eccentricity cycle. Given that 4-6 precession cycles should be present for every one short eccentricity cycle, it is difficult to reconcile these two orbital components using this age option. The potential presence of three additional precession cycles (relative to Option A) in the PETM interval using age model Option B results in a 1:5 short eccentricity to precession cycle ratio, consistent with orbital cycle ratios (Pälike 2005). However, the additional cycles recognized are stratigraphically thinner (~2 m) than the other inferred precession cycles in core BH9/05 (~4-6 m; Figure 5.1). This change in stratigraphic thickness could be caused either by intervals of relatively condensed sedimentation or from non-orbital influences on the time-series.

Thus, given the ambiguous origin of these cycles, cyclostratigraphic analysis of further localities is required in order to test for their presence in other settings. Although it is notable that several cyclostratigraphic studies have been carried out in bathyal settings (Norris and Röhl 1999; Röhl *et al*. 2000, 2007), constructing PETM age models in such localities is complicated by the effects of carbonate dissolution associated with the shoaling of the carbonate compensation depth (Zachos *et al*. 2005; McCarren *et al*. 2008), as well the pronounced change to condensed sedimentation (Farley and Eltgroth 2003; Röhl *et al*. 2007; Murphy *et al*. 2010), making cycle identification subjective. Thus the additional cycles found within core BH9/05 may not be present in such settings owing to a hiatus at the base of the CIE in such localities. However, previous studies on the duration of the PETM CIE have focused on Atlantic and Southern Ocean sites (Norris and Röhl 1999; Röhl *et al*. 2000, 2007; Farley and Eltgroth 2003; Murphy *et al*. 2010), where carbonate dissolution is most intense (Zachos *et al*. 2005; Zeebe and Zachos 2007; McCarren *et al*. 2008). Pacific localities are stratigraphically more complete and thus more suitable for age model construction, but also show a decline in carbonate content, and may therefore be subject to the same problems (e.g. Zachos *et al*. 2003). Analysis in neritic-upper bathyal settings is complicated by elevated sedimentation rates in passive margin locations (John *et al*. 2008; Sluijs *et al*. 2008a), which would alter the stratigraphic thickness of orbitally-derived cycles, thus potentially hindering their identification. Furthermore, erosional unconformities are often present in such successions, and typically truncate the PETM recovery interval (e.g. New Jersey and California: John *et al*. 2008; Tanzania: Handley *et al*. 2008; Kumaru section, New Zealand: Sluijs *et al*. 2008b; Woensdrecht, the Netherlands: Sluijs

et al. 2008b). Given that cyclostratigraphy in terrestrial settings is also potentially complicated by intervals of non-deposition, erosion and autocyclic fluvial avulsion, constructing age models for the PETM in any setting is highly problematic owing to the perturbation of the entire exogenic system. These problems can (in part) therefore explain the array of durations proposed for the PETM (also see Murphy *et al*. 2010, for the discrepancies between ^{3}He and cyclostratigraphic age models).

One approach to minimize the error associated with the duration of the PETM CIE may therefore be to integrate all the age models so far generated to minimize the problems associated with each geographic setting and the methodologies used to derive each age model. However, this approach is also complicated as the records would require correlation *via* carbon isotopic records derived from different proxies in disparate settings. Given that the fractionation effects, sedimentary processes and lag times would differentially alter the various proxies recording carbon cycle perturbation, matching isotopic records between the different sites could result in an erroneous correlation. Thus, in order to move towards a more robust age model for the duration of the PETM CIE, age models for the duration of the CIE must be integrated with long-term (Myr timescale) records from the deep sea (e.g. Westerhold *et al*. 2007; Zachos *et al*. 2010). Such records can indirectly constrain the CIE duration through correlation of the 405 kyr component of orbital forcing extracted from geological records to those from astronomical solutions. Whilst this has already been achieved from Site 1262 (Westerhold *et al*. 2007), replicating this methodology at other localities would mitigate against the effects of carbonate dissolution at Site 1262, and lead to a more robust indirect estimate for the CIE duration.

5.3.3 Testing Arctic PETM Hypotheses

This study of three highly expanded PETM successions in Spitsbergen has generated high-resolution records of the event across a second Arctic setting. Thus, whilst the Spitsbergen sites have provided a wealth of data on the PETM in the high Arctic, it is notable that the event is still only documented from two widely geographically separated localities in the region. Further Arctic PETM localities are therefore required in order to test several hypotheses proposed for the region. A brief summary of the key hypotheses requiring testing is listed below.

5.3.3.1 Hypothesis 1: Summer sea surface temperatures were subtropical (>20°C) in the Arctic during the PETM

Robust quantification of sea surface temperatures in the Arctic region is essential, as such temperatures represent an end member scenario for meridional sea surface temperature gradients, and thus are required to constrain global climate models for

the PETM (Sluijs *et al*. 2008a). To date, sea surface temperatures are only constrained from Site 302-4A using the TEX_{86}' palaeotemperature proxy (Sluijs *et al*. 2006; note that TEX_{86}' differs from TEX_{86} in that isomer GDGT-3 is not included within the temperature calibration). Unfortunately, the thermal maturity of samples from Spitsbergen prevents both TEX_{86} and hydrogen isotopic analysis at this second Arctic locality. Given that temperatures are only derived from one proxy in one nearshore locality across the region, it is difficult to assess how representative these temperature values are for the Arctic. Furthermore, the summer-biased ~23°C temperature obtained from this site during the PETM (Sluijs *et al*. 2006) was obtained using the TEX_{86}' calibration (Sluijs *et al*. 2006). Since the latter study additional calibrations for the TEX_{86} proxy have been proposed (Kim *et al*. 2008, 2010; Liu *et al*. 2009), and analysis of similar samples has indicated results vary by ±3-4°C between laboratories (Schouten *et al*. 2009). Thus derivation of further sea surface temperature data from other Arctic localities is required to test the hypothesis that Arctic sea surface temperatures were >20°C during the PETM.

5.3.3.2 Hypothesis 2: An enhanced hydrological cycle resulted in increased moisture transport to the Arctic region during the PETM CIE, with peak hydrological forcing potentially lagging the onset of carbon injection by 23-60 kyr

In a similar way to sea surface temperature data, hydrogen isotope data have to date only been generated from Site 302-4A (Pagani *et al*. 2006). An enhanced hydrological cycle would be expected during the PETM owing to the global increase in temperatures (Pagani *et al*. 2006), with evidence for enhanced weathering and precipitation supporting such a contention (Ravizza *et al*. 2001; Schmitz and Pujalte 2007). Given that an enhanced hydrological cycle should elevate the flux of deuterium to the high latitudes (Pagani *et al*. 2006), study of hydrogen isotopes from the PETM interval in high northern latitudes could illustrate how the hydrological cycle responds to transient warming. However, whilst the enhanced deuterium flux to Site 302-4A illustrates the intensification of the hydrological cycle at the PETM (Pagani *et al*. 2006), gaps in the core recovered at this site prevent the recognition of potential temporal changes in hydrological intensity. Thus, hydrogen isotopic analysis of another highly expanded Arctic PETM locality could confirm the leads and lags between carbon injection, temperature and hydrology suggested by the results from Spitsbergen described here.

5.3.3.3 Hypothesis 3: Sea level rise and enhanced hydrology drove elevated marine productivity, a decline in oxygen levels and a switch from terrestrial to marine carbon burial in Arctic marginal marine settings

Whilst results from both Spitsbergen and Site 302-4A have provided evidence for coeval sea level rise, elevated moisture transport and increased marine carbon burial (Table 5.1), an increased spatial coverage of Arctic PETM localities is required to test the hypothesis that the Arctic was a site of elevated carbon fixing and sequestration. This scenario can be tested by employing the same methodologies used in this study at other sites. The combination of palynological, sedimentological and geochemical studies across additional sites will therefore further constrain conditions in the Arctic during the PETM, providing important limits on meridional moisture and temperature gradients to feed into and enhance global climate models.

References

Abdul Aziz, H., F.J. Hilgen, G.M. Van Luijk, A. Sluijs, M.J. Kraus, J.M. Pares, and P.D. Gingerich (2008), Astronomical climate control on the paleosol stacking patterns in the upper Paleocene-lower Eocene Willwood Formation, Bighorn Basin, Wyoming, *Geology*, *36*, 531-534.

Agnini, C., P. Macri, J. Backman, H. Brinkhuis, E. Fornaciari, L. Giusberti, V. Luciani, D. Rio, A. Sluijs, and F. Speranza (2009), An early Eocene carbon cycle perturbation at ~52.5 Ma in the Southern Alps: Chronology and biotic response, *Paleoceanography*, *24*, doi:10.1029/2008PA001649.

Backman, J., K. Moran, and D.B. McInroy, L.A. Mayer, and the Expedition 302 Scientists (2006), Arctic coring expedition (ACEX), *Proc. Integrated Ocean Drill. Program*, 302, doi:10.2204/iodp.proc.302.2006.

Bailey, R.J. (2009), Cyclostratigraphic reasoning and orbital time calibration, *Terra Nova*, *21*, 340-351.

Bains, S., R.M. Corfield, and R.D. Norris (1999), Mechanisms of climate warming at the end of the Paleocene, *Science*, *285*, 724-727.

Beerling, D.J., Increased terrestrial carbon storage across the Palaeocene-Eocene boundary, *Paleogeog., Paleoclim., Paleoecol.*, *161*, 395-405.

Benninghoff, W.S. (1962), Calculation of pollen and spores density in sediments by addition of exotic pollen in known quantities, *Pollen et Spores*, *4*, 332-333.

Bice, K.L., and J. Marotzke (2002), Could changing ocean circulation have destabilized methane hydrate at the Paleocene/Eocene boundary? *Paleoceanography*, *17*, doi:10.1029/2001PA000678.

Bijl, P.K., S. Schouten, A. Sluijs, G-J. Reichart, J.C. Zachos, and H. Brinkhuis (2009), Early Palaeogene temperature evolution of the southwest Pacific Ocean, *Nature*, *461*, 776-779.

Bijl, P.K., A.J.P. Houben, S. Schouten, S.M. Bohaty, A. Sluijs, G.-J. Reichart, J.S. Sinninghe Damsté, and H. Brinkhuis (2010), Transient middle Eocene atmospheric CO_2 and temperature variations, *Science*, *330*, 819-821.

Birkenmajer, K., and W. Narebski (1963), Dolerite drift blocks in marine Tertiary of Sorkapp Land and some remarks on the geology of the eastern part of this area, *Norsk Polarinstitutt Årbok 1962*, 68-79.

Birkenmajer, K., J. Fedorowski, and W. Smulikowski (1972), Igneous and fossiliferous sedimentary drift pebbles in the marine Tertiary of Torell Land, Spitsbergen, *Norsk Polarinstitutt Årbok 1970*, 146-164.

Blythe, A.E., and K.L. Kleinspehn (1998), Tectonically versus climatically driven Cenozoic exhumation of the Eurasian plate margin, Svalbard: Fisson track analyses, *Tectonics*, *17*, 621-639.

Boé, J., A. Hall, and X. Qu (2009), September sea-ice cover in the Arctic Ocean projected to vanish by 2100, *Nature Geoscience*, *2*, 341-343.

Bolle, M.P., A. Pardo, K.U. Hinrichs, T. Adatte, K. Von Salis, S. Burns, G. Keller, and N. Muzylev (2000), The Paleocene-Eocene transition in the marginal northeastern Tethys (Kazakhstan and Uzbekistan), *Int. J. Earth Sci.*, *89*, 390-414.

Boucsein, B., and R. Stein (2009), Black shale formation in the late Paleocene/early Eocene Arctic Ocean and paleoenvironmental conditions: New results from a detailed organic petrological study, *Mar. Pet. Geol.*, *26*, 416-426.

Bowen, G.J., and J.C. Zachos (2010), Rapid carbon sequestration at the termination of the Paleocene-Eocene thermal maximum, *Nat. Geosci.*, *3*, 866-869.

Bowen, G.J., D.J. Beerling, P.L. Koch, J.C. Zachos, and T. Quattlebaum (2004), A humid climate state during the Palaeocene/Eocene thermal maximum, *Nature, 432*, 495-499.

Bowen, G.J., P.L. Koch, P.D. Gingerich, R.D. Norris, S. Bains, and R.M. Corfield, (2001), Refined isotope stratigraphy across the continental Paleocene–Eocene boundary on Polecat Bench in the Northern Bighorn Basin, in *Paleocene–Eocene Stratigraphy and Biotic Change in the Bighorn and Clarks Fork Basins, Wyoming, Univ. Michigan Papers on Paleontology*, *33*, edited by P.D. Gingerich, pp. 73-88.

Bown, P., and P. Pearson (2009), Calcareous plankton evolution and the Paleocene/Eocene thermal maximum event: New evidence from Tanzania, *Mar. Micropaleontol.*, *71*, 60-70.

Bralower, T.J. (2002), Evidence for surface water oligotrophy during the Paleocene-Eocene thermal maximum: nannofossil assemblage data from Ocean Drilling

Program Site 690, Maud Rise, Weddell Sea, *Paleoceanography*, *17*, doi:10.1029/2001PA000662.

Bralower, T.J., D.J. Thomas, J.C. Zachos, M.M. Hirschmann, U. Röhl, H. Sigurdsson, E. Thomas, and D.L. Whitney (1997), High resolution records of the late Paleocene thermal maximum and circum-Caribbean volcanism: Is there a causal link? *Geology*, *25*, 963-966.

Brinkhuis, H. (1994), Late Eocene to Early Oligocene dinoflagellate cysts from the Priabonian type-area (Northeast Italy); biostratigraphy and palaeoenvironmental interpretation, *Paleogeog., Paleoclim., Paleoecol.*, *107*, 121–163.

Brinkhuis, H., A.J. Powell, and D. Zevenboom (1992), High-resolution dinoflagellate cyst stratigraphy of the Oligocene/Miocene transition interval in north-west and central Italy, in *Neogene and Quaternary Dinoflagellate Cysts and Acritarchs*, edited by M.J. Head, and J.H. Wrenn, pp. 219-258, Am. Assoc. Stratigr. Palynol. Found., Dallas.

Brinkhuis, H., A.J.T. Romein, J. Smit, and W.J. Zachariasse (1994), Danian-Selandian dinoflagellate cysts from lower latitudes with special reference to the El Kef section, NW Tunisia, *Geol. Fören. Stockholm Förh.*, *116*, 46-48.

Bruhn, R., and R. Steel (2003), High-resolution sequence stratigraphy of a clastic foredeep succession (Paleocene, Spitsbergen): An example of peripheral-bulge-controlled depositional architecture, *J. Sediment. Res.*, *73*, 745-755.

Bujak, J., and H. Brinkhuis (1998), Global warming and dinocyst changes across the Palaeocene/Eocene epoch boundary, in *Late Palaeocene-Early Eocene Biotic and Climatic Events in Marine and Terrestrial Records*, edited by M.-P. Aubry, S.G. Lucas, and W.A. Berggren, pp. 277-295, Columbia University Press, New York.

Channell, J.E.T., D.A. Hodell, B.S. Singer, and C. Xuan (2010), Reconciling astrochronological and $^{40}Ar/^{39}Ar$ ages for the Matuyama-Brunhes boundary and late Matuyama Chron. *Geochem. Geophys. Geosyst.*, *11*, doi: 10.1029/2010GC003203.

Chun, C.O.J., Delaney, M.L., and J.C. Zachos (2010), Paleoredox changes across the Paleocene-Eocene thermal maximum, Walvis Ridge (ODP Sites 1262, 1263 and 1266): evidence from Mn and U enrichment factors, *Paleoceanography*, *25*, doi:10.1029/2009PA001861.

Clyde, W.C., and P.D. Gingerich (1998), Mammalian community response to the latest paleocene Thermal Maximum: An isotaphonomic study in the northern Bighorn Basin, Wyoming, *Geology*, *26*, 1011-1014.

Comiso, J.C., C.L. Parkinson, R. Gersten, and L. Stock (2008), Accelerated decline in the Arctic sea ice cover, *Geophysical Research Letters*, *35*, doi:10.1029/2007GL031972.

Condon, D., B. Schoene, S. Bowring, R. Parrish, N. McLean, S. Noble, and Q. Crowley (2007), EARTHTIME; isotopic tracers and optimized solutions for high-precision U-Pb ID-TIMS geochronology, *Eos, Trans. AGU*, 88.

Cramer, B.S., M.-P. Aubry, K.G. Miller, R.K. Olsson, J.D. Wright, and D.V. Kent (1999), An exceptional chronologic, isotopic, and clay mineralogic record of the latest Paleocene thermal maximum, Bass River, NJ, ODP 174AX, *Bull. Soc. Géol. Fr.*, *170*, 883-897.

Cramer, B.S., J.D. Wright, D.V. Kent, and M. Aubry (2003), Orbital climate forcing of $\delta^{13}C$ excursions in the late Paleocene-early Eocene (chrons C24n-C25n), *Paleoceanography*, *18*, doi:10.1029/2003PA000909.

Crouch, E.M., and H. Brinkhuis (2005), Environmental change across the Paleocene-Eocene transition from eastern New Zealand: A marine palynological approach. *Mar. Micropaleontol.*, *56*, 138-160.

Crouch, E.M., C. Heilmann-Clausen, H. Brinkhuis, H.E.G. Morgans, K.M. Rogers, H. Egger, and B. Schmitz (2001), Global dinoflagellate event associated with the late Paleocene Thermal Maximum, *Geology*, *29*, 315-318.

Crouch, E.M., G.R. Dickens, H. Brinkhuis, M.-P. Aubry, C.J. Hollis, K.M. Rogers, and H. Visscher (2003a), The *Apectodinium* acme and terrestrial discharge during the Paleocene-Eocene Thermal Maximum: new palynological, geochemical and calcareous nannoplankton observations at Tawanui, New Zealand, *Palaeogeogr.*, *Palaeoclimatol.*, *Palaeoecol.*, *194*, 387-403.

Crouch, E.M., H. Brinkhuis, H. Visscher, T. Adatte, M.-P. Bolle (2003b), late Paleocene-early Eocene dinoflagellate cyst records from the Tethys: Further observations on the global distribution of *Apectodinium*, in *Causes and Consequences of Globally Warm Climates in the Early Paleogene*, *Geol. Soc. Am. Spec. Paper*, *369*, edited by S. Wing, P.D. Gingerich, B. Schmitz, and E. Thomas, pp. 113-131, Boulder, Colorado.

Crowley, J.L., B. Schoene, and S.A. Bowring (2007), U-Pb dating of zircon in the Bishop Tuff at the millennial scale, *Geology*, *35*, 1123-1126.

Cui, Y. (2010), Carbon addition during the Paleocene-Eocene thermal maximum: model inversion of a new, high-resolution carbon isotope record from Svalbard, unpublished M.S. thesis, Dep. of Geosci., Pennsylvania State Univ., Pennsylvania, USA.

Cui, Y., L.R. Kump, A. Ridgwell, A.J. Charles, C.K. Junium, A.F. Diefendorf, K.H. Freeman, N.M. Urban, and I.C. Harding (2011), Slow release of fossil carbon during the Paleocene-Eocene thermal maximum, *Nat. Geosci.*, *4*, 481-485.

Dale, B. (1996), Dinoflagellate cyst ecology: Modeling and geological applications, in *Palynology: Principles and applications*, *Am. Assoc. Stratigr. Palynol. Found.*, *3*, edited by J. Jansonius, and D.C. McGregor, pp. 1249-1275, Publishers Press, Salt Lake City, Utah.

Dallanave, E., L. Tauxe, G. Muttoni, and D. Rio (2010), Silicate weathering machine at work: Rock magnetic data from the late Paleocene-early Eocene Cicogna section, Italy, *Geochem. Geophys. Geosyst.*, 11, doi:10.1029/2010GC003142.

Dalland, A. (1977), Erratic clasts in the lower Teriary of Svalbard – evidence of transport by winter ice, *Norsk Polarinstitutt Årbok 1976*, 151-165.

Dalland, A. (1979), Structural Geology and petroleum potential of Nordenskiold land, Svalbard, *Norwegian Sea Symposium, Norsk Petroleumsforening, Tromsø 1979*, 1-20.

Dallmann, W.K., P.S. Midbø, A. Nøttvedt, and R.J. Steel (1999), Tertiary lithostratigraphy, in *Lithostratigraphic Lexicon of Svalbard*, edited by W.K. Dallmann, pp. 215–263, Norsk Polarinstitutt, Tromsø.

de Vernal, A., A. Rochon, J. Turon, and J. Matthiessen (1997), Organic-walled dinoflagellate cysts: palynological tracers of sea surface conditions in middle to high latitude marine environments, *Geobiosciences*, *30*, 905-920.

Dettinger, M.D., M. Ghil, C.M. Strong, W. Weibel, and P. Yiou (1995), Software expedites singular-spectrum analysis of noisy time series. *EOS, Trans. AGU*, *76*, 12, 14, 21.

Devillers, R., and A. de Vernal (2000), Distribution of dinoflagellate cysts in surface sediments of the northern North Atlantic in relation to nutrient content and productivity in surface waters, *Mar. Geol.*, *166*, 103-124.

Dickens, G.R. (2001), Carbon addition and removal during the late Paleocene Thermal Maximum: basic theory and preliminary treatment of the isotope record at ODP Site 1051, Blake Nose, in *Western North Atlantic Palaeogene and Cretaceous Palaeoceanography, Geol. Soc. London Spec. Publ., 183*, edited by D. Kroon, D. Norris, and A. Klaus, pp.293-305.

Dickens, G.R. (2003), Rethinking the global carbon cycle with a large, dynamic and microbially mediated gas hydrate capacitor, *Earth Plant. Sci. Lett.*, *213*, 169-183.

Dickens, G.R. (2011), Methane release from gas hydrate systems during the Paleocene-Eocene thermal maximum and other past hyperthermal events: setting appropriate parameters for discussion, *Clim. Past*, *7*, 1-35.

Dickens, G.R., J.R. O'Neil, D.K. Rea, and R.M. Owen, (1995), Dissociation of oceanic methane hydrate as a cause of the carbon isotope excursion at the end of the Paleocene, *Paleoceanography*, *10*, 965-971.

Dickens, G.R., M.M. Castillo, and J.C.G. Walker (1997), A blast of gas in the latest Paleocene: simulating first order effects of massive dissociation of oceanic methane hydrate, *Geology*, *25*, 259-262.

Diefendorf, A.F., K.E. Mueller, S.L. Wing, P.L. Koch, and K.H. Freeman (2010), Global patterns in leaf ^{13}C discrimination and implications for studies of past and future climate, *PNAS*, *107*, 5738-5743.

Dupuis, C., M-P. Aubry, E. Steurbaut, W.A. Berggren, K. Ouda, R. Magioncalda, B.S. Cramer, D.V. Kent, R.P. Speijer, and C. Heilmann-Clausen (2003), The Dababiya quarry section: Lithostratigraphy, clay mineralogy, geochemistry and paleontology, *Micropaleontology*, *49*, 41-59.

Dypvik, H., L. Riber, F. Burca, D. Rüther, D. Jargvoll, J. Nagy, and M. Jochmann (2011), The Paleocene-Eocene thermal maximum (PETM) in Svalbard – clay mineral and geochemical signals. *Paleogeog., Paleoclim., Paleoecol.*, *302*, 156-169.

Egger, H., C. Heilmann-Clausen, and B. Schmitz (2000), The Paleocene/Eocene-boundary interval of a Tethyan deep-sea section (Austria) and its correlation with the North Sea basin, *Bull. Soc. Géol. France*, *171*, 207-216.

Egger, H., J. Fenner, C. Heilmann-Clausen, F. Rögl, R.F. Sachsenhofer, and B. Schmitz (2003), Paleoproductivity of the northwestern Tethyan margin (Anthering Section, Austria) across the Paleocene-Eocene transition, in *Causes and Consequences of Globally Warm Climates in the Early Paleogene*, *Geol. Soc. Am.*

Spec. Paper, *369*, edited by S. Wing, P.D. Gingerich, B. Schmitz, and E. Thomas, pp. 133-146, Boulder, Colorado.

Egger, H., C. Heilmann-Clausen, and B. Schmitz (2009), From shelf to abyss: Record of the Paleocene/Eocene-boundary in the eastern Alps, Austria, *Geol. Acta*, *7*, 215-227.

Evitt, W.R. (1985), *Sporopollenin dinoflagellate cysts: Their morphology and interpretation*, Am. Assoc. Stratigr. Palynol. Found., Hart Graphics Inc., Austin, Texas.

Farley, K.A., and S.F. Eltgroth (2003), An alternative age model for the Paleocene-Eocene thermal maximum using extraterrestrial ^{3}He, *Earth Planet. Sci. Lett.*, *208*, 135-148.

Fensome, R.A., and G.L. Williams (2004), *The Lentin and Williams Index of Fossil Dinoflagellates, 2004 Edition, Am. Assoc. Stratigr. Palynol., Contribution Series, 42*, Austin, Texas.

Fensome, R.A., J.F. Saldarriaga, and F.J.R. Taylor (1999), Dinoflagellate phylogeny revisited: reconciling morphological and molecular based phylogenies, *Grana*, *38*, 66-80.

Galeotti, S., S. Krishnan, M. Pagani, L. Lanci, A. Gaudio, J.C. Zachos, S. Monechi, G. Morelli, and L. Lourens (2010), Orbital chronology of Early Eocene hyperthermals from the Contessa Road section, central Italy, *Earth Planet. Sci. Lett.*, *290*, 192-200.

Gavrilov, Y.O., L.A. Kodina, I.Y. Lubchenko, and N.G. Muzylev (1997), The late Paleocene anoxic event in epicontinental seas of peri-Tethys and formation of the sapropelite unit: sedimentology and geochemistry. *Lithol. Min. Resour.*, *32*, 427-450.

Gavrilov, Y.O., E.A. Shcherbinina, and H. Oberhänsli (2003), Paleocene-Eocene boundary events in the northeastern Peri-Tethys, in *Causes and Consequences of Globally Warm Climates in the Early Paleogene*, *Geol. Soc. Am. Spec. Paper*, *369*, edited by S. Wing, P.D. Gingerich, B. Schmitz, and E. Thomas, pp. 147-168, Boulder, Colorado.

Ghil, M., R.M. Allen, M.D. Dettinger, K. Ide, D. Kondrashov, M.E. Mann, A. Robertson, A. Saunders, Y. Tian, F. Varadi, P. Yiou (2002), Advanced spectral methods for climatic time series. *Rev. Geophys.*, *40*, 1-41, doi:10.1029/2000RG000092.

Gibbs, S., P. Bown, J. Sessa, T. Bralower, and P. Wilson (2006a), Nannoplankton extinction and origination across the Paleocene-Eocene Thermal Maximum, *Science*, *314*, 1770-1773.

Gibbs, S., T.J. Bralower, P.R. Bown, J.C. Zachos, and L.M. Bybell (2006b), shelf and open-ocean calcareous phytoplankton assemblages across the Paleocene-Eocene thermal maximum: Implications for global productivity gradients, *Geology*, *34*, 233-236.

Gibbs, S.J., H.M. Stoll, P.R. Bown, and T.J. Bralower (2010), Ocean acidification and surface water carbonate production across the Paleocene-Eocene thermal maximum, *Earth Planet. Sci. Lett.*, *295*, 583-592.

Gibson, T.G., and L.M. Bybell (1994), Sedimentary patterns across the Paleocene-Eocene boundary in the Atlantic and Gulf Coastal Plains of the United States, *Bull. Soc. Belge Géol.*, *103*, 237-265.

Gibson, T.G., L.M. Bybell, and J.P. Owens (1993), Latest Paleocene lithologic and biotic events in neritic deposits of southwestern New Jersey, *Paleoceanography*, *8*, 495-514.

Giusberti, L., D. Rio, C. Agnini, J. Backman, E. Fornaciari, F. Tateo, M. Oddone (2007), Mode and tempo of the Paleocene-Eocene Thermal Maximum in an expanded section from the Venetian pre-Alps, *Geol. Soc. Am. Bull.*, *119*, 391-412.

Gleason, J.D., D.J. Thomas, T.C. Moore Jr., J.D. Blum, R.M. Owen, and B.A. Haley (2009), Early to middle Eocene history of the Arctic Ocean from Nd-Sr isotopes in fossil fish debris, Lomonosov Ridge, *Paleoceanography*, *24*, doi:10.1029/2008PA001685.

Greenwood, D.R., Basinger, J.F., and R.Y. Smith (2010), How wet was the Arctic Eocene rainforest? Estimates of precipitation from Paleogene Arctic marcrofloras, *Geology*, *38*, 15-18.

Handley, L., P.N. Pearson, I.K. McMillan, and R.D. Pancost (2008), Large terrestrial and marine carbon and hydrogen isotope excursions in a new Paleocene/Eocene boundary section from Tanzania, *Earth Planet. Sci. Lett.*, *275*, 17-25.

Handley, L., E.M. Crouch, and R.D. Pancost (2011), A New Zealand record of sea level rise and environmental change during the Paleocene-Eocene thermal maximum, *Paleogeog., Paleoclim., Paleoecol.*, *305*, 185-200.

Harding, I.C., A.J. Charles, J.E.A. Marshall, H. Pälike, A.P. Roberts, P.A. Wilson, E. Jarvis, R. Thorne, E. Morris, R. Moreman, R. Pearce, S. Akbari, (2011), Sea level and salinity fluctuations during the Palaeocene/Eocene thermal maximum in Arctic Spitsbergen. *Earth Planet. Sci. Lett.*, *303*, 97-107.

Harland, R. (1973), Dinoflagellate cysts and acritarchs from the Bearpaw Formation (upper Campanian) of southern Alberta, Canada, *Palaeontology*, *16*, 665-706.

Harland, W. (1997), Palaeogene history of Svalbard, in *The Geology of Svalbard*, *Mem. Geol. Soc. London*, *17*, edited by B. Harland, pp. 388-417.

Harland, W.B., B.A. Gaskell, A.P. Heafford, E.K. Lind, and P.J. Perkins (1984), Outline of Arctic post-Silurian continental displacements, in *Petroleum geology of the north European margin*, edited by A.M. Spencer, E. Holter, S.O. Johnsen, A. Mørk, E. Nysaether, P. Songsstad, and Å. Spinnangr, pp.137-148, Graham & Trotman, London.

Harrington, G.J., and C.A. Jaramillo (2007), Paratropical floral extinction in the late-Palaeocene-early Eocene, *J. Geol. Soc. London*, *164*, 323-332.

Heer, O. (1868), *Die Fosslie Flora der Polarländer*, *Miozäne Flora von Spitzbergen*, pp. 155-161, Zürich.

Heer, O. (1870), Die Miozäne flora and fauna Spitzbergens. Mit einem Anhang über die diluvialen Ablagerungen Spitzbergens (Flora fossils Arctica II). *Kongeliga Svenska Vetenskaps Akademiens Handlingar*, *8*, 1-98.

Heer, O. (1876), Beiträge zur fossilen Flora Spitzbergens. Gegründet auf die Sammlungen der schwedischen Expedition vom Jahre 1872 auf 1873 (Flora fossils Arctica IV). *Kongeliga Svenska Vetenskaps Akademiens Handlingar*, *14*, 1-141.

Helland-Hansen, W. (1990), Sedimentation in Paleogene Foreland Basin, Spitsbergen, *Am. Assoc. Pet. Geol. Bull.*, *74*, 260-272.

Higgins, J.A., and D.P. Schrag (2006), Beyond methane: Towards a theory for the Paleocene-Eocene Thermal Maximum, *Earth Planet. Sci. Lett.*, *245*, 523-537.

Hilgen, F.J., K.F. Kuiper, and L.J. Lourens (2010), Evaluation of the astronomical time scale for the Paleocene and earliest Eocene. *Earth Planet. Sci. Lett.*, *300*, 139-151.

Hinnov, L.A., and J.G. Ogg (2007), Cyclostratigraphy and the astronomical time scale, *Stratigraphy*, *4*, 239-251.

Hopmans, E. C., J.W.H. Weijers, E. Schefuß, L. Herfort, J.S. Sinninghe Damsté, and S. Schouten, (2004), A novel proxy for terrestrial organic matter in sediments based on branched and isoprenoid tetraether lipids, *Earth Planet. Sci. Lett.*, *224*, 107-116.

Huang, W.-Y., and W.G. Meinschein (1976), Sterols as source indicators of organic materials in sediments, *Geochim. Cosmochim. Ac.*, *40*, 323-330.

Huntington, H., G. Weller, E. Bush, T.V. Callaghan, V.M. Kattsov, and M. Nuttall (2005), An introduction to the Arctic Climate Impact Assessment, in *Arctic Climate Impact Assessment, Scientific Report*, edited by C. Symon, L. Arris, and B. Heal, pp. 1-20, Cambridge University Press, New York.

Iakovleva, A. I., H. Brinkhuis, and C. Cavagnetto (2001), Late Paleocene-Early Eocene dinoflagellate cysts from the Turgay Strait, Kazakhstan; correlations across ancient seaways, *Palaeogeogr.*, *Palaeoclimatol.*, *Palaeoecol.*, *172*, 243-268.

Intergovernmental Panel on Climate Change [IPCC] (2007), *Climate Change 2007: The Physical Science Basis. Contribution of Working Group I to the Fourth Assessment Report of the Intergovernmental Panel on Climate Change*, edited by S. Soloman, D. Qin, M. Manning, Z. Chen, M. Marquis, K.B. Averyt, M. Tignor, and H.L. Miller, Cambridge University Press, Cambridge, UK.

Jaffey, A.H., K.F. Flynn, L.E. Glendenin, W.C. Bentley, and A.M. Essling (1971), Precision measurement of half-lives and specific activities of ^{235}U and ^{238}U, *Phys. Rev.* C, *4*, 1889-1906.

Jahren, H.A., and L.S.L. Sternberg (2002), Eocene meridional weather patterns reflected in the oxygen isotopes of Arctic fossil wood, *GSA Today*, *12*, 4-9.

Jahren, H.A., and L.S.L. Sternberg (2003), Humidity estimate for the middle Eocene Arctic rainforest, *Geology*, *31*, 463-466.

Jaramillo, C., D. Ochoa, L. Contreras, M. Pagani, H. Carvajal-Ortiz, L.M. Pratt, S. Krishnan, A. Cardona, M. Romero, L. Quiroz, G. Rodriguez, M.J. Rueda, F. de la Parra, S. Morón , W. Green, G. Bayona, C. Montes, O. Quintero, R. Ramirez, G. Mora, S. Schouten, H. Bermudez, R. Navarrete, F. Parra, M. Alvarán, J. Osorno, J.L. Crowley, V. Valencia, and J. Vervoort (2010), Effects of rapid global warming at the Paleocene-Eocene boundary on Neotropical vegetation. *Science*, *330*, 957-961.

Jenkins, C.D. (2000), The ecological significance of foraminifera in the kimmeridgian of southern England, *Grzybowski Found. Spec. Pub.*, *7*, 167-178.

Jiang, S., and S.W. Wise Jr. (2006), Surface-water chemistry and fertility variations in the tropical Atlantic across the Paleocene/Eocene thermal maximum as evidenced by calcareous nannoplankton from ODP Leg 207, Hole 1259B, *Revue de Micropaléontol.*, *49*, 227-244.

John, C.M., S.M. Bohaty, J.C. Zachos, A. Sluijs, S. Gibbs, H. Brinkhuis, and T. Bralower (2008), North American continental margin records of the Palaeocene-Eocene Thermal Maximum: Implications for global carbon and hydrological cycling. *Paleoceanography*, *23*, doi:10.1029/2007PA001465.

Katz, M., D.K. Pak, G.R. Dickens, and K.G. Miller (1999), The source and fate of massive carbon input during the latest Palaeocene Thermal Maximum, *Science*, *286*, 1531-1533.

Kellogg, H.E. (1975), Tertiary stratigraphy and tectonism in Svalbard and continental drift, *Am. Assoc. Pet. Geol. Bull.*, *59*, 465-485.

Kelly, D.C., T.J. Bralower, J.C. Zachos, I. Premoli-Silva, and E. Thomas (1996), Rapid diversification of planktonic foraminifera in the tropical Pacific (ODP Site 865) during the late Paleocene thermal maximum, *Geology*, *24*, 423-426.

Kelly, D.C., T.J. Bralower, and J.C. Zachos (1998), Evolutionary consequences of the latest Paleocene thermal maximum for tropical planktonic foraminifera, *Palaeogeogr.*, *Palaeoclimatol.*, *Palaeoecol.*, *141*, 139-161.

Kelly, D.C., J.C. Zachos, T.J. Bralower, and S.A. Schellenberg (2005), Enhanced terrestrial weathering/runoff and surface ocean carbonate production during the recovery stages of the Paleocene-Eocene thermal maximum, Paleoceanography, *20*, doi:10.1029/2005PA001163.

Kelly, D.C., T.M.J. Nielsen, H. McCarren, J.C. Zachos, and U. Röhl (2010), Spatiotemporal patterns of carbonate sedimentation in the South Atlantic: Implications for carbon cycling during the Paleocene-Eocene thermal maximum, *Palaeogeogr.*, *Palaeoclimatol.*, *Palaeoecol.*, *293*, 30-40.

Kennett, J., and L. Stott (1991), Abrupt deep-sea warming, palaeoceanographic changes and benthic extinctions at the end of the Palaeocene, *Nature*, *353*, 225-229.

Kim, J.-H., S. Schouten, E.C. Hopmans, B. Donner, and J.S. Sinninghe Damsté (2008), Global sediment core-top calibration of the TEX_{86} paleothermometer in the ocean, *Geochim. Cosmochim. Ac.*, *72*, 1154-1173.

Kim, J.-H., J. van der Meer, S. Schouten, P. Helmke, V. Willmott, F. Sangiorgi, N. Koç, E.C. Hopmans, J.S. Sinninghe Damsté (2010), New indices and calibrations derived from the distribution of crenarchaeal isoprenoid tetraether lipids: Implications for past sea surface temperature reconstructions, *Geochim. Cosmochim. Ac.*, *74*, 4639-4654.

Koch, P.L., J.C. Zachos, and P.D. Gingerich (1992), Correlation between isotope records in marine and continental carbon reservoirs near the Palaeocene/Eocene boundary, *Nature*, *358*, 319-322.

Koch, P.L., J.C. Zachos, and D.L. Dettman (1995), stable isotope stratigraphy and paleoclimatology of the Paleogene Bighorn Basin, *Paleogeog., Paleoclim., Paleoecol.*, *115*, 61-89.

Kouli, K., H. Brinkhuis, and B. Dale (2001), *Spiniferites Cruciformis*: a fresh water dinoflagellate cyst? *Rev. Palaeobot. Palynol.*, *113*, 273-286.

Kuiper, K. F., A. Deino, F.J. Hilgen, W. Krijgsman, P.R. Renne, and J.R. Wijbrans (2008), Synchronizing rock clocks of Earth history, *Science*, *320*, 500-504.

Kump, L.R., T.J. Bralower, and A. Ridgwell (2009), Ocean acidification in deep time, *Oceanography*, *22*, 94-107.

Kurtz, A.C., L.R. Kump, M.A. Arthur, J.C. Zachos, and A. Paytan (2003), Early Cenozoic decoupling of the global carbon and sulphur cycles, *Paleoceanography*, *18*, doi:10.1029/2003PA000908.

Laskar, J. (1999), The limits of Earth orbital calculations for geological timescale use, *Phil. Trans. R. Soc. Lond. A.*, *357*, 1735-1759.

Laskar, J., P. Robutel, F. Joutel, M. Gastineau, A.C.M. Correia, and B. Levrard (2004), A long-term solution for the insolation quantities of the Earth, *Astron. Astrophys.*, *428*, 261-285.

Leon-Rodriguez, L., and G.R. Dickens (2010), constraints on ocean acidification associated with rapid and massive carbon injections: The early Paleogene record at Ocean Drilling Project Site 1215, equatorial Pacific Ocean, *Palaeogeogr.*, *Palaeoclimatol.*, *Palaeoecol.*, *298*, 409-420.

Lewis, J., J.D. Dodge, and A.J. Powell (1990), Quaternary dinoflagellate cysts from the upwelling system offshore Peru, Hole 686B, ODP Leg 112, *Proc. Ocean Drill. Program*, *112*, 323-328.

Lippert, P.C., and J.C. Zachos (2007), A biogenic origin for anomalous fine-grained magnetic material at the Paleocene-Eocene boundary at Wilson Lake, New Jersey, *Paleoceanography*, *22*, doi:10.1029/2007PA001471.

Liu, Z., M. Pagani, D. Zinniker, R. DeConto, M. Huber, H. Brinkhuis, S.R. Shah, R.M. Leckie, and A. Pearson (2009), Global cooling during the Eocene-Oligocene climate transition, *Science*, *323*, 1187-1190.

Livšic, J.J. (1974), Palaeogene deposits and the platform structure of Svalbard, *Norske Polarinstitutt skrifter*, *159*, 11-13.

Lourens, L., F. Hilgen, N.J. Shackleton, J. Laskar, and D. Wilson (2004), The Neogene Period, in *A Geologic Time Scale 2004*, edited by F.M. Gradstein, J.G. Ogg, and A.G. Smith, pp. 409-440, Cambridge University Press, Cambridge, UK.

Lourens, L.J., A. Sluijs, D. Kroon, J.C. Zachos, E. Thomas, U. Röhl, J. Bowles, and I. Raffi (2005), Astronomical pacing of late Palaeocene to early Eocene global warming events, *Nature*, *435*, 1083-1087.

Ludwig, K.R., (1991), Isoplot – a plotting and regression program for radiogenic isotope data, *USGS Open File Report*, 91-445.

Lunt, D.J., P.J. Valdes, T. Dunkley-Jones, A. Ridgwell, A.M. Haywood, D.N. Schmidt, R. Marsh, and M. Maslin (2010), CO_2-driven ocean circulation changes as an amplifier of Paleocene-Eocene thermal maximum hydrate destabilization, *Geology*, *38*, 875-878.

Luterbacher, H.P., J.R. Ali, H. Brinkhuis, F.M. Gradstein, J.J. Hooker, S. Monechi, J.G. Ogg, J. Powell, U. Röhl, A. Sanfilippo, and B. Schmitz (2004), The Paleogene Period, in *A Geologic Time Scale 2004*, edited by F.M. Gradstein, J.G. Ogg, and A.G. Smith, pp. 384-408, Cambridge University Press, Cambridge, UK.

Maclennan, J., and S.M. Jones (2007), Regional uplift, gas hydrate dissociation and the origins of the Paleocene-Eocene Thermal Maximum. *Earth Planet. Sci. Lett.*, *245*, 65-80.

Magioncalda, R., C. Dupuis, T. Smith, E. Steurbaut, and P.D. Gingerich (2004), Paleocene-Eocene carbon isotope excursion in organic carbon and pedogenic carbonate: Direct comparison in a continental stratigraphic section, *Geology*, *32*, 553-556.

Manum, S.B., and T. Throndsen (1986), Age of Tertiary formations on Spitsbergen, *Polar Res.*, *4*, 103– 131.

Manum, S.B., T. Bjærke, T. Throndsen, M. Eien (1976), Preservation and abundance of palynomorphs, and observations on thermal alteration in Svalbard, *Norsk Polarinstitutt Årbok 1976*, 121-130.

Marret, F., and K.A.F. Zonneveld (2003), Atlas of modern organic-walled dinoflagellate cyst distribution, *Rev. Palaeobot. Palynol.*, *125*, 1-200.

März, C., B. Schnetger, and H.-J. Brumsack (2010), Paleoenvironmental implications of Cenozoic sediments from the central Arctic Ocean (IODP Expedition 302) using inorganic geochemistry, *Paleoceanography*, *25*, doi:10.1029/2009PA001860.

Mattinson, J.M. (2005), Zircon U-Pb chemical abrasion ("CA-TIMS") method: combined annealing and multi-step partial dissolution analysis for improved precision and accuracy of zircon ages, *Chem. Geol.*, *220*, 47-66.

McCarren, H., E. Thomas, T. Hasegawa, U. Röhl, and J.C. Zachos (2008), Depth dependency of the Paleocene-Eocene carbon isotope excursion: paired benthic and terrestrial biomarker records (Ocean Drilling Program Leg 208, Walvis Ridge), *Geochem. Geophys. Geosyst., 9*, doi:10.1029/2008GC002116.

McInerney, F.A., and S.L. Wing (2011), The Paleocene-Eocene thermal maximum: A perturbation of carbon cycle, climate, and biosphere with implications for the future, *Annu. Rev. Earth Planet. Sci.*, *39*, 489–516.

Mellere, D., P. Plink-Bjorklund and R. Steel (2002), Anatomy of shelf deltas at the edge of a prograding Eocene shelf margin, Spitsbergen, *Sedimentology*, *49*, 1181-1206.

Monechi, S., E. Angori, and K. Von Salis (2000), Calcareous nannofossil turnover around the Paleocene/Eocene transition at Alamedilla (southern Spain), *Bull. Soc. Géol. France*, 4, pp. 477-489.

Moran, K., J. Backman, H. Brinkhuis, S. Clemens, T. Cronin, G. Dickens, F. Eynaud, J. Gattacceca, M. Jakobsson, R. Jordan, R. Kaminski, J. King, N. Koc, A. Krylov, N. Martinez, J. Matthiessen, D. McInroy, T. Moore, J. Onodera, M. O'Regan, H. Pälike, B. Rea, D. Rio, T. Sakamoto, D. Smith, R. Stein, C. St John, I. Suto, N. Suzuki, K. Takahashi, M. Watanabe, M. Yamamoto, J. Farrell, M. Frank, P. Kubik, W. Jokat, and Y. Kristoffersen (2006), The Cenozoic palaeoenvironment of the Arctic Ocean, *Nature*, *441*, 601-605.

Mosar, J., T.H. Torsvik, and BAT team (2002), Opening of the Norwegian and Greenland Seas: Plate tectonics in Mid Norway since the Late Permian, in *BATLAS – Mid Norway plate reconstructions atlas with global and Atlantic perspectives*, edited by E.A. Eide, pp. 48-59, Geol. Surv. Norway.

Mudie, P.J., A.E. Aksu, and D. Yasar (2001), Late Quaternary dinoflagellate cysts from the Black, Marmara and Aegean Seas: variations in assemblages, morphology and paleosalinity, *Mar. Micropaleontol.*, *43*, 155-178.

Müller, R.D., and R.F. Spielhagen (1990), Evolution of the Central Basin of Spitsbergen: towards a synthesis of sediment and plate tectonic history, *Paleogeog., Paleoclim., Paleoecol.*, *80*, 153–172.

Murphy, B.H., K.A. Farley, and J.C. Zachos (2010), An extraterrestrial ^{3}He-based timescale for the Paleocene-Eocene thermal maximum (PETM) from Walvis Ridge, IODP Site 1266, *Geochim. Cosmochim. Ac.*, *74*, 5098-5108.

Nagy, J. (2005), Delta-influenced foraminiferal facies and sequence stratigraphy of Paleocene deposits in Spitsbergen, *Paleogeog., Paleoclim., Paleoecol.*, *222*, 161-179.

Nathorst, A.G. (1910), Beitraege zur Geologie der Baeren-Insel, Spitzbergens und des Koenig Karl-Landes., *Bull. Geol. Inst. Univ. Uppsala*, *10*, 261-416.

Nicolo, M.J., G.R. Dickens, C.J. Hollis, and J.C. Zachos (2007), Multiple early Eocene hyperthermals: their sedimentary expression on the New Zealand continental margin and in the deep sea, *Geology*, *35*, 699-702.

Nicolo, M.J., G.R. Dickens, and C.J. Hollis (2010), South Pacific intermediate water oxygen depletion at the onset of the Paleocene-Eocene thermal maximum as depicted in New Zealand margin sections, *Paleoceanography*, *25*, doi:10.1029/2009PA001904.

Norris, R.D., and U. Röhl (1999), carbon cycling and chronology of climate warming during the Palaeocene/Eocene transition, *Nature*, *401*, 775-778.

Pagani, M., N. Pedentchouk, M. Huber, A. Sluijs, S. Schouten, H. Brinkhuis, J.S. Sinninghe Damsté, G.R. Dickens and the Expedition 302 Scientists (2006), Arctic hydrology during global warming at the Palaeocene/Eocene Thermal Maximum. *Nature*, *442*, 671-675.

Paillard, D., L. Labeyrie, and P. Yiou, (1996), Macintosh program performs time series analysis. *EOS, Trans. AGU*, *77*, 379.

Pälike, H. (2005), Orbital variation (including Milankovitch cycles), in *Encyclopedia of Geology*, vol. 1, edited by R.C. Selley, L.R.M. Cocks, and I.R. Plimer, pp. 410-421, Elsevier, Oxford, UK.

Pälike, H., and F. Hilgen, (2008), Rock clock synchronization, *Nat. Geosci.*, *1*, 282.

Pälike, H., J. Laskar, and N.J. Shackleton, (2004), Geologic constraints on the chaotic diffusion of the solar system, *Geology*, *32*, 929-932.

Panchuk, K., A. Ridgwell, and L. Kump (2008), Sedimentary response to Paleocene-Eocene Thermal Maximum Carbon release: A model-data comparison, *Geology*, *36*, 315-318.

Payne, S.N.J., P.A. Cornick, L.F. Draper, H. Nicholson, A.C. Morton, P. Huggins, and R. Anderton (2005), Mungo Field UK North Sea 22/20, 23/16a: stratigraphy, salt diapirs and reservoir development (or 'the riddle of the sands'), in *Recent Developments in Applied Biostratigraphy*, edited by A.J. Powell, and J.B. Riding, pp.23-42, Micropalaeontol. Soc. Spec. Publ.

Pearson, P.N., B.E. van Dongen, C.J. Nicholas, R.D. Pancost, S. Schouten, J.M. Singano, and B.S. Wade (2007), Stable warm tropical climate through the Eocene Epoch, *Geology*, *35*, 211-214.

Peterson, B.J., R.M. Holmes, J.W. McClelland, C.J. Vörösmarty, R.B. Lammers, A.I. Shiklomanov, I.A. Shiklomanov, and S. Rahmstorf (2002), Increasing river discharge to the Arctic Ocean, *Science*, *298*, 2171-2173.

Peterson, B.J., J. McClelland, R. Curry, R.M. Holmes, J.E. Walsh, and K. Aagaard (2006), Trajectory shifts in the Arctic and subarctic freshwater cycle, *Science*, *313*, 1061-1066.

Powell, A.J., H. Brinkhuis, and J.P. Bujak (1996), Upper Paleocene–lower Eocene dinoflagellate cyst sequence biostratigraphy of south-east England, in *Correlation of the early Paleogene in northwest Europe, Geol. Soc. London. Spec. Publ., 101*, edited by R.W. Knox, R.E. Dunay, and R.M. Corfield, pp. 145-183.

Pross, J., and G. Schmiedl (2002), Early Oligocene dinoflagellate cysts from the Upper Rhine Graben (SW Germany): Paleoenvironmental and plaeoclimatic implications, *Mar. Micropaleontol.*, *45*, 1-24.

Pross, J., and H. Brinkhuis (2005), Organic-walled dinoflagellate cysts as paleoenvironmental indictors in the Paleogene; a synopsis of concepts, *Paläontologische Zeitschrift*, *79*, 53-59.

Pujalte, V., and B. Schmitz (2006), Abrupt climatic and sea level changes across the Paleocene-Eocene boundary, as recorded in an ancient coastal plain setting (Pyrenees, Spain), in *Climate and Biota of the Early Paleogene. Volume of Abstracts, Bilbao*, edited by F. Caballero, E. Apellaniz, J.I. Baceta, G. Bernaola, X. Orue-Etxebarria, A. Payros, V. Pujalte pp. 103.

Pujalte, V., B. Schmitz, J.I. Baceta, X. Orue-Etxebarria, G. Bernaola, J. Dinarès-Turell, A. Payros, E. Apellaniz, F. Caballero, (2009), *Geologica Acta*, *7*, 161-175.

Raffi, I., and B. De Bernardi (2008), Response of calcareous nannofossils to the Paleocene-Eocene thermal maximum: observations on composition, preservation and calcification in sediments from ODP Site 1263 (Walvis Ridge SE Atlantic), *Mar. Micropaleontol.*, *69*, 119-138.

Rahmstorf, S. (2002), Ocean circulation and climate during the past 120,000 years, *Nature*, *419*, 207-213.

Ravizza, G., R.N. Norris, J. Blusztajn, M.-P. Aubry (2001), An osmium isotope excursion associated with the late Palaeocene Thermal Maximum: Evidence of intensified chemical weathering. *Paleoceanography*, *16*, 155-163.

Ravn, J.P.J. (1922), On the Mollusca of the Tertiary of Spitsbergen, *Resultater Norske Spitsbergenekspedisjoner*, *1*, 28.

Renne, P.R. C.C. Swisher, A.L. Deino, D.B. Karner, T.L. Owens, and D.J. DePaolo (1998), Intercalibration of standards, absolute ages and uncertainties in $^{40}Ar/^{39}Ar$ dating, *Chem. Geol.*, *145*, 117-152.

Renne, P.R., R. Mundil, G. Balco, K. Min, and K.R. Ludwig (2010), Joint determination of ^{40}K decay constants and $^{40}Ar^*/^{40}K$ for the Fish Canyon sanidine standard, and improved accuracy for $^{40}Ar/^{39}Ar$ geochronology, *Geochim. Cosmochim. Ac.*, *74*, 5349-5367.

Riber, L. (2009), Paleogene depositional conditions and climatic changes of the Frysjaodden Formation in Central Spitsbergen (sedimentology and mineralogy), Unpublished Masters thesis, *Univ. Oslo*, pp. 1-112.

Ridgwell, A., and D.N. Schmidt (2010), past constraints on the vulnerability of marine calcifiers to massive carbon dioxide release, *Nat. Geosci.*, *3*, 196-200.

Robinson, S.A. (2011), Shallow-water carbonate record of the Paleocene-Eocene thermal maximum from a Pacific Ocean guyot, *Geology*, *39*, 51-54.

Röhl, U., T.J. Bralower, R.D. Norris, and G. Wefer (2000), New chronology for the late Paleocene Thermal Maximum and its environmental implications, *Geology*, *28*, 927-930.

Röhl, U., T. Westerhold, T.J. Bralower, and J.C. Zachos (2007), On the duration of the Paleocene-Eocene Thermal Maximum (PETM), *Geochem. Geophys. Geosyst.*, *8*, doi:10.1029/2007/GC001784.

Schärer, U., 1984. The effect of initial ^{230}Th disequilibrium on young U–Pb ages: the Makalu case, Himalaya. *Earth and Planet. Sci. Lett., 67,* 191–204.

Schmitz, B., and V. Pujalte (2007), Abrupt increase in seasonal extreme precipitation at the Palaeocene-Eocene boundary. *Geology*, *35*, 215-218.

Schmitz, M.D., and B. Schoene (2007), Derivation of isotope ratios, errors and error correlations for U-Pb geochronology using ^{205}Pb-^{235}U-(^{233}U)-spiked isotope dilution thermal ionization mass spectrometric data, *Geochem. Geophys. Geosyst.*, *8*, doi:10.1029/2006GC001492.

Schoene, B., J. Guex, A. Bartolini, U. Schaltegger, and T.J. Blackburn (2010), Correlating the end-Triassic mass extinction and flood basalt volcanism at the 100 ka level, *Geology*, *38*, 387-390.

Schouten, S., M. Woltering, I.C. Rijpstra, A. Sluijs, H. Brikhuis, J.S. Sinninghe Damsté (2007), The Paleocene–Eocene carbon isotope excursion in higher plant organic matter: differential fractionation of angiosperms and conifers in the Arctic, *Earth Planet. Sci. Lett.*, *258*, 581-592.

Schouten, S., E.C. Hopmans, J. van der Meer, A. Mets, E. Bard, T.S. Bianchi, A. Diefendorf, M. Escala, K.H. Freeman, Y. Furukawa, C. Huguet, A. Ingalls, G. Menot-Combes, A.J. Nederbragt, M. Oba, A. Pearson, E.J. Pearson, A. Rosell-Melé, P. Schaeffer, S.R. Shah, T.M. Shanahan, R.W. Smith, R. Smittenberg, H.M. Talbot, M. Uchida, B.A.S. Van Mooy, M. Yamamoto, Z. Zhang, and J.S. Sinninghe Damste (2009), An interlaboratory study of TEX_{86} and BIT analysis using high performance liquid chromatography-mass spectrometry, *Geochem. Geophys. Geosyst.*, 10, doi:10.1029/2008GC002221.

Secord, R., P.D. Gingerich, K.C. Lohmann, and K.G. Macleod (2010), Continental warming preceding the Palaeocene-Eocene thermal maximum, *Nature*, *467*, 955-958.

Sexton, P.F., R.D. Norris, P.A. Wilson, H. Pälike, T. Westerhold, U. Röhl, C.T. Bolton, and S. Gibbs (2011), Eocene global warming events driven by ventilation of oceanic dissolved organic carbon, *Nature*, *471*, 349-353.

Shannon, C.E. (1948), A mathematical theory of communication, *Bell Syst. Tech. J.*, *27*, 379-423 and 623-656.

Sláma, J., J. Košler, D.J. Condon, J.L. Crowley, A. Gerdes, J.M. Hanchar, M.S.A. Horstwood, G.A. Morris, L. Nasdala, N. Norberg, U. Schaltegger, B. Schoene, M.N. Tubrett, and M.J. Whitehouse (2008). Plešovice zircon – A new natural reference material for U-Pb and Hf isotopic microanalysis, *Chem. Geol.*, *249*, 1-35.

Sluijs, A., and H. Brinkhuis (2009), A dynamic climate and ecosystem state during the Paleocene-Eocene Thermal Maximum: inferences from dinoflagellate cyst assemblages on the New Jersey Shelf, *Biogeosciences*, *6*, 1755-1781.

Sluijs, A., J. Pross, and H. Brinkhuis (2005), From greenhouse to icehouse; organic-walled dinoflagellate cysts as paleoenvironmental indicators in the Paleogene, *Earth Sci. Rev.*, *68*, 281-315.

Sluijs, A., S. Schouten, M. Pagani, M. Woltering, H. Brinkhuis, J.S. Sinninghe Damsté, G.R. Dickens, M. Huber, G-J. Reichart, R. Stein, J. Matthiessen, L.J. Lourens, N. Pedentchouk, J. Backman, K. Moran, and the Expedition 302 Scientists (2006), Subtropical Arctic Ocean temperatures during the Palaeocene-Eocene Thermal Maximum, *Nature*, *441*, 610-613.

Sluijs, A., G.J. Bowen, H. Brinkhuis, L.J. Lourens, and E. Thomas (2007a), The Palaeocene-Eocene Thermal Maximum super greenhouse: biotic and geochemical signatures, age models and mechanisms of global change, in *Deep Time Perspectives on Climate Change: Marrying the Signal from Computer Models and Biological Proxies*, *Micropalaeontol. Soc. Spec. Publ.*, edited by M. Williams *et al.*, pp. 323-349, Geol. Soc. London, UK.

Sluijs, A., H. Brinkhuis, S. Schouten, S.M. Bohaty, C.M. John, J.C. Zachos, G. Reichart, J.S. Sinninghe Damste, E.M. Crouch, and G.R. Dickens (2007b), Environmental precursors to rapid light carbon injection at the Palaeocene/Eocene boundary, *Nature*, *450*, 1218-1221.

Sluijs, A., U. Röhl, S. Schouten, H. Brumsack, F. Sangiorgi, J.S. Sinninghe Damsté, and H. Brinkhuis (2008a), Arctic late Paleocene-early Eocene paleoenvironments with special emphasis on the Paleocene-Eocene Thermal Maximum (Lomonosov Ridge, Integrated Ocean Drilling Program Expedition 302), *Paleoceanography*, *23*, doi:10.1029/2007PA001495.

Sluijs, A., H. Brinkhuis, E.M. Crouch, C.M. John, L. Handley, D. Munsterman, S.M. Bohaty, J.C. Zachos, G.-J. Reichart, S. Schouten, R.D. Pancost, J. Sinninghe Damsté, N.L.D.

Welters, A.F. Lotter, and G.R. Dickens, (2008b), Eustatic variations during the Palaeocene-Eocene greenhouse world. *Paleoceanography*, *23*, doi:10.1029/2008PA001615.

Sluijs, A., P.K. Bijl, S. Schouten, U. Röhl, G.-J. Reichart, and H. Brinkhuis (2011), Southern Ocean warming, sea level and hydrological change during the Paleocene-Eocene thermal maximum, *Clim. Past*, *7*, 47-61.

Smith, F.A, S.L. Wing, and K.H. Freeman (2007), Magnitude of the carbon isotope excursion at the Paleocene–Eocene thermal maximum: The role of plant community change, *Earth Planet. Sci. Lett*., *262*, 50–65.

Smith, J.J., S.T. Hasiotis, M.J. Kraus, and D.T. Woody (2009), Transient dwarfism of soil fauna during the Paleocene-Eocene thermal maximum, *PNAS*, *106*, 17655-17660.

Speijer, R.P., and A.M. Morsi (2002), Ostracod turnover and sea-level changes associated with the Paleocene-Eocene thermal maximum, *Geology*, *30*, 23-26.

Speijer, R.P., and T. Wagner (2002), Sea-level changes and black shales associated with the late Paleocene thermal maximum: Organic-geochemical and micropaleontologic evidence from the southern Tethyan margin (Egypt-Israel), in *Catastrophic Events and Mass Extinctions: Impacts and Beyond*, *Geol. Soc. Am. Spec. Pap., 365*, edited by C. Koeberl, and K.G. Macleod, pp. 533-549, Boulder, Colorado.

Stap, L., L.J. Lourens, E. Thomas, A. Sluijs, S. Bohaty, and J.C. Zachos (2010), High-resolution deep-sea carbon and oxygen isotope records of Eocene Thermal Maximum 2 and H2, *Geology*, *38*, 607-610.

Steel, R.J., A. Dalland, K. Kalgraff, and V. Larsen (1981), The central Tertiary basin of Spitsbergen: Sedimentary development of a sheared-margin basin, in *Geology of the North Atlantic Borderland*, *Can. Soc. Pet. Geol. Mem.*, *7*, edited by J.W. Kerr, and A.J. Fergusson, pp. 647–664.

Steel, R.J., J. Gjelberg, W. Helland-Hansen, K. Kleinspehn, A. Nøttvedt, and M. Rye-Larsen (1985), The Tertiary strike-slip basins and orogenic belt of Spitsbergen, in *Strike-Slip Deformation, Basin Formation, and Sedimentation*, *Soc. Econ. Paleontol. Mineral. Spec. Publ.*, vol. 37, edited by K.T. Biddle, and N. Christie-Blick, pp. 339-359. Tulsa, Oklahoma, USA.

Stein, R., B. Boucsein, and H. Meyer (2006), Anoxia and high primary productivity in the Palaeogene central Arctic Ocean: First detailed records from Lomonosov Ridge, *Geophys. Res. Lett.*, *33*, doi:10.1029/2006GL026776.

Steurbaut, E., R. Magioncalda, C. Dupuis, S. Van Simaeys, E. Roche, and M. Roche (2003), Palynology, paleoenvironments, and organic carbon isotope evolution in lagoonal Paleocene-Eocene boundary settings in North Belgium, in *Causes and Consequences of Globally Warm Climates in the Early Paleogene*, *Geol. Soc. Am. Spec. Paper*, *369*, edited by S. Wing, P.D. Gingerich, B. Schmitz, and E. Thomas, pp. 291-317, Boulder, Colorado.

Stockmarr, J. (1971), Tablets with spores used in absolute pollen analysis, *Pollen et Spores*, *13*, 615-621.

Storey, M., R.A. Duncan, and C.C. Swisher III (2007), Paleocene-Eocene thermal maximum and the opening of the northeast Atlantic, *Science*, *316*, 587-589.

Stroeve, J., M. Serreze, S. Drobot, S. Gearheard, M. Holland, J. Maslanik, W. Meier, and T. Scambos (2008), Arctic sea ice extent plummets in 2007, *EOS Transactions of the American Geophysical Union*, *89*, doi:10.1029/2008EO020001.

Svensen, H., S. Planke, A. Malthe-Sorenssen, B. Jamtveit, R. Myklebust, T. Eidem, and S. Rey (2004), Release of methane from a volcanic basin as a mechanism for initial Eocene global warming, *Nature*, *429*, 542-545.

Svensen, H., S. Planke, and F. Corfu (2010), Zircon dating ties NE Atlantic sill emplacement to initial Eocene global warming, *J. Geol. Soc. London*, *167*, 433-436.

Swisher, C.C., Dingus, L., and Butler, R.F., (1993) $^{40}Ar/^{39}Ar$ dating and magnetostratigraphic correlation of the terrestrial Cretaceous–Paleogene boundary and Puercan Mammal Age, Hell Creek – Tullock formations, eastern Montana, *Canadian Journal of Earth Sciences, 30, 1981-1996*.

Takeda, K., and K. Kaiho (2007), Faunal turnovers in central Pacific benthic foraminifera during the Paleocene-Eocene Thermal Maximum, *Palaeogeogr.*, *Palaeoclimatol.*, *Palaeoecol., 251*, 175-197.

Thomas, D.J., J.C. Zachos, T.J. Bralower, E. Thomas, S. Bohaty (2002), Warming the fuel for the fire: evidence for the thermal dissociation of methane hydrate during the Paleocene-Eocene thermal maximum, *Geology*, *30*, 1067-1070.

Thomas, E. (1998), Biogeography of the late Paleocene benthic foram extinction, in *Late Palaeocene-Early Eocene Biotic and Climatic Events in Marine and Terrestrial Records*, edited by M.-P. Aubry, S.G. Lucas, and W.A. Berggren, pp. 214-243, Columbia University Press, New York.

Thomson, D. J. (1982), Spectrum estimation and harmonic analysis, *IEEE Procs.*, *70*, 1055-1096.

Tipple, B.J., M. Pagani, S. Krishnan, S.S. Dirghangi, S. Galeotti, C. Agnini, L. Giusberti, and D. Rio (2011), Coupled high-resolution marine and terrestrial records of carbon and hydrologic cycles variations during the Paleocene–Eocene Thermal Maximum (PETM), *Earth Planet. Sci. Lett.*, *311*, 82-92.

Torrence, C., and G.P. Compo (1998), A practical guide to wavelet analysis, *Bull. Am. Meteorol. Soc.*, *79*, 61-78.

Tremolada, F., and T.J. Bralower (2004), Nannofossil assemblage fluctuations during the Paleocene-Eocene thermal maximum at Sites 213 (Indian Ocean) and 401 (North Atlantic Ocean): Palaeoceanographic interpretations, *Mar. Micropaleontol.*, *52*, 107-116.

Tripati, A., and H. Elderfield (2005), Deep-sea temperature and circulation changes at the Paleocene-Eocene thermal maximum, *Science*, *308*, 1894-1898.

Tyson, R.V. (1995), *Sedimentary Organic Matter*, Chapman & Hall, London, UK.

Uhl, D., C. Traiser, U. Griesser, and T. Denk (2007), Fossil leaves as palaeoclimate proxies in the Palaeogene of Spitsbergen (Svalbard), *Acta Palaeobot.*, *47*, 89-107.

Uroza, C.A., and R.J. Steel (2008), A highstand shelf-margin delta system from the Eocene of West Spitsbergen, Norway, *Sediment. Geol.*, *203*, 229-245.

Van Simaeys, S., H. Brinkhuis, J. Pross, G.L. Williams, and J.C. Zachos (2005), Arctic dinoflagellate migrations mark the strongest Oligocene glaciations. *Geology*, *33*, 709-712.

Varadi, F., B. Runnegar, M. Ghil (2003), Successive refinements in long-term integrations of planetary orbits, *Astrophys. J.*, *592*, 620-630.

Volkman, J.K. (1986), A review of sterol markers for marine and terrigenous organic matter, *Org. Geochem.*, *9*, 83-99.

Volkman, J.K. (1988), Biological marker compounds as indicators of the depositional environments of petroleum source rocks, in *Lacustrine Petroleum Source Rocks*,

Geol. Soc. London Spec. Publ., *40*, edited by A.J. Fleet, K. Kelts, and M.R. Talbot, pp. 103-122, Blackwell Scientific Publications, Oxford, UK.

Vonderbank, K. (1970), Geologie und Fauna der tertiaren Ablagerungen Zentral-Spitzbergens, *Norske Polarinstitutt skrifter*, *153*, 1-119.

Waddell, L.M., and T.C. Moore Jr. (2008), Salinity of the Eocene Arctic Ocean from oxygen isotope analysis of fish bone carbonate, *Paleoceanography*, *23*, doi:10.1029/2007PA001451.

Walker, J.C.G., P.B. Hays, and J.F. Kasting (1981), A negative feedback mechanism for the long-term stabilization of Earth's surface temperature, *J. Geophys. Res.*, 9776-9782.

Wall, D., and Dale, B. (1973), Paleosalinity relationships of dinoflagellates in the late Quaternary of the Black Sea-A summary, *Geoscience and Man*, *7*, 95-102.

Wall, D., B. Dale, G.P. Lohmann, and W.K. Smith (1977), The environmental and climatic distribution of dinoflagellate cysts in the North and South Atlantic and adjacent seas, *Mar. Micropaleontol.*, *30*, 319-343.

Wang, M., and J.E. Overland (2009), A sea ice free summer Arctic within 30 years? *Geophysical Research Letters*, *36*, doi:10.1029/2009GL037820.

Weedon, G. (2003), *Time-Series Analysis and Cyclostratigraphy: Examining stratigraphic records of environmental cycles*, Cambridge University Press, Cambridge, UK.

Weijers, J.W.H., S. Schouten, A. Sluijs, H. Brinkhuis, and J.S. Sinninghe Damsté (2007), Warm Arctic continents during the Palaeocene-Eocene thermal maximum, *Earth Planet. Sci. Lett.*, *261*, 230-238.

Weller, P., and R. Stein (2008), Palaeogene biomarker records from the central Arctic Ocean (Integrated Ocean Drilling Program Expedition 302): organic carbon sources, anoxia, and sea surface temperature, *Paleoceanography*, *23*, doi:10.1029/2007PA001472.

Westerhold, T., and U. Röhl (2009), High resolution cyclostratigraphy of the early Eocene – new insights into the origin of the Cenozoic cooling trend, *Clim. Past*, *5*, 309-327.

Westerhold, T., U. Röhl, J. Laskar, I. Raffi, J. Bowles, L.J. Lourens, and J.C. Zachos (2007), On the duration of magnetochrons C24r and C25n and the timing of early Eocene global warming events: implications from the Ocean Drilling Program Leg

208 Walvis Ridge depth transect, *Paleoceanography*, *22*, PA2201, doi:10.1029/2006PA001322.

Westerhold, T., U. Röhl, I. Raffi, E. Fornaciari, S. Monechi, V. Reale, J. Bowles, and H.F. Evans (2008), Astronomical calibration of Paleocene time, *Palaeogeogr.*, *Palaeoclimatol.*, *Palaeoecol.*, *257*, 377-403.

Westerhold, T., U. Röhl, H.K. McCarren, and J.C. Zachos (2009), Latest on the absolute age of the Paleocene-Eocene thermal maximum (PETM): new insights from exact stratigraphic position of key ash layers +19 and -17, *Earth Planet. Sci. Lett.*, *287*, 412-419.

Wing, S., H. Bao, P.L. Koch (2000), An early Eocene cool period? Evidence for continental cooling during the warmest part of the Cenozoic, in *Warm Climates in Earth History*, edited by B.T. Huber, K.G. Macleod, and S.L. Wing, pp. 197-237, Cambridge University Press, Cambridge, UK.

Wing, S.L., G.J. Harrington, F.A. Smith, J.I. Bloch, D.M. Boyer, and K.H. Freeman (2005), Transient floral change and rapid global warming at the Paleocene-Eocene boundary, *Science*, *310*, 993-996.

Wood, G.D., A.M. Gabriel, and J.C. Lawson (1996), Palynological techniques – processing and microscopy, in *Palynology: Principles and applications*, *Am. Assoc. Stratigr. Palynol. Found.*, *3*, edited by J. Jansonius, and D.C. McGregor, pp. 29-50, Publishers Press, Salt Lake City, Utah.

Zachos, J.C., M. Pagani, L. Sloan, E. Thomas, K. Billups (2001), Trends, rhythms, and aberrations in global climate 65 Ma to present, *Science*, *292*, 686-693.

Zachos, J.C., M.W. Wara, S. Bohaty (2003), A transient rise in tropical sea surface temperature during the Paleocene-Eocene Thermal Maximum, *Science*, *302*, 1551-1554.

Zachos, J.C., D. Kroon, P. Blum, J. Bowles, P. Gaillot, T. Hasegawa, E.C. Hathorne, D.A. Hodell, D.C. Kelly, J-H. Jung, S.M. Keller, Y.S. Lee, D.C. Leuschner, Z. Liu, K.C. Lohmann, L. Lourens, S. Monechi, M. Nicolo, I. Raffi, C. Riesselman, U. Röhl, S.A. Schellenberg, D. Schmidt, A. Sluijs, D. Thomas, E. Thomas, and H. Vallius (2004), *Proceedings of the Ocean Drilling Program, Initial Reports*, *208*. College Station, Texas.

Zachos, J.C., U. Röhl, S.A. Schellenberg, A. Sluijs, D.A. Hodell, D.C. Kelly, E. Thomas, M. Nicolo, I. Raffi, L.J. Lourens, H. McCarren, and D. Kroon, (2005), Rapid

acidification of the ocean during the Paleocene-Eocene Thermal Maximum, *Science*, *308*, 1611-1615.

Zachos, J., S. Schouten, S. Bohaty, T. Quattlebaum, A. Sluijs, H. Brinkhuis, S. Gibbs, and T. Bralower (2006), Extreme warming of the mid-latitude coastal ocean during the Paleocene-Eocene Thermal Maximum: Inferences from TEX_{86} and isotope data, *Geology*, *34*, 737-740.

Zachos, J.C., S.M. Bohaty, C.M. John, H. McCarren, D.C. Kelly, and T. Nielsen (2007), The Palaeocene-Eocene carbon isotope excursion: constraints from individual shell planktonic foraminifer records, *Phil. Trans. R. Soc. A.*, *365*, 1829-1842.

Zachos, J.C., G.R. Dickens, and R.E. Zeebe (2008), An early Cenozoic perspective on greenhouse warming and carbon-cycle dynamics, *Nature*, *451*, 279-283.

Zachos, J.C., H. McCarren, B. Murphy, U. Röhl, T. Westerhold (2010), Tempo and scale of late Paleocene and early Eocene carbon isotope cycles: implications for the origin of hyperthermals, *Earth Planet. Sci. Lett.*, *299*, 242-249.

Zeebe, R., and J.C. Zachos (2007), Reversed deep sea carbonate ion basin gradient during the Paleocene-Eocene Thermal Maximum. *Paleoceanography*, *22*, doi:10.1029/2006PA001395.

Zeebe, R.E., J.C. Zachos, and G.R. Dickens (2009), Carbon dioxide forcing alone insufficient to explain Palaeocene-Eocene Thermal Maximum warming, *Nat. Geosci.*, *2*, 576-580.

Zonneveld, K.A.F., G.J.M. Versteegh, and G.J. De Lange (2001), Palaeoproductivity and post-depositional aerobic organic matter decay reflected by dinoflagellate cyst assemblages of the Eastern Mediterranean S1 sapropel, *Marine Geology*, *172*, 181-195.

Zonneveld, K.A.F., G.J.M. Versteegh, and M. Kodrans-Nsiah (2008), Preservation and organic chemistry of late Cenozoic organic-walled dinoflagellate cysts: A review, *Mar. Micropaleontol.*, *68*, 179-197.

Zonneveld, K.A.F., L. Chen, J. Möbius, M.S. Mahmoud (2009), Environmental significance of dinoflagellate cysts from the proximal part of the Po River discharge plume (off southern Italy, eastern Mediterranean), *J. Sea Res.*, *62*, 189-213.